NASA/CR-2007-214880

Multi-Functional Sandwich Composites for Spacecraft Applications: An Initial Assessment

Daniel O. Adams, Nicholas Jason Webb, Cody B. Yarger, Abigail Hunter, and Kelli D. Oborn
University of Utah, Salt Lake City, Utah

June 2007

The NASA STI Program Office . . . in Profile

Since its founding, NASA has been dedicated to the advancement of aeronautics and space science. The NASA Scientific and Technical Information (STI) Program Office plays a key part in helping NASA maintain this important role.

The NASA STI Program Office is operated by Langley Research Center, the lead center for NASA's scientific and technical information. The NASA STI Program Office provides access to the NASA STI Database, the largest collection of aeronautical and space science STI in the world. The Program Office is also NASA's institutional mechanism for disseminating the results of its research and development activities. These results are published by NASA in the NASA STI Report Series, which includes the following report types:

- TECHNICAL PUBLICATION. Reports of completed research or a major significant phase of research that present the results of NASA programs and include extensive data or theoretical analysis. Includes compilations of significant scientific and technical data and information deemed to be of continuing reference value. NASA counterpart of peer-reviewed formal professional papers, but having less stringent limitations on manuscript length and extent of graphic presentations.

- TECHNICAL MEMORANDUM. Scientific and technical findings that are preliminary or of specialized interest, e.g., quick release reports, working papers, and bibliographies that contain minimal annotation. Does not contain extensive analysis.

- CONTRACTOR REPORT. Scientific and technical findings by NASA-sponsored contractors and grantees.

- CONFERENCE PUBLICATION. Collected papers from scientific and technical conferences, symposia, seminars, or other meetings sponsored or co-sponsored by NASA.

- SPECIAL PUBLICATION. Scientific, technical, or historical information from NASA programs, projects, and missions, often concerned with subjects having substantial public interest.

- TECHNICAL TRANSLATION. English-language translations of foreign scientific and technical material pertinent to NASA's mission.

Specialized services that complement the STI Program Office's diverse offerings include creating custom thesauri, building customized databases, organizing and publishing research results ... even providing videos.

For more information about the NASA STI Program Office, see the following:

- Access the NASA STI Program Home Page at ***http://www.sti.nasa.gov***

- E-mail your question via the Internet to help@sti.nasa.gov

- Fax your question to the NASA STI Help Desk at (301) 621-0134

- Phone the NASA STI Help Desk at (301) 621-0390

- Write to:
  NASA STI Help Desk
  NASA Center for AeroSpace Information
  7115 Standard Drive
  Hanover, MD 21076-1320

NASA/CR-2007-214880

Multi-Functional Sandwich Composites for Spacecraft Applications: An Initial Assessment

Daniel O. Adams, Nicholas Jason Webb, Cody B. Yarger, Abigail Hunter, and Kelli D. Oborn
University of Utah, Salt Lake City, Utah

National Aeronautics and
Space Administration

Langley Research Center
Hampton, Virginia 23681-2199

Prepared for Langley Research Center
under Grant NAG1-03085

June 2007

Available from:

NASA Center for AeroSpace Information (CASI)
7115 Standard Drive
Hanover, MD 21076-1320
(301) 621-0390

National Technical Information Service (NTIS)
5285 Port Royal Road
Springfield, VA 22161-2171
(703) 605-6000

ABSTRACT

Current spacecraft implement relatively uncoupled material and structural systems to address a variety of design requirements, including structural integrity, damage tolerance, radiation protection, debris shielding and thermal insulation. This investigation provided an initial assessment of multi-functional sandwich composites to integrate these diverse requirements. The need for radiation shielding was addressed through the selection of polymeric constituents with high hydrogen content, such as a polyethylene (PE) foam core and Spectra® fiber composite facesheets. Radiation shielding tests were performed at Brookhaven National Laboratory for five candidate sandwich composite components as well as two complete sandwich composite specimens. Additionally, computational simulations were performed using the heavy ion code GRNTRN to predict the nuclear fragmentation of high-energy ions within these sandwich materials. To provide increased damage tolerance and debris shielding, manufacturing techniques were developed to incorporate transverse stitching reinforcement, internal Spectra®/epoxy layers, and a self-healing ionomer membrane. Flatwise tensile and core shear testing were used to assess the interlaminar strength of proposed sandwich configurations, and identify any material compatibility or manufacturing-related problems. Quasi-static indentation testing and analysis was performed to assess the improvements in damage tolerance produced by transverse stitching reinforcements. To assess the effects of a space environment, thermal expansion behavior of the candidate foam materials was investigated under a vacuum and increasing temperature. Finally, a thermal expansion model was developed for foam under vacuum conditions and its predictive capability assessed.

TABLE OF CONTENTS

1. INTRODUCTION

Current spacecraft designs include materials and structural systems engineered to satisfy a variety of requirements, including structural integrity, damage tolerance, radiation protection, debris/micrometeoroid shielding, and thermal insulation. These diverse design requirements are currently satisfied through the use of relatively uncoupled material and structural systems, each designed for a specific function. Current designs commonly use an aluminum shell to provide structural integrity. Heavy parasitic shielding is added to satisfy radiation protection requirements but is not used to carry structural loads. Debris and micrometeoroid protection is added through the use of an offset wall to shatter and reduce the initial energy of an object. As a result, current spacecraft are relatively heavy, and thus costly to transport into orbit. This research investigation focused on addressing these diverse design requirements using a multifunctional sandwich composite concept. As shown in Figure 1, this concept utilizes lightweight core materials bonded to a series of fiber reinforced facesheets. Transverse reinforcements are used to address damage tolerance as well as structural integrity requirements.

In this investigation, initial emphasis was placed on selecting sandwich constituents that would provide beneficial radiation shielding. Three sandwich configurations were selected for assessment, each featuring facesheets composed of Spectra® 900 fabric (ultra-high molecular weight polyethylene) infiltrated with epoxy resin. The configurations were distinguished by the use of different closed-cell foams as core materials: polyethylene terephthalate (PET), polyethylene (PE), and polypropylene (PP). Generally these polymeric materials are not suitable for structural applications. In a sandwich configuration, however, it is proposed that these materials can provide a structural system which also offers radiation shielding and thermal insulation. Furthermore, it is proposed that the incorporation of transverse reinforcement and internal facesheet/membrane layers will significantly improve their structural integrity, damage tolerance and space debris/micrometeoroid shielding.

The previously mentioned sandwich composite constituents typically exhibit poor chemical bonding characteristics. Thus, emphasis was placed on the development of an appropriate manufacturing technique capable of producing a viable sandwich composite. It was found that this could be accomplished using a Vacuum Assisted Resin-Transfer Molding (VARTM) process. Following the production of sandwich panels of each of the three configurations, mechanical testing was performed to evaluate their mechanical properties for structural applications. Flatwise tensile testing (ASTM C 297 [1]) and core shear testing (ASTM C 273 [2]) were used to assess the interlaminar normal and shear strength of the sandwich configurations. These test methods were selected for use in identifying material compatibility problems associated with the facesheet and core materials as well as manufacturing-related problems such as core crushing and improper facesheet consolidation. Additionally, these tests were used to investigate the effects of including transverse reinforcements to the sandwich configurations.

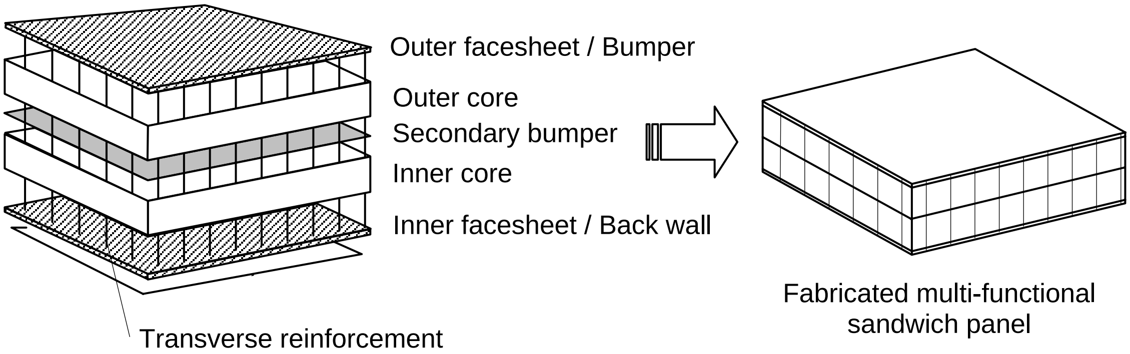

Figure 1. Proposed multifunctional sandwich composite.

Quasi-static indentation testing was performed to evaluate the effects of transverse reinforcements and sandwich configuration on the damage tolerance of multifunctional sandwich composites. Energy absorption was determined and an increased understanding of damage evolution during loading was obtained. To gain further understanding of the effects of transverse reinforcement and facesheet location on damage tolerance following indentation and penetration, finite element modeling was performed using ANSYS 8.0 [3].

Upon completion of mechanical testing, additional testing was performed to evaluate the proposed sandwich constituents in a simulated space environment that included elevated temperature and the application of a vacuum. The results of this testing were used to assess the operating range of potential sandwich configurations and to evaluate the predictive capabilities of an analytical model for foam expansion. Characterization data of the foam for use in the selected model was obtained using scanning electron microscopy (SEM) and tensile testing (ASTM D 638 [4]) of the foam resin.

2. LITERATURE REVIEW

Sandwich panels use a lightweight core material to separate two stiff, strong facesheets. Facesheet materials are typically composed of some type of fiber-reinforced laminate, while standard core materials are typically cellular in nature, such as honeycombs, balsa wood or polymeric foams. This sandwich configuration yields a significantly higher moment of inertia in comparison with that of a simple laminate manufactured from the same number of layers of facesheet material. Thus sandwich composites offer an efficient structure for use in applications involving bending and buckling loads, and have been used extensively in aerospace applications where weight reduction is critical [5].

Additional manufacturing techniques can be used to further enhance the attractive properties of sandwich composites. The introduction of vertical (orthogonal) through-the-thickness stitching reinforcement has been demonstrated to effectively increase out-of-plane tensile strength, interlaminar shear strength, damage tolerance, and energy absorption [6]. Further examination of angled (biased) through-the-thickness stitching has demonstrated additional improvements over orthogonal through-the-thickness stitching for stiffness under three point bending testing and in damage tolerance for insert pull-out testing [7, 8]. Improvements in the energy absorption of sandwich structures can be made by influencing the debonding mechanisms during loading. Such improvements can be achieved with the insertion of an interior facesheet that lies between the two outer facesheets [9].

The above listed factors provide justification for selecting sandwich composites with transverse reinforcement and internal facesheet/membrane layers to meet structural requirements as well as to achieve damage tolerance and debris/micrometeoroid shielding. Through the selection of the constituents of the sandwich composite, further tailoring of the composite properties can be accomplished to increase its multifunctional behavior.

Radiation is a top biological concern for astronauts embarking on long-term missions, such as the proposed mission to Mars [10]. Since hydrogen has the propensity to fragment ions, hydrogen-containing materials such as polymers are good candidates for shielding materials. Additionally, hydrogen is particularly effective in undergoing elastic collisions with secondary neutrons generated within the shield, thereby reducing the neutrons' energies and making them susceptible for energy absorption by other hydrogen atoms or elements [11,12,13]. For this reason, an emphasis was placed on the use of polymeric foam cores with high hydrogen content and Spectra® fiber reinforced facesheets in this investigation.

Spectra® fibers, made from ultra-high molecular weight polyethylene, are used by Honeywell International Inc. [14] in their Spectra Shield® product for ballistics protection because of their high-modulus and high-energy absorption characteristics. Spectra® fibers also have excellent tensile characteristics, with a specific strength that is ten times that of steel. Improved impact protection can therefore be obtained by selecting Spectra® fiber as the reinforcement for facesheets in a sandwich composite.

Additional impact protection can be included by incorporating a DuPont^{TM} Surlyn® [15] membrane layer in the sandwich composite. Surlyn, a poly(ethylene-co-methacrylic acid) (EMAA) ionomer-based material, has been studied extensively for its ability to "self-heal" following impact puncture [16, 17, 18]. Self-healing has been observed for objects with velocities from 300 to 1200 ft/s [16] with varying degrees of recovery, including a return to an airtight seal [18], which is of particular interest for space applications.

The above listed factors provide justification for selecting sandwich composites in general to meet structural requirements as well as damage tolerance and debris/micrometeoroid shielding. Through selection of the constituents of the sandwich composite further tailoring of the composite properties can be accomplished to increase its multifunctional behavior.

Closed-cell polymeric foam cores can also be used to provide excellent thermal insulation [5]. In this investigation, composite sandwich panels were successfully manufactured with two different core materials separated by an internal facesheet layer. This assembly allows for an additional core section to provide increased thermal protection. It is noted that the use of advanced polyimide foams for thermal insulation has received attention from NASA Langley Research Center (LaRC) [19, 20] and may be incorporated into a sandwich configuration.

Significant research has been performed to investigate the thermal expansion of polymeric foam materials. Polyethylene foam in particular has been studied extensively using thermomechanical analysis to better understand the effect of cell size [21], density [22] and amount of copolymer (EVA) [23] on thermal expansion. Research has demonstrated [24] that the Coefficient of Thermal Expansion (CTE) for polyethylene: (1) shows minimal variation over the range of 0 to 40°C; (2) is approximately equal to that of the base polymer for densities greater than 80 kg/m^3; (3) is inversely related to the tensile modulus; and (4) can be dependent upon cell structure, including anisotropy. Several different models have been proposed in the literature to predict thermal expansion of polymeric foams in general. The models vary in complexity from simple strut-less membrane and membrane-less strut models [25] to more advanced considerations such as a regular Kelvin foam model [26]. The research completed to date, however, has only considered thermal expansion at normal atmospheric pressure. No extension has been made to consider the behavior of foam within a vacuum, which would increase the role of gas expansion that has already been shown to be significant under atmospheric conditions [22].

3. MATERIAL SELECTION

3.1 Core Material

As discussed in Chapter 2, previous researchers have shown that polymeric materials with high hydrogen content may provide effective radiation shielding in a space environment. Based on these findings, an assortment of commercially-available foam materials with significant levels of hydrogen were obtained from a variety of suppliers. As shown in Table 1 these foam materials included polyethylene, polyethylene terephthalate (PET), polyurethane, polyester, polystyrene and polypropylene. Initially both open-cell and closed-cell foams were obtained. After a preliminary investigation into the manufacturing of sandwich panels, it was determined that closed cell foams were better suited for use in the Vacuum Assisted Resin Transfer Molding (VARTM) processing method selected for manufacturing. Thus, the investigation into open-cell foam core materials was discontinued.

Table 1. Foam Materials Obtained for Investigation

Material	Supplier	Open/Closed Cell	Available Densities (kg/m^3)
Polyethylene	Cellect [27]	Open	32
	Dow [28]	Closed	32, 64, 96, 144
	Fortifoam [29]	Closed	96, 160, 192, 256, 320
	Merryweather [30]	Closed	32, 128
	Sealed Air [31]	Closed	32
	Voltek [32]	Closed	24, 32, 64, 128, 160, 192, 240, 256, 320
PET	Alcan Baltek [33]	Closed	128, 208
	Fagerdala World Foams [34]	Closed	110, 125, 130, 150, 350
Polyurethane	Keystone [35]	Open	40, 48
	Gen. Plastics [36]	Closed	48, 64, 160, 320
	Illbruck [37]	Open	96, 144, 240
Polyester	Crest [38]	Open	25, 48, 64
Polystyrene	Marko [39]	n/a	32, 64
Polypropylene	JSP [40]	Closed	72, 128, 192

Based upon radiation shielding simulations (to be presented in the following chapter), polyethylene (PE), polyethylene terephthalate (PET) and polypropylene (PP) were shown to produce greater radiation shielding than the baseline aluminum and thus were believed to be effective at providing radiation shielding in a space environment. Once preliminary sandwich construction revealed that these three foam core materials could be used in the selected manufacturing process, they were used exclusively for further assessment. More detailed information on these selected foams is provided in Table 2, including density, manufacturer, and chemical composition.

3.2 Facesheet Material

Similar to the material selection process for core materials, interest was placed on obtaining facesheet materials with high hydrogen content. Of particular interest was the ultra-high molecular weight polyethylene fiber known as Spectra® [14]. Due to concerns that woven Spectra fabric may not perform well using Vacuum Assisted-Resin Transfer Molding (VARTM) processing, however, woven carbon fabric was also considered. The two specific fibers used in the facesheet layers of the multifunctional sandwich composites were T300 carbon and Spectra 900. Once the feasibility of using Spectra fabric facesheets in the VARTM process had been established, however, the use of carbon fiber facesheets in specimen manufacturing and mechanical testing was discontinued due to its reduced radiation shielding effectiveness. For all sandwich configurations, the matrix material used in the facesheets was an epoxy consisting of EPON^{TM}/EPIKOTE^{TM} Resin 862 combined with EPIKURE^{TM} Curing Agent 9553 (mixture ratio of 100:16.9) [41].

Table 2. Closed-Cell Foams Used as Core Materials
in Multifunctional Sandwich Composites

Core Material	**Core Density, kg/m^3**	**Manufacturer**	**Chemical Composition (Mass %)**
Polyethylene (PE)	24 – 320	Voltek LLC	85.6% C 14.4% H
Polypropylene (PP)	72 – 192	JSP Int’l	85.6% C 14.4% H
Polyethylene Terephthalate (PET)	110 – 350	Fagerdala World Foams	62.5% C 4.2% H 33.3% O

3.3 Self-Healing Material

A variety of different, commercially available materials are known to exhibit self-healing properties. Notable examples include React-A-Seal®, Nucrel® and Surlyn® [16]. Surlyn was selected for use in this investigation based on the availability of information from previous research done in coordination with Dr. Emilie Siochi at NASA Langley Research Center [17].

4. SANDWICH PANEL FABRICATION

4.1 Vacuum Assisted Resin Transfer Molding (VARTM)

A Vacuum-Assisted Resin Transfer Molding (VARTM) process was selected for use in the manufacturing of sandwich panels. VARTM is a low cost, out-of-autoclave process used previously by the University of Utah to successfully manufacture a variety of sandwich panels, including configurations with vertical through-the-thickness stitching reinforcement [42, 43]. In this process, a specified lay-up of facesheet fiber reinforcement is placed on both sides of the foam core material. A layer of porous Teflon-coated fiberglass (release layer) is then placed over the exposed layer of both facesheets, followed by a layer of perforated plastic mesh. This lay-up configuration is depicted in Figure 2. The Teflon-coated fiberglass layer is used to prevent the plastic mesh and other surfaces from becoming bonded to the facesheets, while the perforated mesh is added to assist in the flow of resin. This setup is then placed on a flat aluminum mold which is also covered with a Teflon-coated fiberglass layer, and the entire assembly is then placed in a vacuum bag as shown in Figure 3.

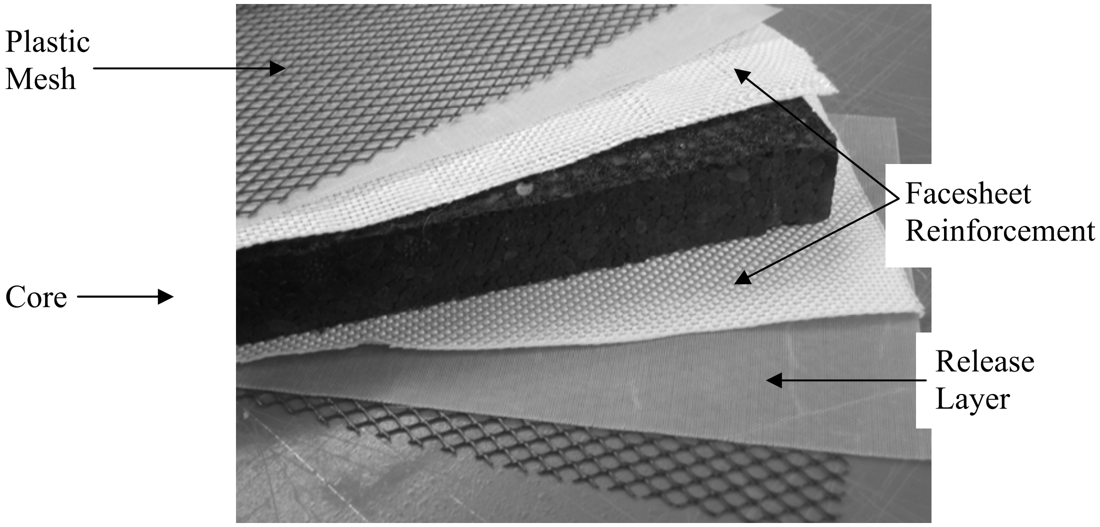

Figure 2. Lay-up configuration for VARTM processing.

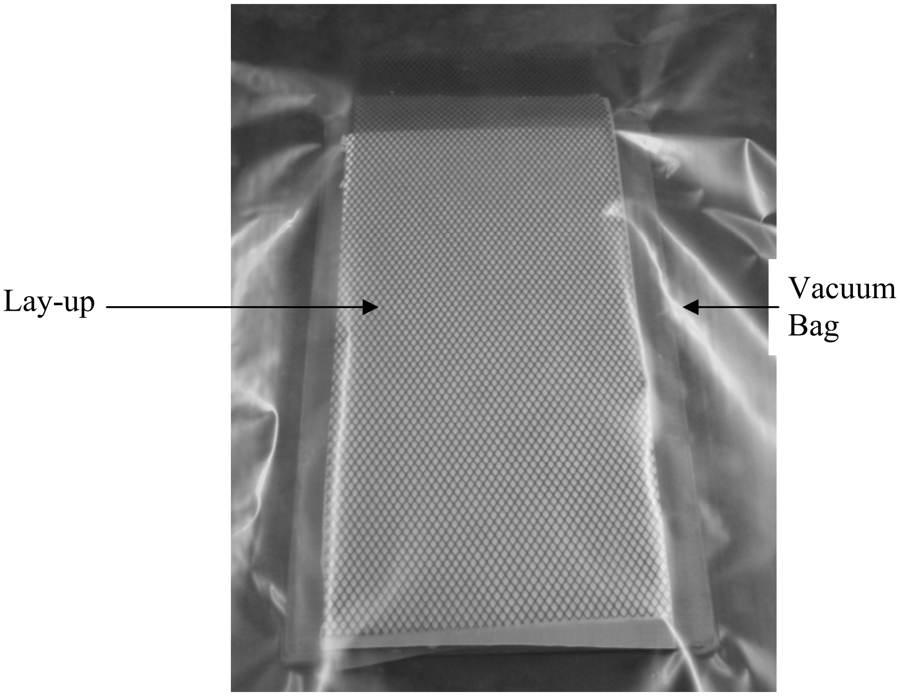

Figure 3. Placing of the lay-up into a vacuum bag.

Following this, a permeable material often referred to as breather cloth is placed such that it makes a vapor path from the back of the sandwich panel to a vacuum hose connected to a vacuum pump. A piece of tubing is then placed adjacent to one edge of the sandwich panel, separated by Teflon-coated fiberglass, and is used to supply resin to the assembly. The vacuum bag is sealed over the sandwich assembly as well as the resin/vacuum hoses using vacuum sealant tape. An overall view of this sealed lay-up is provided in Figure 4, with a detailed view of the seal around the vacuum hose shown in Figure 5.

Figure 4. Vacuum bag and hose sealed with vacuum tape.

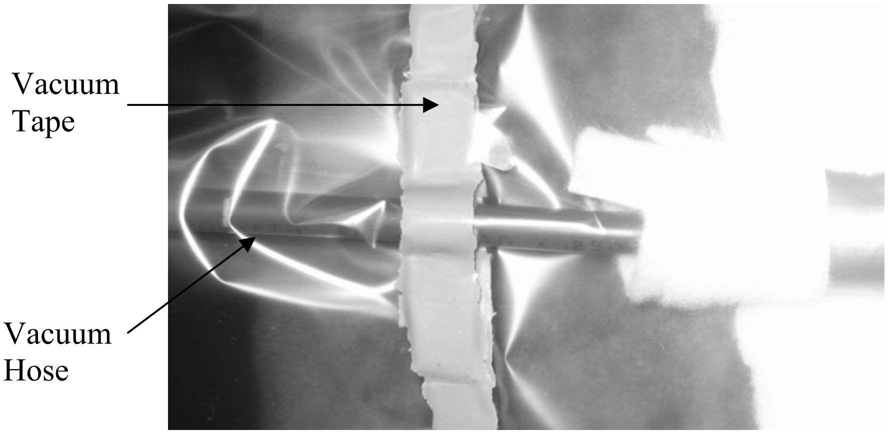

Figure 5. Bag and hose sealed with vacuum tape.

After sealing of the vacuum bag, the inlet hose is clamped and the vacuum pump is used to remove air from inside the bag. The inlet hose is then placed into the container of epoxy resin matrix and unclamped, allowing resin to be drawn through the sandwich panel. A series of photographs depicting resin being drawn through a sandwich panel is provided in Figure 6. Once the resin had completely infiltrated the entire sandwich panel, the inlet hose was clamped off and the assembly was placed in a convection oven and allowed to cure at 50°C for two hours.

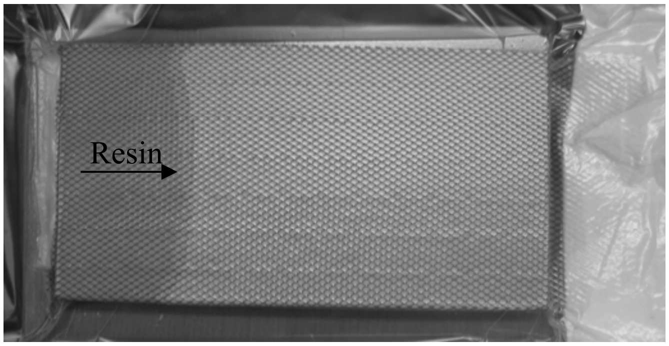

a. Initial infiltration.

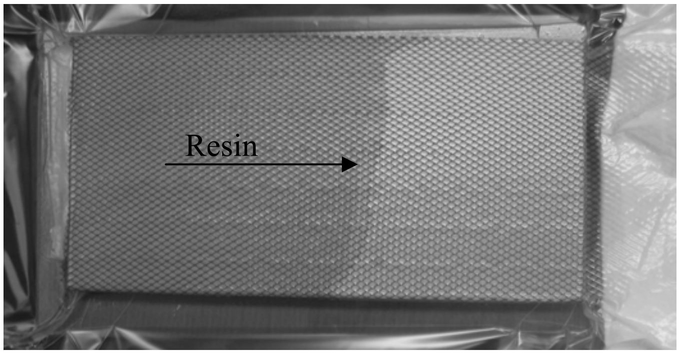

b. Midway through infiltration process.

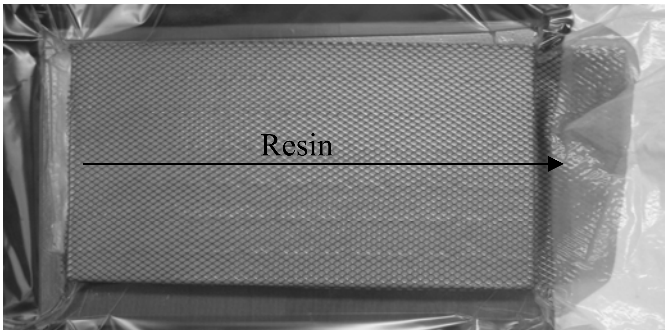

c. Infiltration completed.

Figure 6. Resin infiltration of a sandwich panel.

4.2 Manufacturing of Multifunctional Sandwich Composite Prototypes

Once the constituents described above had been successfully used to manufacture relatively thick sandwich composites, fabrication methods were developed for incorporating Spectra 900 transverse reinforcements (stitches), an intermediate "bumper" facesheet layer as well as an internal self-healing ionomer layer to enhance the multifunctional aspect of the sandwich composites. These methods were incorporated into the sandwich constructions following a progressive approach, as will be discussed below.

4.2.1 Vertical Through-the-Thickness Stitching

The first step in the progressive fabrication approach was the integration of vertical through-the-thickness stitching using Spectra 900 yarn. Prior to resin infiltration, each sandwich assembly was stitched through-the-thickness using Spectra 900 yarn. A modified lockstitch was used, placing the intersection between the stitch yarn and the bobbin yarn at the lower surface of the panel rather than at an interior location as illustrated in Figure 7 and Figure 8.

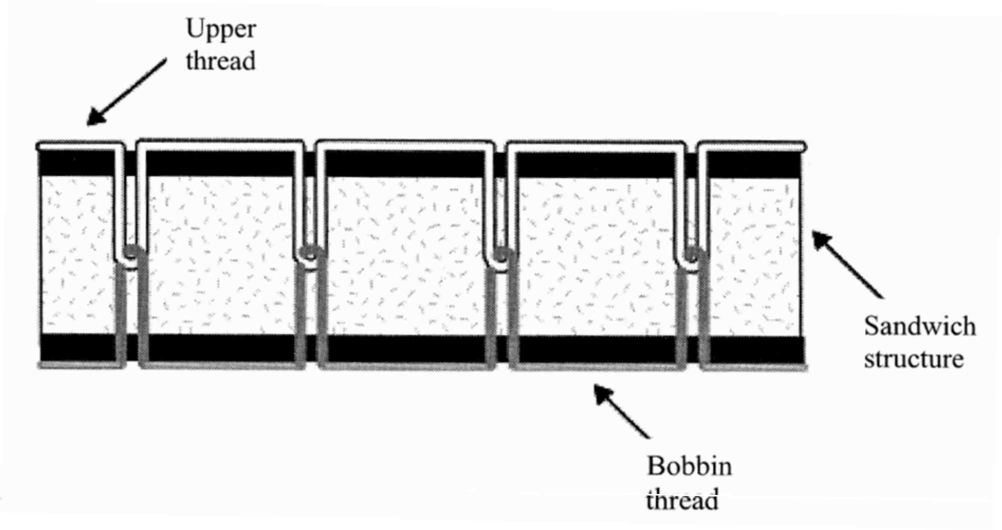

Figure 7. Diagram of a traditional lockstitch..

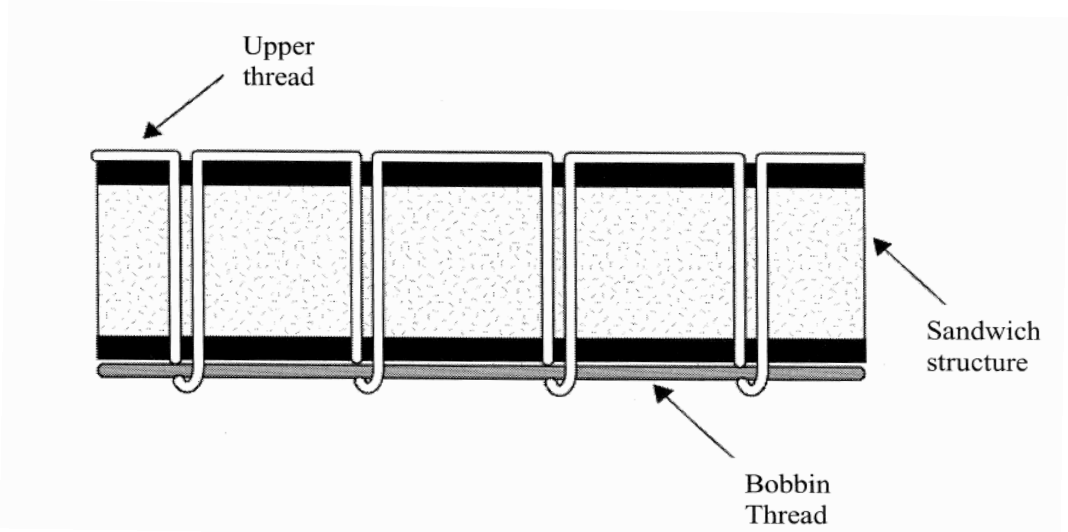

Figure 8. Diagram of the modified lockstitch used in this investigation.

Stitches were inserted by hand using pre-made stitch holes, although in a production environment the stitching process would be automated and would likely utilize multiple-needle stitching machines. Specimens with two different densities of vertical through-the-thickness stitching were created: 0.16 stitch/cm^2 (Figure 9) and 0.62 stitch/cm^2 (Figure 10). For the lower stitch density, the pre-made stitch holes were created using a milling operation with a size 55 drill bit, whereas the higher stitch density holes were inserted by a three-axis CNC water jet cutting machine with a 0.51 mm nozzle. These operations were performed to generate a template in the foam core that allowed hand stitching to be performed while keeping the proper stitch orientation and tension. These machining operations also eliminated the need for thick stitching needles thereby minimizing the amount of excess resin introduced into the sandwich. Once each panel had been stitched by hand, the panel was infiltrated using the VARTM process as described previously.

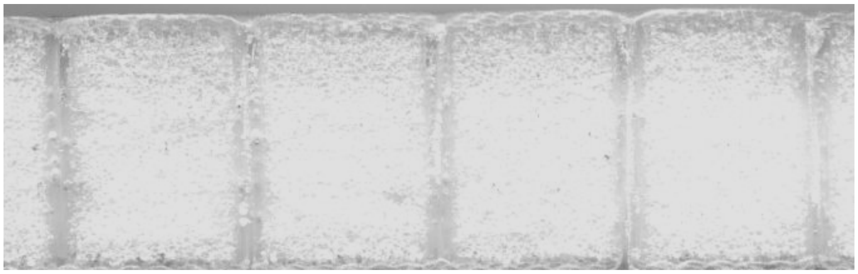

Figure 9. 0.16 stitch/cm^2 stitch density.

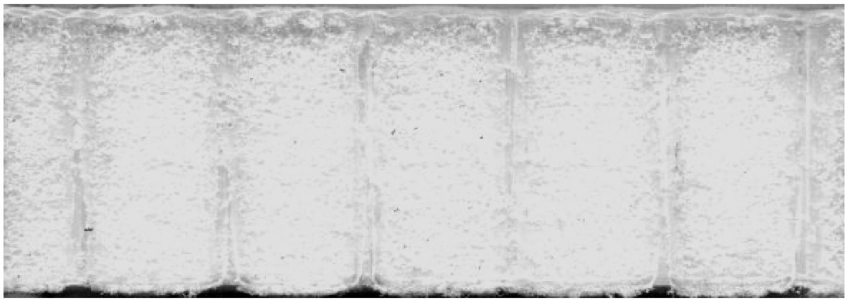

Figure 10. 0.62 stitch/cm^2 stitch density.

4.2.2 Internal Facesheet

The next fabrication step featured the incorporation of the previously discussed through-the-thickness stitching and an internal facesheet layer. This prototype multifunctional sandwich configuration is shown in Figure 11. This prototype consists of two outer facesheets and an internal facesheet made from woven Spectra 900 fabric. The 3.7 mm thick facesheet layers are separated by two different polymeric foam layers: a 25 mm thick PE layer and a 51 mm thick PET layer. The first step in the manufacturing of this configuration was machining the stitch holes in each core layer. After assembly of the exterior and internal facesheet layers as well as the two core layers, the entire assembly was hand stitched through the thickness using the modified lock stitch method as discussed previously.

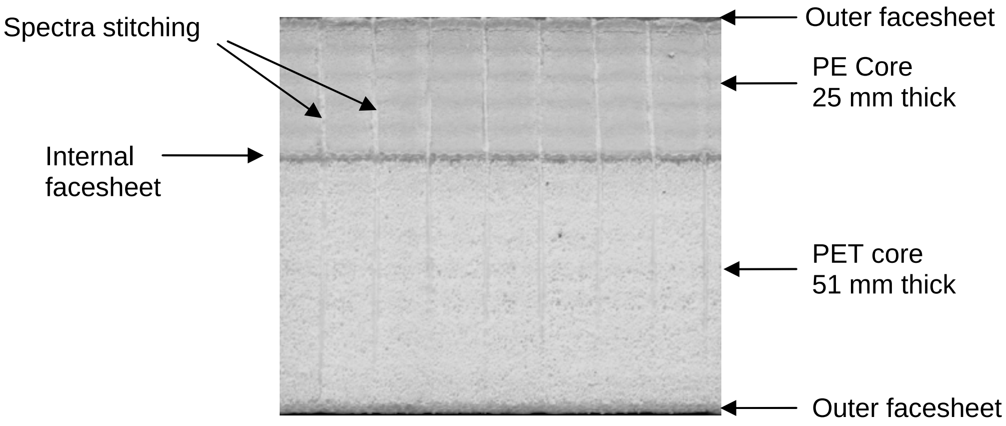

Figure 11. Multifunctional stitched sandwich composite with internal facesheet.

4.2.3 Self-Healing Ionomer Layer

The next fabrication step focused on the addition of a self-healing ionomer layer. The specific ionomer material chosen was DuPont^{TM} Surlyn® (EMAA ionomer), which has been shown to exhibit self-healing properties following projectile impact [16, 17]. The Surlyn layer is incorporated into the sandwich using a melt-bond procedure that consists of melting a 6.4 mm thick layer between two sections of 19 mm thick PET foam using a hot press at 150°C as shown in Figure 12. This procedure is used to create a mechanical bond between the constituents. Following the melt bond procedure, a cutting operation is used to square off the edges. A CNC milling operation is then used to generate stitch holes through the thickness of the Surlyn embedded core. This core then replaces the inner core section shown in Figure 11 and the remaining manufacturing follows the procedure outlined in Section 4.2.2. A completed prototype with this configuration is shown in Figure 13.

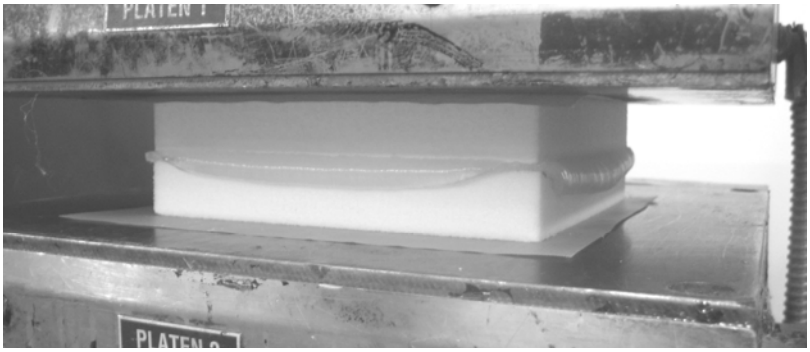

Figure 12. Final stages of the melt bond procedure.

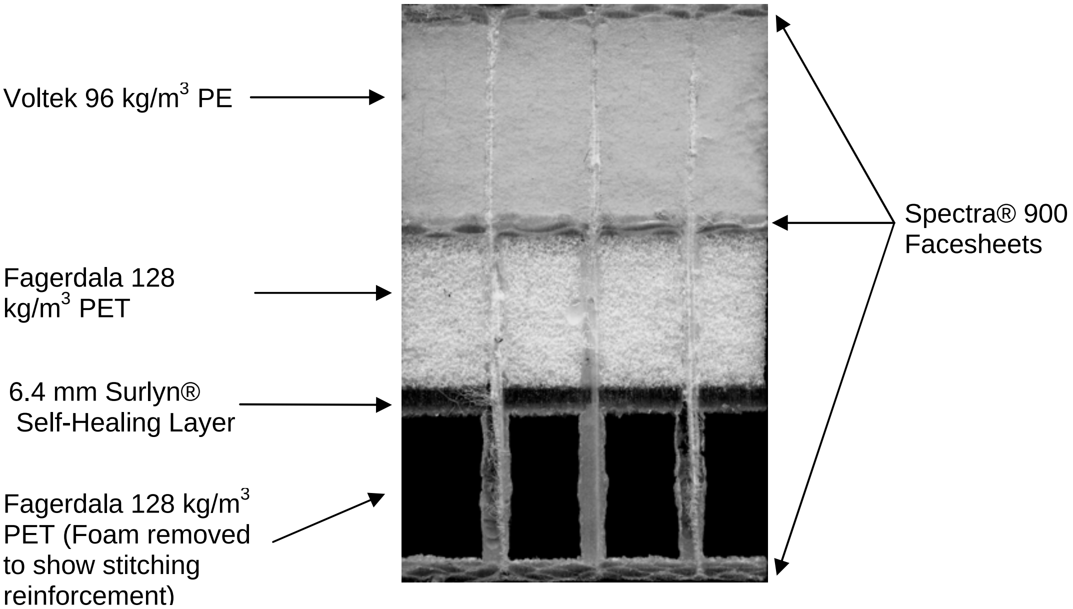

Figure 13. Multifunctional stitched sandwich with intermediate facesheet and Surlyn layer.

4.2.4 Angled Through-the-Thickness Reinforcement

The final stage focused on developing a method for altering the through-the-thickness orientation of stitching. Using a five-axis CNC water jet cutting machine with the same nozzle used for vertical through-the-thickness stitching, a truss-like network of holes at 90° and 42.5° were machined into core specimens. Stitching was then incorporated by hand using a modified lockstitch approach as described previously. An example of this type of through-the-thickness stitching is provided in Figure 14.

Figure 14. Angled through-the-thickness stitching of sandwich composite.

4.3 Manufacturing of Specimens for Radiation Shielding Experimentation

At the request of NASA Langley Research Center, samples of six different configurations were manufactured for radiation testing. The six configurations were: a Spectra laminate, a carbon laminate, PET foam, polyurethane foam, a carbon/polyurethane sandwich and a Spectra/PET sandwich. The two sandwich configurations manufactured for radiation shielding experiments are shown in Figure 15 and Figure 16. For all samples, the thicknesses and core densities were chosen to produced samples with an areal weight of 5 g/cm^2. Although the densities and amounts of constituents used greatly exceeded that associated with the construction of multifunctional sandwich prototypes and test specimens, the methods used in the manufacturing process were unaltered.

Figure 15. 5g/cm^2 carbon/polyurethane sandwich composite.

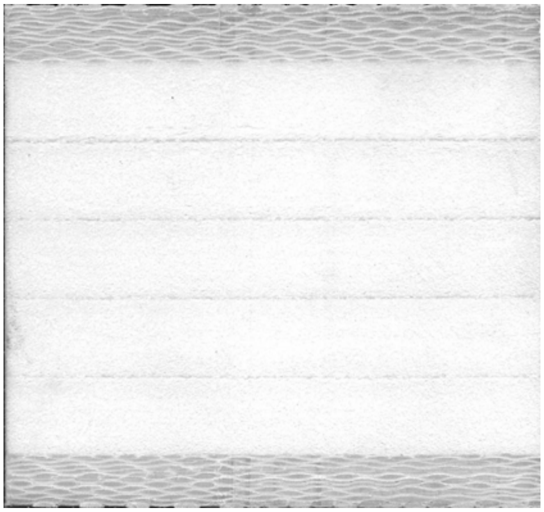

Figure 16. 5g/cm^2 Spectra/PET sandwich composite.

5. RADIATION SHIELDING STUDIES

5.1 Introduction

For human exploration in space, the shielding of ionizing radiation is important to mitigate the risk factors associated with long-duration space flights. The ionizing radiation in space emanates from three sources that include energetic ions formed from stripping the electrons from natural elements [44]. These sources of radiation are associated with different processes and are identified as those of galactic origin (Galactic Cosmic Rays, GCR), solar origin (Solar Particle Events, SPE), and trapped protons and electrons due to the Earth's geomagnetic field (Induced or Trapped). Figure 17 shows the space radiation environment for most ionized particles.

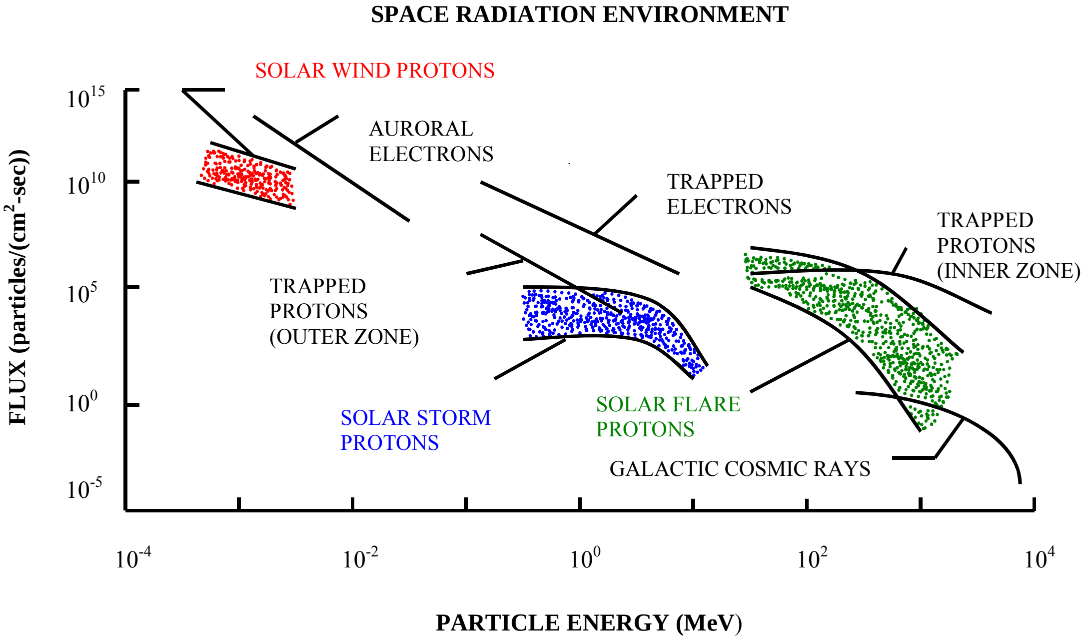

Figure 17. Trapped, solar interplanetary, and GCR radiation. environments

In prior manned space missions, GCR-induced biological damage was considered negligible since the mission times were relatively short and the main radiation concern was the very intense SPE events, which can rise unexpectedly to high levels, delivering an extremely high dose of radiation after only several hours of exposure.

Long duration missions at low earth orbit (LEO), such as an annual stay onboard the International Space Station (ISS) at an altitude of 400 km and the new evolutionary lunar-

Mars exploration initiative (Crew Exploration Vehicle, CEV), introduce new challenges in designing astronauts' protection habitats [45]. The accumulation of exposures due to GCR at high inclination LEO such as ISS can significantly increase the risks of cancer to the astronauts. As for deep space exploration a large contribution of the exposure to the astronauts is through the ions with high charge and energy (HZE), for which there is little experience on the examination of shield properties or biological responses. These ions are more hazardous to human tissue than low-energy particles, such as protons.

NASA's thrust into long duration space exploration will entail crew exposures to significant levels of HZE GCRs that will have importance consequences on vehicle and habitat design, and on mission profiles [46]. Shielding materials that contain elements with a high charge/mass ratio offer improved fragmentation of impacting HZEs compared to aluminum which acts to reduce biological hazards [47]. Composite materials composed of aliphatic polymers with high hydrogen content are, therefore, ideal candidates for new, multifunctional space structures to simultaneously carry structural loads and provide radiation protection. Thus, six polymeric specimens were selected and subjected to physical radiation testing and numerical simulation. Evaluation of shielding effectiveness for heavy ion GCR particles was performed with energies larger than 1 MeV/n.

5.2 Radiation Testing

Radiation shielding tests were performed for five candidate sandwich composite components as well as two complete sandwich composite specimens. Component materials included epoxy resin, two facesheet composites incorporating either Spectra or carbon fibers in an epoxy matrix, and two core materals composed of polyethylene terephthalate (PET) foam or polypropylene (PP). Additionally, two complete sandwich constructions were subjected to radiation shielding testing. All seven materials to be tested were fabricated with an areal weight of 5g/cm^2. Table 3 lists the physical properties of each candidate material. In addition to the seven materials described above, aluminum was included in the simulations for use as a reference shielding material.

Beam exposure measurements were performed at the Brookhaven National Laboratory Alternating Gradient Synchroton (BNL-AGS). Candidate materials were bombarded with HZE ions characteristic of a significant part of GCR heavy ion spectrum. Transmitted primary ions and charged fragments produced in the nuclear collisions inside the target materials were measured near the beam axis. For each material, incident ^{35}Cl ion particles with an approximate beam kinetic energy of 1 GeV/n was used.

Table 3 Candidate Sandwich Materials Investigated For Radiation Shielding

Material	**Description**	**Density (g/cm^3)**	**Thick. (cm)**	**Thick. (g/cm^2)**	**Chemical Composition (mass%)**
Resin 1	Epoxy resin block	1.12	4.48	5.00	70.1% C 7.6% H 16.8% O 5.5% N
Facesheet 1	Spectra/epoxy facesheet	1.04	4.79	5.00	77.3% C 10.7% H 9.0% O 3.0% N
Facesheet 2	Carbon/epoxy composite	1.44	3.47	5.00	83.5% C 3.6% H 7.10% O 5.8% N
Core 1	PET foam block	0.35	14.29	5.00	62.5% C 4.2% H 33.3% O
Core 2	PP foam block	0.19	26.68	5.00	85.6% C 14.4% H
Sandwich Composite 1	0.35g/cm^3 PET/Spectra facesheet	0.52	9.59	4.99	69.9% C 7.4% H 21.4% O 1.3% N
Sandwich Composite 2	FR6720 Polyurethane/carbon facesheet	0.53	9.44	5.00	75.2% C 4.6% H 13.2% O 6.4% N 0.3% P <1% Trace elements

Figure 18 shows a simplified schematic representation of data acquisition electronics used at BNL. The ^{35}Cl energy at the extraction point from the typical AGS ring is slightly above 1 GeV/n, After passing through upstream beam-line elements and detectors, however, the beam energy at the entrance to the target is approximately 1 GeV/n. The data acquisition system is made of a series of silicon detectors with thicknesses of 300 µm ("TR"), 3 mm (d3mmU and d3mm1-4), and 1 mm position sensitive (PSD1-2) devices. A charged particle passing through the silicon device liberates one electron-hole pair per 3.6 eV of energy deposited. The detectors downstream of the target subtend small angles around the beam axis. Thus for most events, the detector records a single primary ion or a small number of fragments at or near the beam velocity. The resulting digital signal (voltage) was amplified, digitized and stored for offline post analysis [48].

Data obtained by the detectors were normalized to the total number of fragments generated and are shown in Figure 19. It is evident that the induced fragment profiles are very similar for all of the various polymeric materials tested. Results obtained for each material, along with results obtained from numerical simulation, are discussed separately in the following section

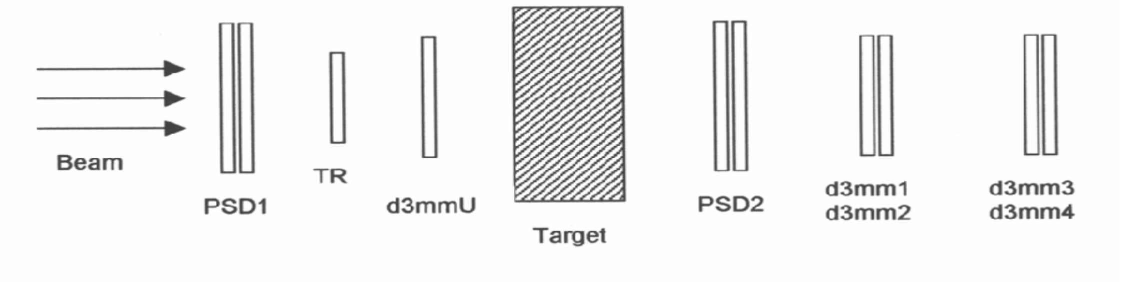

Figure 18. Schematic of detector configuration.

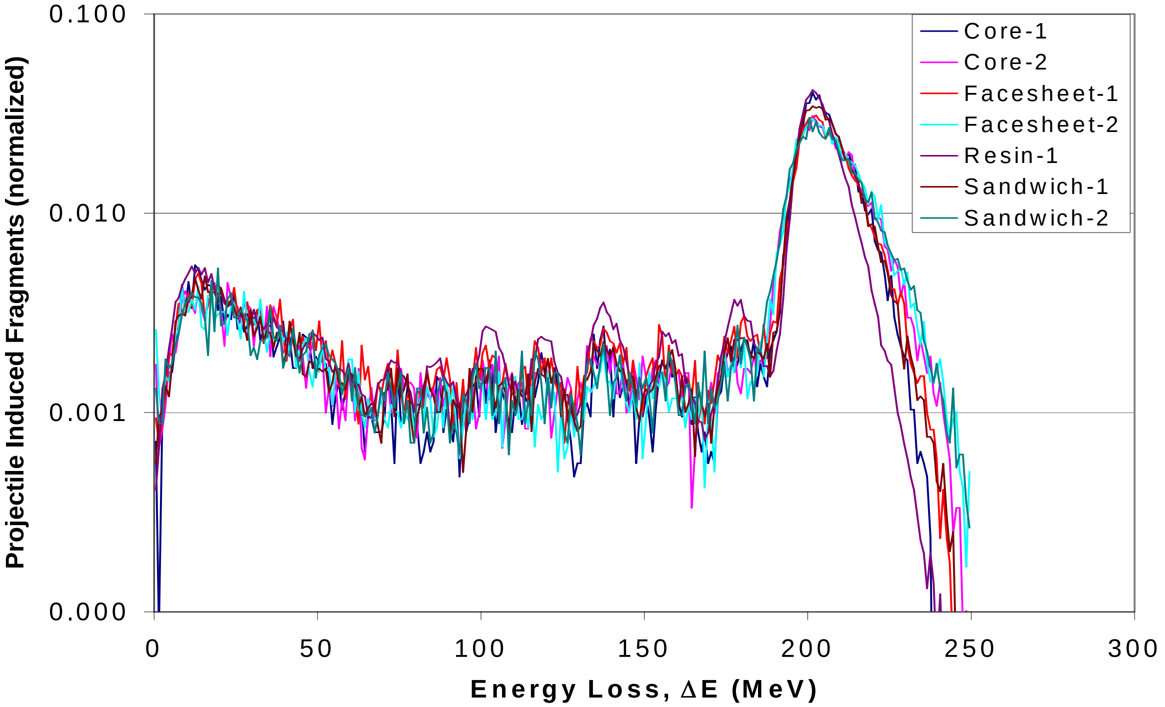

Figure 19. Test data of chlorine (^{35}Cl) at 1 GeV/n on 5 gm/cm^2 samples using a 2.0 mm Silicon detector.

5.3 GRNTRN Simulation of Radiation Fluences

Computational simulations to assess the radiation shielding capabilities of candidate sandwich materials were performed using the heavy ion code GRNTRN (GReeN's function high charge Z and Energy TRaNsport) developed at NASA Langley Research Center [49, 50]. GRNTRN is a deterministic ionizing radiation transport code that predicts the nuclear fragmentation of high-energy ions within a selected target material. The calculation of secondary nucleon formation is key to assessing the mitigation of biological hazards through radiation shield designs.

GRNTRN simulations were performed on each sample to determine the material's ability to fragment highly energetic chlorine ion particles. Chlorine (^{35}Cl) was used for physical testing and is a species in the spectrum of GCR heavy ions. Such highly energetic particles lose little energy within the target material. However, they can be fragmented into lower energy particles that reduce the total dose per incident ion absorbed by astronauts.

The GRNTRN calculations were calibrated with the experimental data to account for test energies and detector losses. The energy losses where determined using 2.0 mm Silicon detectors. The result of these calibrations is shown below in Figure 20 through Figure 26.

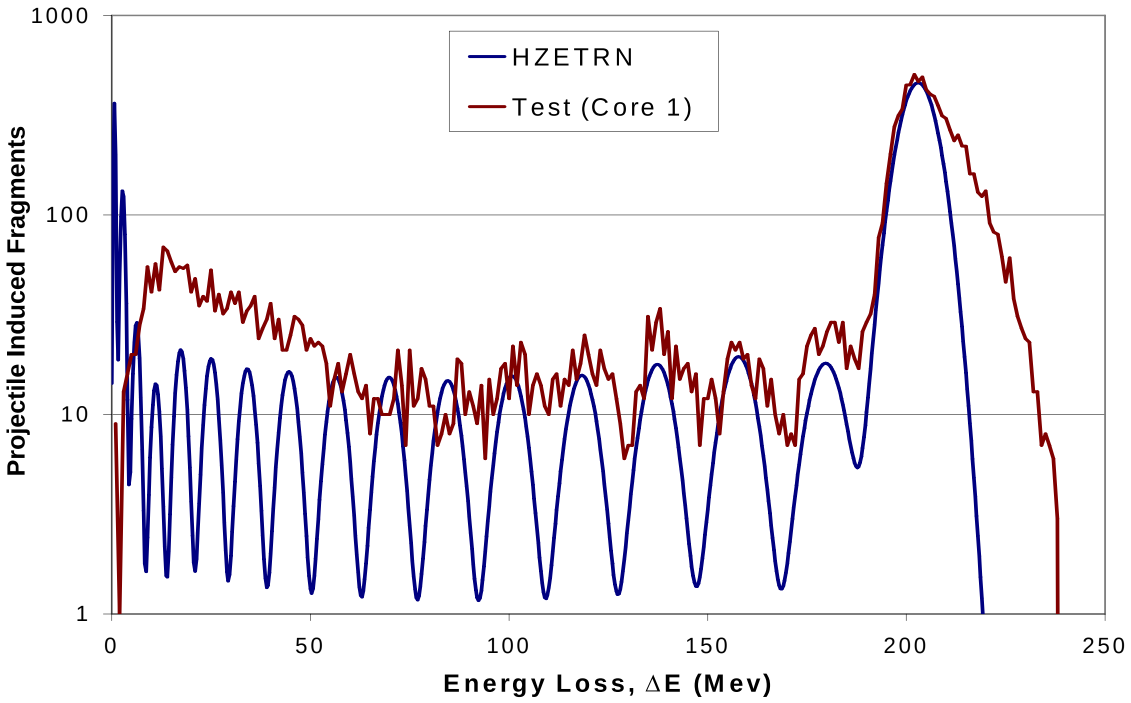

Figure 20. Calibration of GRNTRN simulation with test data of induced fragmentation in a 1 GeV/n chlorine (^{35}Cl) beam using the Core 1 (PET foam block) sample.

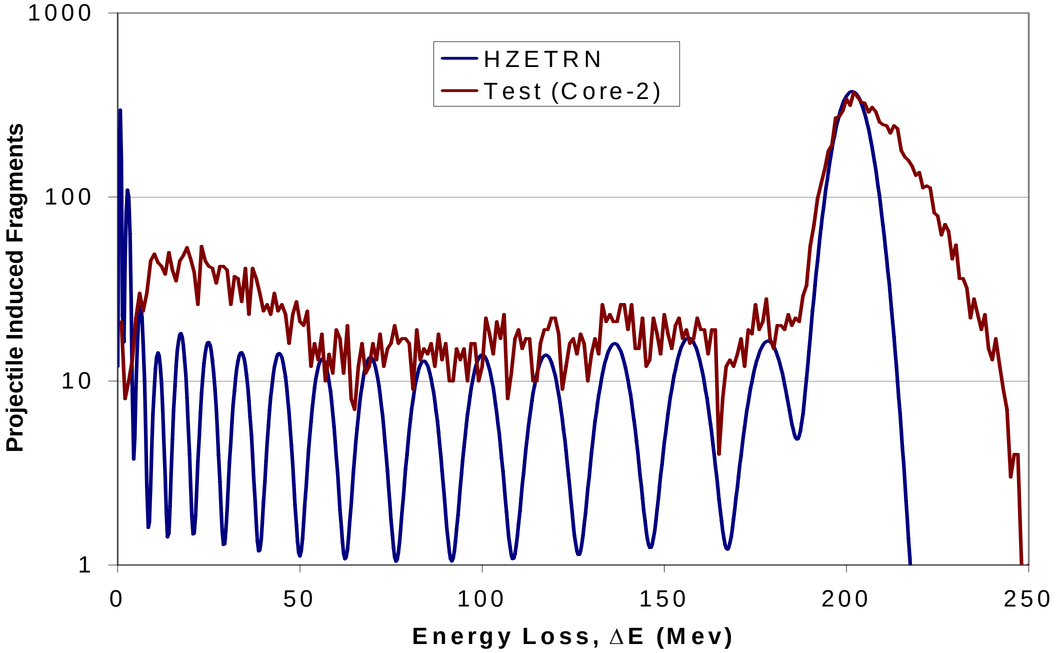

Figure 21. Calibration of GRNTRN simulation with test data of induced fragmentation in a 1 GeV/n chlorine (^{35}Cl) beam using the Core 2 (PP foam block) sample.

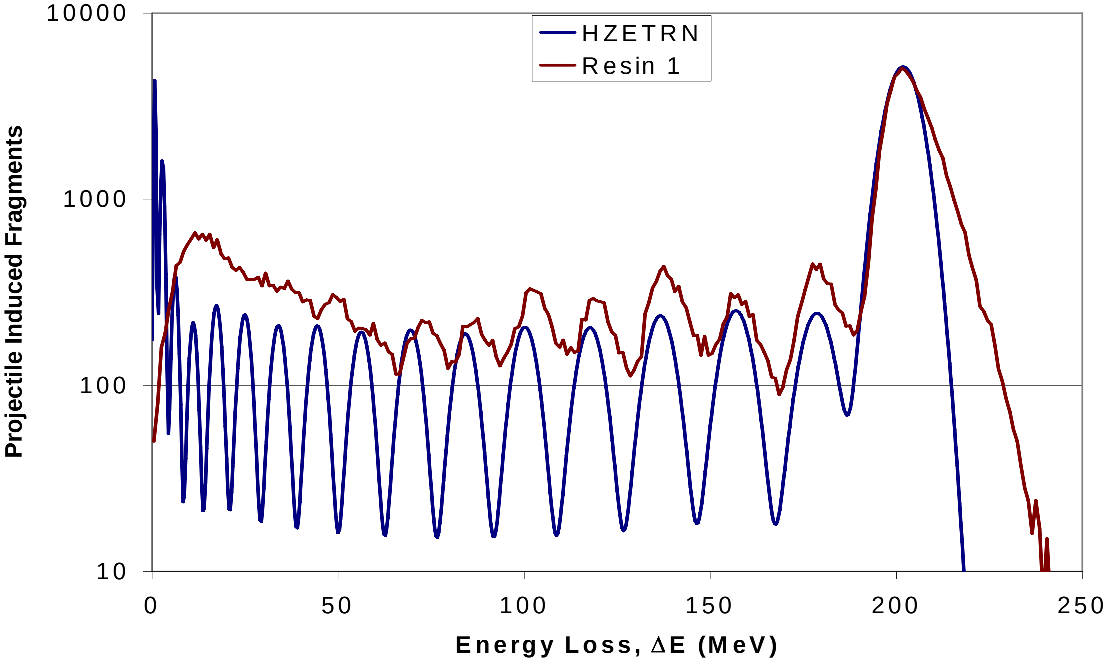

Figure 22. Calibration of GRNTRN simulation with test data of induced fragmentation in a 1 GeV/n chlorine (^{35}Cl) beam using the Resin 1 (epoxy resin block) sample.

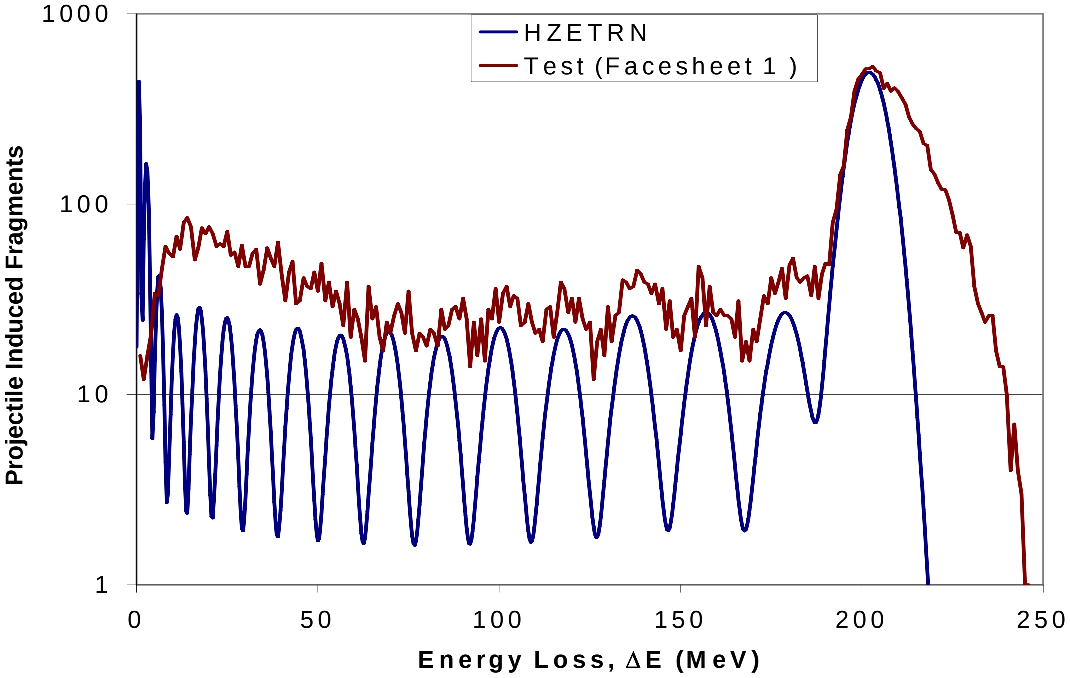

Figure 23. Calibration of GRNTRN simulation with test data of induced fragmentation in a 1 GeV/n chlorine (^{35}Cl) beam using the Facesheet 1 (Spectra/epoxy) sample.

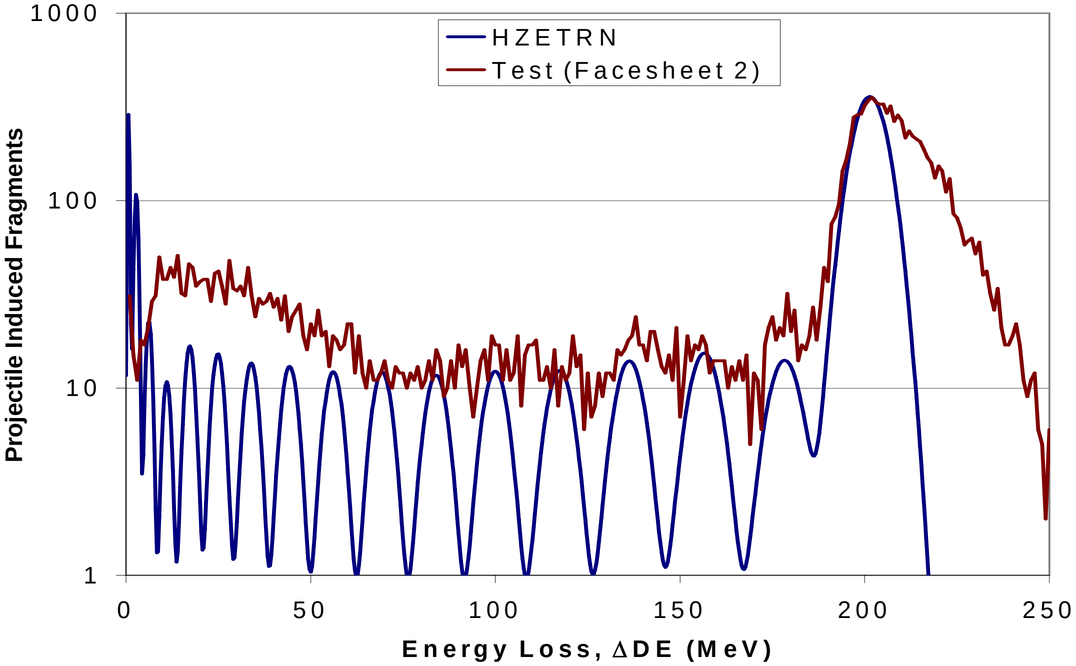

Figure 24. Calibration of GRNTRN simulation with test data of induced fragmentation in a 1 GeV/n chlorine (^{35}Cl) beam using the Facesheet 2 (carbon/epoxy) sample.

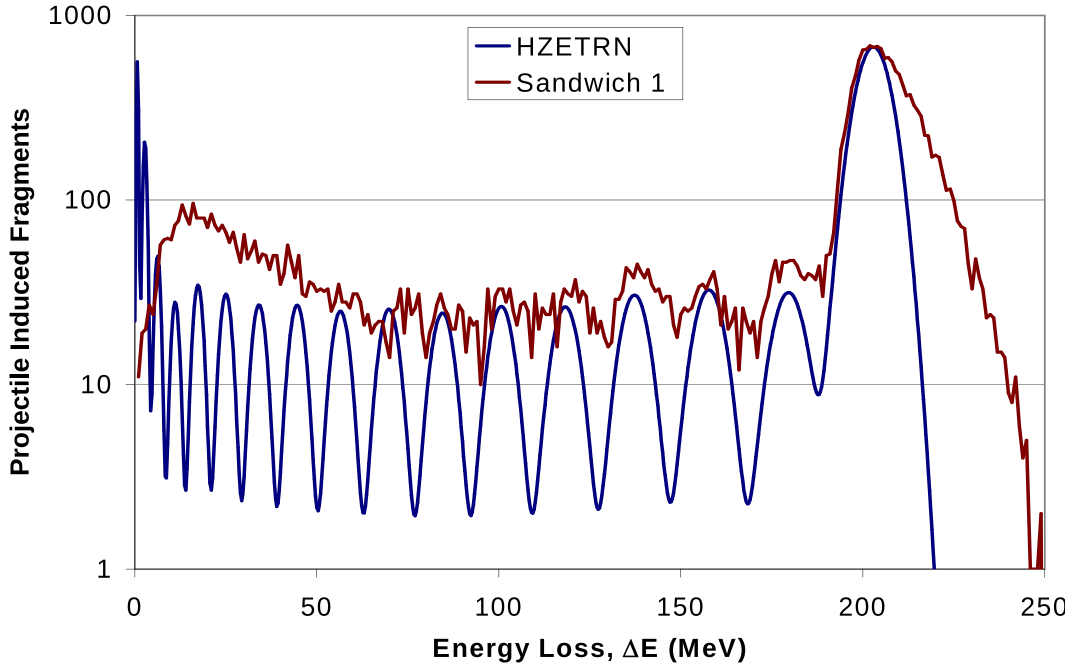

Figure 25. Calibration of GRNTRN simulation with test data of induced fragmentation in a 1 GeV/n chlorine (^{35}Cl) beam using the Sandwich 1 sample.

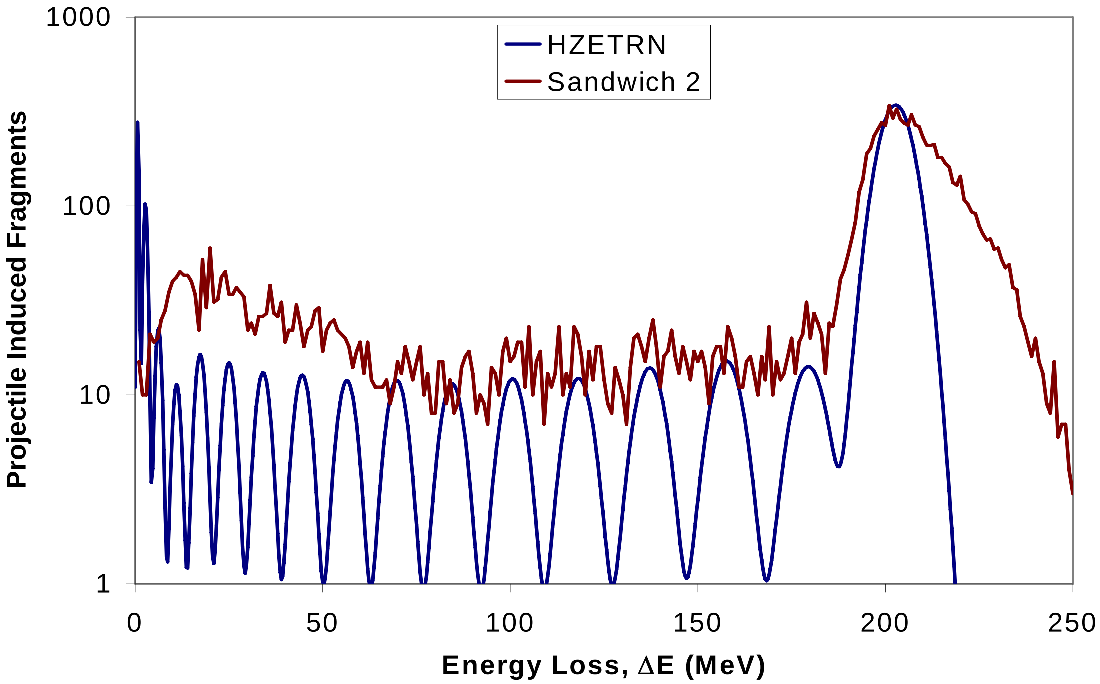

Figure 26. Calibration of GRNTRN simulation with test data of induced fragmentation in a 1 GeV/n chlorine (^{35}Cl) beam using the Sandwich 2 sample.

The calibrated GRNTRN simulations of induced fragments are assembled in Figure 27. Each simulation has been normalized to the total number of fragments predicted. The simulation of elemental aluminum has been included for comparison. During each calibration shown in Figure 20 through Figure 26, information regarding energy and fluxes were generated and used in a final series of simulations to predict the spectrum of ion fractions surviving from the initial chlorine beam. These comparisons are shown in Figure 27. This plot shows the energy spectra of the samples as received by the silicon detectors. Note that the peaks in the simulated energy loss spectra as collected by the detectors correspond to individual fragment charges for all samples. Note that for all samples, the right hand peak in the figure is from the surviving primary iron beam whereas the peaks to the left show the amount of lower energy fragments produced by nucleon removal yielding ions of decreasing atomic number. .For example, the next peak to the left of Cl is for P fragments, followed by Si fragments, etc. Additionally, Figure 27 shows that a slightly greater amount of lower energy fragments is produced in the seven sandwich materials relative to the aluminum.

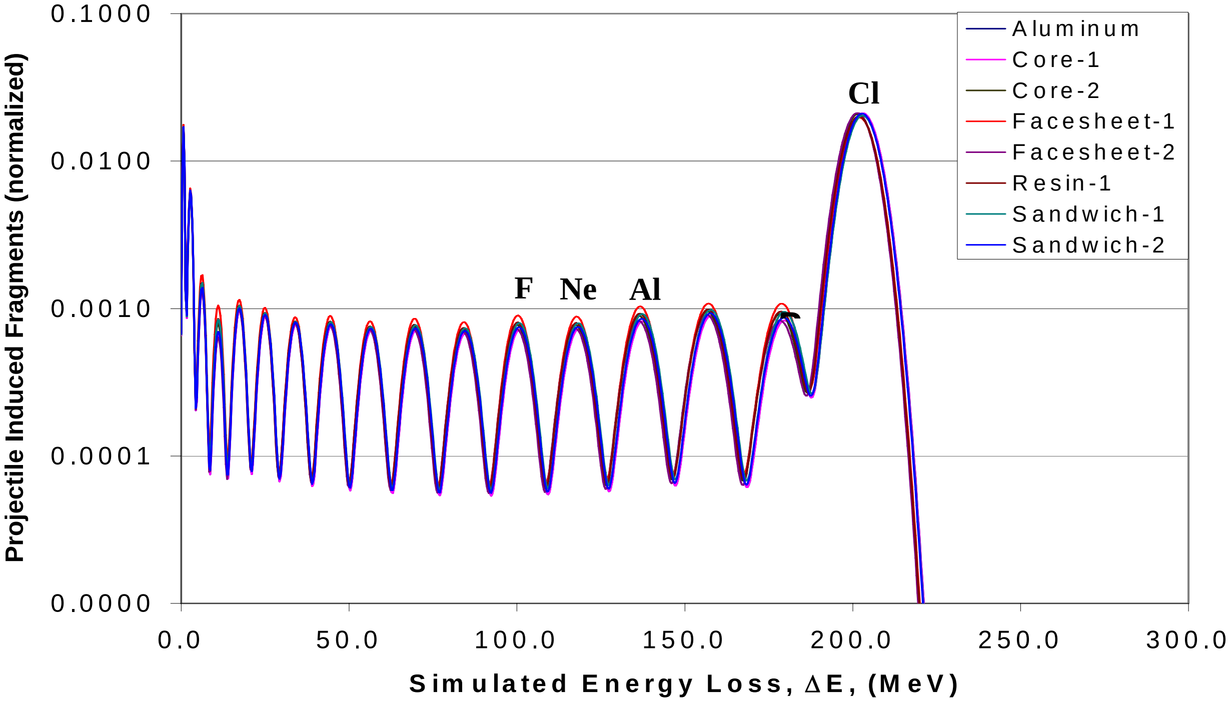

Figure 27. Compilation of calibrated GRNTRN simulations of induced fragments for each sample. Data is normalized to the total number of fragments generated by impact of chlorine (^{35}Cl) ions at 1 GeV/n.

Figure 28 shows the fraction of the primary beam surviving after propagating through each of the eight 5 gm/cm^2 samples. This figure shows that aluminum caused the least amount of fragmentation and, hence, the highest fraction of the primary iron beam survived. In addition, note that with the exception of the primary ion, the magnitude of surviving charges in aluminum is considerably less than in any of the six candidate material samples. This result indicates higher levels of fragmentation in the candidate polymeric materials and that fraction survival plots for these materials are more distributed over lower-energy particles. Thus, the likelihood of fragmentation is increased in the seven candidate sandwich materials compared to aluminum.

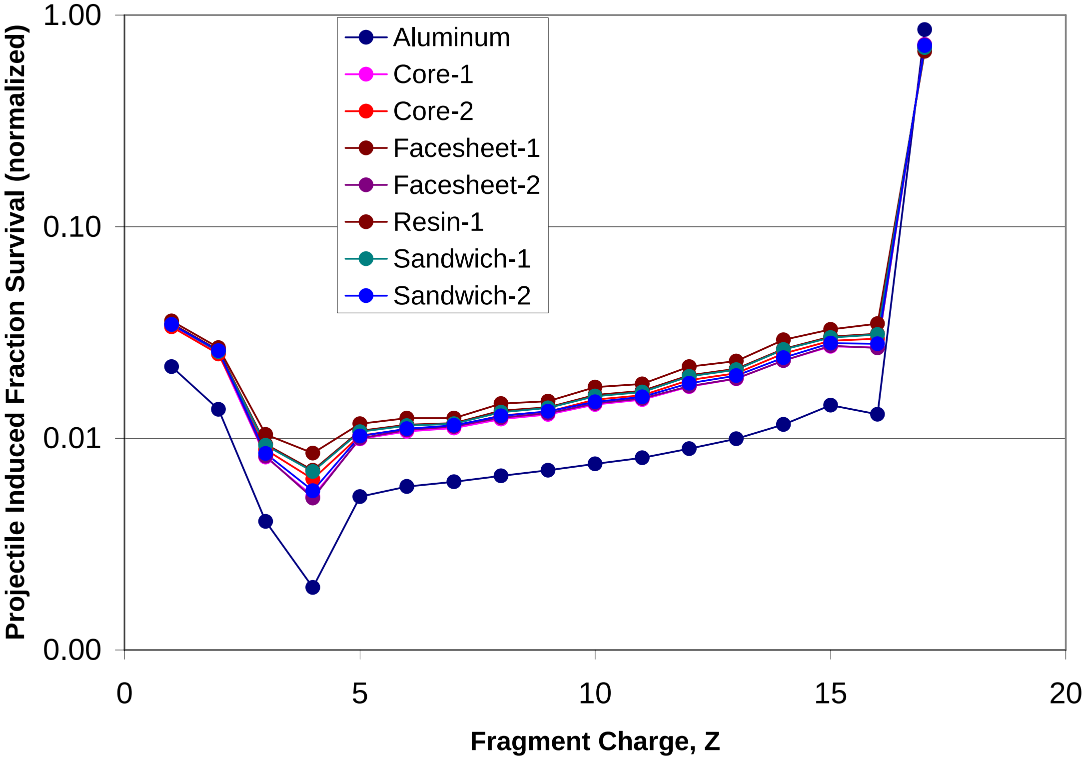

Figure 28. Comparison of induced fragmentation generated by impact of chlorine (^{35}Cl) ions at 1 GeV/n with selected target materials.

6. MATERIALS COMPATABILITY TESTING

Flatwise tensile testing (ASTM C 297 [1]) and core shear testing (ASTM C 273 [2]) were used to assess the interlaminar normal and shear strength of selected prototype multifunctional sandwich configurations. These test methods were selected for use in identifying material compatibility problems associated with the selected sandwich constituent. By evaluating the performance of the bond between constituents relative to the performance of the constituents alone, manufacturing-related problems such as core crushing and improper facesheet consolidation could also be identified using the selected tests.

6.1 Flatwise Tensile Testing

6.1.1 Specimen Configurations

Testing was performed using the three sandwich material configurations described in Table 4. The facesheets were composed of Spectra® 900 woven fabric measuring 2.1 mm thick infiltrated with an epoxy consisting of EPON™/EPIKOTE™ Resin 862 combined with EPIKURE™ Curing Agent 9553 (mixture ratio of 100:16.9). The three foam core materials measured 21 mm thick, resulting in all specimens having an overall thickness of 25 mm. Within each material configuration outlined in Table 4, testing was performed on specimens manufactured with four different transverse reinforcement configurations: non-stitched, vertically stitched (0.16 stitch/cm^2 and 0.62 stich/cm^2 densities) and angle stitched.

Table 4. Sandwich Configurations Used for Flatwise Tensile Testing

Sandwich Configuration	**Core Material**	**Core Density (kg/m^3)**	**Core Supplier**	**Facesheet**
1	PE	128	Voltek LLC	Spectra®/Epoxy
2	PP	128	JSP Int'l	Spectra®/Epoxy
3	PET	125	Fagerdala World Foams	Spectra®/Epoxy

6.1.2 Testing Methods and Procedures

Sandwich panels for all configurations were manufactured using the VARTM process as detailed previously in Chapter 4. Individual sandwich specimens were cut from each sandwich panel to nominal cross-sectional dimensions of 76 mm x 76 mm. The top and bottom surfaces of the facesheets were then lightly sandblasted and cleaned with acetone in preparation for adhesive bonding to steel loading blocks. Bonding was accomplished using Loctite® Hysol® 907 [51], a two-part, room-temperature cure paste adhesive. The steel loading blocks were used as part of the overall load train to transmit tensile load into the specimen core through the facesheets as depicted in Figure 29. All flatwise tensile testing was performed using an electromechanical testing machine with National Instruments data acquisition software.

Following the completion of a round of testing, the steel loading blocks were cleaned and prepared for remounting. The cleaning process involved manually removing core and facesheet material from the Loctite® Hysol® 907 epoxy, and then dissolving the epoxy using the commercially available solvent Dynasolve® 185 [52]. The bonding surface of each steel loading block was subsequently sandblasted to remove any remaining epoxy or other surface impurity.

Displacement measurements were made using two specially-designed extensometers (Figure 30) calibrated using an Epsilon Technology Corporation model 3590 extensometer calibrator. These extensometers, with a nominal 30.5 mm gage length, spanned the entire thickness of the sandwich composites and attached to plastic tabs mounted on the steel loading block fixtures (Figure 31 and Figure 32). The plastic tabs were used to provide a more compliant surface for the extensometer contact points and prevent slippage. The primary purpose of these extensometers was to monitor the uniformity of loading across the specimen and to detect the presence of bending during loading. The extensometers were also used to obtain displacement measurements for use in modulus determinations.

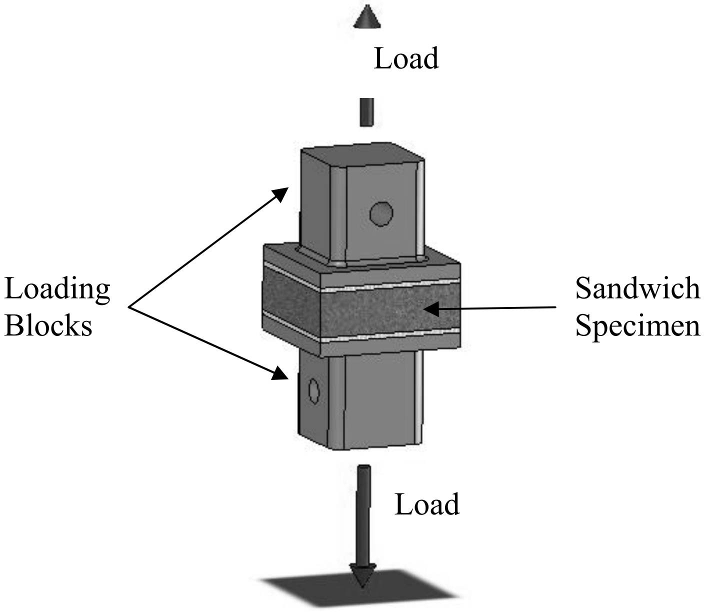

Figure 29. Flatwise tension testing setup.

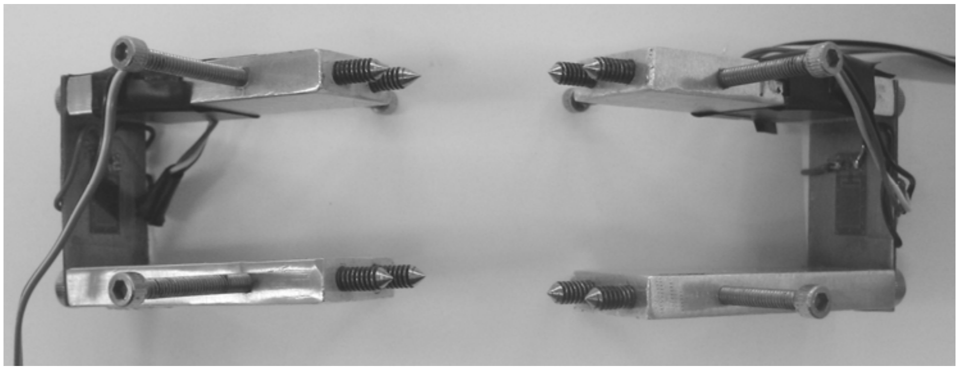

Figure 30. Extensometers used for flatwise tension testing.

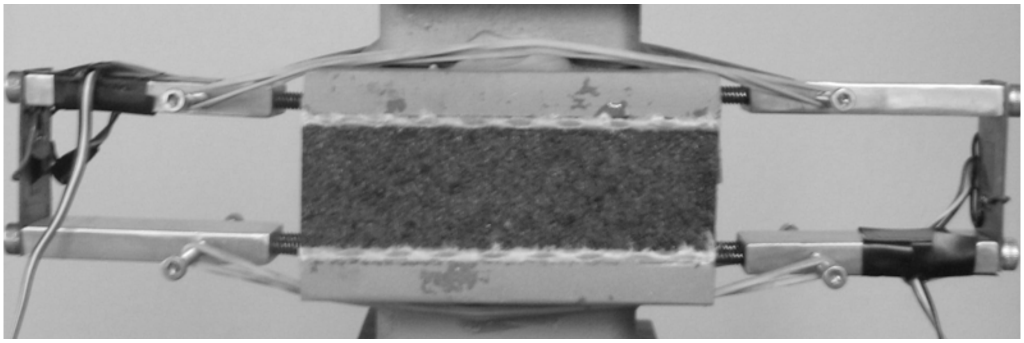

Figure 31. Extensometers spanning a flatwise tensile specimen.

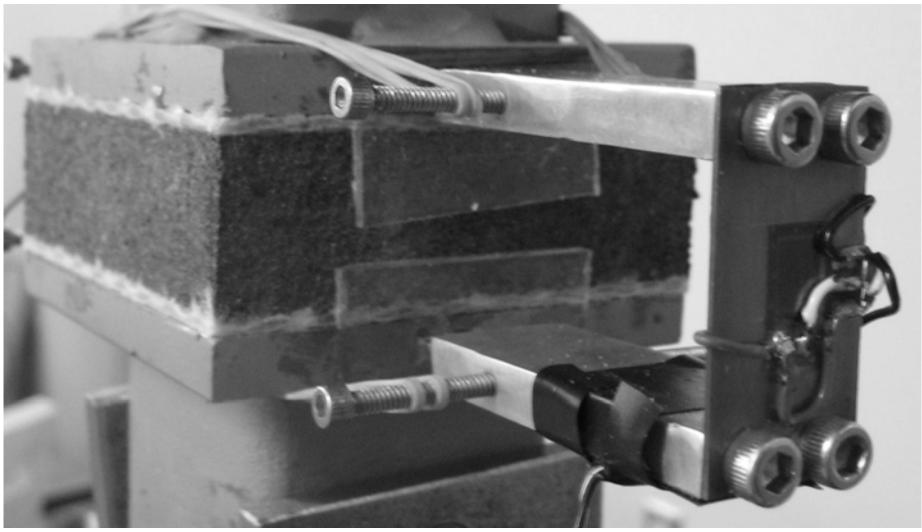

Figure 32. Plastic tabs used to avoid slippage of the extensometers.

Load data was collected using an Interface [53] 10,000 lb-force load cell. The first step in the data reduction process was to calculate stress and strain values from the extensometer and load cell data, using the following equations

$$\varepsilon = \frac{\Delta L}{L} \tag{1}$$

$$\sigma = \frac{P}{A} \tag{2}$$

where in Equation (1) ε is the strain of the specimen, Δ*L* is measured displacement from the extensometer in millimeters and *L* is the gauge length of the extensometer, also in millimeters. In Equation (2), σ is the stress in the specimen in Pascals, *P* is the applied load in Newtons and *A* is the cross-sectional area in square meters.

The ultimate flatwise tensile strength for the four sandwich configurations was calculated using Equation (2) where *P* is the highest load recorded during the test. The modulus of elasticity was found by calculating the slope of a simple linear fit from the stress-strain response of the material over the initial linear elastic region during a flatwise tensile test. A representative stress-strain plot in the linear elastic region is shown in Figure 33.

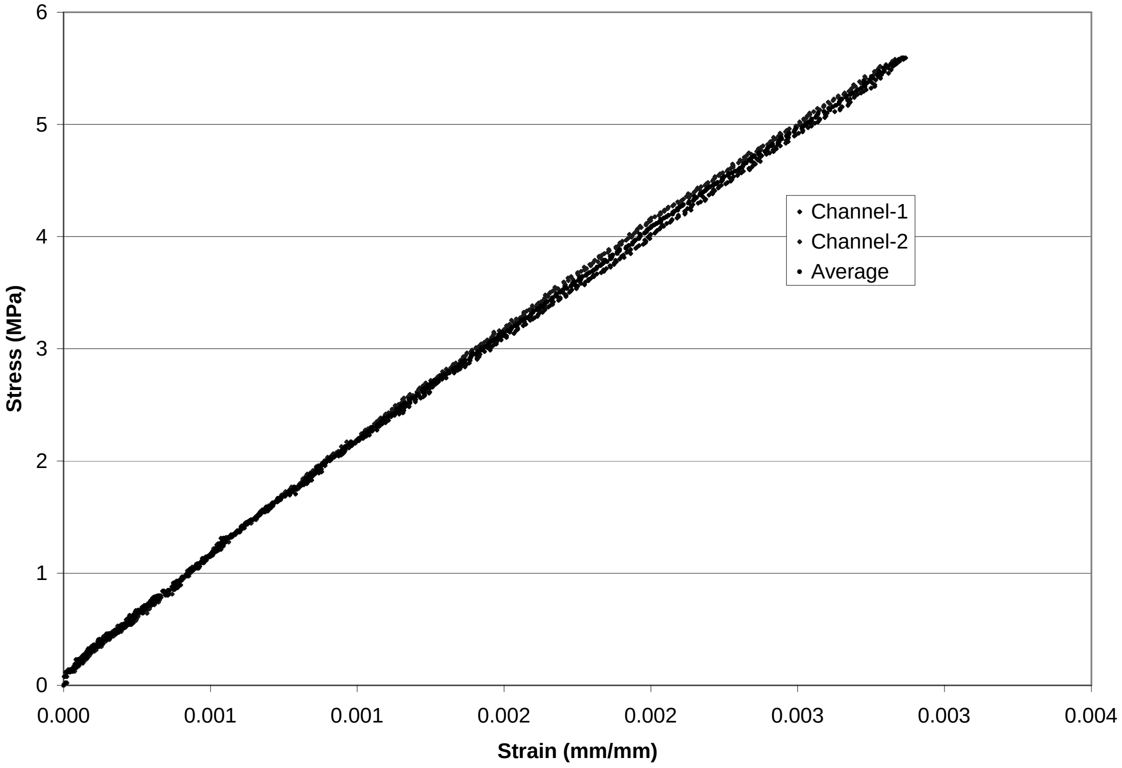

Figure 33. Representative stress-strain response (initial linear region) for a flatwise tensile test.

6.1.3 Flatwise Tension Test Results

Table 5 through Table 7 provide a summary of the flatwise tension testing results. Included in these tables are the ultimate tensile strength and elastic modulus for each specimen tested. Also shown are the mean, standard deviation and coefficient of variation for these data. A visual comparison of the mean and standard deviation of the tensile strength and elastic modulus data is also provided in the form of bar graphs in Figure 34 and Figure 35, respectively.

Table 5. Tensile Testing Results: Voltek PE Core (Configuration 1)

Stitching	Tensile Strength (MPa)	Modulus of Elasticity (MPa)
Non-Stitched	0.92 0.94 0.84 0.91 **Average = 0.90** **Std Dev = 0.04** **Coeff. Of Variation = 4.91%**	10.9 11.0 10.4 8.6 **Average = 10.2** **Std Dev = 1.13** **Coeff. Of Variation = 11.1%**
Vertically Stitched 0.16 stitch/cm^2	0.87 0.94 0.94 0.92 **Average = 0.92** **Std Dev = 0.03** **Coeff. Of Variation = 3.59%**	21.8 16.4 19.3 25.2 **Average = 20.7** **Std Dev = 3.73** **Coeff. Of Variation = 18.0%**
Vertically Stitched 0.62 stitch/cm^2	1.69 1.79 1.82 1.94 1.72 1.59 1.82 1.84 **Average = 1.78** **Std Dev = 0.11** **Coeff. Of Variation = 6.05%**	47.8 47.3 41.6 44.1 46.1 46.3 47.1 48.2 **Average =46.1** **Std Dev = 2.20** **Coeff. Of Variation = 4.77%**
Angle Stitched	0.76 0.80 0.58 0.80 0.67 0.66 **Average = 0.71** **Std Dev = 0.09** **Coeff. Of Variation = 12.35%**	19.8 23.4 18.3 18.3 20.6 20.2 **Average = 20.1** **Std Dev = 1.86** **Coeff. Of Variation = 9.26%**

Table 6. Tensile Testing Results: JSP PP Core (Configuration 2)

Stitching	Tensile Strength (MPa)	Modulus of Elasticity (MPa)
Non-Stitched	0.74 0.74 0.67 0.52 0.62 0.51 **Average = 0.63** **Std Dev = 0.10** **Coeff. Of Variation = 16.06%**	80.5 91.6 78.8 77.0 81.6 88.2 **Average = 83.0** **Std Dev = 5.69** **Coeff. Of Variation = 6.86%**
Vertically Stitched 0.16 stitch/cm^2	0.81 0.63 0.75 0.67 0.66 0.53 0.61 0.74 **Average = 0.67** **Std Dev = 0.09** **Coeff. Of Variation = 12.92%**	97.1 84.0 88.9 80.7 93.9 68.6 78.8 83.5 **Average = 84.4** **Std Dev = 9.02** **Coeff. Of Variation = 10.68%**
Vertically Stitched 0.62 stitch/cm^2	1.45 1.47 1.47 1.49 1.57 1.40 1.43 1.45 **Average = 1.47** **Std Dev = 0.05** **Coeff. Of Variation = 3.46%**	217.4 193.2 187.0 215.3 181.6 184.6 178.3 203.2 **Average = 195** **Std Dev = 15.2** **Coeff. Of Variation = 7.79%**
Angle Stitched	0.99 1.14 0.94 0.98 0.93 1.04 0.92 0.98 **Average = 0.99** **Std Dev = 0.07** **Coeff. Of Variation = 7.12%**	146.5 129.7 132.6 127.9 119.4 119.6 167.4 118.4 **Average = 133** **Std Dev = 16.81** **Coeff. Of Variation = 12.67%**

Table 7. Tensile Testing Results: Fagerdala PET Core (Configuration 3)

Stitching	Tensile Strength (MPa)	Modulus of Elasticity (MPa)
Non-Stitched	1.22 1.08 1.29 1.28 1.23 1.19 1.38 1.37 **Average = 1.25** **Std Dev = 0.10** **Coeff. Of Variation = 7.93%**	66.6 65.3 73.0 69.1 73.1 72.1 78.7 70.2 **Average = 71.0** **Std Dev = 4.22** **Coeff. Of Variation = 5.95%**
Vertically Stitched 0.16 stitch/cm^2	1.49 1.51 1.60 1.60 1.52 **Average = 1.55** **Std Dev = 0.05** **Coeff. Of Variation = 3.45%**	117.6 125.2 150.8 126.3 132.2 **Average = 130** **Std Dev = 12.52** **Coeff. Of Variation = 9.60%**
Vertically Stitched 0.62 stitch/cm^2	1.22 1.19 1.02 1.06 0.99 1.02 1.14 **Average = 1.09** **Std Dev = 0.09** **Coeff. Of Variation = 8.34%**	250.4 219.2 184.7 213.4 185.3 201.6 264.4 **Average = 217** **Std Dev = 30.7** **Coeff. Of Variation = 14.16%**
Angle Stitched	0.61 0.54 0.63 0.67 0.69 0.63 0.66 **Average = 0.63** **Std Dev = 0.05** **Coeff. Of Variation = 7.64%**	120.3 129.7 122.8 126.9 138.1 132.7 124.0 **Average = 128** **Std Dev = 6.20** **Coeff. Of Variation = 4.85%**

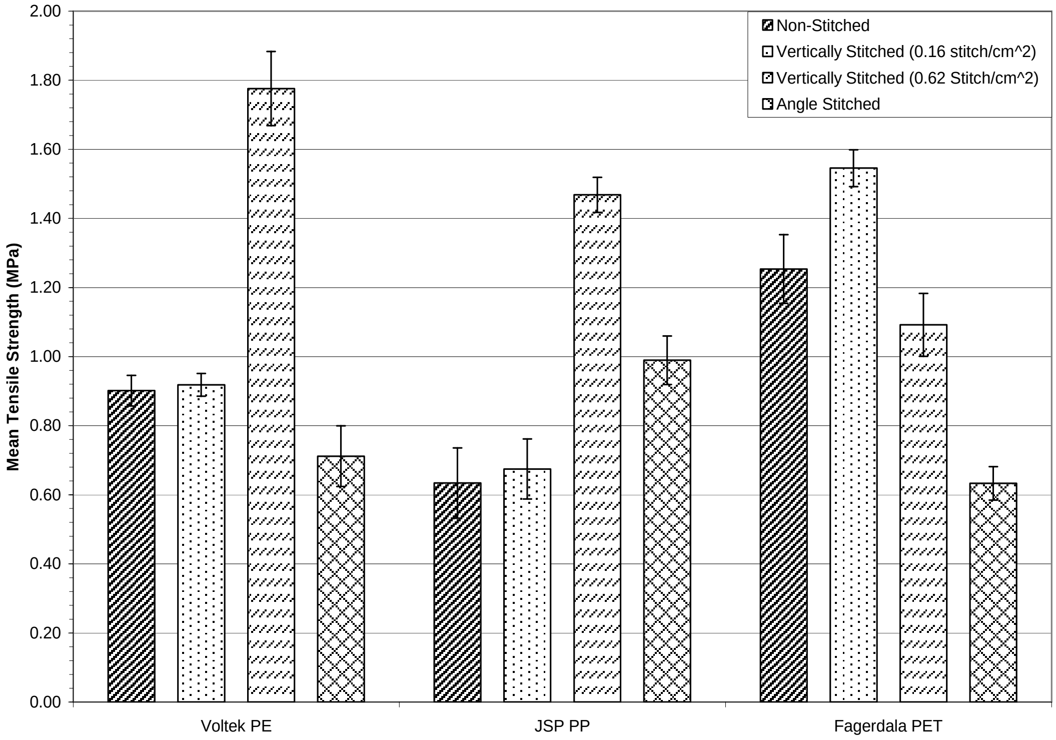

Figure 34. Tensile strength results from flatwise tensile testing.

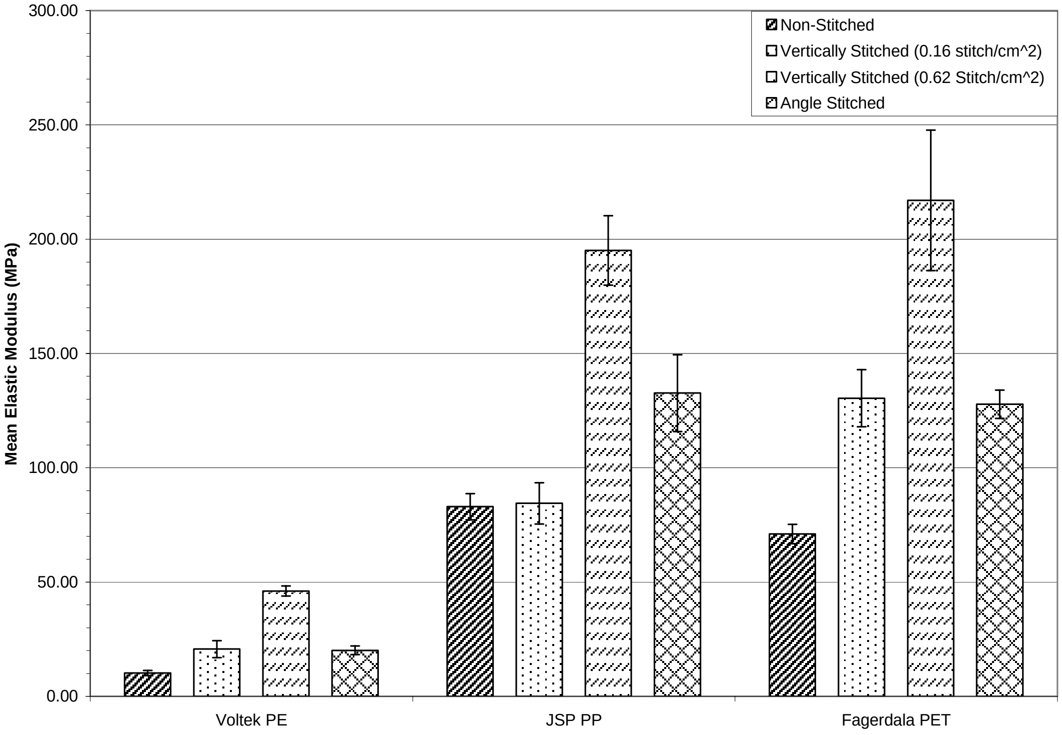

Figure 35. Elastic modulus results from flatwise tensile testing.

6.1.4 Discussion of Non-Stitched Configurations

From Figure 34 and Table 5 through Table 7 it can be seen that for the non-stitched configurations, the Fagerdala PET foam had the highest average tensile strength at 1.25 MPa, followed by Voltek PE and JSP PP at 0.90 and 0.63 MPa, respectively. The aforementioned Tables and Figure 35 show the elastic modulus for the non-stitched configurations. The PP and PET specimens displayed similar values for elastic modulus at 83.0 and 71.0 MPa, respectively. In contrast, the PE foam had a significantly lower modulus, measuring 10.2 MPa. These tensile strength and elastic modulus values will serve as the baseline for comparing the effect of transverse reinforcement.

A plot of the typical load versus displacement response of the non-stitched specimens is shown in Figure 36. During the test, loading progressed smoothly up to the maximum load. It should be noted that the brief dips in the load during the linear region of the tests correspond to a pause in the test at which time the extensometers were removed. This dip is most pronounced in the PE specimen curve due to the significantly higher compliance of the core. This compliance is also responsible for the reduced slope of the PE specimen in comparison with the PET and PP specimens, which share similar values of elastic modulus.

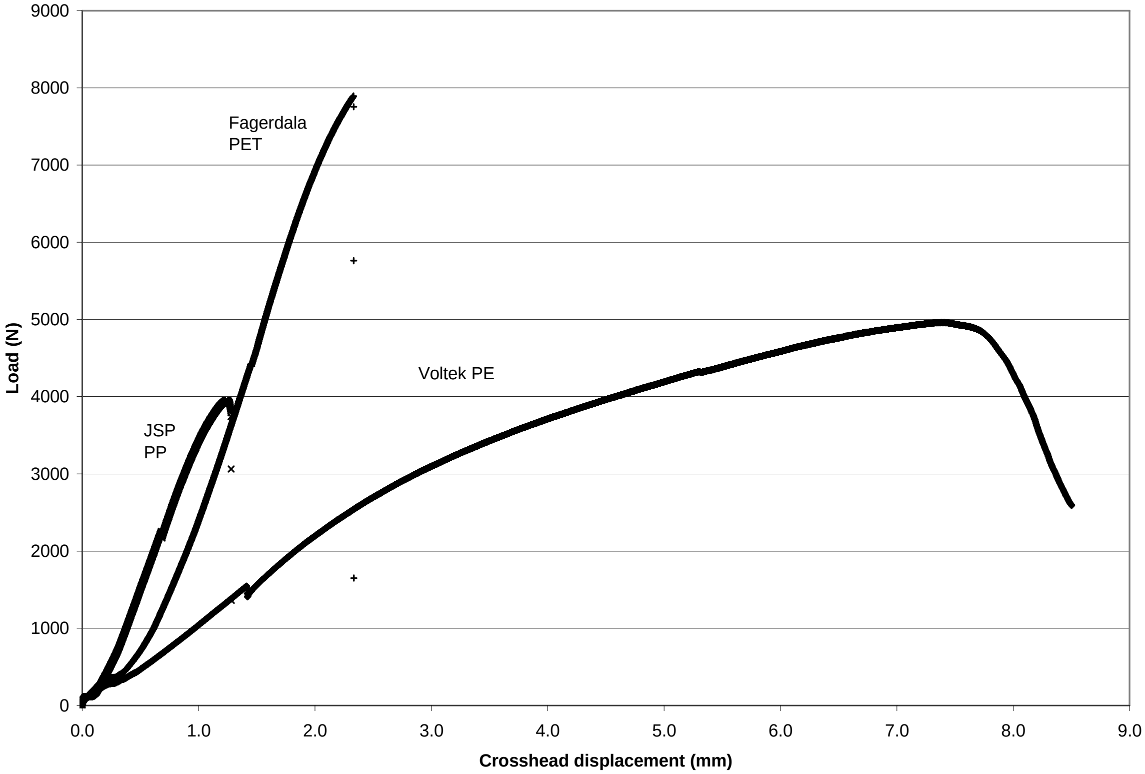

Figure 36. Representative load-displacement curves from non-stitched specimens.

Figure 37 shows a representative failure observed in the PET specimens. These specimens consistently failed in the core, away from the facesheet interfaces. The core material remained bonded to each facesheet following failure, indicating that the bond strength between the core and facesheet is greater than the strength of the core itself. This behavior was observed despite traditional difficulty associated with bonding PE materials. As shown in Figure 36, this failure was accompanied by a sudden load drop.

In contrast, the PE and PP specimens did not exhibit a sudden failure, but rather a gradual decrease in load as shown in Figure 36. This response was determined to be associated with a progressive delamination, in which the facesheet gradually peels away from the core. A representative PP specimen exhibiting this type of failure is illustrated in Figure 38.

These results suggest that the difference in observed failure modes is due to the strength of the bond between the facesheet and core material. Ruptured cells are present along the surface of the PET foam, which allow resin to partially infiltrate the core and create mechanical interlocking between the core and facesheet. In contrast, the PP and PE core materials do not allow sufficient infiltration to occur, thus limiting the strength of the interface.

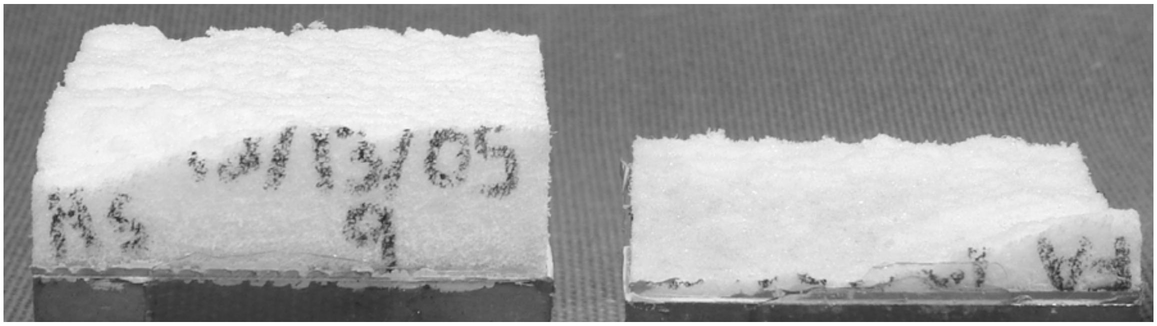

Figure 37. Core failure of a non-stitched PET specimen.

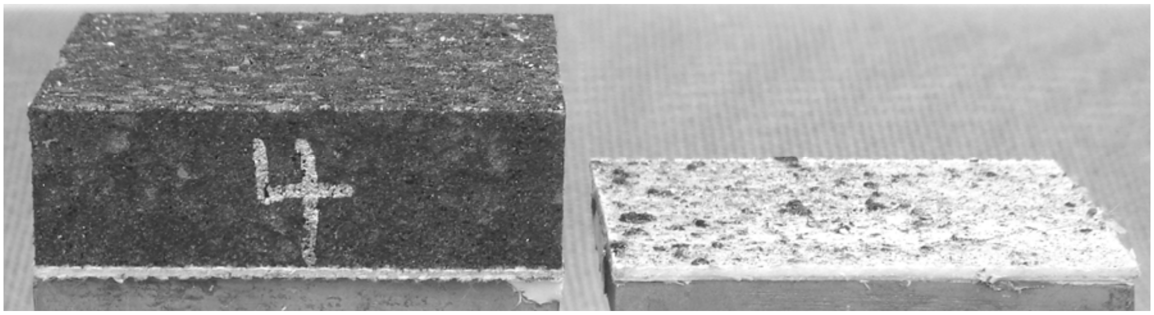

Figure 38. Delamination failure of a non-stitched PP specimen.

6.1.5 Discussion of 0.16 stitch/cm^2 Configurations

Figure 34 and Table 5 through Table 7 demonstrate that for the 0.16 stitch/cm^2 configurations, the Fagerdala PET foam had the highest average tensile strength at 1.55 MPa, followed by Voltek PE and JSP PP at 0.92 and 0.67 MPa, respectively. These results correspond to an improvement in tensile strength of 24%, 6.3% and 2.2% over the non-stitched PET, PE and PP specimens, respectively. Figure 35, as well as the Tables mentioned above, show the elastic modulus for the 0.16 stitch/cm^2 configurations. The PET specimen displayed the highest average elastic modulus at 130.4 MPa followed by the PP specimens with a modulus of 84.5 MPa. As with the non-stitched configurations, the PE foam had a significantly lower modulus measuring 20.7 MPa. All three configurations showed higher average values of elastic modulus in comparison with the non-stitched configurations, with improvements of 84% for PET, 1.8% for PP and 102% for PE.

Typical load versus displacement diagrams for the 0.16 stitch/cm^2 specimens are shown in Figure 39. For all three configurations, loading progressed smoothly up to point of maximum load. As discussed in the preceding section, the slight dip in load observed during the initial linear region corresponds to the removal of the extensometers. Although the stiffness of the PE foam doubled with the introduction of stitching at a density 0.16 stitch/cm^2 this value was significantly lower than the PP and PET specimens as shown by the lower slope in Figure 39.

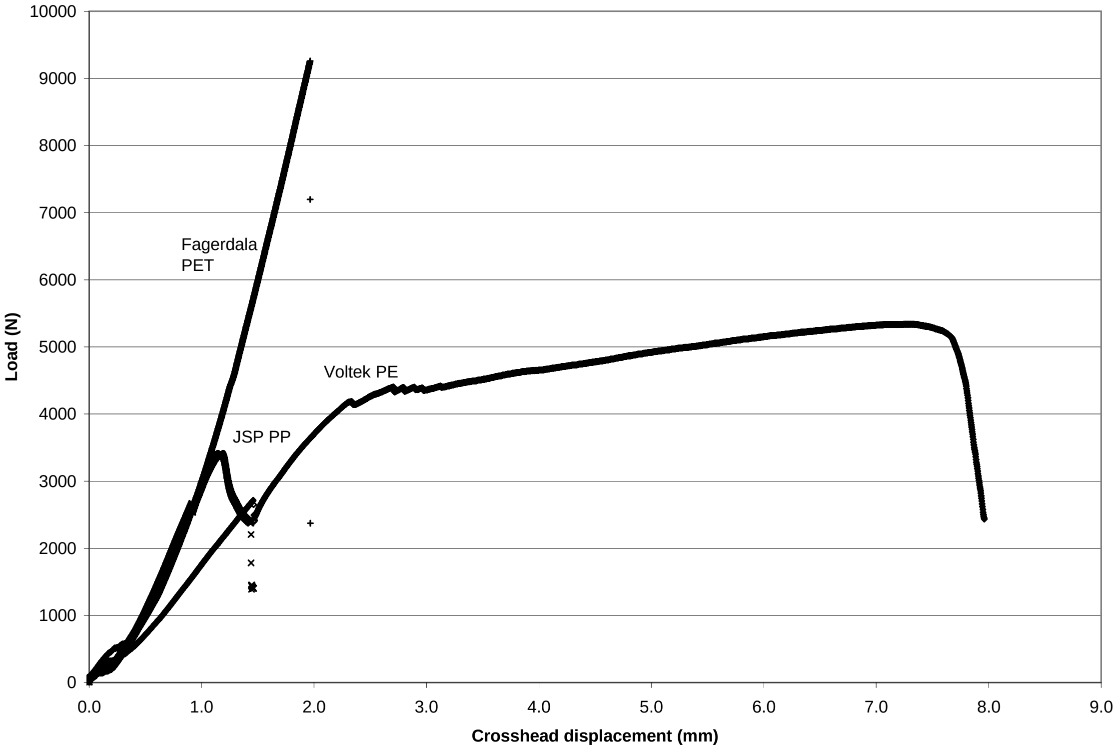

Figure 39. Representative load-displacement curves from 0.16 stitch/cm^2 specimens.

As seen with the non-stitched configuration, the 0.16 stitch/cm^2 PET specimens consistently exhibited a sudden failure. This response can be seen in Figure 39 as a sudden drop in load immediately following the maximum value. Core failure occurred following a progressive failure of the stitching, which was detected audibly. A photograph of the fracture surface of a representative core failure is shown in Figure 40. As shown in the figure, core material remained bonded to each facesheet and all stitches following failure. These observations suggest that the bond strength between these constituents is greater than the core itself, as discussed with the non-stitched configuration. Further inspection of the failed stitches revealed that failure occurred consistently at the loop in stitch yarn, as shown in Figure 41.

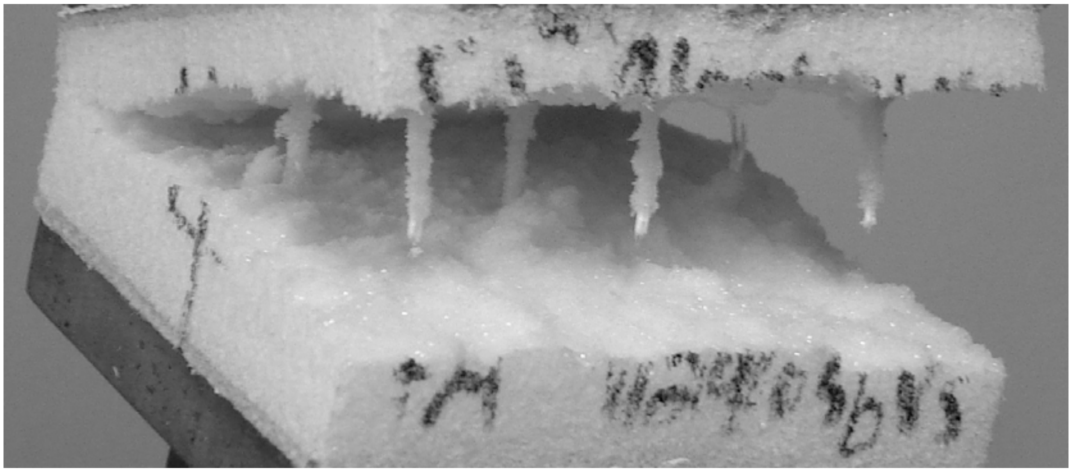

Figure 40. Fracture surface of a 0.16 stitch/cm^2 PET specimen.

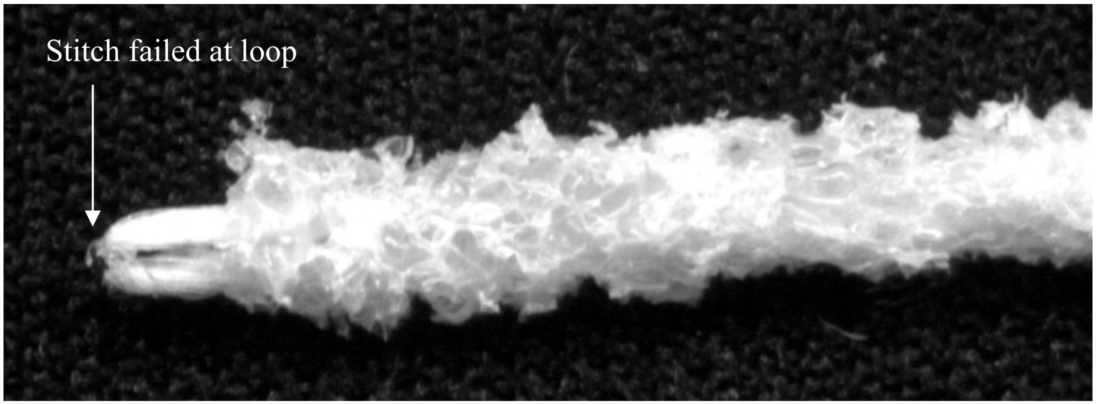

Figure 41. Magnified view of a failed stitch from a PET specimen.

The PE and PP 0.16 stitch/cm^2 specimens consistently exhibited delamination failure as observed with the non-stitched configuration. This can be seen in Figure 39 which shows a gradual drop in load following the maximum load. For both the PE and PP specimens, delamination of the facesheet occurred following initial failure of a row of stitches and progressed across the specimen cross section as stitches continued to fail. A photograph of this type of failure is shown in Figure 42 for a PE specimen. In contrast to the 0.16 stitch/cm^2 PET specimens, no core material remained bonded to the facesheets or stitches in the PE and PP specimens.

Inspection of the specimens following failure revealed that two modes of failure occurred in the stitches. The predominant mode observed was failure of the bobbin thread, allowing the stitch thread to remain intact. The second mode observed was failure of the stitch thread at the stitch-facesheet interface, leaving the bobbin thread undamaged. Evidence of these two modes of failure is shown below in Figure 43 and Figure 44.

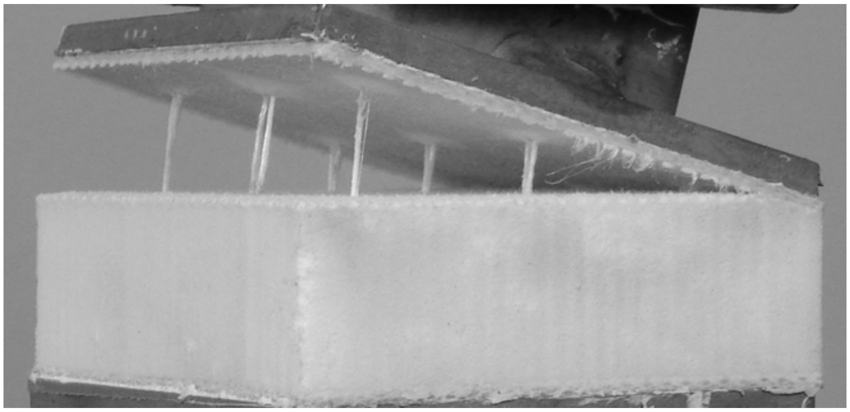

Figure 42. Representative delamination failure of a 0.16 stitch/cm^2 PE specimen.

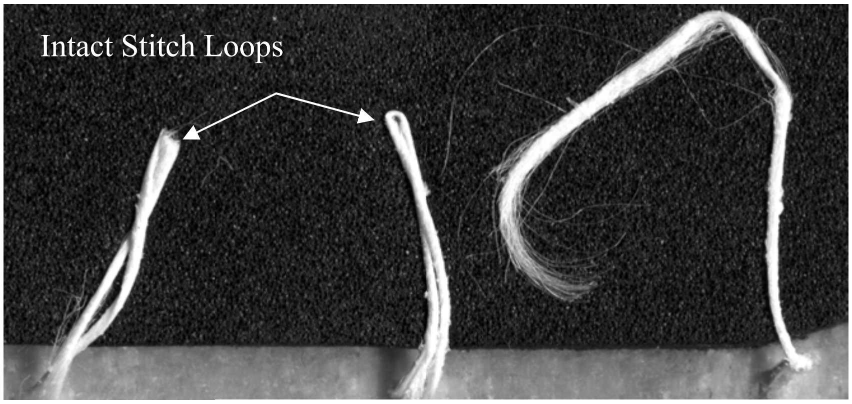

Figure 43. A stitch row demonstrated combined stitch and bobbin thread failure.

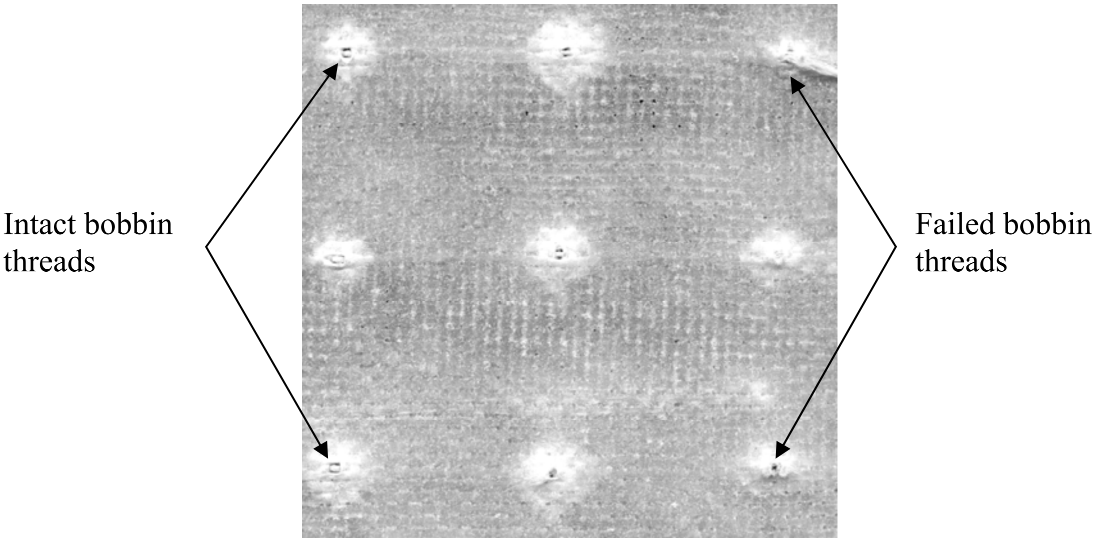

Figure 44. Facesheet from a PE sandwich showing intact and failed bobbin threads.

As observed with the non-stitched PE and PP specimens, the facesheet/core bond created between constituents is lower in strength than the core material. This is indicated by the absence of core material on the stitches or facesheets following failure. These results suggest that the load in the stitches was not distributed to the surrounding core, resulting in high loads in the bobbin thread leading to its failure.

6.1.6 Discussion of 0.62 stitch/cm^2 Configurations

Figure 34 and Table 5 through Table 7 show that for the 0.62 stitch/cm^2 configurations, the Voltek PE foam had the highest average tensile strength at 1.78 MPa, followed by JSP PP and Fagerdala PET at 1.47 and 1.09 MPa, respectively. These results correspond to an improvement in tensile strength of 97% and 132% over the non-stitched PE and PP specimens, respectively. In contrast, the Fagerdala PET specimen showed a reduction in tensile strength over the non-stitched configuration of 13%. The elastic modulus for the 0.62 stitch/cm^2 configurations are shown in Figure 35. The PET specimen displayed the highest average elastic modulus at 217.0 MPa followed by the PP specimens with a modulus of 195.1 MPa. As with the previous configurations, the PE foam had a significantly lower modulus, measuring 46.1 MPa. All three configurations showed higher average values of elastic modulus versus the non-stitched configurations with improvements of 205% for PET, 135% for PP and 351% for PE.

Typical load versus displacement diagrams for the 0.62 stitch/cm^2 specimens are shown in Figure 45. During the test, loading of the PE and PP specimens progressed smoothly up to the point of maximum load. In contrast, the PET specimens loaded smoothly only until the initial failure, shown as point A in Figure 45. After this initial failure, the specimens reloaded and experienced one or two additional failure events (point B) before eventually reaching the point of maximum load (point C) at which point catastrophic failure was observed. As discussed in the preceding section, the slight dip in load observed during the initial linear region corresponds to the removal of the extensometers. Although the stiffness of the PE foam increased approximately 3.5 times over that of the non-stitched configuration, this value was still significantly lower than that of the PP and PET specimens as shown by the reduced slope in Figure 45.

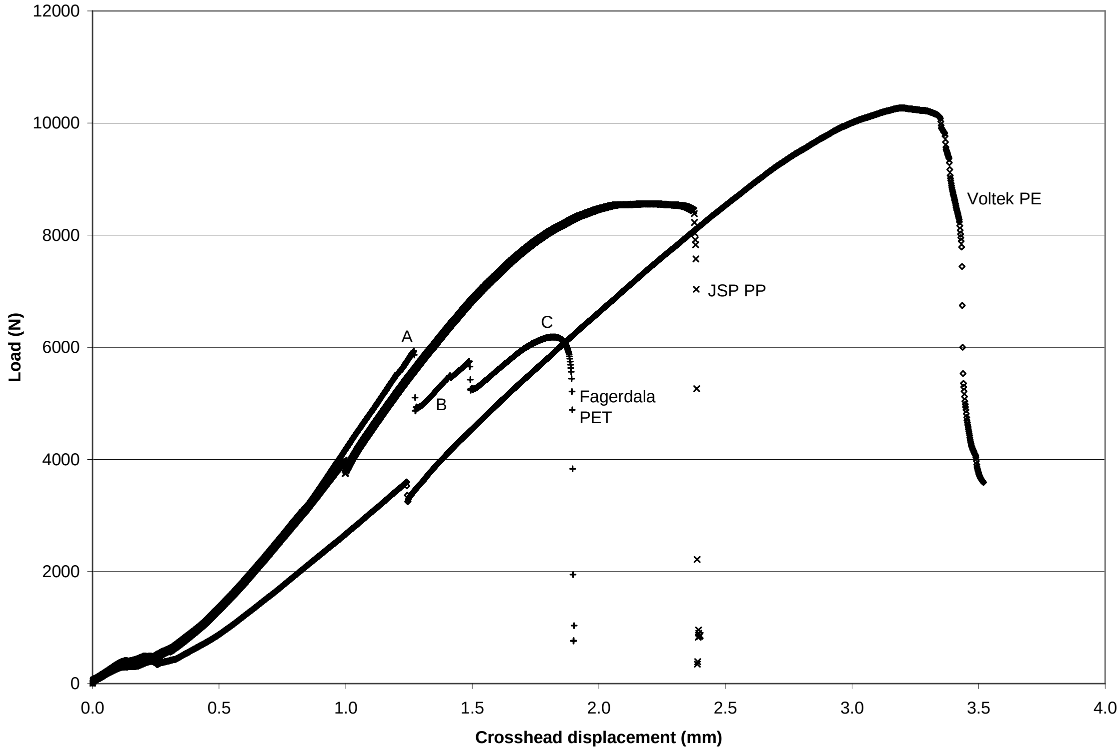

Figure 45. Representative load-displacement curves for 0.62 stitch/cm^2 specimens.

As observed with the two previous configurations, the 0.62 stitch/cm^2 PET specimens consistently exhibited a sudden failure. This response can be seen from the sawtooth appearance of the load versus deflection curve in Figure 45, indicating an abrupt reduction in load following each failure event. A progressive failure of the stitching was detected audibly leading up to the first drop in load at point A. Because the core material was well bonded to the stitches, the initial failure of the stitches appeared to introduce damage into the core. Due to the significantly greater stitch density, this damage was more pronounced than in the 0.16 stitch/cm^2 density configuration. Additionally, core cracking occurred at a a lower load (point A) than that for core failure in the non-stitched and 0.16 stitch/cm^2 configurations. Loading continued over segment B, widening the previously initiated crack. The specimens eventually experienced ultimate catastrophic failure (point C) following the fracture of all stitches. Due to the higher incidence of internal damage induced by initial stitch failure, lower ultimate tensile strengths were consistently observed at the 0.62 stitch/cm^2 density. A representative specimen that has undergone this failure progression is shown in Figure 46.

a. Initial stage of cracking.

b. Propagation of crack.

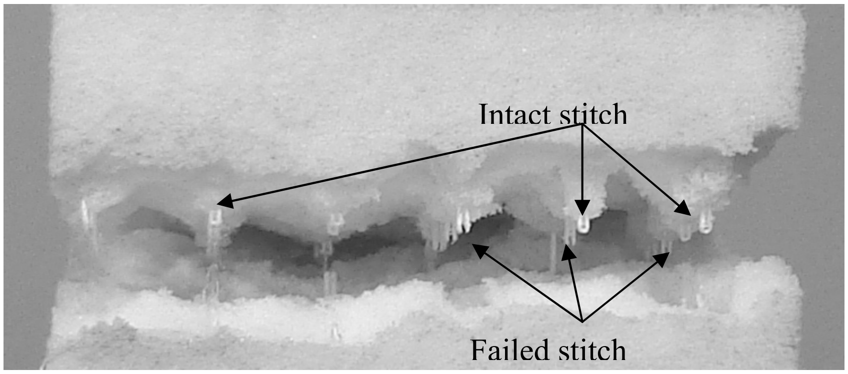

c. Catastropic failure of specimen.

Figure 46. Damage evolution for a 0.62 stitch/cm^2 PET specimen.

Figure 46c shows that a combination of intact and broken stitch threads are present following ultimate failure. As discussed in the preceding section for the 0.16 stitch/cm^2 configuration, failure occurred consistently at the loop in the stitch yarn for PET specimens. Following initial failure of the stitches, however, the core material began to crack, which severely degraded the load carrying capacity of the core. Thus, following the initial failure of the specimen (Point A), the load was carried predominantly by the stitches, causing a greater load on the bobbin thread. As a result, bobbin thread failure was also observed.

The PE and PP 0.62 stitch/cm^2 specimens consistently exhibited a facesheet/core delamination failure as observed previously. This failure appears in Figure 45 as a gradual reduction in slope near the point of ultimate failure, with a particularly noticeable plateau for the PP specimen. As with the lower 0.16 stitch/cm^2 density specimens, delamination of the facesheet occurred following initial failure of a row of stitches and progressed along the cross-section of the specimen as stitches continued to fail. This progressive failure is shown in Figure 47 for a PP specimen, which shows the specimen peel away from the lower facesheet, exposing broken stitches.

a. Initial edge delamination.

b. Failure of first stitch row.

c. Propagation of delamination.

Figure 47. Progressive delamination failure of a representative 0.62 stitch/cm^2 PP specimen.

6.1.7 Discussion of Angle Stitched Configurations

Figure 34 and Table 5 through Table 7 show that for the angle stitched configurations, the JSP PP foam had the highest average tensile strength at 0.99 MPa, followed by the Voltek PE and Fagerdala PET at 0.71 and 0.63 MPa, respectively. These results correspond to an improvement in tensile strength of the PP specimens of 56% over the non-stitched configuration. In contrast both the PE and PET specimens showed a reduction in tensile strength over the non-stitched configurations of 21% and 49%, respectively. The same tables discussed above and Figure 35 present the elastic modulus for the angle stitched configurations. The PP specimens displayed the highest average elastic modulus at 133 MPa, slightly higher than the PET specimens which had an average modulus of 128 MPa. As with all the previous configurations, the PE foam had a significantly lower modulus measuring 20.1 MPa. All three configurations showed higher average values of elastic modulus versus the non-stitched configurations with specific improvements of 60% for PP, 80% for PET and 97% for PE.

Representative load versus displacement curves from the angle stitched specimens are shown in Figure 48. The PE specimens loaded smoothly up to the maximum load, at which point catastrophic failure was observed. The PET specimens also loaded smoothly until first failure, after which load increased gradually to a maximum value. The PP specimens displayed a unique loading pattern in which load was applied smoothly to a maximum load, after which the applied load fell gradually, creating a pronounced “knee” in the plot. This response was followed by a subsequent period of unloading, in which the load decreased at a significantly lower rate until abrupt failure occurred. This failure resulted in a rapid decrease in applied load and was followed quickly by another abrupt failure resulting in the catastrophic failure of the specimen.

As discussed in the preceding section, the slight dip in load observed during the initial linear region in the specimens corresponds to the removal of the extensometers. Note that as with all preceding configurations the PE specimen displayed a significantly lower modulus.

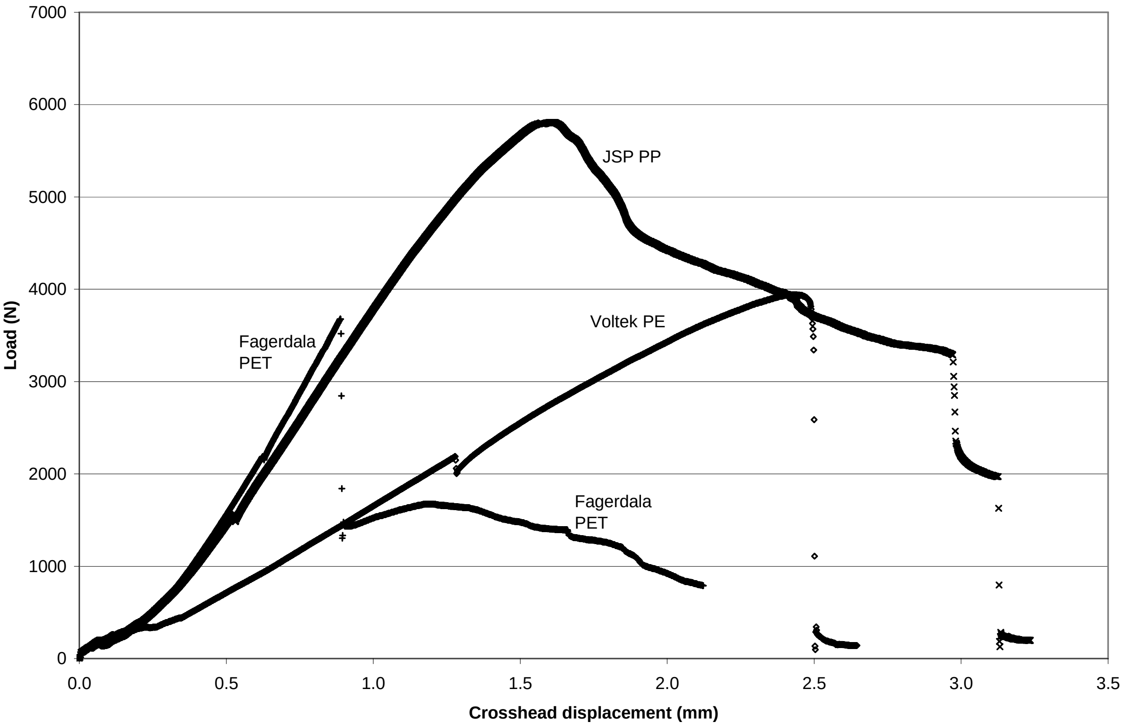

Figure 48. Representative load-displacement curves from angle stitched specimens.

Similar to the previous PET configurations, the angle stitched PET specimens consistently exhibited a sudden failure. As witnessed with the 0.62 stitch/cm^2 PET specimens, failure of the angle stitched PET specimens followed a progressive approach. Audible detection indicated the failure of the vertical stitches in the pattern, leading up to the initial failure. At this point, significant core cracking occurred, as shown in Figure 49. However the specimen did not separate into two halves. Rather, the applied load increased as the angled stitches in the pattern rotated towards the direction of loading. As the stitches continued to rotate, they were subjected to an increasing proportion of the load transmitted through the sandwich, resulting in their eventual catastrophic failure.

Figure 49. Core cracking in angle stitched PET specimen following vertical stitch failure.

The fact that the lowest observed tensile strength for the PET specimens occurred with the angle stitched configuration can be explained in terms of core damage. As discussed previously, the PET was found to be particularly susceptible to damage. Thus, significant core damage would be expected during the rotation of the angled stitches towards the out-of-plane loading direction. The load carrying capacity of the core would therefore be reduced, leading to an increased percentage of the load being supported by the vertical stitching. This in turn would cause premature cracking and subsequent failure.

In contrast, the PE and PP specimens continued to exhibit progressive delamination failure following stitch failure, as outlined in previous sections. Alignment of the angled stitches within the PE specimens during the test was better accommodated by the greater toughness and compliance of this material relative to PET. Core damage was still induced, however, leading to the poor performance relative to the vertically stitched sandwich configurations. The PP specimens appeared to withstand the rotation of the angled stitches the best, resulting in performance second only to that of the 0.62 stitch/cm^2 configuration.

6.1.8 Discussion of Transverse Reinforcement Effects by Material Type

In this section, the effects of transverse reinforcement on sandwich performance are reviewed for each core material type. The underlying causes of the noted effects are as reported in the preceding sections.

Figure 50 shows representative load versus displacement curves for PE specimens of each stitching configuration. It can be seen that the stitch density has a pronounced effect on sandwich behavior. For the 0.16 stitch/cm^2 stitch density, the load versus deflection curve is similar to that of the non-stitched configuration albeit with an improvement in modulus of elasticity. For the 0.62 stitch/cm^2 configuration, it is apparent that the modulus of elasticity is again improved but with the result that the yield period is shortened and followed by abrupt failure of the specimen. Because the angle stitched specimens share the same density of vertical stitches as the 0.16 stitch/cm^2 configuration, they were expected to have a similar modulus of elasticity. This is confirmed in Figure 50, which shows the angled stitches having a negative effect on the performance of the sandwich.

Figure 51 shows representative load versus displacement curves for PP specimens of each of the four stitching configurations. The stitch density is shown to have an effect on the performance of the sandwich. Of particular note, the 0.16 stitch/cm^2 configuration has a lower strength than the non-stitched configuration with no improvement in the modulus of elasticity. In contrast, specimens with the 0.62 stitch/cm^2 stitch density show pronounced increases in both strength and modulus of elasticity while the angle stitched specimens show a intermediate level of improvement.

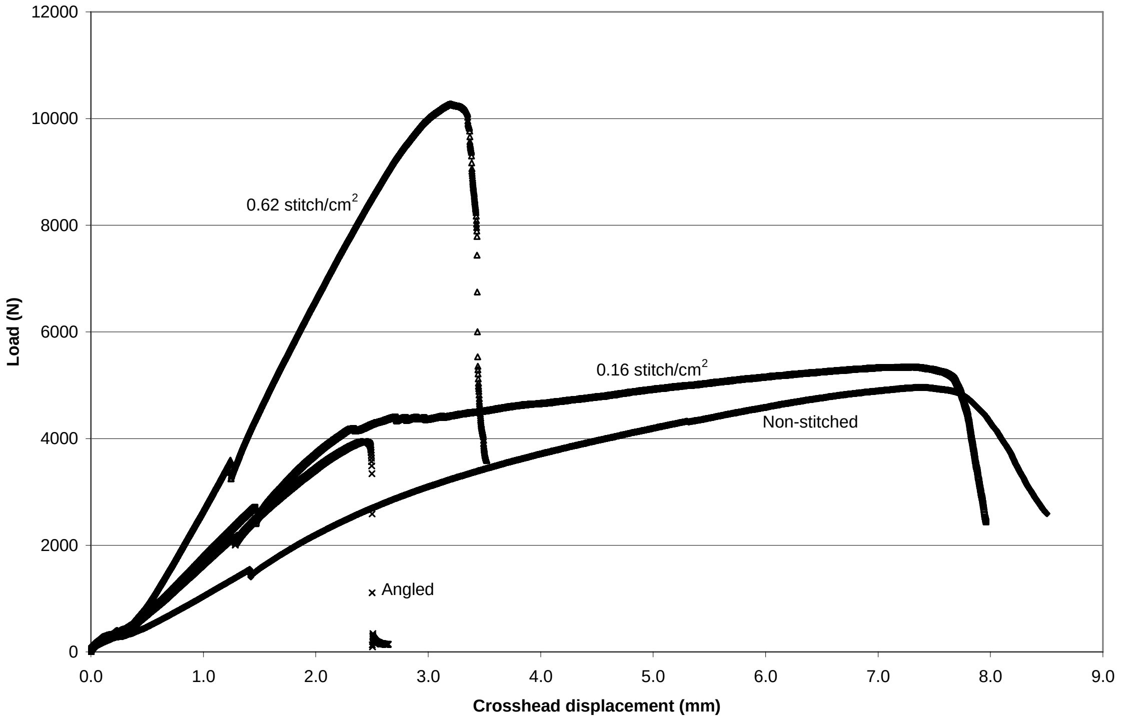

Figure 50. Representative load-displacement curves from PE specimens.

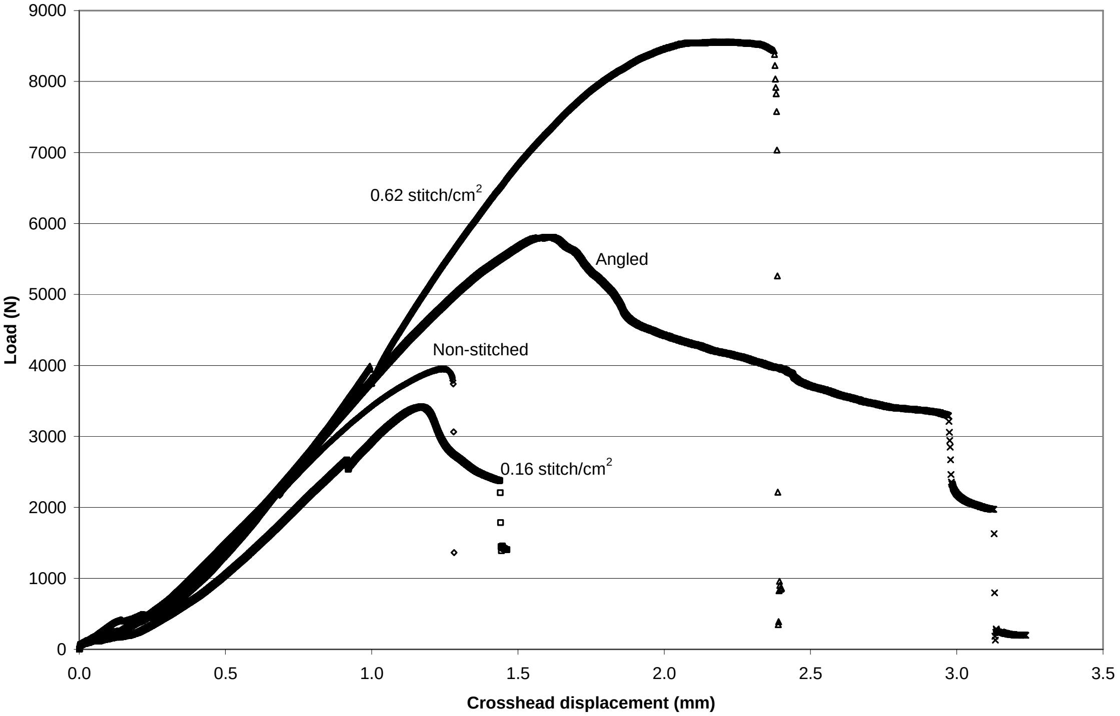

Figure 51. Representative load-displacement curves from PP specimens.

Figure 52 shows representative load versus displacement curves for PET specimens of each configuration. For this core material, the stitch density is shown to have a significant effect on sandwich behavior. Improvements in modulus of elasticity and ultimate tensile strength were observed with the 0.16 stitch/cm^2 configuration. The addition of 0.62 stitch/cm^2 and angled stitching reinforcement also caused improvements in the modulus of elasticity, but with a reduction in tensile strength compared to the non-stitched configuration.

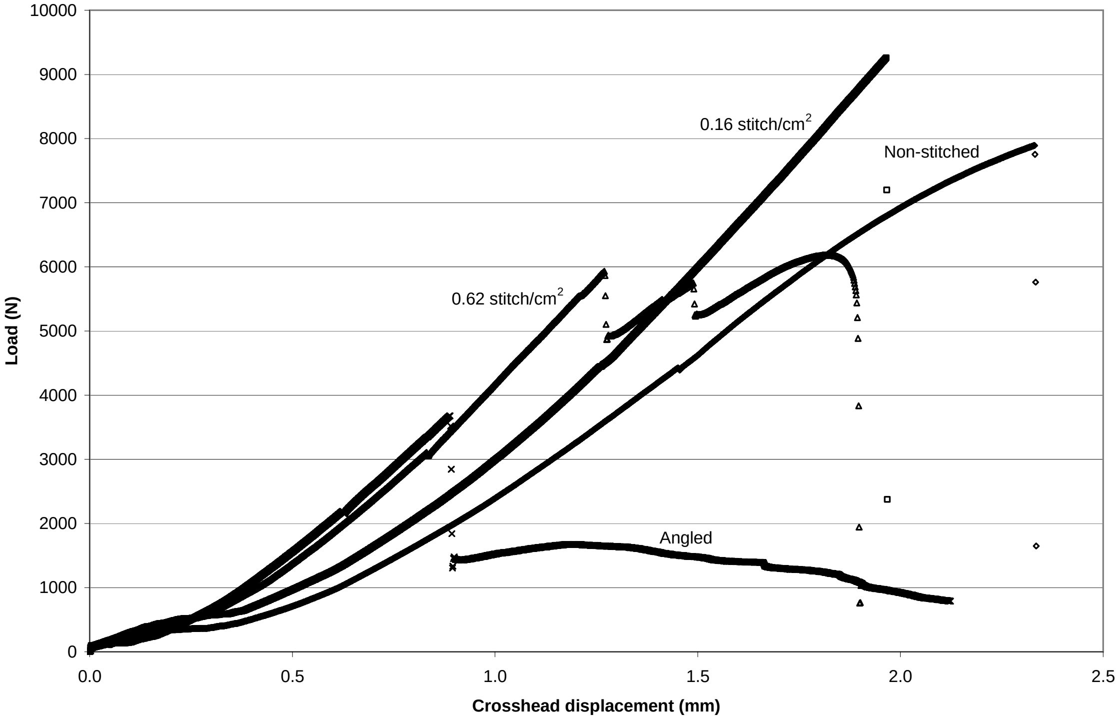

Figure 52. Representative load-displacement curves from PET specimens.

6.1.9 Assessment of Self-Healing Ionomer Layer

As described previously in Section 4.2.3, prototype sandwich configurations were fabricated which contained an internal self-healing ionomer layer. Two different thicknesses of DuPont^{TM} Surlyn® (EMAA ionomer), were selected for use: 3.2 mm and 6.4 mm. The Surlyn layer was incorporated between two layers of PET foam using a melt-bond procedure in a heated press. To assess the bond strength between the Surlyn layer and the adjacent PET foam, additional flatwise tensile testing was performed. In addition to investigating two thicknesses of Surlyn, the temperature and duration of the hot-presses were investigated. Table 8 lists the manufacturing parameters investigated using three different sandwich panels. The relatively long press times resulted from the poor heat transfer from the heated platens of the press to the ionomer layer sandwiched between PET foam layers. The purpose of investigating these parameters was to determine their effect on the out-of-plane tensile strength of the sandwich composite in general and the bond between the Surlyn and PET core in particular.

Table 8. Variables Investigated Using Hot Press Manufacturing Method

Panel Number	**Surlyn Layer Thickness**	**Press Time (min)**	**Press Temp (^oC)**
1	3.2 mm	240	149°
2	3.2 mm	330	113°
3	6.4 mm	110	138°

Flatwise tensile testing of specimens from the three panels listed in Table 8 was performed following the procedure outlined previously in Section 6.1.2. Results from flatwise tensile testing of the panels manufactured using the hot-press method are presented in Table 9. Included in these tables are the ultimate tensile strength and modulus of elasticity for each specimen tested. Also shown are the mean, standard deviation and coefficient of variation for these data. As shown previously in Table 7 and discussed in Section 6.1.4, this sandwich configuration yielded an average tensile strength of 1.25 MPa and a modulus of elasticity of 71.0 MPa without the Surlyn layer present. Comparing these values to those obtained with the Surlyn layer present (between the PET foam layers), a significant degradation in both tensile strength and modulus is observed for all three panels. These results indicate that the hot-press manufacturing method used to bond the Surlyn to the PET foam was degrading the mechanical properties of the Fagerdala PET foam.

To further investigate the relative impact of the heat and pressure aspects of the hot-press method, eight additional PET foam specimens were manufactured and subjected to flatwise tensile testing. Three of these foam specimens underwent heating in a convection oven at 149°C for 149 minutes. Three additional specimens were placed under a compressive stress equal to that experienced during the hot-press method (approximately 70 kPa) for 120 minutes, but without the application of heat. The final two specimens were used as controls, having no heat or pressure applied. Results of flatwise tensile testing on these eight specimens are shown in Table 10. Interestingly, both heating and applied pressure were shown to produce an increase in the modulus of elasticity.

Table 9. Flatwise Tensile Testing Results for Surlyn/PET Specimens Manufactured Using the Original Hot-Press Method

Panel	Tensile Strength (MPa)	Modulus of Elasticity (MPa)
Panel 1 Thickness: 3.2 mm Time: 240 min Temp: 149 °C	0.70	51.5
	0.63	49.0
	0.77	51.0
	0.45	49.5
	0.58	49.6
	0.81	49.3
	0.92	50.4
	0.61	52.2
	Average = 0.68	**Average = 50.31**
	Std Dev = 0.15	**Std Dev = 1.16**
	Coeff. Of Variation = 21.83%	**Coeff. Of Variation = 2.31%**
Panel 2 Thickness: 3.2 mm Time: 330 min Temp: 113 °C	1.03	52.3
	0.68	61.6
	1.00	54.4
	0.66	54.9
	0.86	57.2
	0.64	59.6
	0.66	59.3
	0.80	55.6
	Average = 0.92	**Average = 56.86**
	Std Dev = 0.03	**Std Dev = 3.12**
	Coeff. Of Variation = 3.59%	**Coeff. Of Variation = 5.49%**
Panel 3 Thickness: 6.4 mm Time: 110 min Temp: 138 °C	1.05	66.0
	1.00	63.6
	0.95	58.5
	1.13	61.3
	0.69	58.6
	1.02	56.9
	0.76	61.9
	0.82	60.7
	Average = 0.93	**Average =60.9**
	Std Dev = 0.15	**Std Dev = 2.99**
	Coeff. Of Variation = 16.60%	**Coeff. Of Variation = 4.91%**

Table 10. Flatwise Tensile Testing Results for Surlyn/PET Subjected to Heat or Compression

Identification	Tensile Strength (MPa)	Modulus of Elasticity (MPa)
Heated PET Time: 110 min Temp: 149 °C	0.66 0.79 0.81 **Average = 0.75** **Std Dev = 0.08** **Coeff. Of Variation = 10.78%**	117.1 121.7 114.4 **Average = 117.7** **Std Dev = 3.68** **Coeff. Of Variation = 3.12%**
Compressed PET Time: 120 min Temp: N/A	1.14 0.93 0.82 **Average = 0.97** **Std Dev = 0.16** **Coeff. Of Variation = 16.94%**	102.6 103.2 102.4 **Average = 102.7** **Std Dev = 0.44** **Coeff. Of Variation = 0.43%**
Control PET Time: N/A Temp: N/A	1.09 0.71 **Average = 0.90** **Std Dev = 0.27** **Coeff. Of Variation = 29.57%**	99.85 95.99 **Average =97.92** **Std Dev = 2.73** **Coeff. Of Variation = 2.79%**

Following this second round of tensile tests, a modified procedure was used to bond the Surlyn layer between two sections of PET core material. In this method, a layer of Surlyn was heated in a convection oven and then placed between two sections of unheated PET core. The sandwich was then held under a pressure of 70 kPa in a hot press (with no additional heating) until the specimen had fully cooled, in order to create a melt-bond similar to that obtained with the hot-press method. The convection oven temperatures and Surlyn heating times used are listed in Table 11.

Table 11. Temperature and Specimen Heating Time Used for the Pre-Heated Surlyn Pressing

Surlyn thickness	**Time (min)**	**Temp (^{o}C)**
3.2 mm	145	127
3.2 mm	105	165
6.4 mm	165	132
6.4 mm	17	140

Table 12 presents the flatwise tensile test results obtained from foam specimens with an embedded Surlyn layer fabricated using the pre-heated Surlyn method. The highest tensile strength and modulus of elasticity were obtained when the Surlyn was preheated at 138^{o}C. The tensile strength obtained for this condition was 1.13 MPa. As shown previously in Table 7, this foam yielded an average tensile strength of 1.25 MPa. Thus the reduction in tensile strength was minimized using the 138^{o}C preheated Surlyn melt-bonding procedure.

Table 12. Flatwise Tensile Testing Results for Surlyn/PET Specimens Manufactured Using the Pre-Heated Surlyn Pressing Method

Surlyn Layer Preheating	Tensile Strength (MPa)	Modulus of Elasticity (MPa)
Thickness: 3.2 mm Temp: 127 °C Time: 145 min	0.70	51.5
	0.63	49.0
	0.77	51.0
	0.45	49.5
	0.58	49.6
	0.81	49.3
	0.92	50.4
	0.61	52.2
	Average = 0.68	**Average = 50.31**
	Std Dev = 0.15	**Std Dev = 1.16**
	Coeff. Of Variation = 21.83%	**Coeff. Of Variation = 2.31%**
Thickness: 3.2 mm Temp: 165 °C Time: 105 min	1.03	52.3
	0.68	61.6
	1.00	54.4
	0.66	54.9
	0.86	57.2
	0.64	59.6
	0.66	59.3
	0.80	55.6
	Average = 0.92	**Average = 56.86**
	Std Dev = 0.03	**Std Dev = 3.12**
	Coeff. Of Variation = 3.59%	**Coeff. Of Variation = 5.49%**
Thickness: 6.4 mm Temp: 132 °C Time: 165 min	1.05	66.0
	1.00	63.6
	0.95	58.5
	1.13	61.3
	0.69	58.6
	1.02	56.9
	0.76	61.9
	0.82	60.7
	Average = 0.93	**Average =60.9**
	Std Dev = 0.15	**Std Dev = 2.99**
	Coeff. Of Variation = 16.60%	**Coeff. Of Variation = 4.91%**
Thickness: 6.4 mm Time: 17 min Temp: 140^{o}C	1.06	37.97
	0.91	37.33
	1.00	41.35
	1.19	40.05
	1.18	44.00
	1.04	39.67
	0.79	24.79
	Average = 1.02	**Average = 40.45**
	Std Dev = 0.14	**Std Dev = 2.43**
	Coeff. Of Variation = 13.64%	**Coeff. Of Variation = 6.00%**

Approximately 70% of the specimens manufactured using the pre-heated Surlyn pressing method failed within the PET foam layers away from the bondline between the Surlyn and PET. A representative foam failure is shown in Figure 53. The remaining 30% of the specimens failed at the bond between the Surlyn and the PET foam as shown in Figure 54. No correlation was observed between failure location and tensile strength, however.

Figure 53. Representative PET foam failure.

Figure 54. Representative PET/Surlyn bond failure.

In summary, good mechanical bonding was obtained between PET foam and Surlyn layers by preheating the Surlyn and melt-pressing it to the adjacent foam layers. The best mechanical properties were obtained when the Surlyn was preheated to 138^{o}C and melt-bonded to the adjacent PET foam layers under an applied pressure of 70 kPa.

6.2 Core Shear Testing

6.2.1 Specimen Configurations

Core shear testing was performed on the same three sandwich material configurations used for flatwise tensile testing. For convenience, these configurations are repeated in Table 13. As with the flatwise tensile specimens, all facesheets were composed of Spectra® 900 woven fabric measuring 2.1 mm thick and infiltrated with an epoxy consisting of EPON^{TM}/EPIKOTE^{TM} Resin 862 combined with EPIKURE^{TM} Curing Agent 9553 (mixture ratio of 100:16.9). The three foam core materials all measured 21 mm in thickness, resulting in all specimens having an overall thickness of 25 mm. As with flatwise tensile testing, the sandwich configurations listed in Table 13 were manufactured with four different forms of transverse reinforcement: non-stitched, vertically stitched (0.16 stitch/cm^2 and 0.62 stich/cm^2 densities) and angle stitched.

Table 13. Sandwich Configurations Used for Core Shear Testing

Sandwich Configuration	**Core Material**	**Core Density (kg/m^3)**	**Core Supplier**	**Facesheet**
1	PE	128	Voltek LLC	Spectra®/Epoxy
2	PP	128	JSP Int'l	Spectra®/Epoxy
3	PET	125	Fagerdala World Foams	Spectra®/Epoxy

6.2.2 Testing Methods and Procedures

For core shear testing (ASTM C 273), a series of rectangular 50 mm x 300 mm specimens were prepared from the sandwich panels in the same manner as flatwise tensile specimens (Section 6.1.2). The core shear test is similar to a simple lap shear test; however, the load is applied such that the sandwich specimen is loaded at a slight angle to the plane of the facesheets. Fixtures are used that enable a tensile load to be applied through a line connecting opposite corners of the sandwich specimen as shown in Figure 55. Core shear testing was performed using an electromechanical testing machine with National Instruments data acquisition software. Displacement measurements were obtained using the same extensometers that were used for flatwise tensile testing. These extensometers, with a nominal 30.5 mm gage length, were attached to aluminum angle pieces that were bonded to the steel loading plates as shown in Figure 56. Thus, the extensometers measured the relative axial motion occurring between the opposing faces of the sandwich composite specimen.

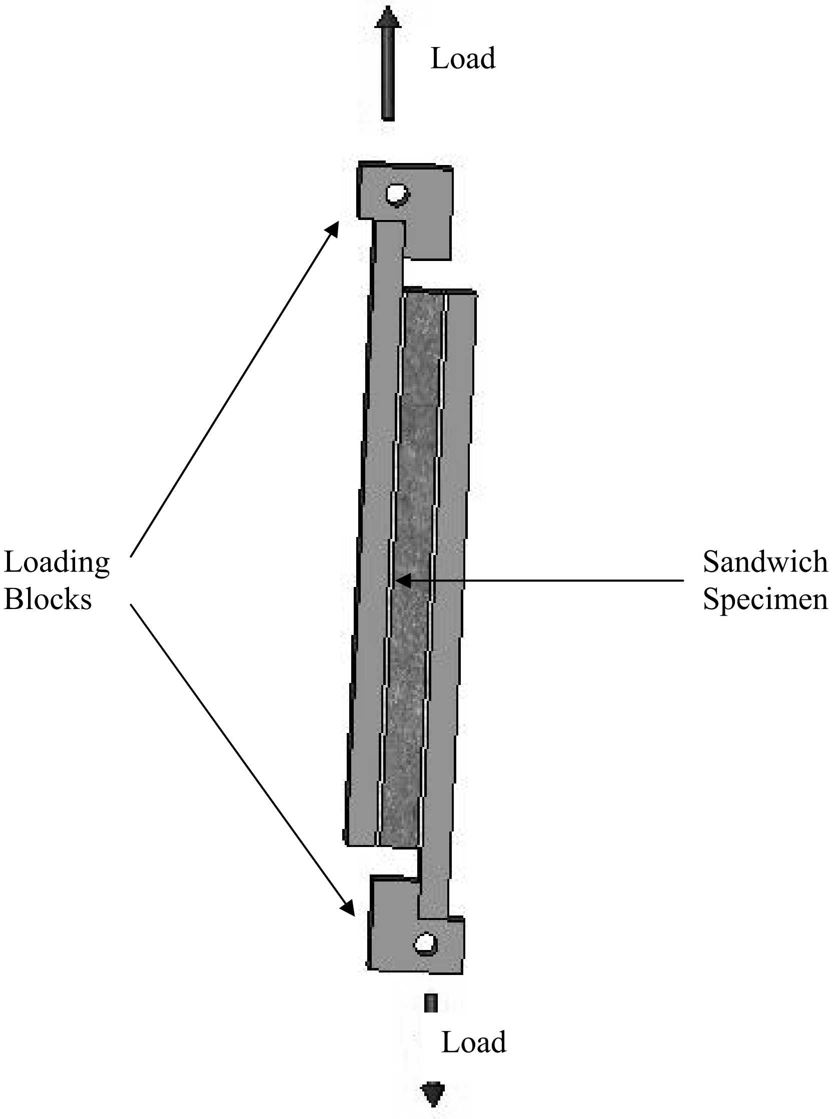

Figure 55. Core shear testing setup.

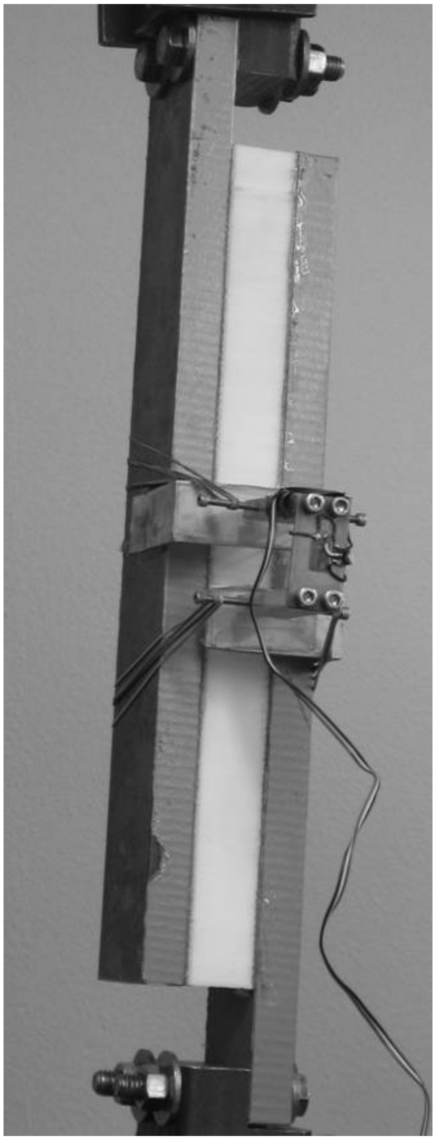

Figure 56. Core shear specimen with extensometer.

Stress and strain values were obtained using Equation (1) and Equation (2), as outlined in Section 6.1.2. The ultimate shear strength was calculated as the stress corresponding to the maximum load recorded during the test. The shear modulus was found using the expression

$$G = \frac{St}{Lb} \quad , \tag{3}$$

where G is the core shear modulus in Pascals, S is the slope of the initial portion of the load deflection curve in Newtons per meter, L is the length of the specimen, t is the thickness, and b is the width, all in meters. Similar to the calculation of the elastic modulus for a flatwise tensile test, the value of S was determined by taking the slope of a linear fit for the linear elastic region of the load-deflection curve as shown in Figure 57.

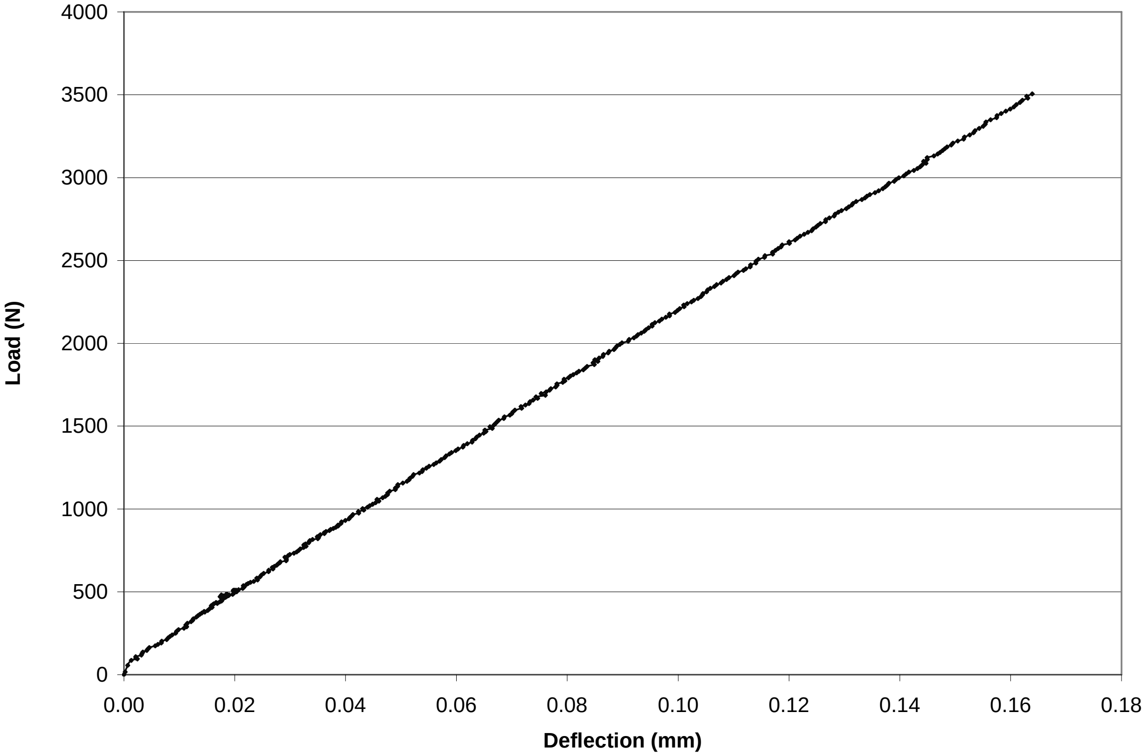

Figure 57. Representative load-deflection response (initial linear region) for a core shear test.

6.2.3. Core Shear Test Results

Table 14 through Table 16 provide a summary of the core shear testing results. Included in these tables are the ultimate shear strength and shear modulus for each specimen tested. Also shown are the mean, standard deviation, and coefficient of variation for these data. A visual comparison of the mean and standard deviation of the data is also provided in the form of bar graphs in Figure 58 and Figure 59.

Table 14. Core Shear Testing Results: Voltek PE Core (Configuration 1)

Stitching	Ultimate Shear Strength (MPa)	Shear Modulus (MPa)
Non-Stitched	0.27 0.26 0.25 0.30 0.23 0.26 **Average = 0.26** **Std Dev = 0.02** **Coeff. Of Variation = 9.50**	3.19 2.78 2.43 2.49 2.54 2.36 **Average = 2.63** **Std Dev = 0.31** **Coeff. Of Variation = 11.7**
Vertically Stitched 0.16 Stitch/cm^2	0.45 0.44 0.49 **Average = 0.46** **Std Dev = 0.03** **Coeff. Of Variation = 5.97**	2.16 2.18 2.02 **Average = 2.12** **Std Dev = 0.08** **Coeff. Of Variation = 4.00**
Vertically Stitched 0.62 Stitch/cm^2	1.84 1.86 1.87 1.88 1.88 **Average = 1.87** **Std Dev = 0.02** **Coeff. Of Variation = 0.99**	2.25 2.01 1.98 1.96 2.05 **Average = 2.05** **Std Dev = 0.12** **Coeff. Of Variation = 5.71**
Angle Stitched	0.68 0.55 0.43 0.45 0.61 0.67 0.60 0.48 **Average = 0.56** **Std Dev = 0.10** **Coeff. Of Variation = 17.4**	4.14 3.89 3.60 3.94 4.11 3.34 4.01 3.88 **Average = 3.86** **Std Dev = 0.27** **Coeff. Of Variation = 7.01**

Table 15. Core Shear Testing Results: JSP PP Core (Configuration 2)

Stitching	Ultimate Shear Strength (MPa)	Shear Modulus (MPa)
Non-Stitched	0.73 0.68 0.65 0.67 0.63 **Average = 0.67** **Std Dev = 0.04** **Coeff. Of Variation = 5.56**	31.2 26.2 25.1 22.5 21.3 **Average = 25.3** **Std Dev = 3.88** **Coeff. Of Variation = 15.3**
Vertically Stitched 0.16 Stitch/cm^2	0.69 0.55 0.56 0.58 0.60 **Average = 0.59** **Std Dev = 0.06** **Coeff. Of Variation = 9.28**	22.1 15.1 13.9 19.1 18.3 **Average = 17.7** **Std Dev = 3.25** **Coeff. Of Variation = 18.4**
Vertically Stitched 0.62 Stitch/cm^2	1.32 1.37 1.27 1.33 1.36 **Average = 1.33** **Std Dev = 0.04** **Coeff. Of Variation = 3.02**	34.3 33.1 32.3 32.4 33.8 **Average = 33.2** **Std Dev = 0.85** **Coeff. Of Variation = 2.56**
Angle Stitched	0.94 0.93 0.93 0.79 0.87 0.89 **Average = 0.89** **Std Dev = 0.06** **Coeff. Of Variation = 6.35**	40.4 42.3 38.8 30.0 39.9 37.2 **Average = 38.1** **Std Dev = 4.31** **Coeff. Of Variation = 11.3**

Table 16. Core Shear Testing Results: Fagerdala PET Core (Configuration 3)

Stitching	Ultimate Shear Strength (MPa)	Shear Modulus (MPa)
Non-Stitched	0.79 0.77 0.79 0.82 0.79 **Average = 0.79** **Std Dev = 0.02** **Coeff. Of Variation = 2.55**	21.0 20.5 21.6 21.4 21.5 **Average = 21.2** **Std Dev = 0.46** **Coeff. Of Variation = 2.19**
Vertically Stitched 0.16 Stitch/cm^2	0.58 0.50 0.53 0.54 0.56 0.48 **Average = 0.53** **Std Dev = 0.04** **Coeff. Of Variation = 7.1**	28.5 34.4 31.8 33.5 35.6 33.1 **Average = 32.8** **Std Dev = 2.46** **Coeff. Of Variation = 7.5**
Vertically Stitched 0.62 Stitch/cm^2	1.07 0.99 1.03 1.16 1.03 **Average = 1.06** **Std Dev = 0.07** **Coeff. Of Variation = 6.26**	33.7 34.5 34.6 35.7 36.7 **Average = 35.1** **Std Dev = 1.18** **Coeff. Of Variation = 3.38**
Angle Stitched	0.65 0.64 0.65 0.68 **Average = 0.66** **Std Dev = 0.02** **Coeff. Of Variation = 2.62**	39.4 36.6 36.4 37.9 **Average = 37.6** **Std Dev = 1.37** **Coeff. Of Variation = 3.64**

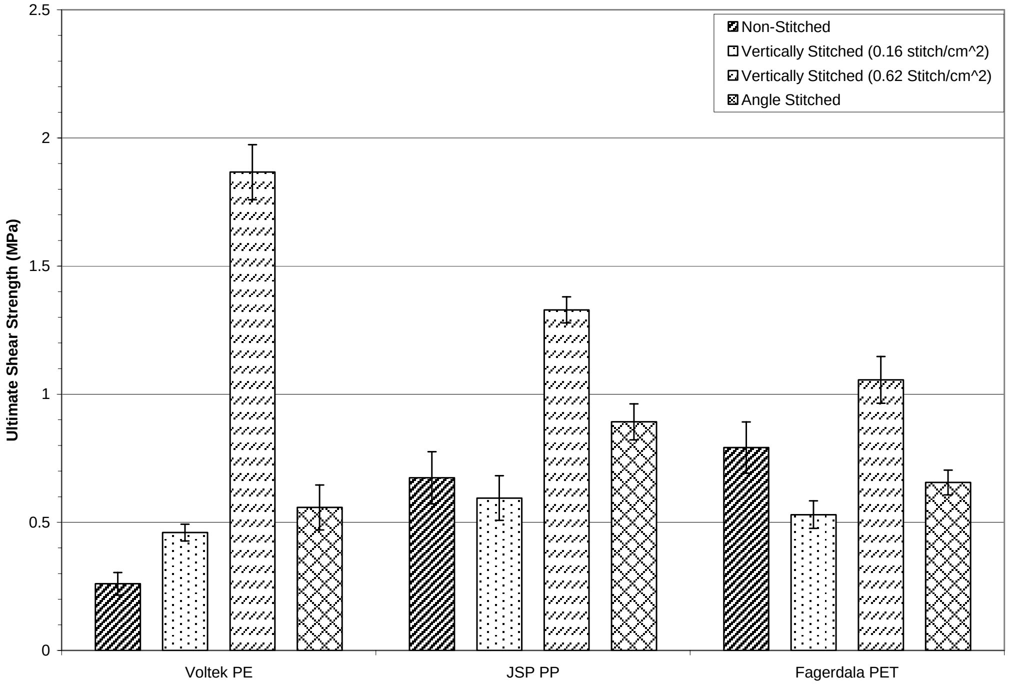

Figure 58. Ultimate shear strength results from core shear testing.

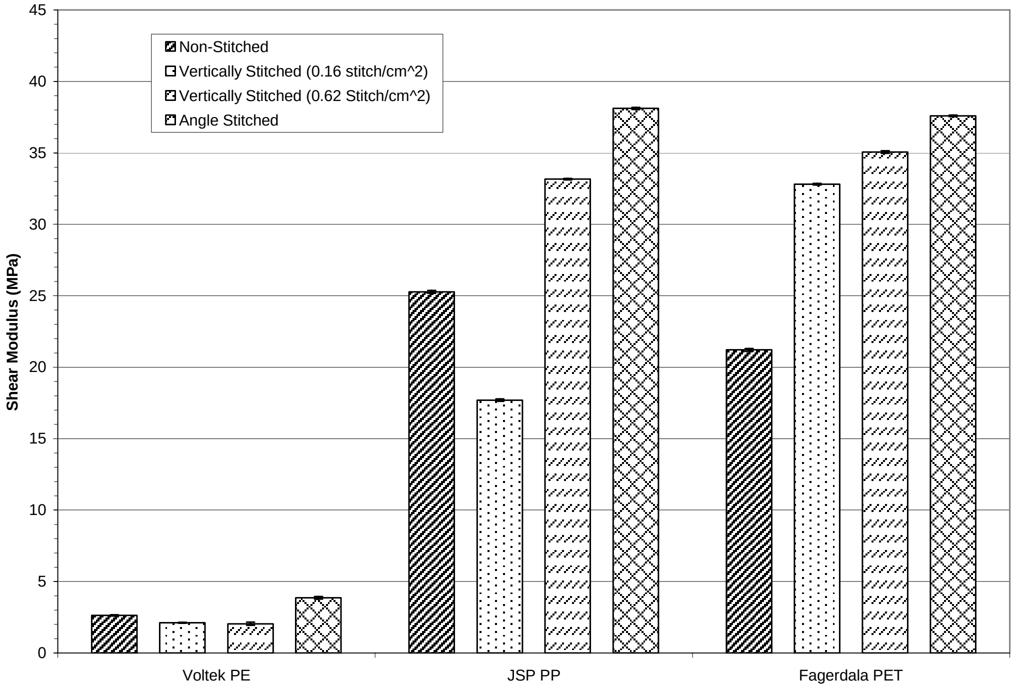

Figure 59. Shear modulus results from core shear testing.

6.2.4 Discussion of Non-Stitched Configurations

Figure 58 and Table 14 through Table 16 show that for the non-stitched configurations, the Fagerdala PET foam had the highest average shear strength at 0.79 MPa, followed by JSP PP and Voltek PE at 0.67 and 0.26 MPa, respectively. Figure 59 shows the shear modulus for the non-stitched configurations. The PP and PET specimens displayed similar values for shear modulus at 25.3 and 21.2 MPa, respectively. The PE foam had a lower shear modulus measuring 2.63 MPa. These shear strength and shear modulus values will serve as the baseline for comparing the affect of transverse reinforcement.

Typical load-displacement diagrams for the non-stitched specimens are shown Figure 60. During the test, loading progressed smoothly up to the maximum load. As with flatwise tensile testing, the brief dips in the load during the linear region of the tests correspond to a pause in the test at which time the extensometers were removed.

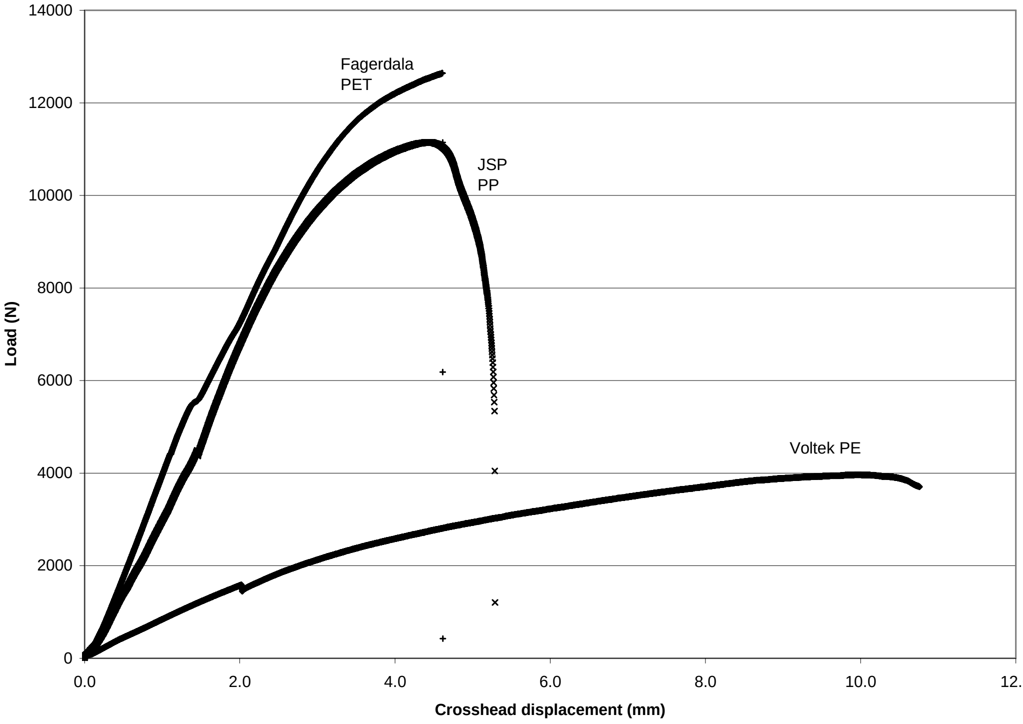

Figure 60. Representative load-displacement curves from core shear testing of non-stitched specimens.

Figure 61 shows a representative failure observed in the PET specimens. These specimens consistently failed in the core, away from the facesheet interfaces. As shown in Figure 60, this failure was accompanied by a sudden drop in load immediately following the maximum load. As observed with flatwise tensile testing, core material remained bonded to each facesheet following failure, indicating that the bond strength between the core and facesheet is greater than the strength of the core itself.

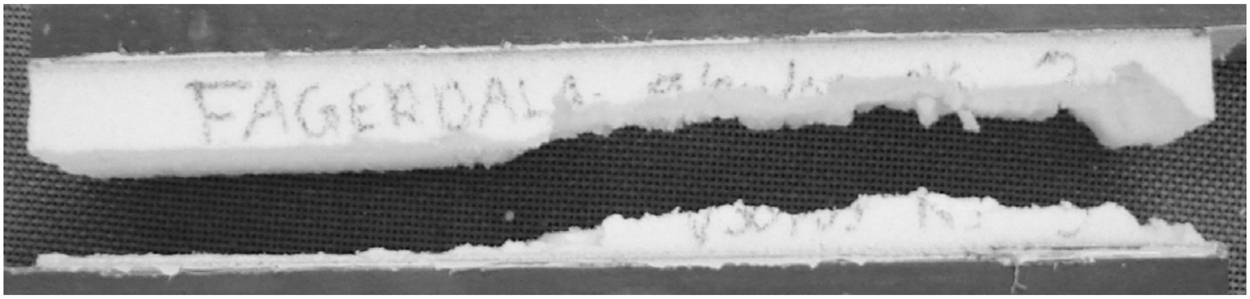

Figure 61. Core failure of a PET non-stitched specimen.

In contrast, the PE and PP specimens did not exhibit a sudden failure, but rather a gradual decrease in load as shown in Figure 60. This response was associated with progressive delamination, in which the facesheet gradually peels away from the core starting at an edge of the specimen as shown in Figure 62. As loading continued, delamination progressed until the facesheet had completely separated from the core. A representative PP specimen exhibiting this mode of failure is illustrated in Figure 63.

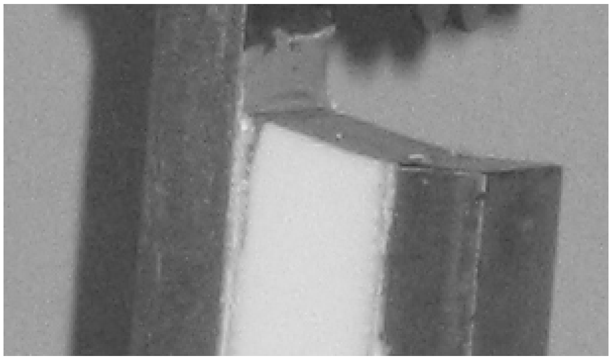

Figure 62. Delamination in a non-stitched PE core shear specimen.

Figure 63. Complete delamination failure of a non-stitched PP core shear specimen.

As discussed with the non-stitched flatwise tensile testing results, the difference in failure mode between the PET, PE and PP specimens suggests a difference in bonding quality between the sandwich constituents. The PET specimens show the highest value of bond strength, resulting in core failure. In contrast, the PP and PE core materials do not appear to form a sufficiently strong bond with the facesheet, resulting in failure of the interface.

6.2.5 Discussion of 0.16 stitch/cm^2 Configurations

Figure 58 and Table 14 through Table 16 show that for the 0.16 stitch/cm^2 configurations, the JSP PP foam had the highest average shear strength at 0.59 MPa, followed by Fagerdala PET and Voltek PE at 0.53 and 0.46 MPa, respectively. Of these configurations, only the PE improved in shear strength with the addition of stitches, by a value of 77% over the non-stitched configuration. In contrast, the PET and PP decreased by 33% and 12%, respectively, relative to the non-stitched configurations. Figure 59 shows the shear modulus for the 0.16 stitch/cm^2 configurations. The PET specimens displayed the highest average shear modulus at 32.8 MPa followed by the PP specimens with a modulus of 17.7 MPa. As with the non-stitched configurations, the PE foam had a significantly lower modulus, measuring 2.12 MPa. In comparison with the non-stitched results, the PP and PE specimens showed reductions in modulus of 19% and 30%, respectively, while the PET specimens increased in average shear modulus by 55%.

Typical load-displacement diagrams for the 0.16 stitch/cm^2 specimens are shown in Figure 64. For all three configurations, loading progressed smoothly up to the maximum load. As discussed previously, the slight dip in load observed during the linear region corresponds to the removal of the extensometers.

As observed with the non-stitched configuration, the 0.16 stitch/cm^2 PET specimens consistently exhibited sudden failure associated with a sudden drop in load immediately following the maximum load. In contrast with the non-stitched configuration, core failure occurred prior to stitch failure, leaving the sandwich intact. Core cracking generally occurred between vertical stitch columns at an angle of approximately 45°. Such cracking was most pronounced near the ends of the specimen, as depicted in Figure 65. The PE and PP 0.16 stitch/cm^2 specimens consistently exhibited delamination failure, as evidenced by the gradual drop in load immediately following the maximum load in Figure 64.

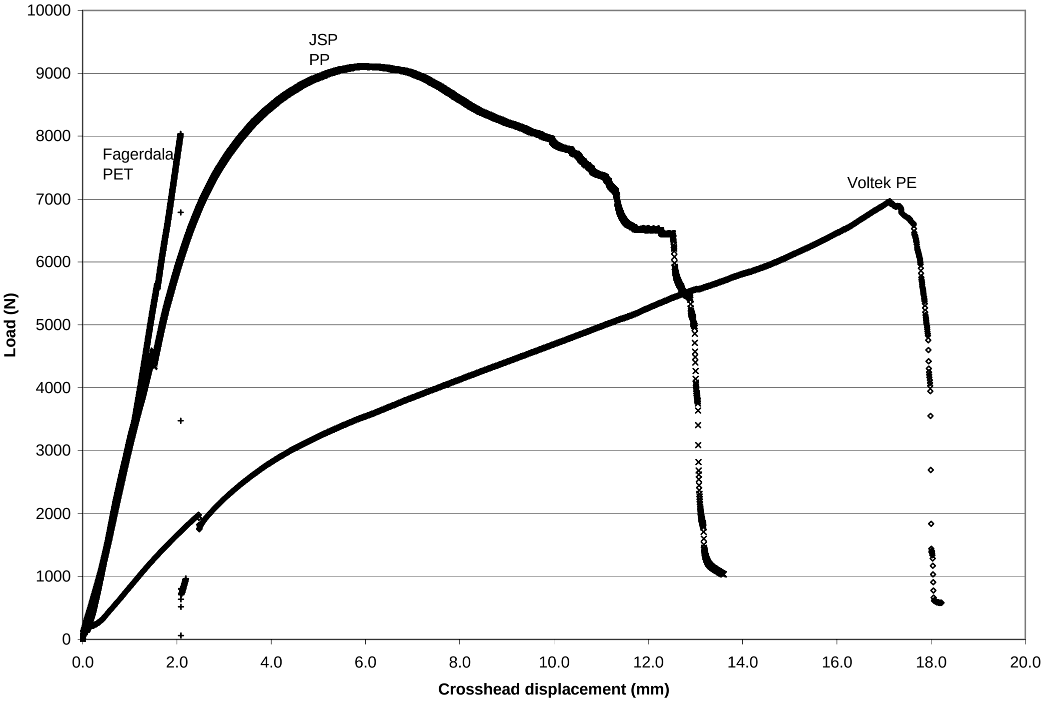

Figure 64. Representative load-displacement curves from core shear testing of 0.16 stitch/cm^2 specimens.

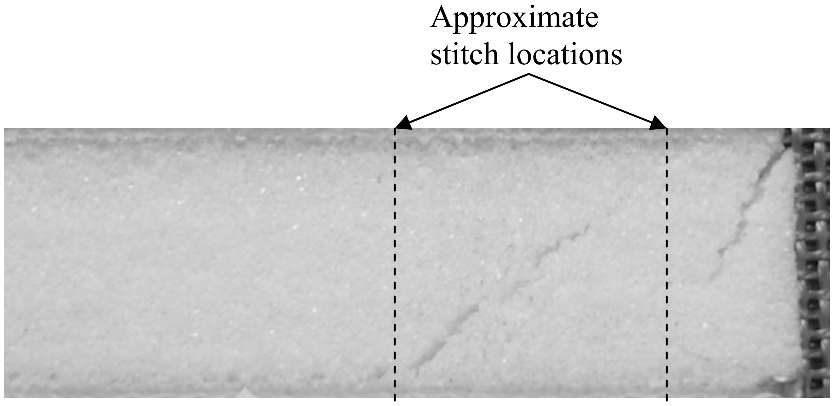

Figure 65. Core cracking in a 0.16 stitch/cm^2 PET core shear specimen.

For both the PE and PP specimens, delamination of the facesheet initiated at the leading edge of the specimen, as shown in Figure 66 for a representative PP specimen. Delamination progressed up to the first intact row of stitches, until stitch failure occurred, after which delamination growth continued. This growth pattern repeated along the length of the specimen until the facesheet completely separated from the core. A photograph of this type of failure is shown in Figure 67 for a PE specimen. Note that this failure mechanism produces the increase in shear deformation as indicated by the increased crosshead displacement over that observed for the non-stitched configurations.

Figure 66. Initiation of delamination at the leading edge of a 0.16 stitch/cm^2 PP specimen

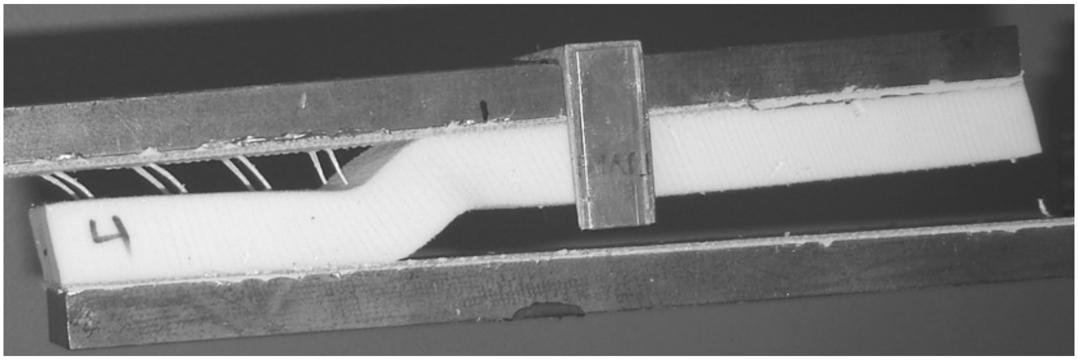

Figure 67. Delamination failure of a 0.16 stitch/cm^2 PE specimen.

The decrease in shear strength observed with the PET and PP core shear specimens can be related to core damage. The load applied to each specimen during core shear testing is initially perpendicular to the vertical stitches. This stitch orientation results in minimal load being supported by the stitches initially. As the test progresses and the specimen deforms in shear, the orientation of the stitches moves toward alignment with the direction of the load. As this occurs, the stitches must rotate through the core material, introducing significant internal damage, particularly for the more brittle PET core material. This damage is believed to degrade the load-carrying capacity of the core leading to failure at loads below those of the non-stitched configuration. In contrast, the tougher, more compliant PE foam appeared better able to withstand the rotation associated with the stitches without pronounced reduction in core material strength.

The reduction in shear modulus for the PE and PP specimens is likely associated with the poor bonding between the stitches and core, which inhibits transmission of the shear load between stitches and core. As a result, during loading the core behaves as if it were non-stitched, but with damage caused by the introduction of stitch holes. In contrast, the bond between the PET core and stitching is superior, explaining the observed improvement in shear modulus.

6.2.6 Discussion of 0.62 stitch/cm^2 Configurations

Figure 58 and Table 14 through Table 16 show that for the 0.62 stitch/cm^2 configurations, the Voltek PE foam had the highest average shear strength at 1.87 MPa, followed by JSP PP and Fagerdala PET at 1.33 and 1.06 MPa, respectively. These results correspond to an improvement in shear strength relative to the unstitched configurations of 620%, 132%, and 33% for the PE, PP, and PET specimens, respectively. Figure 59 shows the shear modulus for the 0.62 stitch/cm^2 configurations. The PET and PP specimens had similar average shear modulus values at 35.1 MPa and 33.2 MPa, respectively. As with the previous configurations, the PE foam had a significantly lower modulus, measuring only 2.1 MPa. Both the PET and PP specimens had higher average values of shear modulus versus the non-stitched configurations with improvements of 66% for PET and 31% for PP. In contrast, the further addition of vertical stitching to the PE specimens led to a reduction in the shear modulus of 22% versus the non-stitched configuration.

Typical load-deflection diagrams for the 0.62 stitch/cm^2 specimens are provided in Figure 68. During testing, loading of the PE and PP specimens progressed smoothly up to the maximum load. In contrast, the PET specimens loaded smoothly only until initial failure. After this initial failure, the load on the specimen increased overall, but with brief, frequent periods of load reduction. This loading pattern continued until the maximum load was reached, at which point the load dropped dramatically.

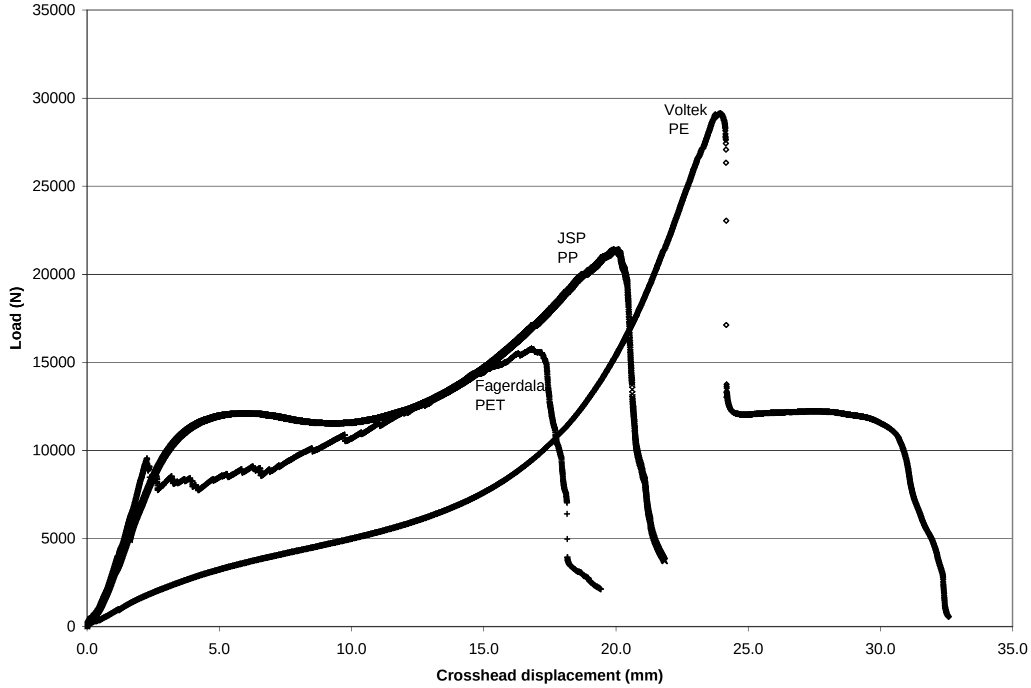

Figure 68. Representative load-displacement curve for core shear testing of 0.62 stitch/cm^2 specimens.

As seen with the previous configurations, the 0.62 stitch/cm^2 PET specimens consistently exhibited sudden failure. Unique to this configuration, however, the PP specimens also displayed sudden failure. This response can be seen from the pronounced load drop associated with the initial failure of these specimens shown in Figure 68. Further evidence of this behavior in the PET configuration is illustrated by the jagged curve following initial failure. Core failure occurred prior to stitch failure, leaving the sandwich specimen intact. Core cracking generally occurred between vertical stitch columns at an angle that joined the upper and lower ends of adjacent stitches. Unlike the 0.16 stitch/cm^2 PET specimens, the 0.62 stitch/cm^2 PET and PP specimens exhibited more pronounced core cracking along the entire length of the specimens. A series of photographs depicting progressive failure of a PET specimen is shown in Figure 69. This same behavior was observed for the PP specimens, resulting in similar damage characteristics as shown in Figure 70.

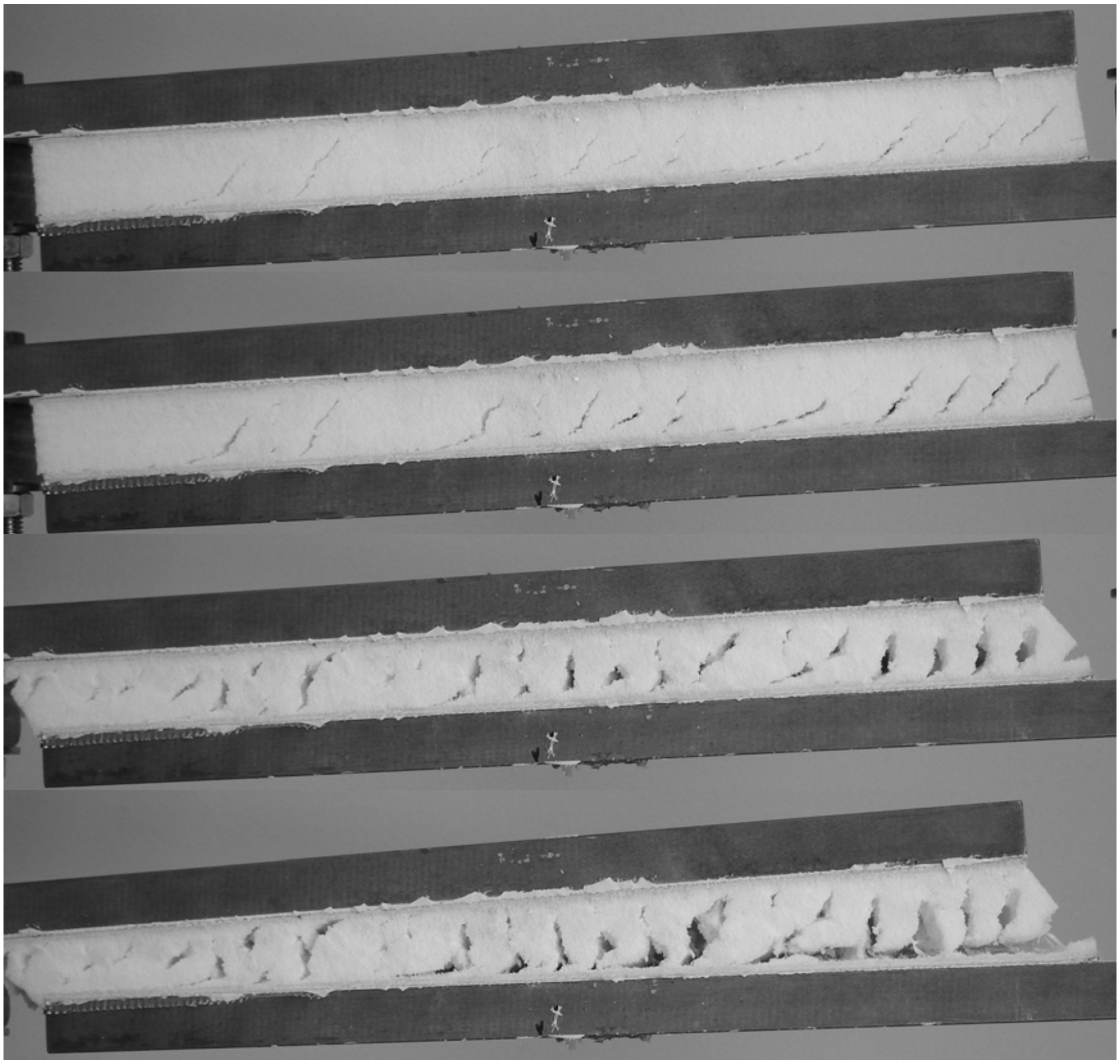

Figure 69. Progressive core cracking in a 0.62 stitch/cm^2 PET core shear specimen.

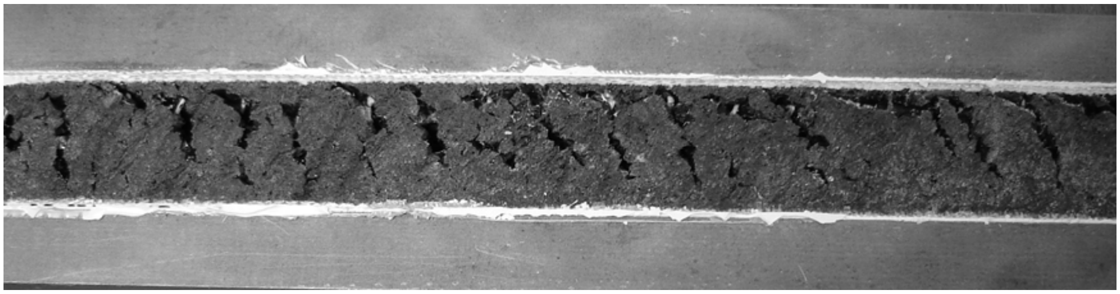

Figure 70. Core cracking in a 0.62 stitch/cm^2 PP core shear specimen.

During loading, the PE 0.62 stitch/cm^2 specimens exhibited extensive shear deformation resulting in a through-the-thickness compaction of the core. A series of photographs showing this progressive compaction is shown in Figure 71. As loading continued, progressive failure of the stitches was detected audibly, leading to complete delamination of the facesheet from the core, as shown below in Figure 72. As with the 0.16 stitch/cm^2 configuration, delamination of the facesheet initiated at the leading edge of the specimen, as evident in Figure 71.

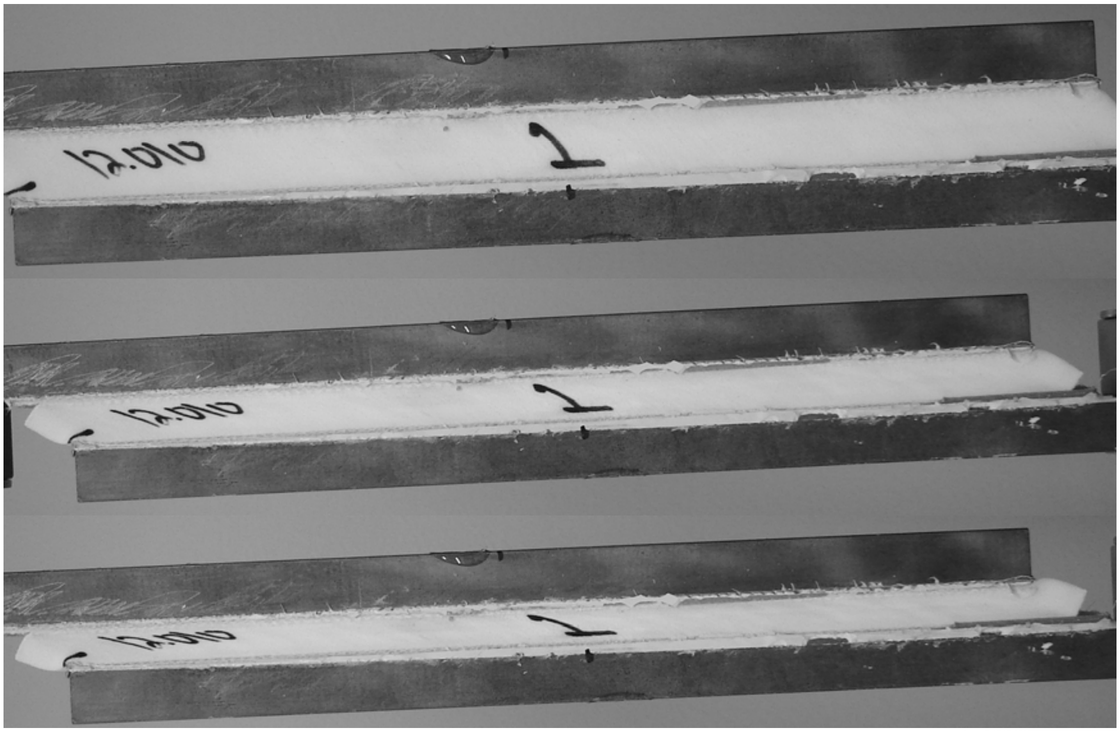

Figure 71. Core compaction of a 0.62 stitch/cm^2 Voltek PE core shear specimen.

Figure 72. Delamination failure of a 0.62 stitch/cm^2 Voltek PE core shear specimen.

An increase in shear strength was observed for all three core materials as a result of the stitching. This improvement was produced by the stitches bearing the majority of the load and is credited to the significantly higher stitch density. The increased load carried by the stitches effectively nullifies the greater damage introduced to the core due to rotation of the stitches. As was observed in the 0.16 stitch/cm^2 configuration, this effect is most pronounced for the PE specimens.

6.2.7 Discussion of Angle Stitched Configurations

From Figure 58 and Table 14 through Table 16, the angle stitched configuration using the JSP PP foam had the highest average shear strength at 0.89 MPa, followed by Fagerdala PET and Voltek PE at 0.66 and 0.56 MPa, respectively. These results correspond to an improvement in shear strength of the PP and PE specimens of 32% and 114%, respectively, over the non-stitched configurations. In contrast the PET specimens showed a reduction in shear strength over the non-stitched configuration of 17%. The same tables discussed above and Figure 59 present the shear modulus data for the angle-stitched configurations. The PP and PET specimens had nearly identical average shear modulus with specific values of 38.1 MPa and 37.6 MPa, respectively. As with all the previous configurations, the PE foam had a significantly lower modulus, measuring 3.86 MPa. All three configurations showed higher average values of shear modulus than the non-stitched configurations with improvements of 51% for PP, 77% for PET and 47% for PE.

Representative load-deflection curves for the angle-stitched specimens are provided in Figure 73. In general, all of the specimens loaded smoothly up to their respective maximum loads; however, there are distinct points along each curve where slight load drops occur. After initial failure, the PET specimens demonstrated repeated unloading/reloading behavior, creating a jagged curve until ultimate specimen failure. The PE and PP specimens both unloaded gradually following the maximum load.

As seen with the previous configurations, the angle-stitched PET specimens consistently exhibited sudden core failure. Unique to this configuration, however, the PP specimens displayed a combination of core failure and delamination. Delamination initiated at the top and bottom edges of the specimen and was followed by core cracking. The delamination portion of this failure is visible as a gradual load drop across the knee of the load vs. deflection curve in Figure 73. Photographs illustrating the initial delamination and eventual failure of the core are shown in Figure 74 and Figure 75, respectively. The PE specimens consistently exhibited delamination failure following progressive failure of the stitching.

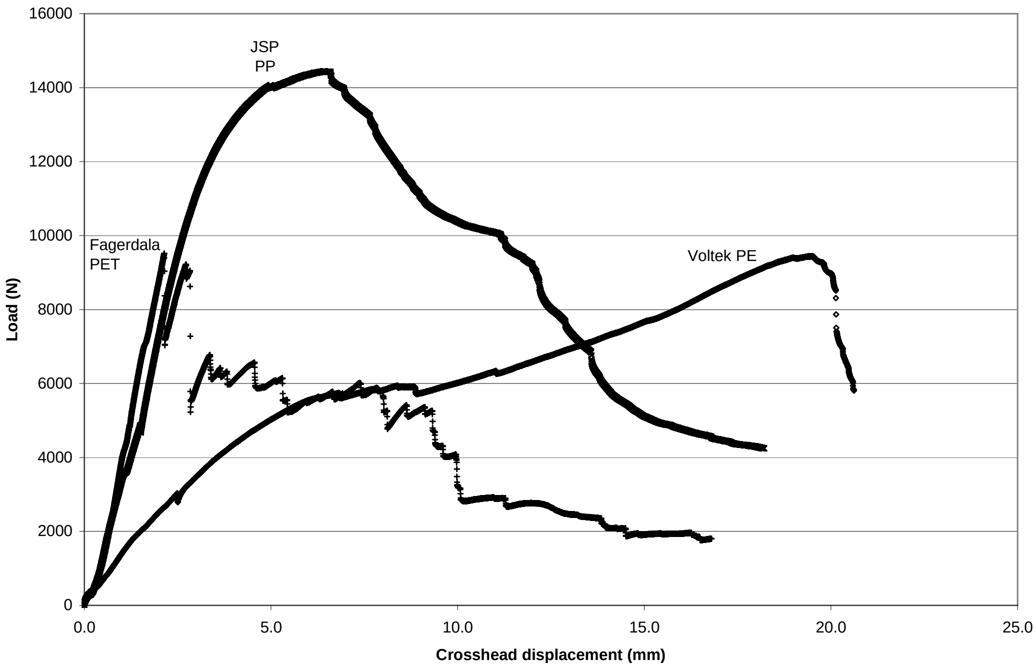

Figure 73 Representative load-displacement curve for core shear testing of angle-stitched specimens.

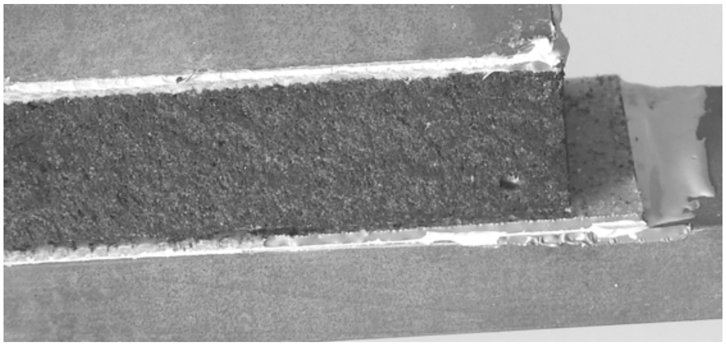

Figure 74. Edge delamination in an angle-stitched PP core shear specimen.

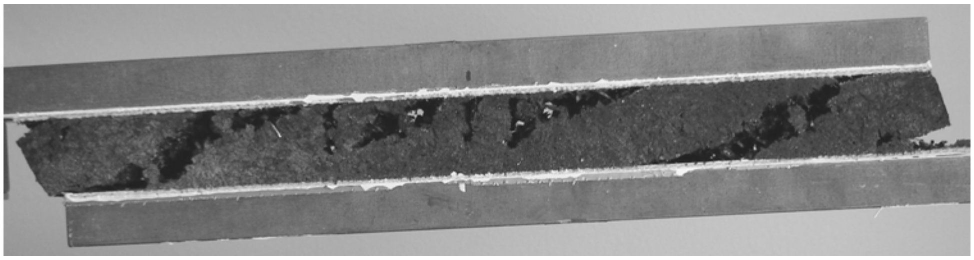

Figure 75. Core failure of an angle-stitched PP core shear specimen.

The reduction in shear strength of the angle-stitched PET core specimens relative to the non-stitched configuration is believed to be associated with the introduction of damage. Note that similar behavior was observed in the 0.16 stitch/cm^2 configuration, which has the same density of vertical stitches. The angle-stitched configuration, however, did perform better than the 0.16 stitch/cm^2 configuration due to the additional load carrying capacity of the angled stitches. Similar improvements were observed with the PP core shear specimens. Improvement in shear strength for the PE specimens can be attributed to the compliance of the core as outlined in the preceding sections.

Improvements in shear modulus were observed for all specimen configurations due to the orientation of the angled stitching. This stitch orientation allows a greater portion of the load to be carried by the stitches from the outset of the test, increasing the stiffness of the sandwich specimen under shear loading.

6.2.8. Discussion of Transverse Reinforcement Effects by Material Type

This section provides a review of the effects of transverse reinforcement on sandwich performance for each type of core material. The underlying causes of the noted effects are as reported in the preceding sections.

Figure 76 shows representative load versus displacement curves for PE specimens of each configuration. These results show that the stitch density has a pronounced effect on shear strength. With increasing density of vertical stitching, the shear strength is improved dramatically. The increase of shear strength seen for the angle-stitched specimens is related to the stitch orientation being in-line with the applied. As discussed previously, the shear modulus of the PE foam core specimens is not significantly affected by the introduction of vertical stitching alone. In contrast, the angle-stitched configuration allows a greater portion of the load to be carried by the stitches from the outset of the test, increasing the stiffness of the sandwich.

Figure 77 shows representative load versus displacement curves for PP specimens of each of the four sandwich configurations. The performance of vertically stitched specimens is highly dependent on the stitch density. A decrease in shear strength and shear modulus is observed for the 0.16 stitch/cm^2 density while increases are observed for the 0.62 stitch/cm^2 configuration. Both shear modulus and shear strength also increased for the angled configuration; however, the shear strength was lower than that recorded for the 0.62 stitch/cm^2 specimens.

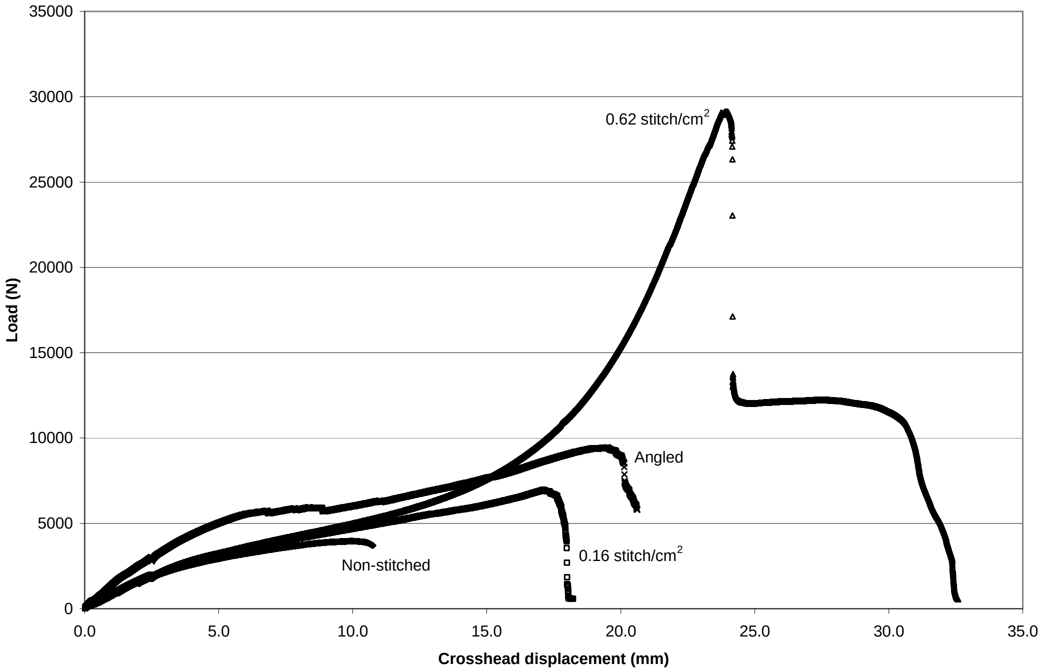

Figure 76. Representative load-displacement curve from core shear testing of PE specimens.

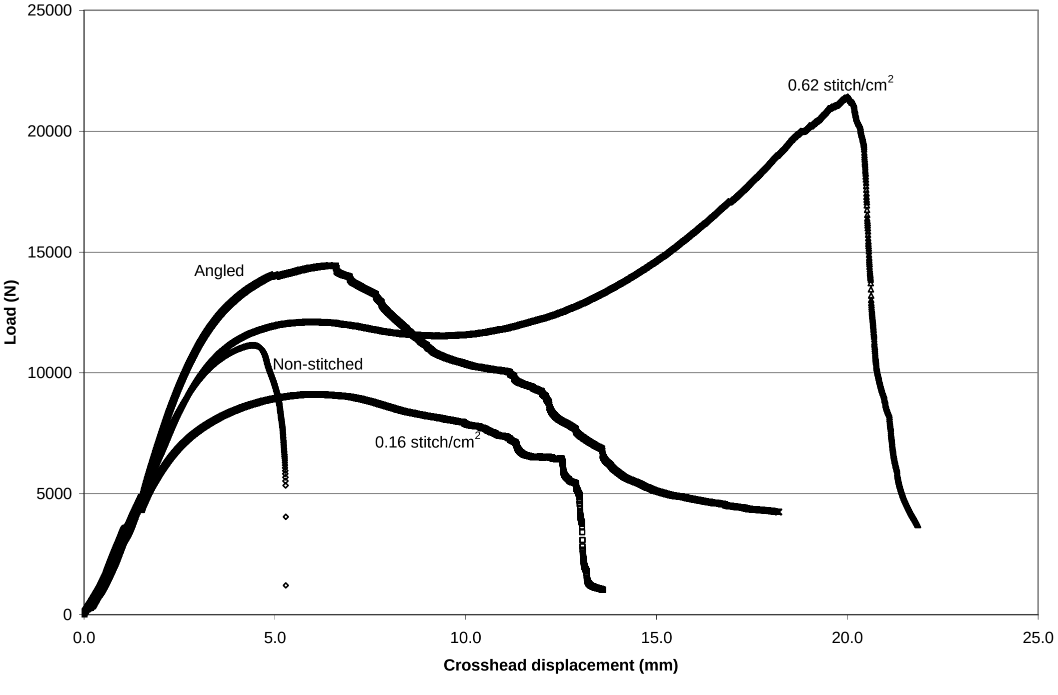

Figure 77. Representative load-displacement curve from core shear testing of PP specimens.

Figure 78 shows representative load versus displacement curves for PET specimens of each configuration. All stitching configurations improved the shear modulus for the PET specimens with the greatest improvement observed for the angle-stitched configuration. Improvements to shear strength were observed for the 0.16 stitch/cm^2 configuration while this property decreased for the other stitch configurations.

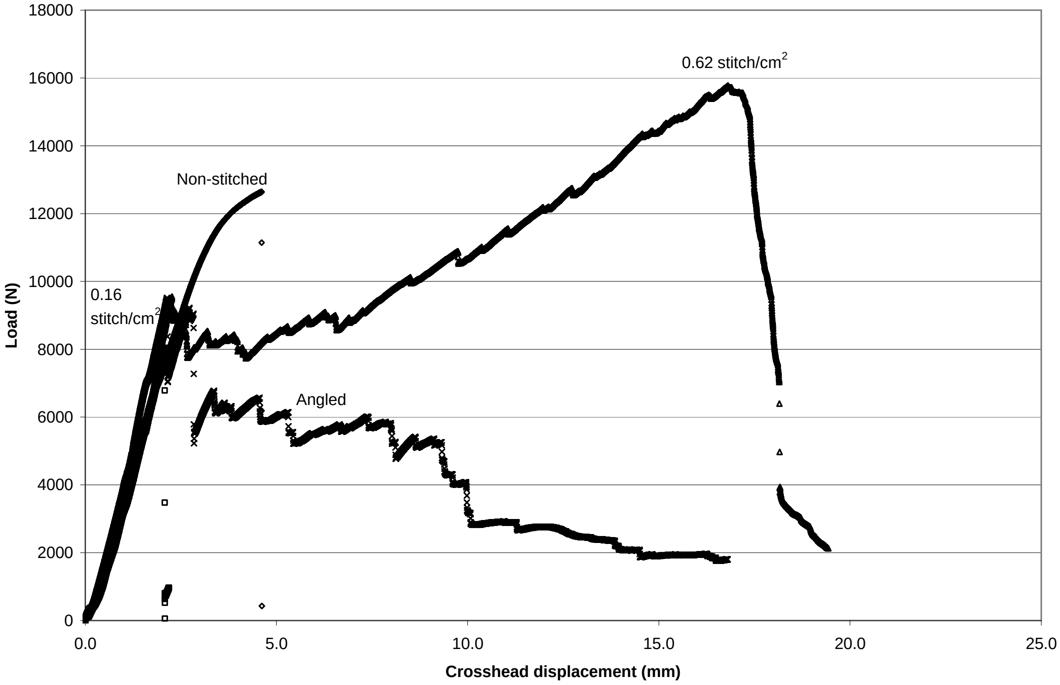

Figure 78. Representative load-displacement curve for core shear testing of PET specimens.

7. QUASI STATIC INDENTATION TESTING

7.1 Quasi-Static Indentation Testing Methods and Procedures

Quasi-static indentation testing was performed using a Measurements Technology Inc. (MTI) electromechanical testing machine. For these tests a 5 mm flat-faced indenter was driven centrally through simply supported sandwich specimens at a rate of 6.0 mm/min until failure was achieved. The testing apparatus is illustrated in Figure 79. The 127 mm diameter simple support was manufactured from aluminum plate stock per ASTM D 6264 with a CNC milling operation. The indenter was manufactured from steel rod on a turning center and is shown in Figure 80. As a starting point, the indenter size was chosen such that the indenter face would fit within the medium classification of meteoroid and space debris as defined by NASA Reference Publication 1408 [54]. However, the reader should be informed that these tests were not aimed at modeling or assessing meteoroid or space debris impact on multifunctional sandwich configurations. In preparation for testing, square specimens measuring 153 mm were cut form larger sections of panel. Next, a small hole was machined in the center of the specimen, exposing the core just beneath the top outer facesheet. The hole diameter was selected to provide approximately 1 mm of clearance between the indenter and the facesheet. This machining operation allowed the test to produce an internal indentation of the multifunctional sandwich composite, thus focusing on the mechanical behavior of the interior laminate and the damage tolerance provided through the addition of transverse reinforcements. Furthermore the use of a partial thickness hole aided in minimizing the indenter rod diameter by allowing the outer section of core to provide support against buckling as the indenter loaded the interior laminate layer. Load data was collected using an Interface 44.5 kN load cell.

The first step in the data reduction process was to generate a load versus indenter displacement curve. The energy absorption (J) was then found by numerically integrating the data using the trapezoidal method,

$$J = \sum_{1}^{n-1} \left[\left(X_{n+1} - X_n \right) \frac{\left(P_{n+1} + P_n \right)}{2} \right], \tag{4}$$

where J is the energy absorption (Joules), X is the displacement of the indenter face (mm), and P is the load (N). The maximum load and displacement were taken to be the largest values recorded during the test. Damage tolerance of all four specimen configurations was investigated by taking sequential photographs of equivalent sandwich specimen cross-sections at increasing load levels. Prior to photographing the specimens, an ink-based dye penetrate was applied to the cross-section surface revealing the damage accrued during the tests.

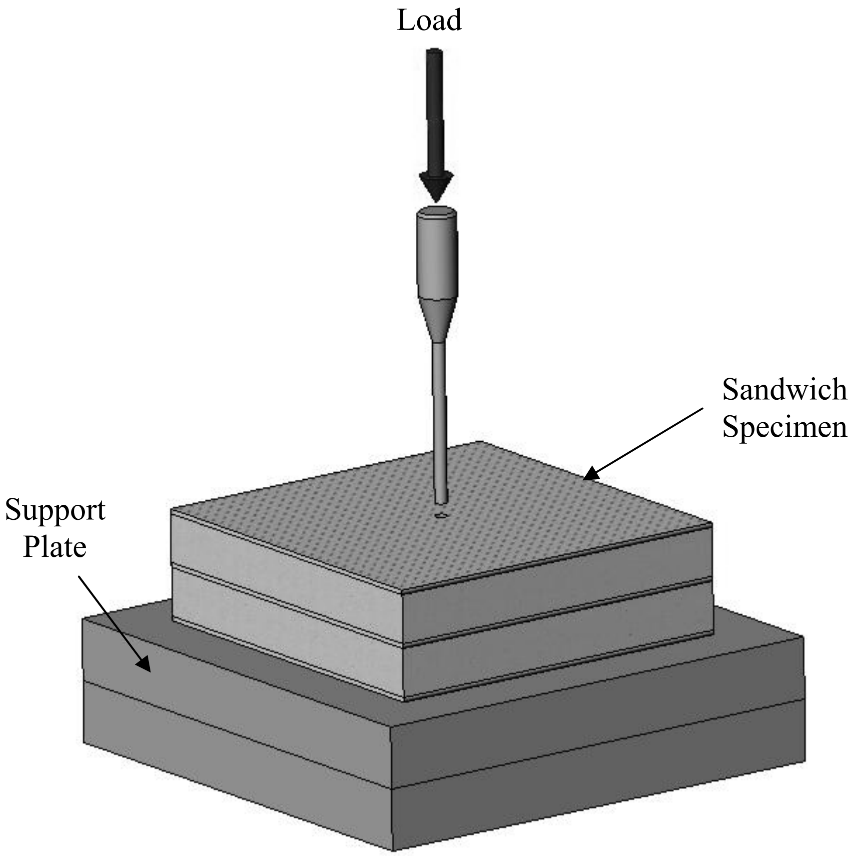

Figure 79. Quasi-static indentation testing apparatus.

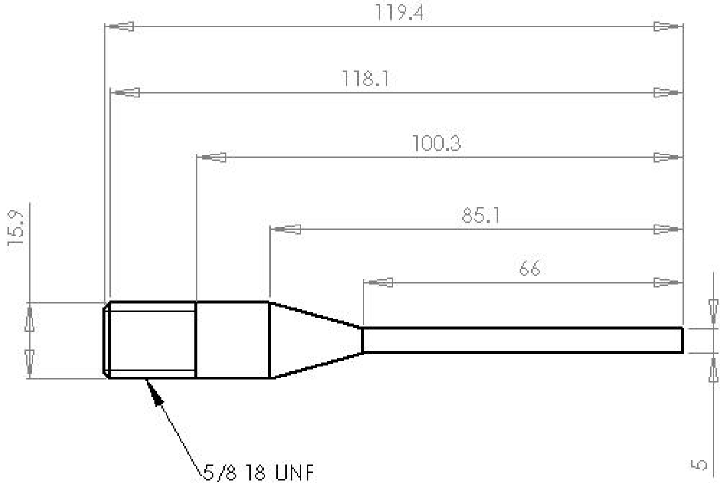

Figure 80. 5 mm indenter manufactured for quasi-static indentation testing (units = mm).

7.2 Quasi-Static Indentation Testing Results and Discussion

Table 17 provides a summary of the quasi-static indentation testing results for each of the four stitching configurations considered. Included in this table are the maximum load, maximum indenter-face displacement and energy absorption of each specimen tested. Also shown are the mean and standard deviation for these data. Table 17 shows that the non-stitched configuration sustained the highest maximum load (5,225 N) followed by the 0.16 stitch/cm^2, 0.62 stitch/cm^2 and multi-layer configuration with maximum load values of 5,191 N, 4,600 N and 2,922 N, respectively. Prior to sandwich failure, a maximum indenter displacement of 56.8 mm was recorded for the 0.16 stitch/cm^2 configuration. This peak displacement was followed by the multi-layer configuration with a value of 55.8 mm and the non-stitched and 0.62 stitch/cm^2 specimens with values of 53.5 mm and 48.9 mm, respectively. The greatest energy absorption was achieved by the 0.16 stitch/cm^2 configuration, with an average value of 82 J followed by the non-stitched, multi-layer and 0.62 stitch/cm^2 configurations with values of 68.9 J, 65.2 J and 48.5 J, respectively.

7.2.1 Non-Stitched Configuration

Figure 81 shows a representative load versus indenter displacement plot obtained from the non-stitched configuration. Figure 82 shows sequential cross-sectional photographs of equivalent non-stitched specimens loaded up to different levels of damage. The letters shown on the load versus indenter displacement plot indicate the load levels corresponding to the photographs shown in Figure 82. From the onset of loading, core crushing and densification occurred directly beneath the indenter face. This observation was based on the low load levels and saw-tooth pattern observed in region A of the load versus displacement curve shown in Figure 82. At about 12 mm of applied displacement, the change in slope of the load versus displacement curve resulted from initial loading of the interior laminate. As loading continued, separation of the interior laminate from the upper core initiated at point B as shown in Figure 82B. This behavior continued as the indenter penetrated further into the sandwich, resulting in the eventual failure of the interior laminate. Evidence of this is shown in Figure 81 by the pronounced drop in load at point D. The corresponding damage accrued by the sandwich at this stage of the test is shown in Figure 82C and 82D. Following interior laminate failure, sections of this laminate were driven into the lower core causing damage and densification of core material directly under the indenter. This result corresponds with the higher load required to initiate and sustain core crushing over region E of the load versus displacement curve in Figure 81. Figure 82D also shows evidence of core cracking leading up to and following failure of the interior laminate. A considerable amount of spring-back was detected visually and audibly following the failure of this layer. As the indenter loaded the interior laminate, the entire panel is forced to elastically warp. Upon the indenter puncturing the interior laminate, strain energy is released causing the panel to rapidly return to a lesser deformed state. Further specimen examination following the conclusion of the test revealed that upon interior laminate failure, this layer completely separated from the upper core via tensile core failure as shown in Figure 83. The change in slope of the load indenter-face displacement curve following region E is believed to be due to initial loading of the lower facesheet. Continued loading resulted in the progression of core cracking and eventual separation of the lower facesheet (point F) as shown in Figure 82 F. During the final stages of the test, wrinkling of the lower facesheet was observed as shown in Figure 84. After the onset of wrinkling, the facesheet began to slide relative to the support at which time the test was stopped. Following unloading of the sandwich specimens it was observed that the facesheets were permanently deformed, showing signs of warping.

Table 17. Results of Quasi-Static Indentation Testing

Configuration	Maximum Load (N)	Maximum Displacement (mm)	Energy Absorption (J)
Non-Stitched	5777 5218 5180 **Average = 5225** **Std Dev = 48.2**	55.0 53.7 54.7 **Average = 53.5** **Std Dev = 0.70**	64.1 68.5 74.0 **Average = 68.9** **Std Dev = 5.00**
Vertically Stitched 0.16 stitch/cm^2	5445 5038 5091 **Average = 5191** **Std Dev = 223**	55.3 55.4 59.8 **Average = 56.8** **Std Dev = 2.6**	81.7 73.6 90.7 **Average = 82.0** **Std Dev = 8.6**
Vertically Stitched 0.62 stitch/cm^2	4517 4010 5272 **Average = 4600** **Std Dev = 635**	50.9 47.6 48.3 **Average = 48.9** **Std Dev = 1.7**	46.8 45.5 53.3 **Average = 48.5** **Std Dev = 4.2**
Multi-layer Sandwich	2715 2308 3709 **Average = 2922** **Std Dev = 721**	55.3 55.2 57.0 **Average = 55.8** **Std Dev = 1.0**	60.8 60.4 74.2 **Average = 65.2** **Std Dev = 7.8**

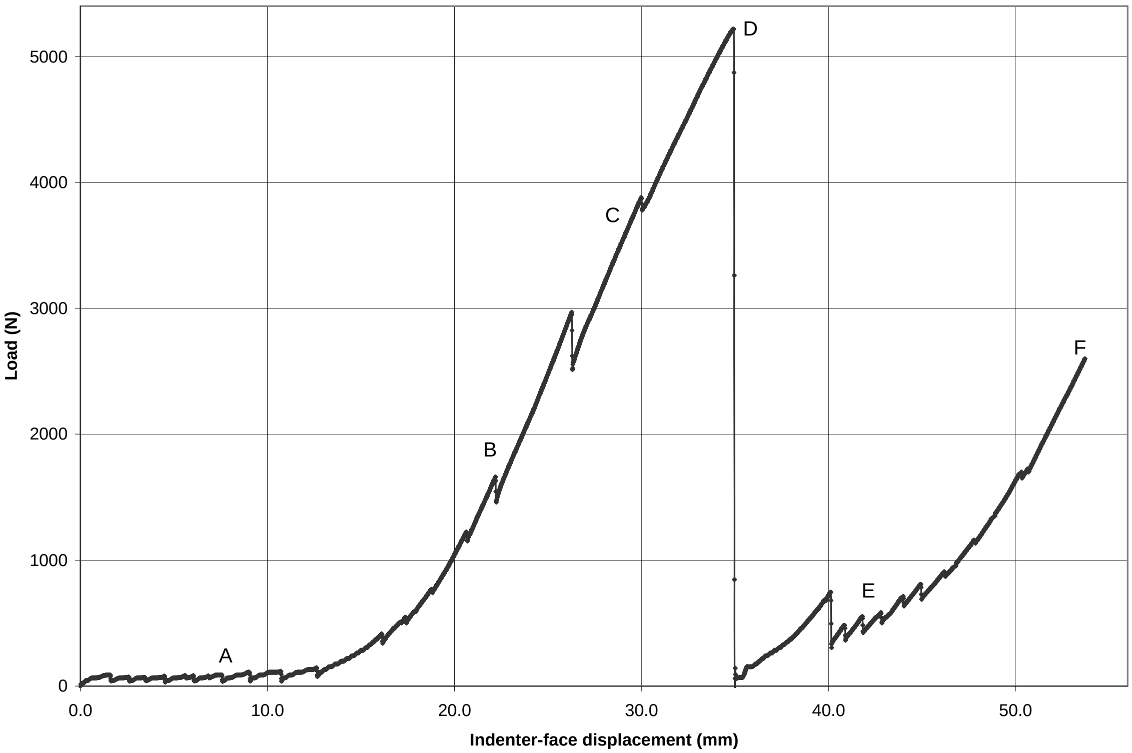

Figure 81. Representative load indenter displacement curve for a non-stitched sandwich specimen.

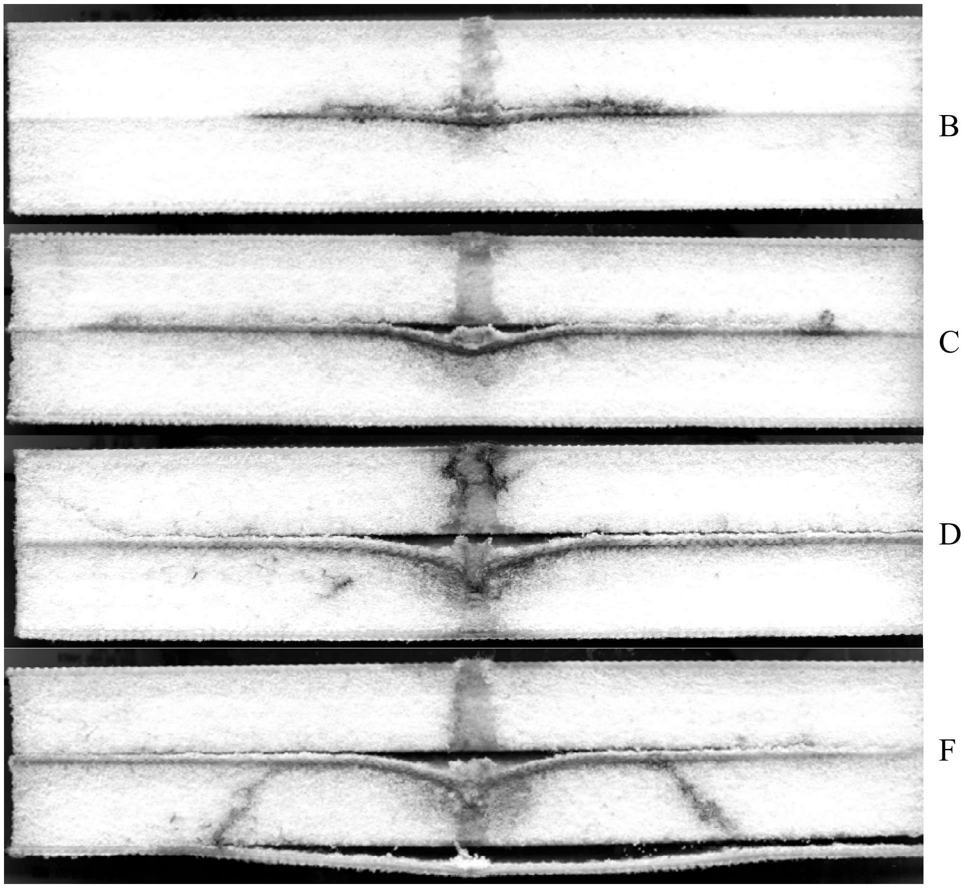

Figure 82. Damage evolution for loading of non-stitched specimens.

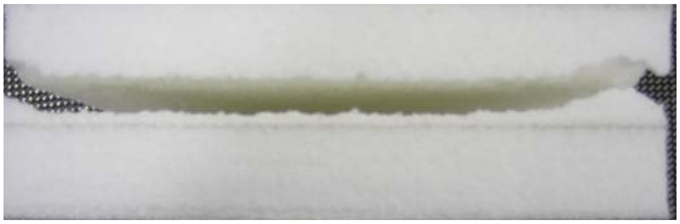

Figure 83. Separation of interior laminate from the upper core following failure

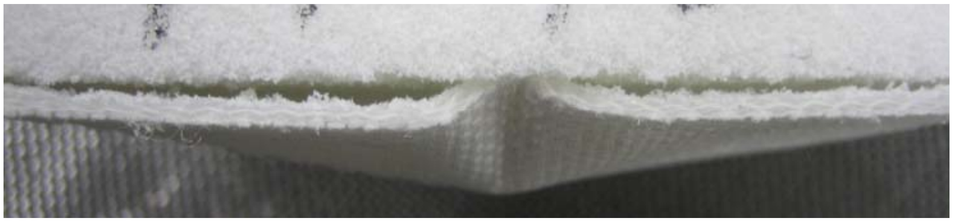

Figure 84. Lower facesheet wrinkling following partial separation from the lower core.

7.2.2. 0.16 stitch/cm^2 Configuration

Figure 85 shows a representative load versus indenter displacement plot obtained from the 0.16 stitch/cm^2 configuration. Figure 86 shows cross-sectional photographs of equivalent 0.16 stitch/cm^2 specimens loaded up to different levels of damage. The letters shown on the load versus indenter displacement plot indicate the load levels corresponding to the photographs shown in Figure 86.

As observed with the non-stitched configurations, initial loading of the 0.16 stitch/cm^2 specimens resulted in core crushing and core material densification directly under the indenter face. This observation was based on the jagged characteristics of the load versus indenter displacement plot over region A in Figure 85 and is seen photographically in Figure 86 B. As with the previous configuration the change in slope of the load versus indenter displacement curve corresponds to loading of the interior laminate layer. Shown in Figure 86 B is core cracking near the interior laminate-core interface. Delamination of the interior laminate also starts to occur during this portion of the test. Continued loading resulted in failure of stitches that join the interior laminate and upper facesheet which was detected audibly. This is shown in the graph by the drop in load just prior to the maximum load at C. Comparing the lateral cracks in Figure 82C with Figure 86C it is clear that the presence of the 0.16 stitch/cm^2 reinforcement inhibited displacement and separation of the interior laminate from the upper section of core. The stitches also aided in transferring load from the laminate and facesheets to the core, inducing a greater amount of damage in the upper and lower core sections. Further loading resulted in combined tensile and shear plug failure of the interior laminate as shown in Figure 86C.

As described previously, following interior laminate failure a significant amount of spring back was detected visually and audibly. Due to the build up and release of strain energy following interior laminate failure, portions of the laminate were driven into the lower core causing a significant amount of damage and material compression. This is evidenced by the zero load recorded over the corresponding displacement following point C. It is believed that material was pushed down creating a void for the indenter to travel through. Eventual loading of the lower facesheet ensued, resulting in the rise in load leading up to point D. The corresponding damage at this point of the test can be seen in Figure 86D and reveals a significant amount of core cracking. Failure of the stitching that joined the lower facesheet and interior laminate was detected audibly and is shown by the jagged characteristics over region D and photographically in Figure 86E. Bobbin stitch failure on the lower facesheet was also detected during this segment of the test and is shown in Figure 87.

Final failure of the sandwich specimen resulted from combined tensile and shear plug failure of the lower facesheet illustrated in Figure 88. Unlike the non-stitched configuration, no extensive separation between the facesheet, interior laminate and core occurred leaving the sandwich intact. The presence of the stitches also induced more cracking in the core as seen by comparing Figure 82 to Figure 86. This can also explain the increased energy absorption for this configuration over the non-stitched configuration (Table 17). Permanent deformation of the interior laminate and lower facesheet was observed following unloading of the sandwich specimens.

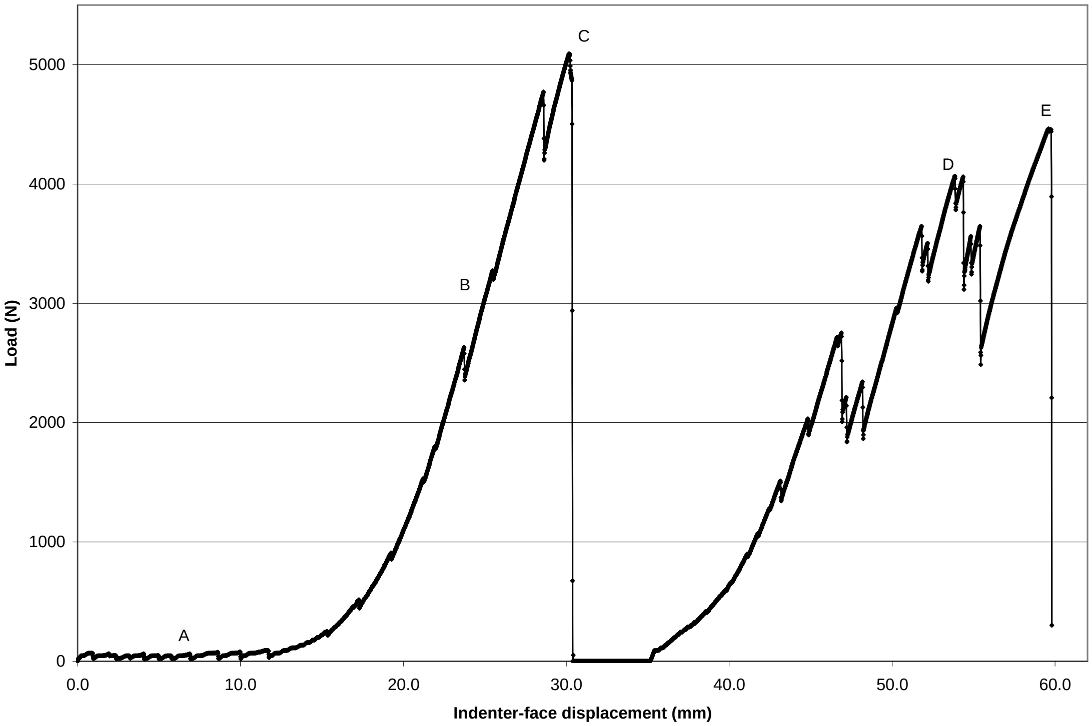

Figure 85. Representative load vs. indenter displacement curve for a 0.16 stitch/cm^2 sandwich specimen.

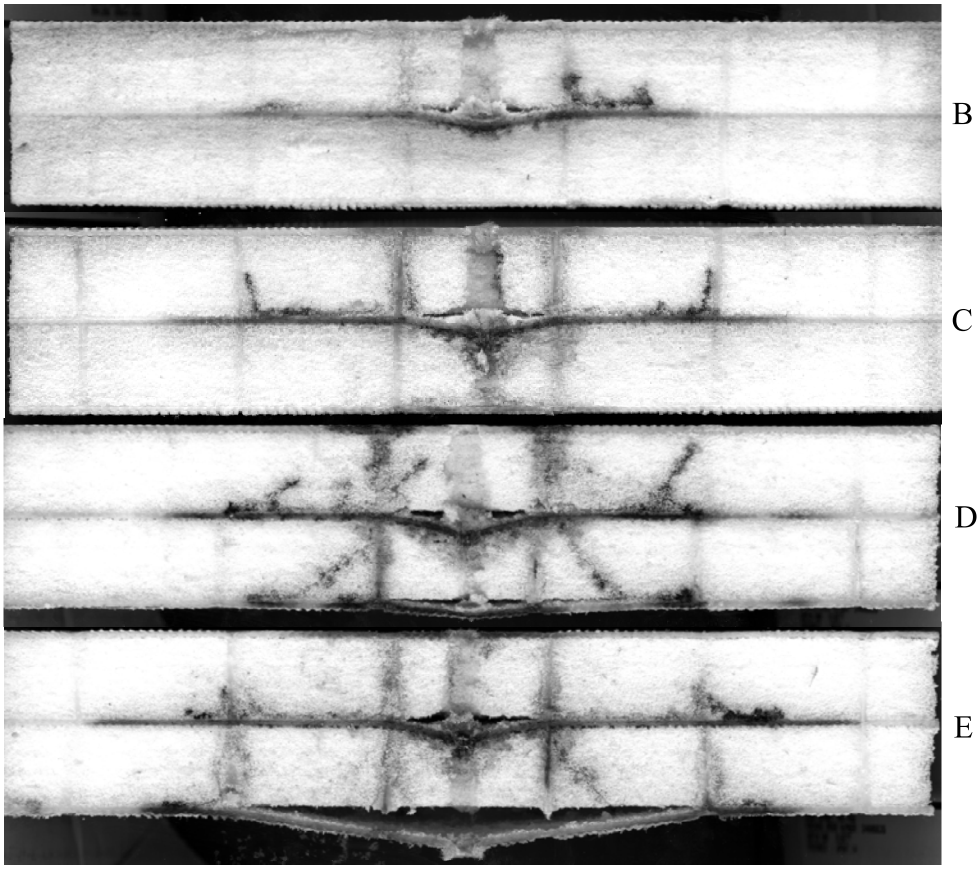

Figure 86. Damage evolution of 0.16 stitch/cm^2 sandwich specimens.

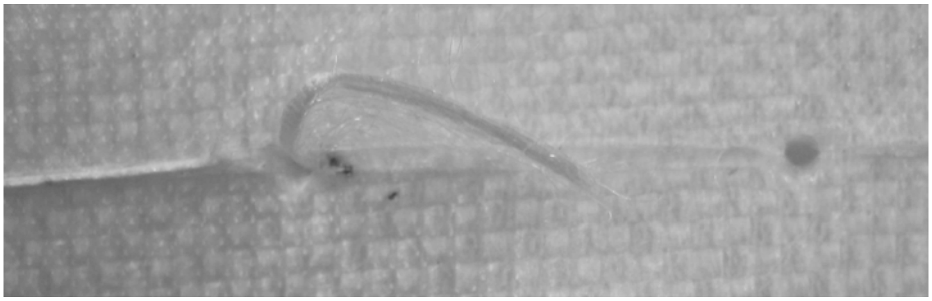

Figure 87. Bobbin stitch failure on the lower facesheet preceding sandwich failure.

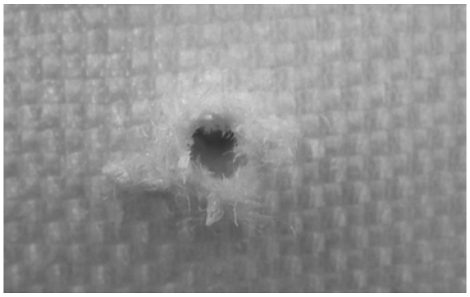

Figure 88. Shear plug and tensile failure of the lower facesheet.

7.2.3. 0.62 stitch/cm^2 Configuration

Figure 89 shows a representative load versus indenter displacement plot obtained for the 0.62 stitch/cm^2 configuration. Figure 90 shows sequential photographs of equivalent 0.62 stitch/cm^2 specimens loaded up to different levels of damage. The letters shown in the load versus indenter displacement plot indicate the load levels corresponding to the photographs seen in Figure 90.

As observed with the previous configurations, initial loading of the 0.62 stitch/cm^2 specimens resulted in core crushing and material densification. This is shown by the sharp saw-tooth characteristics of the load versus indenter displacement plot over region A in Figure 89 and is seen photographically in Figure 90B. The increased slope of the load versus indenter displacement curve prior to point B corresponds to loading of the interior laminate. Similar to the 0.16 stitch/cm^2 configuration diagonal and facesheet/laminate-core interface cracks were formed in the core and are shown in Figure 90B. Further loading resulted in stitch failure between the interior laminate and upper facesheet which was detected audibly. This is indicated in the plot by the drop in load prior to the maximum load at C. Continued loading resulted in failure of the interior laminate shown in Figure 90C. As with the previous configurations a significant amount of spring back was detected visually and audibly. As described previously, portions of the laminate were driven into the lower core section causing a significant amount of damage and material compression. This is evidenced by the zero load recorded over the ensuing displacement following point C and indicated the material was damaged allowing the indenter to travel with no resistance. A significant amount of core cracking also occurred over this region of the test (Figure 90C). Eventual loading of the lower facesheet resulted in a rise in load shown in Figure 91 and corresponding damage in Figure 90E.

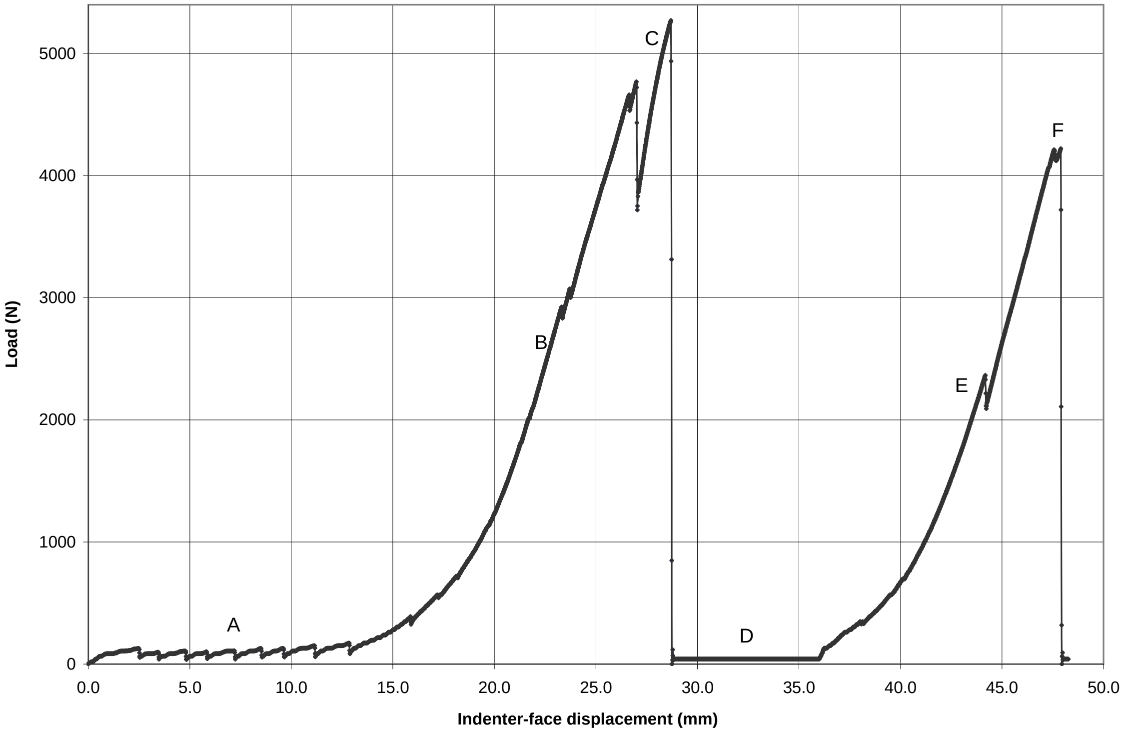

Figure 89. Representative load vs. indenter displacement curve for a 0.62 stitch/cm^2 sandwich specimen.

Unlike the 0.16 stitch/cm^2 configuration, failure of the stitching that joined the lower and interior laminate was not detected. This is shown by the smooth loading of the lower facesheet, up to point F, compared to that seen for the interior laminate (points B - C). Final failure of the sandwich specimen resulted from shear plug and tensile failure of the lower facesheet as shown in Figure 90F. As with the 0.16 stitch/cm^2 configuration no extensive separation between the facesheet and core occurred leaving the sandwich intact. The amount of permanent deformation following unloading was less substantial for this configuration. The relative difference in facesheet deformation between the two stitch densities is shown in Figure 91

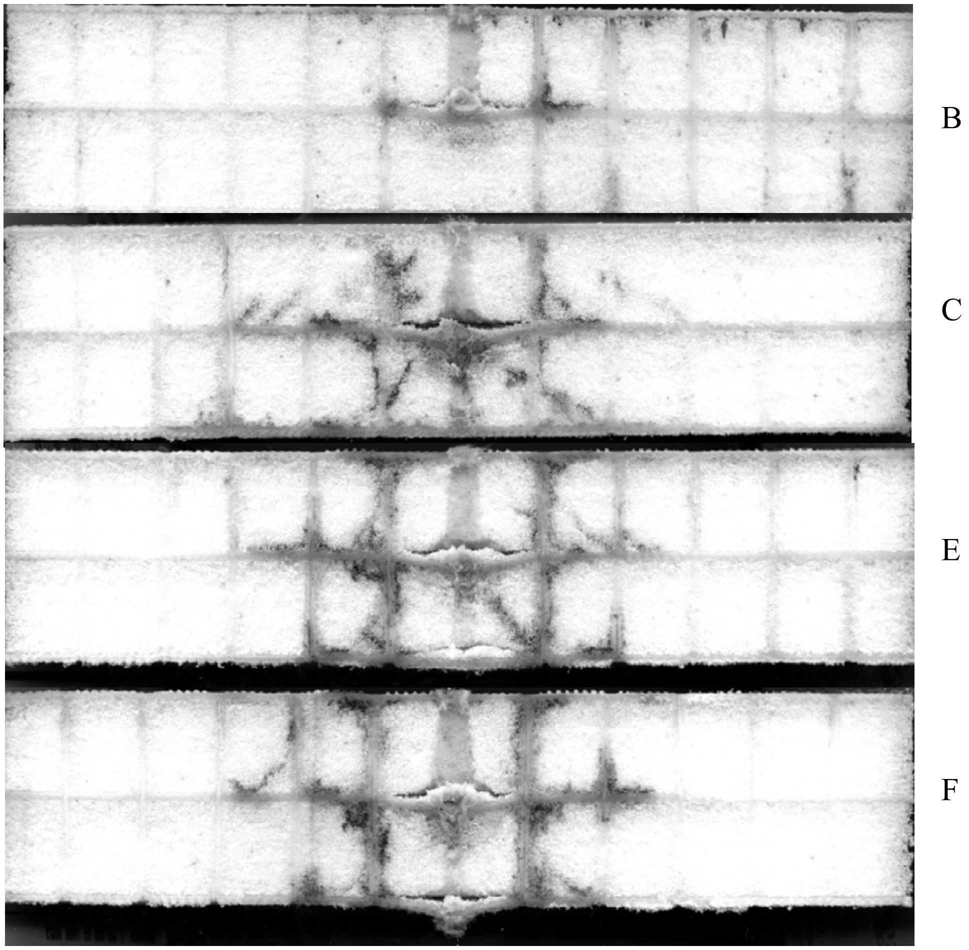

Figure 90. Damage evolution of 0.62 stitch/cm^2 sandwich specimens.

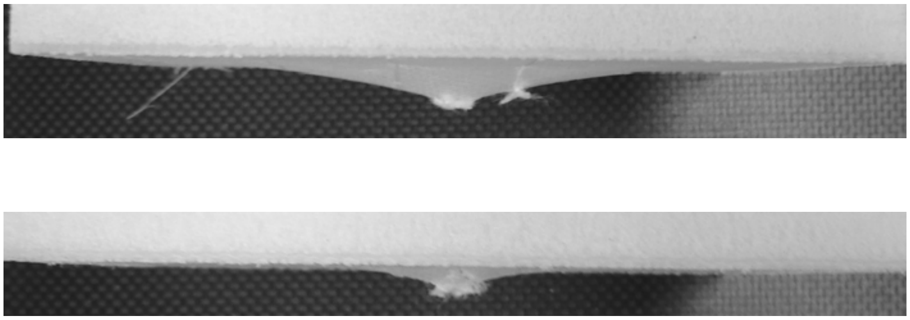

Figure 91. Permanent deformation of the lower facesheet for the 0.16 stitch/cm^2 (upper) and 0.62 stitch/cm^2 (lower) configurations.

7.2.4 Multi-Layer Configuration

Figure 92 shows a representative load versus indenter displacement curve for the multi-layer configuration. The sequential pictures seen in Figure 93 show the damage progression over the course of the test for equivalent multi-layer specimens. The letters shown in the load versus indenter displacement plot indicate the load levels corresponding to the photographs shown in Figure 93.

As observed with the previous configurations, region A of Figure 92 shows initial loading of the specimen resulted in core crushing and material densification directly under the indenter face. Loading of the first interior lamina, indicated by the change of slope following region A, caused minor separation from the core as seen in Figure 93B. Failure of the first and subsequent interior lamina (point B - D) occurred at a much lower load than the non-stitched, 0.16 stitch/cm^2 and 0.62 stitch/cm^2 configurations. This is due to the reduction of interior lamina thickness and thus strength for these specimens compared to the previous configurations. Upon failure of the interior lamina in previous configurations, sections of material were pushed downward, damaging and compressing core material onto the following layer. The thinner core sections did not allow for a void to be created and is shown by the sharp rise in load immediately following failure after point B, in contrast to the zero loads seen for previous configurations following interior laminate failure. This pattern continued as the indenter penetrated the following two interior lamina indicated over regions C and D in Figure 92. From the figure, evidence of separation of the interior lamina from the core is visible by the sharp drops in load leading up to the failures at points C and D of the load versus indenter displacement plot. This is also confirmed by Figure 93C and D which shows evidence of delamination, of the interior lamina from the core, during this segment of the test.

The extent of separation of internal lamina from the core for this configuration is considerably less than that observed for the non-stitched configuration and is associated with the reduced thickness of the interior layers. The reduced load required to cause failure of the interior lamina did not allow for sufficient material separation to occur before the lamina was penetrated. As the indenter proceeded, loading of the lower face sheet ensued resulting in eventual near complete separation of the lower facesheet from the lower core (point E) shown in Figure 93E. As with the non-stitched configurations, facesheet wrinkling was observed which lead to motion of the sandwich relative to the support and thus completion of the test. As observed with the preceding configurations, permanent deformation of the lower facesheet and interior lamina was detected.

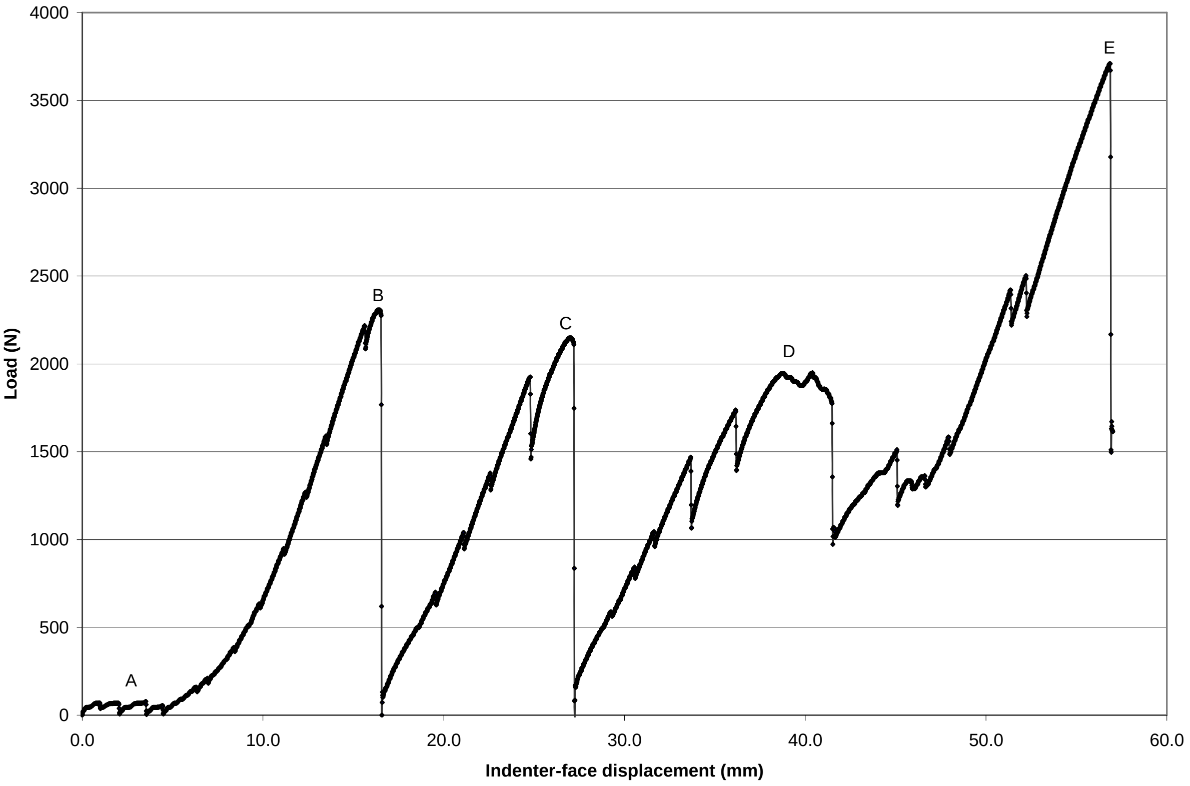

Figure 92. Representative load vs. indenter displacement curve for the multi-layer configuration.

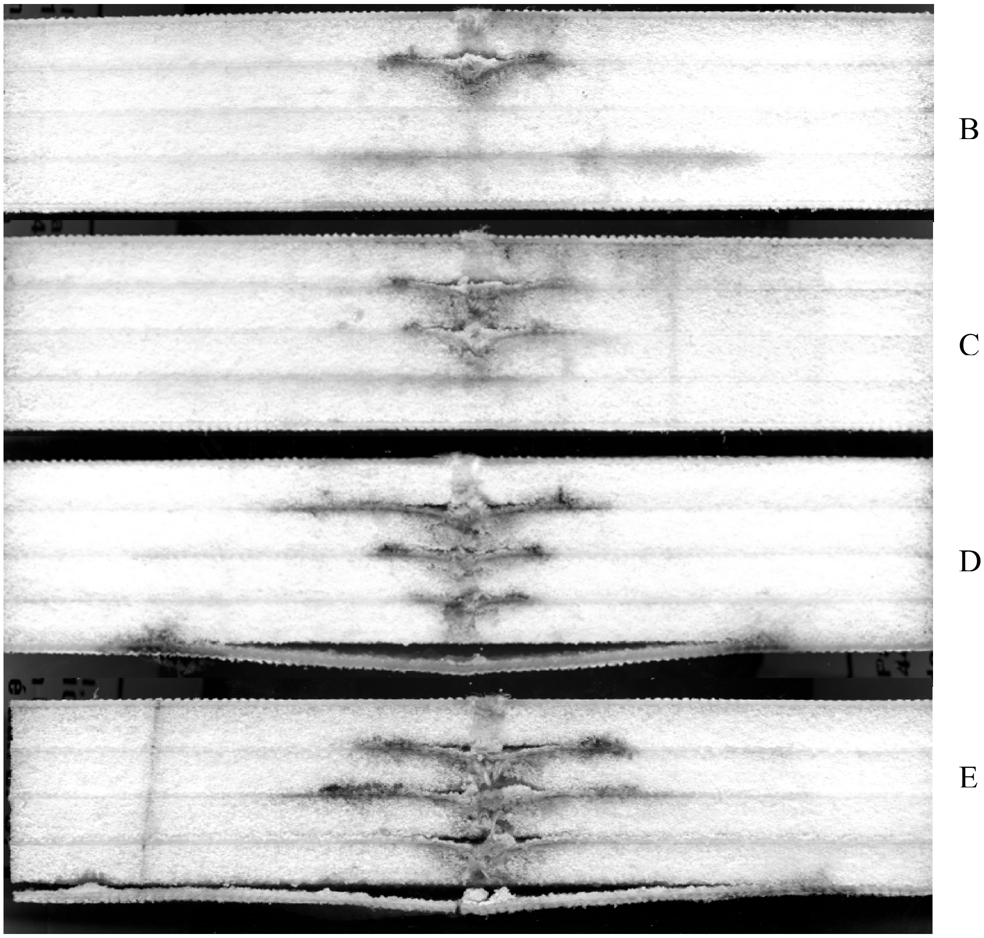

Figure 93. Damage evolution of multi-layer sandwich configuration.

8. ANALYSIS OF QUASI STATIC INDENTATION TESTS

Finite element analyses were conducted using ANSYS 8.0 [3] for the four sandwich configurations subjected to quasi-static indentation testing. The purpose of these analyses was to gain a better understanding of the effects of stitching and interior laminate arrangement on the induced state of stress and damage tolerance of sandwich specimens.

8.1 Material Properties

A total of three constituent materials were modeled in the analyses:

1. Facesheets consisting of woven cross-ply Spectra fabric infiltrated with epoxy resin (EPON^{TM}/EPIKOTE^{TM} Resin 862 combined with EPIKURE^{TM} Curing Agent 9553) [41].
2. PET foam core.
3. Transverse reinforcement stitching consisting of unidirectional Spectra fiber yarn also infiltrated with epoxy resin (EPON^{TM}/EPIKOTE^{TM} Resin 862 combined with EPIKURE^{TM} Curing Agent 9553) [41].

Table 18 lists the mechanical properties used in the model for all sandwich constituents. The estimate material properties were found with a combination of empirical methods and published data. Three-point bending testing (ASTM C 393) was performed on five specimens of woven Spectra-epoxy facesheets and PET foam core. These tests were used to approximate the modulus E_1 and E_2 for the facesheets and E_1, E_2 and E_3 for the core. Load and deflection data was recorded over the linear region of the test and used in conjunction with Equation (5) to determine the modulus of elasticity,

$$E = \left(\frac{PL^3}{48\delta I} \right), \tag{5}$$

where E is the modulus of elasticity (GPa), *P* is the applied load (N), *L* is the specimen length (mm), *I* is the moment of inertia (mm^4) and δ is the centerline deflection of the beam (mm).

E_3 for the facesheets was approximated to be 1.10E+01 GPa, and was taken from published data for a carbon laminate that utilized the same resin system as the Spectra facesheets [55]. Values for $\upsilon_{12,}$ υ_{13} and υ_{32} for the facesheets were also taken from the same carbon laminate and approximated at 0.35, 0.26 and 0.26 respectively. Poisson's ratio values for $\upsilon_{12,}$ υ_{13} and υ_{32} for the core were approximated at 0.28 by considering published values of similar polyurethane closed cell foam of the same density [56].

Table 18. Material Properties of Sandwich Constituents for Computational Analysis

Material	E_1 (GPa)	E_2 (GPa)	E_3 (GPa)	G_{12} (GPa)	G_{13} (GPa)	G_{32} (GPa)	υ_{12}	υ_{13}	υ_{32}
Spectra/Epoxy Facesheet	2.61E+01	2.61E+01	1.10E+01	3.90E+00	4.10E+00	4.10E+00	0.35	0.26	0.26
PET Foam Core	1.98E-01	1.98E-01	1.98E-01	7.72E-02	7.72E-02	7.72E-02	0.28	0.28	0.28
Spectra/Epoxy Stitching	7.57E+00	NA	NA	3.15E+00	NA	NA	0.2	NA	NA

The shear modulus of the foam was obtained using the relation

$$G = \left(\frac{E}{2(1+\nu)} \right), \tag{6}$$

where E is the modulus of elasticity of the material in the direction being considered (GPa) and ν is Poisson's ration for the given plane. Values of G_{12}, G_{32} and G_{13} for the facesheets was approximated in the same manner as E and found to be 3.9E+00, 4.1E+00 and 4.1E+00 GPa respectively.

The modulus of elasticity in the fiber direction of the stitches were found by considering the stiffness of PET Spectra sandwich specimens subjected to flatwise tensile testing. Two sandwich configurations were considered for determining the modulus: non-stitched and 16 stitch/cm^2. The transverse stiffness of these sandwich specimens was determined using the expression

$$k = \left(\frac{EA}{L} \right), \tag{7}$$

where k is the stiffness (N/mm), E is the modulus of elasticity (GPa), A is the area (mm^2), and L is the length of the specimen in-line with the load (mm). By considering the stiffness of the 0.16 stitch/cm^2 configurations and breaking up the relative components, the following expression was derived for the total stiffness of the sandwich composite:

$$\left(\frac{E_{0.16 stitch/cm^2} A_{total}}{L} \right)_{total} = \left(\frac{E_{foam} A_{foam}}{L} \right) + \left(\frac{E_{stitches} A_{stitches}}{L} \right) \tag{8}$$

When loading in the through-the-thickness direction, the contribution of the facesheets to the overall stiffness can be neglected. Solving for E_{stitch} in Equation (8) results in the expression

$$E_{stitch} = \left[\left(\frac{E_{0.16stitch/cm^2} A_{total}}{L} \right) - \left(\frac{E_{foam} A_{foam}}{L} \right) \right] \left(\frac{L}{A_{stitch}} \right). \tag{9}$$

Considering the relative areas of each material and the predetermined value of modulus for the non-stitched configuration, E_{stitch} in the fiber direction was calculated to be 7.57E+00 GPa.

8.2 Modeling Approach

Two-dimensional axisymmetric finite element modeling was performed to model the quasi-static indentation test. Figure 94 shows the modeled region revolved one-fourth of the around the circumference. The plane modeled was the same as that examined for damage progressions following mechanical testing as discussed previously in section 7.3.

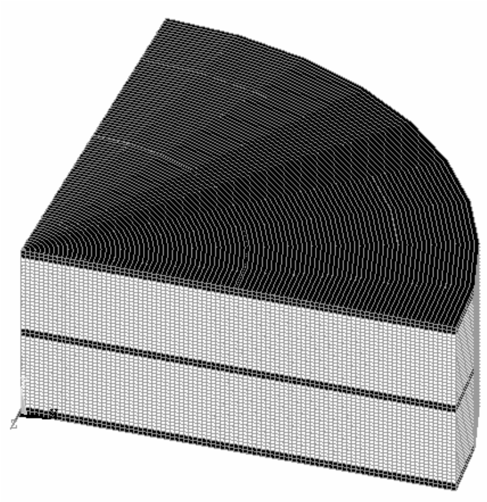

Figure 94. Partially revolved section illustrating the use of axisymmetry.

The finite element meshes used for each stitch configuration are shown in Figure 95a-d. As indicated in Figure 95, note that the meshes shown span half the cross section of the specimen. Thus, the mesh extends from the center of the panel to one corner of the square specimen.

For the non stitched configuration (Figure 95a), each section of foam core consisted of 1920 elements with 96 used across the length and 20 through the thickness. The facesheets and internal laminate were modeled with a total of 192 elements each with 96 across the length and 2 through the thickness. Both the core and facesheets utilized a two-dimensional 8-node mixed quadrilateral-triangular element (Plane82 in ANSYS 8.0) and were chosen for their capability to be used as an axisymmetric element. The corresponding element size was 1.02 mm high and 1.12 mm long.

For the 0.16 stitch/cm^2 and 0.62 stitch/cm^2 configurations, the three-dimensional array of stitches had to be modeled in a two-dimensional plane. A plane-stress overlay approach [57] was used in which stitches were modeled in the two-dimensional plane using plane stress (beam) elements. The plane-stress stitch elements were coupled to the axisymmetric sandwich composite elements along the length of each stitch using nodal coupling. The foam core and facesheets for both stitched configurations were modeled with the same type and number of elements used in the non stitched configuration (Figure 95b and c). The stitches for both configurations consisted of two-dimensional two-node beam elements (Beam4 in ANSYS 8.0). The element length used for the stitch elements was 0.99 mm to match the element height of the axisymmetric elements.

The multi-layer configuration (Figure 95d) also utilized the Plane82 element with each section of core consisting of 920 elements with 96 across the length and 10 through the thickness, each measuring 1.02 mm high and 1.12 mm long. The outer facesheets were modeled in the same manner as the three previous configurations with 192 elements, 2 elements through the thickness and 96 across the length. The interior layers were modeled with 96 elements each with 1 element through the thickness and 96 across the length.

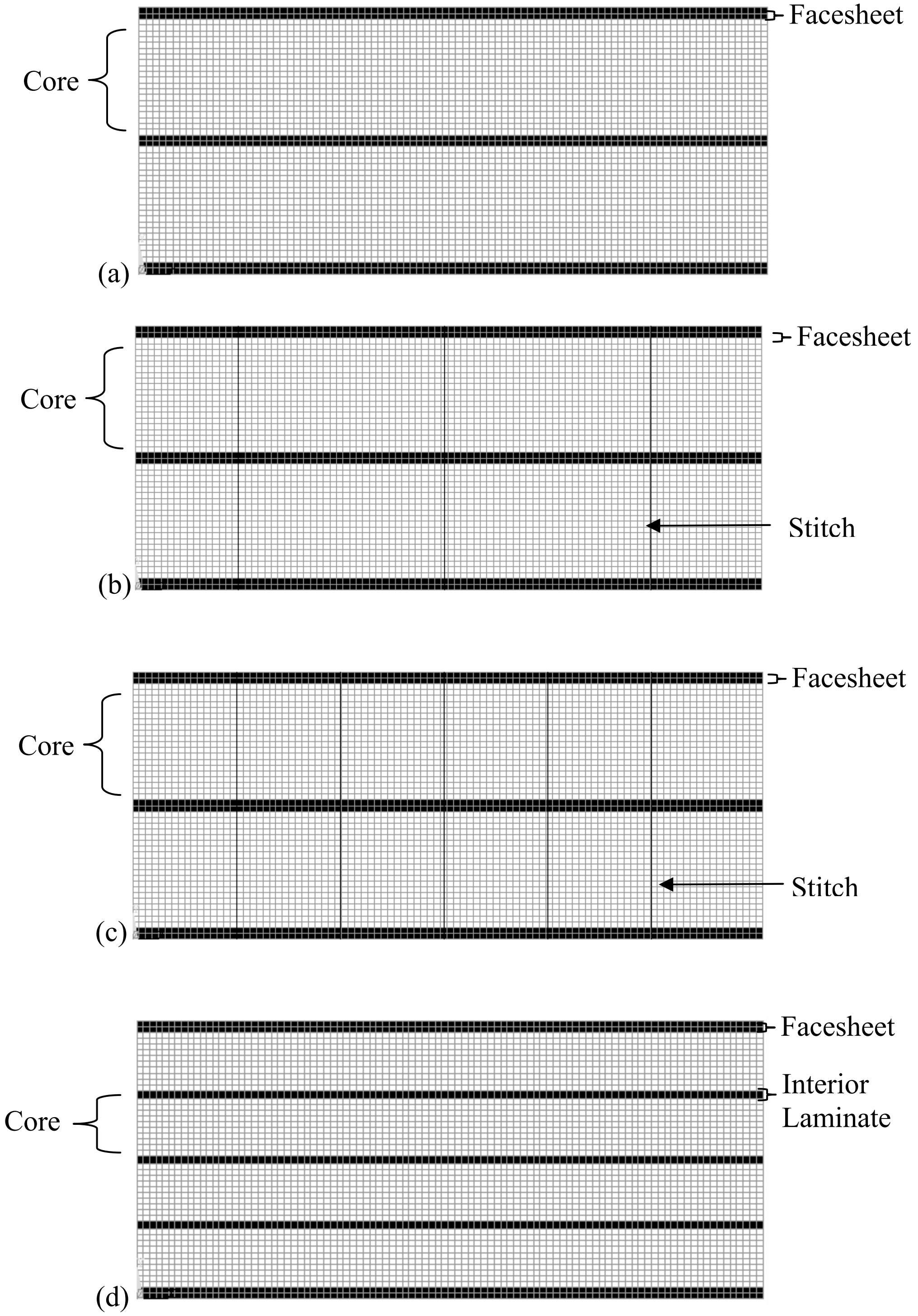

Figure 95. (a) Meshed non-stitched configuration, (b) Meshed 0.16 stitch/cm^2 configuration, (c) Meshed 0.62 stitch/cm^2 configuration and (d) Meshed multi-layer configuration.

Boundary conditions were placed on the model that constrained a node at the radial location where the test specimens contacted the circular support plate, 63.5 mm from the vertical centerline. This node was constrained against translation in all three coordinate directions, but allowed rotation, enabling the sandwich to bend as observed during mechanical testing. All model specimens were loaded at the interior laminate at a value equal to the maximum load observed during mechanical testing. The maximum load during quasi-static indentation testing was observed to be approximately 5.0 kN for configurations 1 – 3. The maximum load on the interior layer for configuration 4 was observed to be approximately 2.9 kN. To implement this load application into the axisymmetric model, the entire load was divided up evenly across nodes that represented the location of half the contact area of the indenter (2.5 mm). Figure 96 illustrates the applied boundary conditions and loading condition implemented for all configurations.

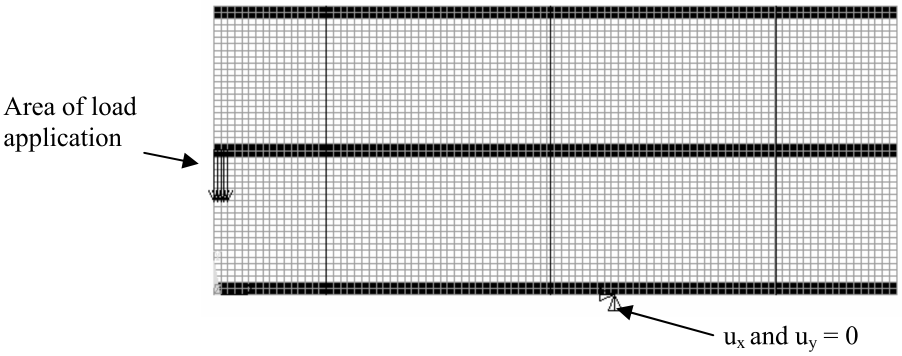

Figure 96. Representative boundary and loading conditions applied for computational modeling.

8.3 Validation of Analysis Methodology

To assess the validity of the element overlay approach for incorporating stitching into the axisymmetric model, additional modeling was performed. The overlay approach was used in a simple finite element model to calculate the through-the-thickness modulus for the two vertically stitched sandwich configurations. The predicted modulus values were compared to those obtained using a simple spring model. This model considered the facesheets and core as springs in series while stitches were considered as an additional spring element in parallel with the remaining laminate. The spring model for a sandwich specimen that included stitching is illustrated in Figure 97.

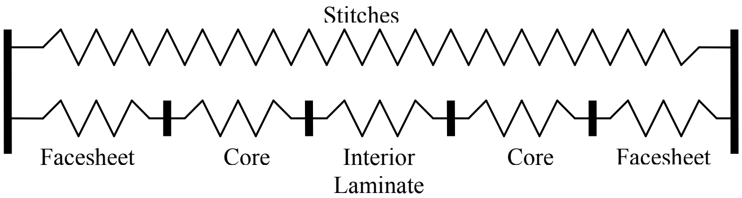

Figure 97. Spring model for stitched sandwich specimen.

The total through-the-thickness stiffness of the sandwich specimen was calculated using the expression

$$k_{total} = \left(\frac{1}{\dfrac{3}{k_f} + \dfrac{2}{k_c}} \right) + k_s\,, \tag{10}$$

where k_{total} is the stiffness (N/m) of the entire sandwich specimen, and k_f, k_c and k_s are the stiffness (N/m) constants of the facesheet, core and stitching respectively. The sandwich specimen stiffness values were compared to those obtained from finite element analysis. Finite element analysis was performed by applying a uniform compression load to the sandwich specimen models. Corresponding through-the-thickness displacement values were used to calculate the sandwich specimen stiffness using the expression

$$k = \left(\frac{F}{\delta} \right), \tag{11}$$

where k is the sandwich stiffness (N/m), F is the load applied to the sandwich (N) and δ is the displacement of the top facesheet (m). Table 19 shows the sandwich stiffness determined analytically and from finite element analysis for the non-stitched, 0.16 stitch/cm^2 and 0.62 stitch/cm^2 sandwich configurations. Also shown is the percent difference between these values. Results show that the global stiffness values generated by the model are greater than those predicted analytically. This result is expected, as the spring model does not consider the Poisson effect that is present in finite element model of the sandwich configuration. This effect is enhanced by the relatively stiff facesheets resisting the ability of the more compliant core to deform laterally, especially at the facesheet-core interface where the two materials are bonded. Although the difference between the two models was significant, the trend of increasing stiffness with increasing stitch density was similar. Thus, the overlay approach used in the finite element modeling was determined to be properly accounting for the through-the-thickness stitching.

Table 19. Comparison of Through-The-Thickness Sandwich Stiffness Obtained From Analytical and Finite Element Models

Sandwich Configuration	Analytical Stiffness (N/m)	Finite Element Stiffness (N/m)	% Difference
Non-stitched	1.05E + 06	1.28E + 06	22.3
0.16 stitch/cm^2	1.11E + 06	1.38E + 06	24.1
0.62 stitch/cm^2	1.26E + 06	1.46E + 06	15.4

8.4 Results from Finite Element Analysis

In the following sections, results from finite element analysis are presented for each sandwich configuration investigated. The non-stitched configuration is presented first and is intended to serve as a baseline for assessing the effects of stitching. Contour plots are used to display the variations in the in-plane stress components throughout the specimen. Additionally, line plots are used to show the through-the-thickness stress distribution in the stitches.

8.4.1 Non-Stitched Configuration

Figure 98 through Figure 100 show stress contours for the two in-plane normal stresses (σ_x and σ_y) and the in-plane shear stress (τ_{xy}) induced in the core of the non-stitched sandwich configuration. The coordinate values shown are given in mm and the contour stresses are in units of MPa. Figure 98 shows that the horizontal component of normal stress, $\sigma_{x,}$ is concentrated primarily around the interface between the interior laminate and core at the initiation site of delamination. This result indicates that a majority of the bending stress is carried by the comparatively stiff facesheets. Figure 101 confirms this observation, showing relatively high stresses in the lower facesheet of the sandwich compared to those observed in the core. The bottom section of the facesheet shown includes the area between the sandwich centerline and 1.2 cm beyond the support.

The highest magnitudes of the vertical stress component $\sigma_{y,}$ are located directly underneath the delaminated section of the interior laminate in the lower section of core. This location corresponds well with the damage observed during mechanical testing for this configuration. Thus, these stresses are believed to be the driving mechanism for the facesheet delamination and core crushing observed experimentally.

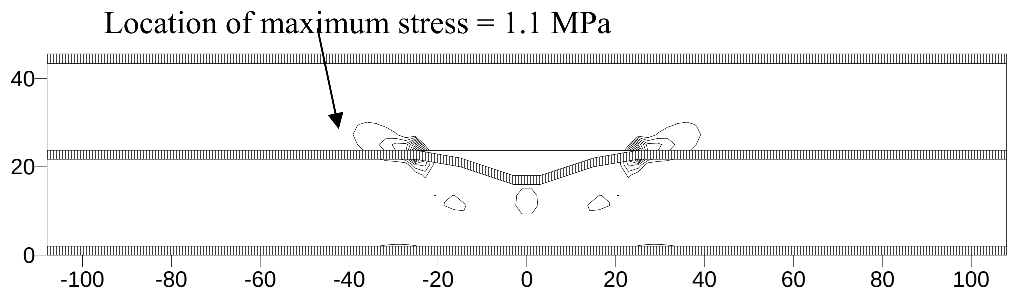
Location of maximum stress = 1.1 MPa

Figure 98. σ_x stress distribution in non-stitched configuration.

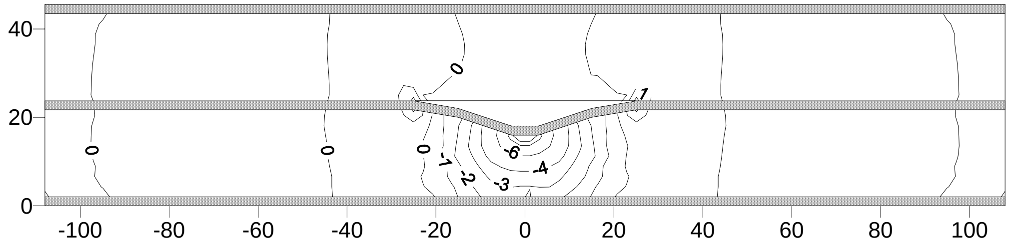

Figure 99. σ_y stress distribution in non-stitched configuration.

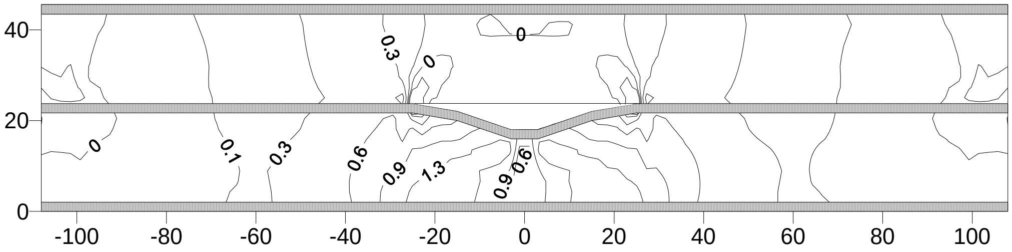

Figure100. τ_{xy} stress distribution in non-stitched configuration.

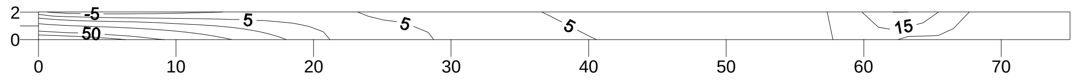

Figure101. σ_x stress distribution in non-stitched configuration lower facesheet.

Shear stresses, τ_{xy}, in the sandwich core are present in bands running top to bottom with the highest shear stresses present under the delamination site. Bands of shear stress located near the edge of the delamination site are in the range of the ultimate shear strength observed for the PET core material during core shear testing. This finding is in agreement with cracks observed in this areas of the sandwich specimens following indentation testing.

8.4.2 0.16 stitch/cm^2 Configuration

Figure 102 through Figure 104 show stress contour plots for σ_x, σ_y, and τ_{xy} in the core regions of the 0.16 stitch/cm^2 sandwich configuration. The σ_x stress contours are shown to follow a similar pattern to those in the non-stitched configuration, albeit the stresses are distributed over a larger area. As with the non-stitched configuration, the majority of stress oriented in the horizontal direction induced by bending is carried in the outer facesheets. This result is evident in Figure 105, which shows relatively larger stresses in the lower facesheet compared to those seen in the core.

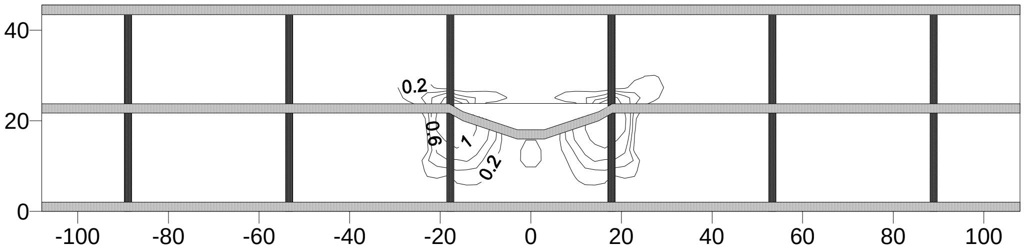

Figure 102. σ_x stress distribution in 0.16 stitch/cm^2 configuration.

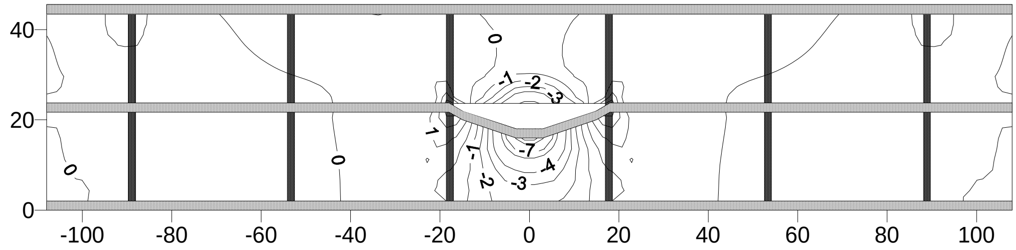

Figure 103. σ_y stress distribution in 0.16 stitch/cm^2 configuration.

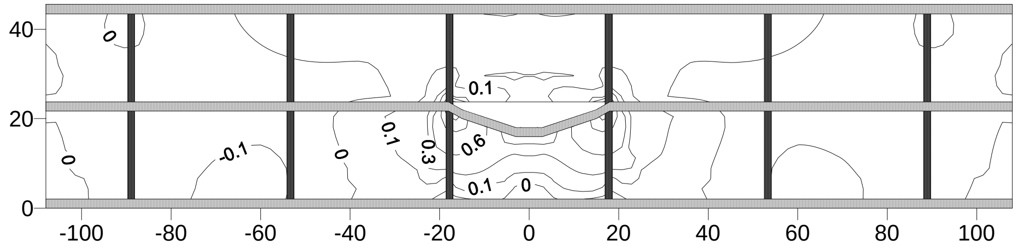

Figure 104. τ_{xy} stress distribution in 0.16 stitch/cm^2 configuration.

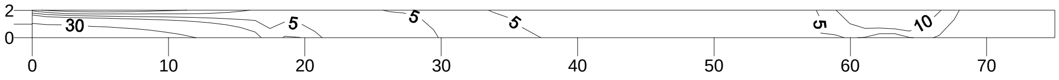

Figure 105. σ_x stress distribution in 0.16 stitch/cm^2 configuration lower facesheet.

The distribution of the σ_y stresses follows a similar pattern as the non-stitched configuration, with a large stress concentration around and under the delamination site. Figure 103 shows that implementation of stitching distributes stresses to the upper section of core above the delamination site. This finding agrees with damage observed in this area following mechanical testing.

Shear stresses τ_{xy} in the sandwich core are not as widely distributed as those in the non-stitched configuration, and are concentrated around the interior stitches. These regions were shown to be the primary locations of core damage during mechanical testing.

Figure 106 shows the axial stress in the stitches through-the-thickness of the sandwich. Stitch-1 corresponds to the inner-most stitch, and stitch-3 to the outer stitch. As expected, the highest stresses are seen in the inner-most stitch as it lies adjacent to the loading area. This stitch location is credited with preventing delamination propagation seen in the interior facesheet of the non-stitched specimens. The highest stitch stresses are located at the interface between the stitch, interior laminate and facesheet.

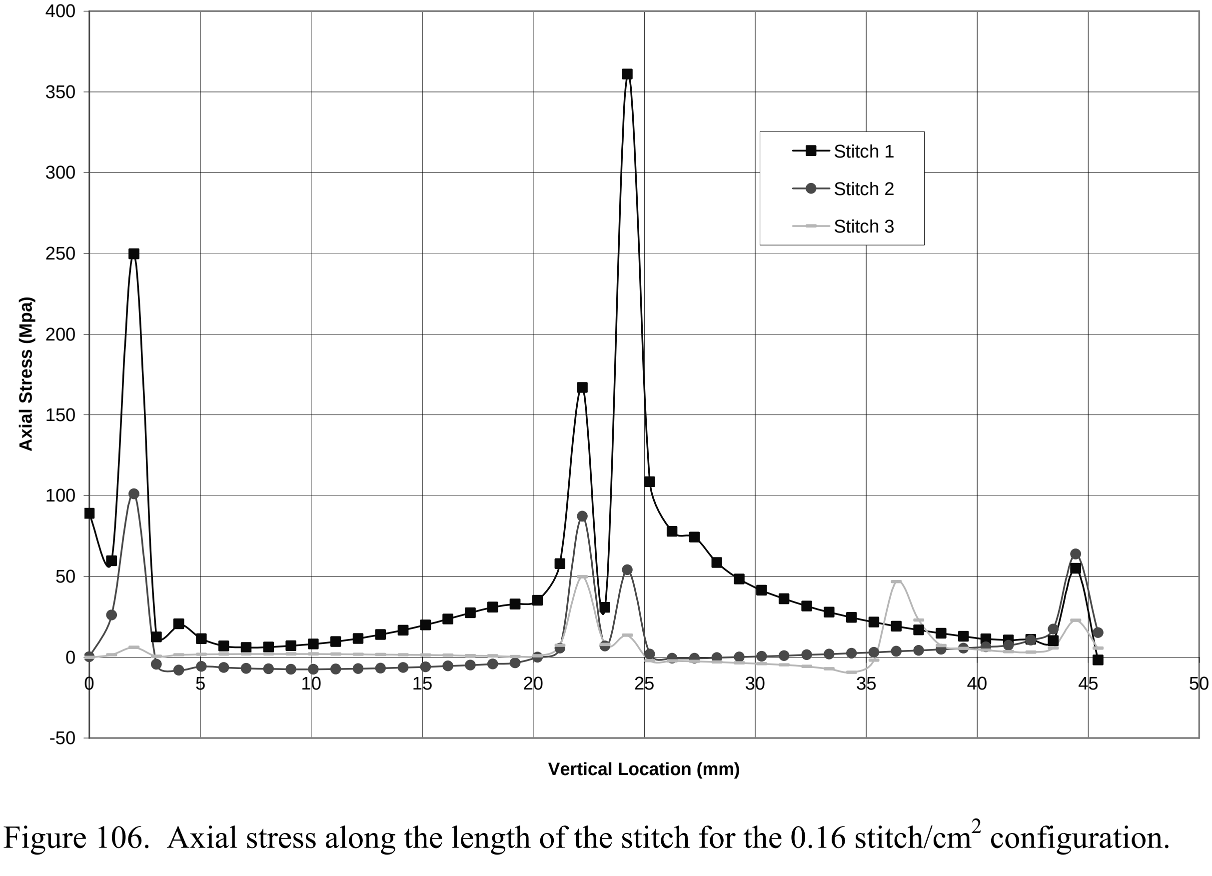

Figure 106. Axial stress along the length of the stitch for the 0.16 stitch/cm^2 configuration.

8.4.3 0.62 stitch/cm^2 Configuration

Figure 107 through Figure 109 show stress contour plots for σ_x, σ_y, and τ_{xy} in the core regions of the 0.62 stitch/cm^2 sandwich configuration. As seen with the 0.16 stitch/cm^2 configurations, the horizontal normal stress σ_x is concentrated around the delamination area and cover a slightly larger area compared to the non-stitched configuration. The outer facesheets carry the majority of the stress induced by bending as discussed previously as evidenced by the high stresses seen in the lower facesheet (Figure 110).

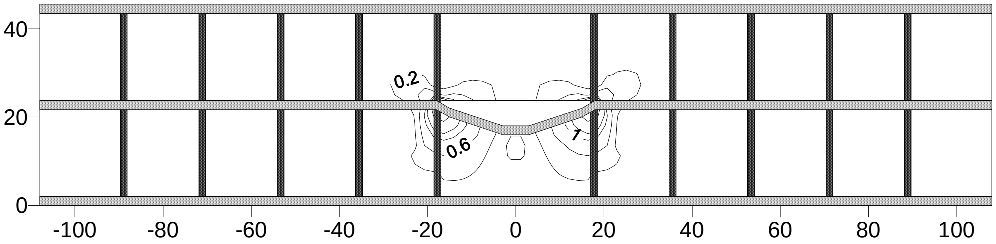

Figure 107. σ_x stress distribution in 0.62 stitch/cm^2 configuration.

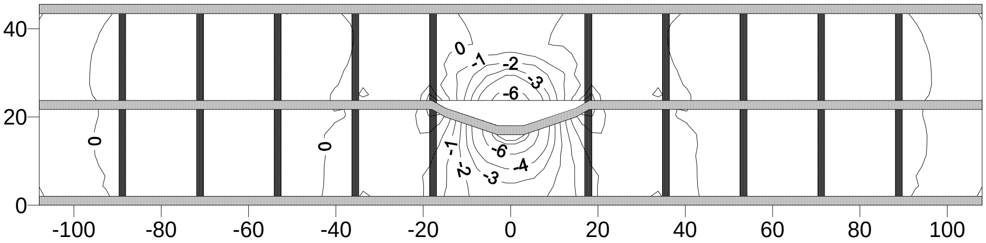

Figure 108. σ_y stress distribution in 0.62 stitch/cm^2 configuration.

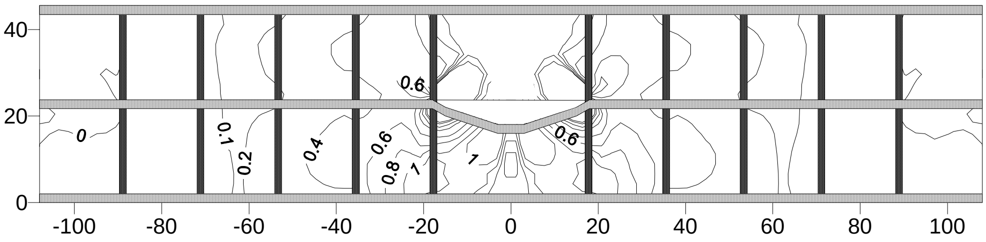

Figure 109. τ_{xy} stress distribution in 0.62 stitch/cm^2 configuration.

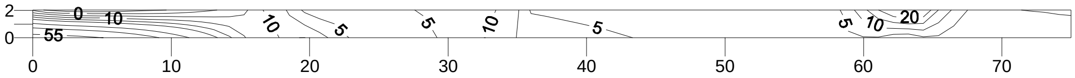

Figure 110. σ_x stress distribution in 0.62 stitch/cm^2 configuration lower facesheet.

The normal stresses in the vertical direction, σ_y, also show a similar pattern to the 0.16 stitch/cm^2 configuration but with greater magnitude. These stresses are concentrated above and below the delamination area contributing to the damage observed in this region following indentation testing.

Shear stresses, τ_{xy}, are not as widely distributed as observed in the non-stitched configuration, and are concentrated around the interior stitches. As with the 0.16 stitch/cm^2 configuration, the majority of core damage occurred in this region during indentation testing, with core cracking taking place along the stitch and between stitches.

Figure 111 shows the axial stress in the stitches through-the-thickness of the sandwich. Stitch-1 corresponds to the inner-most stitch, and stitch-5 to the outer stitch. As seen with the previous configuration, the highest stresses are produced in the interior stitch. As discussed previously, the inner stitches were observed to fail during indentation testing. Stitch-1 shows a similar pattern to those observed in the 0.16 stitch/cm^2 configuration with the highest stresses located at the interface between the stitch, the interior laminate and the facesheet.

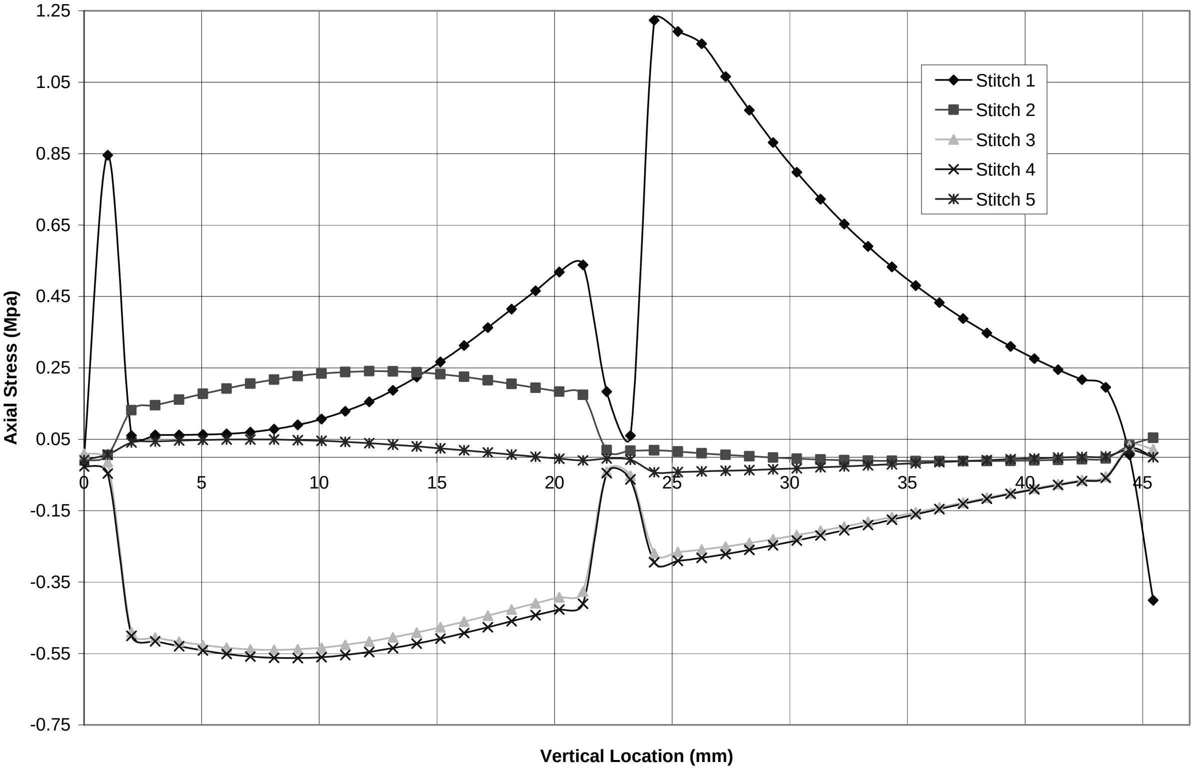

Figure 111 Axial stress along the length of the stitch for the 0.62 stitch/cm^2 configuration.

8.4.4 Multi-Layer Configuration

Figure 112 through Figure 114 show stress contour plots for σ_x, σ_y, and τ_{xy} in the core regions of the multi-layer sandwich configuration. As observed for the previous configurations the normal stresses acting in the horizontal direction, σ_x, are primarily located around the delamination site. These core stresses are considerably smaller than those observed in the facesheets as shown for the lower facesheet in Figure 115.

The σ_y stress distribution (Figure 112) follows a similar pattern as the non-stitched configuration, with a large concentration of stress around and under the delamination site of the two upper interior layers. This result was expected, as the main damage mechanisms observed during mechanical testing was delamination and core crushing directly underneath the delamination site. The τ_{xy} shear stress distribution (Figure 113) in the sandwich core for the multi-layer configuration are of lower magnitude and are significantly less distributed than in the non-stitched and stitched configurations.

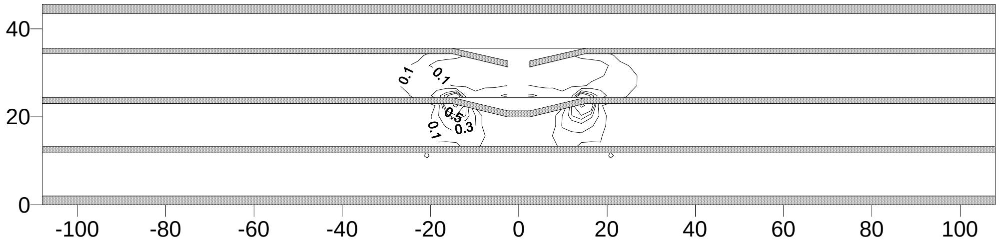

Figure 112. σ_x stress distribution in multi-layer configuration.

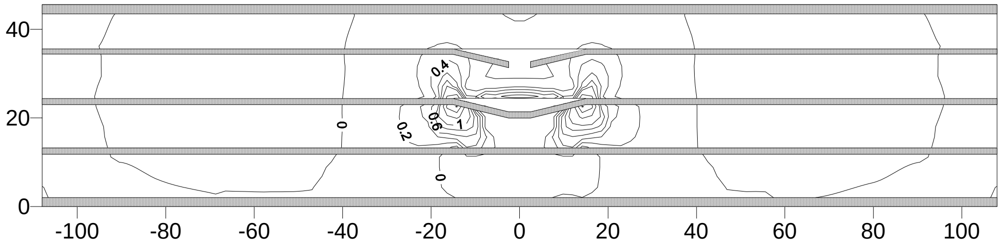

Figure 113. σ_y stress distribution in multi-layer configuration.

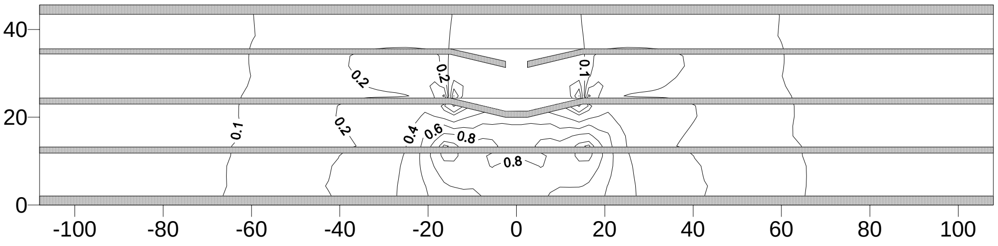

Figure 114. τ_{xy} stress distribution in multi-layer configuration.

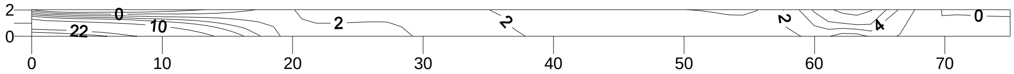

Figure 115. σ_x stress distribution in multi-layer configuration lower facesheet.

9. SPACE ENVIRONMENTAL TESTING

9.1 Background and Motivation

In order to assess the ability of the proposed sandwich materials to be used in a space environment, it was necessary to quantify their response to the simultaneous conditions of vacuum and elevated temperature. Removal of atmospheric pressure is of particular concern with the foam core, as this causes internal pressure loading of the cells which can lead to undesirable deformations. Dependent upon foam characteristics such as material, density and cell geometry, the foam may deform in a negligible manner due to the internal pressure loading. It is also possible, however, for the internal pressure to be sufficient to cause pronounced expansion of the foam, gradual degassing, or even cell rupture and rapid degassing. Either type of degassing leads to a significant decrease in the size of a foam specimen, and typically induces some amount of warping. The introduction of elevated temperature exacerbates the problems associated with the application of a vacuum by causing degradation in the material properties of the foam, and by increasing the pressure internal to the foam cells due to gas expansion. From preliminary testing performed at the outset of the project, it was known that the selected core materials may be vulnerable to these conditions, as illustrated in Figure 116, which shows a 32 kg/m^3 Voltek PE specimen before and after application of vacuum and heating.

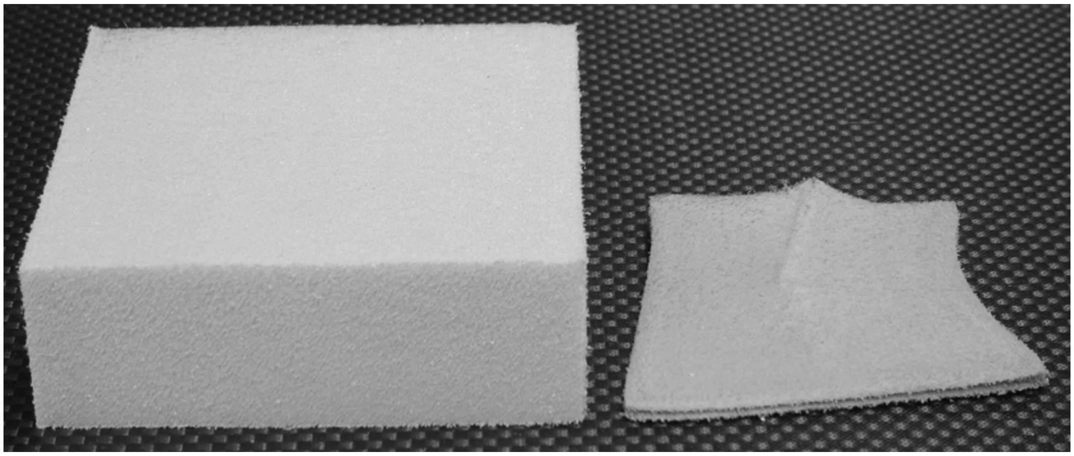

Figure 116. Comparison of 32 kg/m^3 Voltek PE foam before and after application of a space environment.

In light of this background information, the goal of environmental testing was to acquire a better understanding of how the selected materials being investigated would behave in a space environment. In order to accomplish this, an experimental apparatus was developed which allowed expansion/contraction of a specimen to be measured while being subjected to a vacuum and elevated temperature. From this information, strain and coefficient of thermal expansion (CTE) values could be calculated and an acceptable operating range of temperature could be determined for each specimen.

Based upon the results from mechanical testing, it was determined that the PET configurations displayed the most promise for structural applications. This conclusion was reached based upon the observed failure mode, strength qualities and general core characteristics, as outlined in Chapter 6. For this reason, the focus of environmental testing was to assess PET sandwich configurations; however, PE specimens were also tested for comparison purposes. Of particular interest was the incorporation of transverse reinforcements to alleviate any potential problems encountered with foam specimen expansion.

9.2 Design of the Experimental Apparatus

As outlined in the preceding section, the goal of environmental testing was to examine the expansion/contraction of proposed materials and sandwich configurations in a simulated space environment. The selected apparatus therefore had to be capable of subjecting a specimen to the combined effects of vacuum and heating, while providing displacement measurements with sufficient sensitivity to \detect geometrical changes of a given specimen over small temperature ranges, ideally less than 3°C. This section will describe the testing apparatus developed to meet these criteria.

For simulation of the space environment a NAPCO® E series Model 5851 vacuum oven obtained through Precision Scientific [58] was used in conjunction with a Welch [59] DUOSEAL® vacuum pump. Using this system, a steady-state vacuum pressure of approximately 88 kPa could be attained in comparison with a typical atmospheric pressure at the University of Utah near 100 kPa. The maximum temperature of the heating plate of the vacuum oven was approximately 150°C.

A combination of lasers and mirrors was used to make accurate displacement measurements. Although the design progressed through several iterations, the underlying concept remained unchanged. In this concept a mirror was placed across the specimen being tested as well as a reference material with a known, low coefficient of thermal expansion (CTE). Due to the significantly higher CTE of the specimen, the mirror would tend to pivot on the reference as the specimen would expand or contract. The rotation could be detected by shining a laser onto the mirror through the glass front of the vacuum oven and measuring the movement of the reflected laser light along a flat surface. The measured laser movement could then be related to the dimensional change of the specimen using a calibration with known materials.

The test set-up implemented from this concept is shown schematically in Figure 117 and Figure 118. As indicated in the schematics (side views), the oven is placed on its back surface such that the glass-window door is facing in the upward direction. This was necessary to take advantage of gravity to keep the specimen level and to provide contact pressure between the mirror and specimen. In order to facilitate ease of use, a mirror angled at a nominal 45° angle was placed above the window to the vacuum oven. This allowed the laser to be placed horizontally and the measuring surface to be placed vertically. In the initial position shown in Figure 117, the laser light reflects back directly into the laser, which serves as a means to zero the system prior to the test. As the specimen is heated, it undergoes dimensional changes, as shown in Figure 118, causing the mirror to rotate and thus altering the angle of incidence and reflection of the laser light. Notice that this system is capable of detecting both the increase and decrease in specimen size, indicated by the direction (up or down) that the reflected laser light moves along the measuring surface.

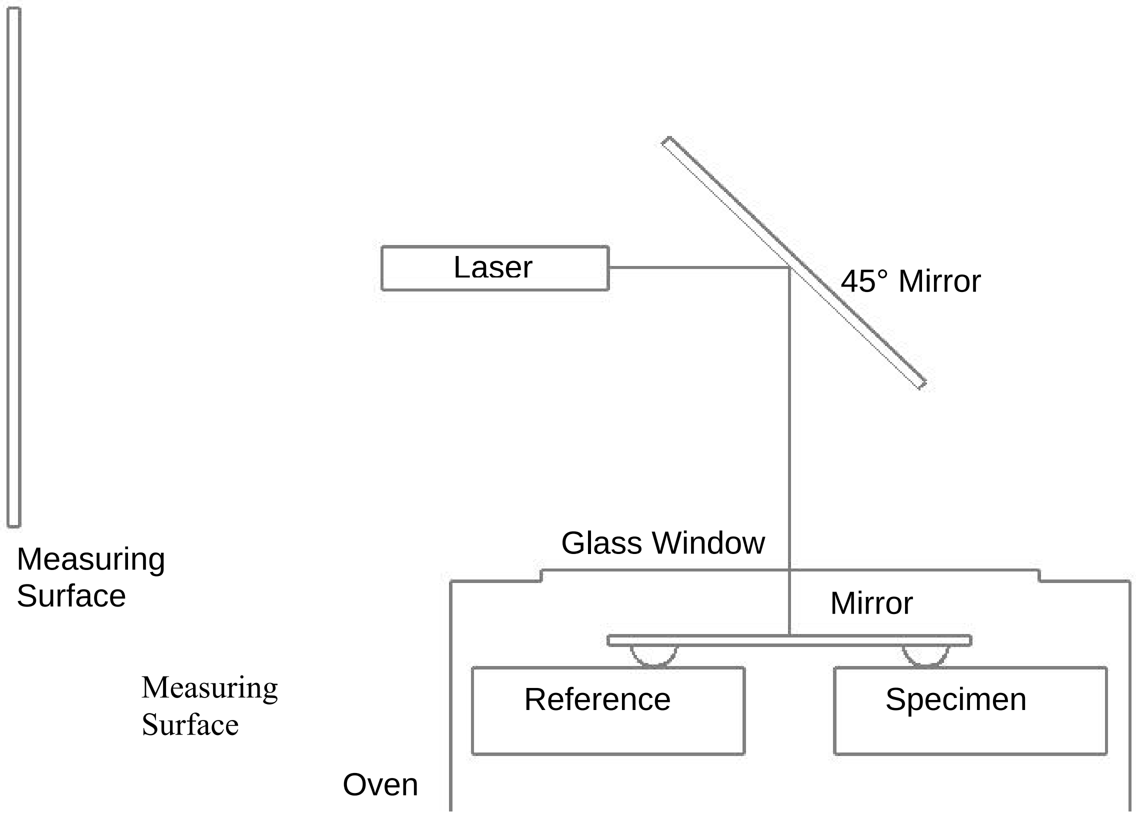

Figure 117. Schematic presenting a side view of the final measurement design in the initial position.

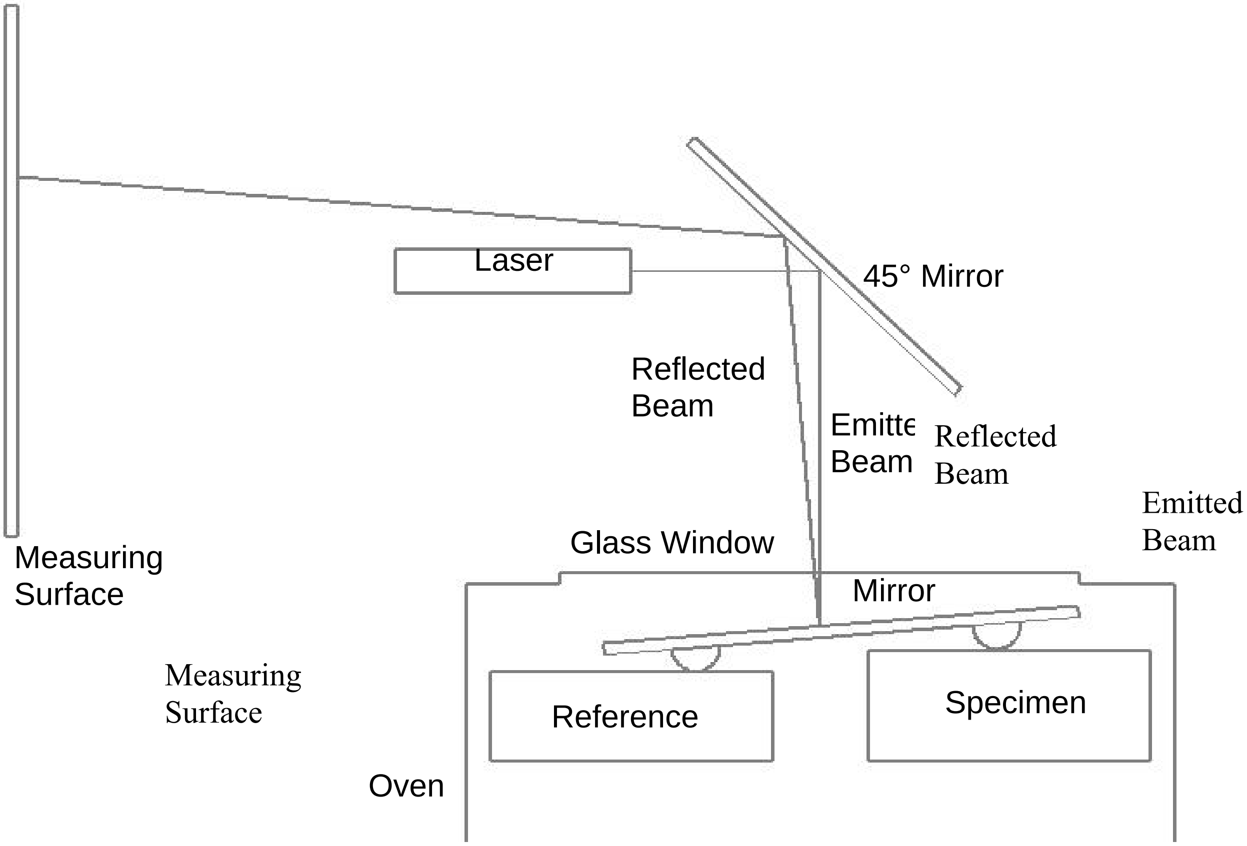

Figure 118. Schematic presenting a side view of the final measurement design in a displaced position.

For this concept to function properly, sufficient displacement amplification must be obtained to allow reliable and accurate measurements of the specimen displacement. The term "displacement amplification" is used here in reference to the ratio between the actual length measured from the laser movement and the corresponding change in thickness of the specimen. There are four fundamental parameters that are of critical importance in controlling the amplification: the size (specifically thickness) of the specimen, the distance between pivot points of the specimen mirror, the distance from that mirror to the 45° mirror, and the distance from the 45° mirror to the measurement surface. The distance between the pivot points on the mirror introduces a geometric constraint on the ratio between the change in specimen thickness and the amount of rotation induced in the mirror. The distances between the mirrors and to the measurement surface both directly influence the amount of amplification through trigonometric relationships. For optimal detection, the mirror pivot length would be minimized while the thickness of the specimen and the distances between the mirrors and measurement surface would be maximized.

In practice there are significant constraints placed upon the allowable range of each of those parameters. In particular, the size of the specimens was kept nominally at 76 mm x 76 mm x

25 mm, to correspond with the dimensions used during flatwise tensile testing. These dimensions were selected because both tests involve out-of-plane measurements, and they allow for a reasonable number of stitches to be included at the lower 0.16 stitch/cm^2 density of transverse reinforcement. The thickness of the specimen is therefore directly controlled, but by setting the cross-sectional area of the specimen, a minimum limit is also placed upon the mirror pivot length. In order to avoid uneven loading by the weight of the mirror pressing upon the specimen, it is desirable to have the pivot point line up with the center of the specimen. This dictates that the mirror must be at least 38 mm in length, which will cover only the half-length of the specimen. In order to provide pivot attachment on the reference, this length must be increased to at least 50 mm in practicality. Note that this distance is not just equal to the specimen length (75 mm) because although shown as equal in Figure 117 and Figure 118, the reference is not required to be of the same cross-sectional dimensions as the specimen, but rather needs only to be of equal thickness. Additionally, the reference material would be of sufficient hardness that off-center loading would not cause the potential unequal deformations that would be witnessed with a foam specimen.

With these constraints, the only available parameters to control the amplification of the system were the distance between the specimen mirror and the 45° mirror as well as the distance between the 45° mirror and the measurement surface. In order to maximize the amplification, the distance between the specimen mirror and the 45° mirror was set at the highest level that could be tolerated given the physical confines of the laboratory environment. A portable measuring surface was then constructed with a measurement range from ground level to a height of 3.2 m. To assess the proper location of the wall, trial specimens such as that shown in Figure 116 were tested, and the surface was located such that the test would take advantage of the entire measurement range.

It is now appropriate to describe in greater detail the physical implementation of the design concept. The material selected for the reference was GE Clear Fused Quartz (CFQ) [60] obtained from GM Associates [61]. This material was selected because of its low CTE (5.5×10^{-7} °C^{-1}, 20-320^{o}C), cost, and availability. Both the specimen and reference material were placed on an aluminum plate which rests inside the vacuum oven on sections of common window glass. The window glass was necessary to raise the plate above obstructions on the back surface of the vacuum oven. Note that both the glass and aluminum plate will experience expansion as a result of heating. The only expansion of interest, however, is in the out-of-plane direction and as can be discerned from the schematics in Figure 117 and Figure 118. Thus, uniform movement in the vertical direction will not influence the angle of incidence/reflection of the laser light and thus will not alter the measured values appreciably. Note that the distance between the 45° mirror and the specimen mirror will decrease as a result of this expansion, however the amount decreased is orders of magnitude smaller than that of the actual distance and thus has only a negligible impact on the system.

A solid model of the plate that was used to hold the specimen and reference material is shown in Figure 119. Notice that rails were implemented to constrain the movement of the specimen such that the mirror did not become unacceptably off-center, while still allowing the specimen enough degrees of freedom to expand without inhibition. All surfaces in contact with the specimen were coated with a layer of single-sided Teflon tape to minimize any warping or impedance of the specimen expansion due to frictional effects.

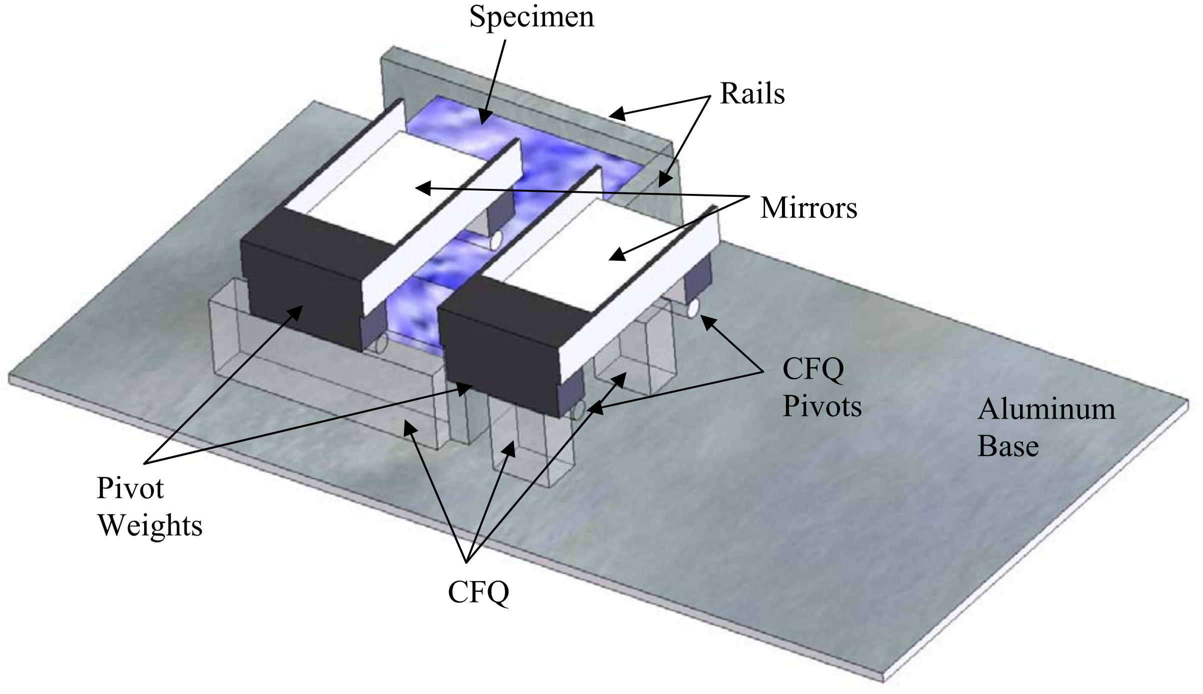

Figure 119. Plate used to hold specimen and reference material.

As shown in Figure 119, during actual implementation it was found that a second mirror was necessary. This mirror rests on two pieces of reference material of equal thickness, and thus can be used to detect effects attributed to warping of the vacuum oven during the course of a test. These reference values were subtracted from the measured specimen values to provide increased accuracy.

Due to inherent variability in the dimensions of the specimens, it was not possible for the reference material and specimen to be exactly equal in thickness for each test. This resulted in a mirror that was not perfectly horizontal when the test began, and was accounted for by zeroing the system. This was accomplished through the use of adjustable fixtures for the lasers and 45° mirror. The lasers, one for the specimen and one for the reference, were held in rings with set screws as shown in Figure 120. The set screws allowed the lasers to be adjusted with six degrees of freedom.

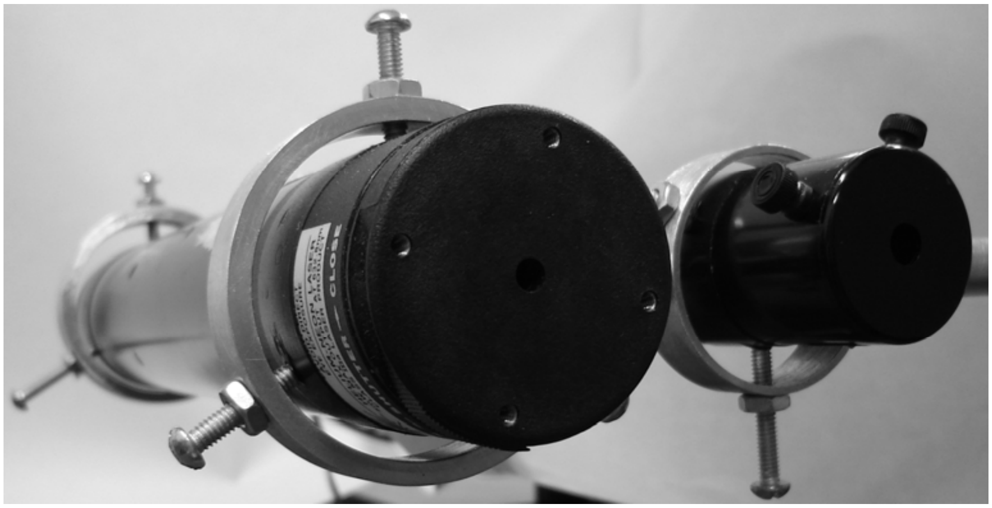

Figure 120. Photograph depicting the adjustable fixture designed for laser mounting.

The 45° mirror was supported on a system of rotating bases that allowed the mirror to be rotated along two perpendicular planes, as seen in Figure 121 and Figure 122. With this degree of adjustability in the laser and mirror mounts, it was possible to zero the system to the state shown in Figure 117, where each laser was reflected back into itself. All tests were started from this point.

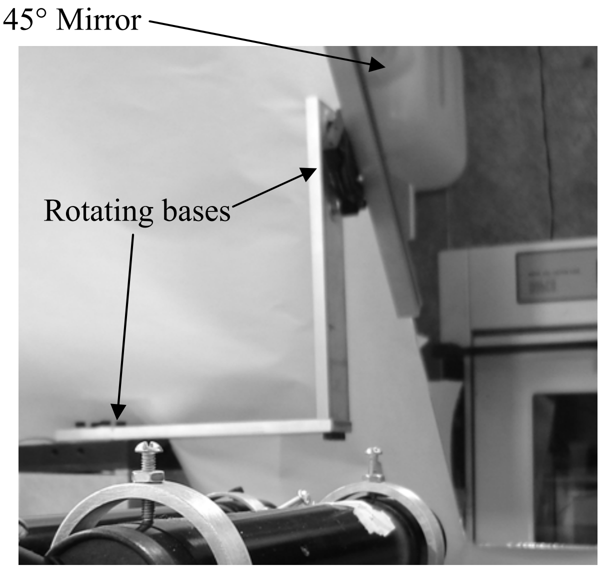

Figure 121. Photograph of 45° mirror holder with rotating bases.

Figure 122. Close-up photograph of the top rotating base on the 45° mirror holder.

Note that with this initial state, it was not possible to measure the laser light on the measuring surface until sufficient displacement of the specimen had raised the light above the radius of the laser itself. In order to avoid this loss of data, a 1.6 mm thick section of clear fused quartz was placed under both the specimen and reference mirrors, to provide an initial offset. Clear fused quartz was used to minimize the amount of expansion that would be attributed to the material, but note that since this same amount of material is applied to the reference specimen, any expansion/contraction would be subtracted from the specimen results.

Following initial testing, it was determined that additional weight placed on each mirror directly above the pivot point on the clear fused quartz (Figure 119) reduced the amount of noise in the data by promoting smoother rotation. All subsequent testing utilized this method. It should also be mentioned that initial testing revealed that the path of the laser was not significantly affected by passing through the glass of the vacuum oven. This was confirmed by marking the location of the laser light with the door fully open, and then making subsequent marks as the door was incrementally closed to examine the potential affect of angle of incidence to the glass. No changes in the location of the laser on the measuring surface could be detected during this test.

The final note involves the collection of temperature data. The data was collected using type-K thermocouples placed in the vacuum oven. Initially two measurements of specimen temperature were obtained, using two thermocouples placed at the center of the cross-section of the specimen, at heights corresponding to a quarter of the thickness and half the thickness. Due to the insulating nature of foam it was felt that significant temperature gradients might be observed. Following initial testing, however, it was discovered that the two temperatures were consistently within 1°C of each other, and thus only the middle temperature was recorded in subsequent experiments. Note also that in order to insert the thermocouple wire into the specimen, a hole first had to be drilled. Traditionally, that hole would need to be sealed to prevent air circulation from altering the reading. Because the test operates within a vacuum, however, this was not a concern and thus no sealant was used in order to avoid any potential influence on the deformation of the foam, particularly in the case of catastrophic collapse as seen in Figure 116. The vacuum oven temperature was obtained using a thermocouple which was suspended in the oven at the height of the specimen, and was used as a control of the heating rate of the specimen by trying to maintain a relatively constant difference between oven and specimen temperature.

9.3 Calibration of the Experimental Apparatus

As defined in the preceding section, the displacement amplification of the apparatus is the ratio between the actual length measured from the laser movement and the change in thickness of the specimen. This factor was calculated by simulating specimen displacement by inserting 0.0025 mm thick wedges between the specimen mirror and a representative specimen block. The addition of each layer produced an amount of laser light movement on the measurement surface that could be accurately read, while still allowing for a significant number of data points to be recorded. The total range of measurability was divided into three smaller sections from which data was obtained. By sampling over the entire range it was possible to verify that the displacement amplification factor is constant over the range of an entire test.

This calibration was performed at two different locations of the measurement surface. The two different locations were necessary in order to preserve acceptable readability for all types of specimens, due to the wide range in CTE observed. A representative plot showing the high degree of linearity in the data obtained is provided in Figure 123. The overall average R^2 value for all sections at both distances was 0.9981 with a standard deviation of 0.0012. The overall displacement amplification value for the three sections at the nearer measurement surface distance was found to be 173.7 with a standard deviation of 2.41. For the greater measurement surface distance, the average displacement amplification was 257.9 with a standard deviation of 3.11.

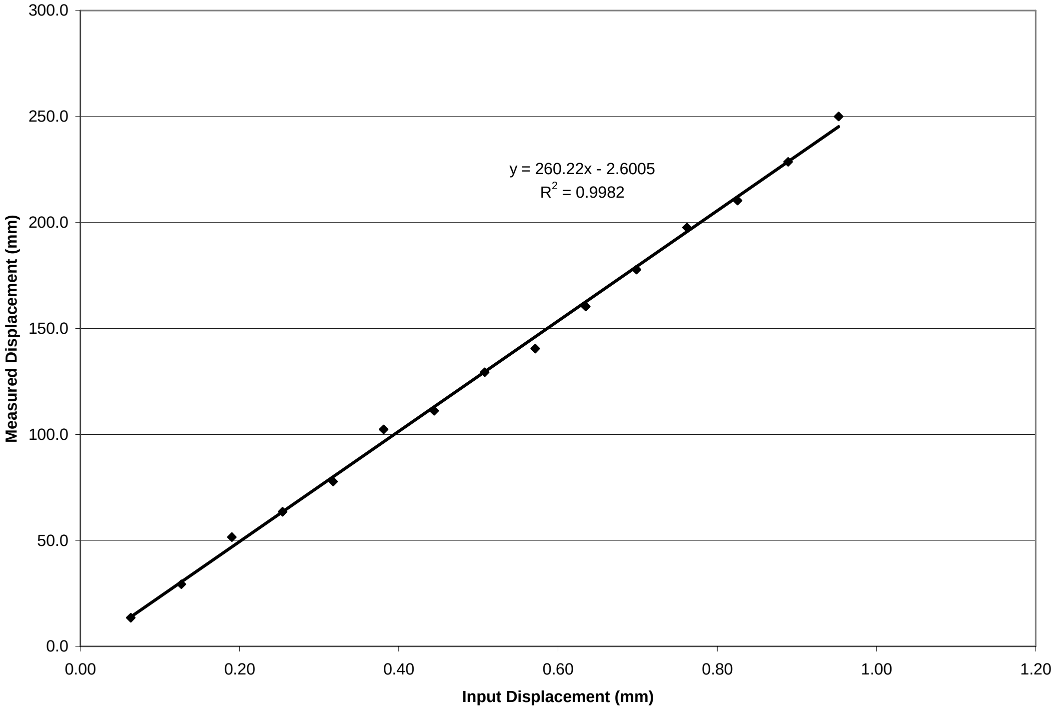

Figure 123. Calibration data for the experimental apparatus.

9.4 Specimen Configurations

Testing was performed using the six specimen configurations described in Table 20. Three specimens of each configuration were tested. The facesheets, where applicable, were composed of Spectra® 900 woven fabric measuring 2.1 mm thick infiltrated with an epoxy consisting of EPON^{TM}/EPIKOTE^{TM} Resin 862 combined with EPIKURE^{TM} Curing Agent 9553 (mixture ratio of 100:16.9). The two foam core materials were machined to a thickness of 21 mm, resulting in sandwich specimens having an overall thickness of approximately 25 mm. All stitched specimens had a density of 0.16 stitch/cm^2.

Table 20. Specimen Configurations Used for Environmental Testing

Configuration	Core Material	Nominal Core Density (kg/m^3)	Facesheet	Stitching
1	PE	128	None	None
2	PE	128	Spectra®	Spectra®
3	PE	128	T300 carbon	Kevlar® [62]
4	PET	125	None	None
5	PET	125	Spectra®	Spectra®
6	PET	125	T300 carbon	Kevlar®

9.5 Testing Methods and Procedures

All sandwich configurations (configurations 2, 3, 5, and 6) were manufactured using the VARTM process as detailed in Chapter 4. Individual specimens were cut from each sandwich or foam panel to nominal areal dimensions of 76 mm x76 mm. Once the specimens had been cut, a hole was machined into the side of the specimen to allow placement of a thermocouple wire. For specimens without stitching, the hole was placed in the center of the cross-section, to a depth of one-half the width of the specimen. In the case of stitched specimens, the hole was drilled to half the width of the specimen, but offset from the center of the cross-section to avoid damaging the stitches. Once the hole had been machined, the exact dimensions and weight of each specimen were recorded.

After the specimen had been measured, the thermocouple wire was attached to the specimen, and the specimen was placed on the specimen tray as depicted in Figure 119. The two lasers were then turned on, and zeroed by adjusting the apparatus until the emitted light was reflected back upon itself. The measurement surface was then placed in the proper location (near or far) based on knowledge gained about expansion values from preliminary testing of the specimens. The clear fused quartz offset pieces were then placed under the specimen and reference mirrors, such that the reflected laser light appeared on the measurement surface. At this point, the door to the oven was closed and sealed.

The location of the specimen and reference lasers were recorded directly on newsprint paper securely attached to the measurement surface. Each location was noted with a time, which was recorded in a spreadsheet along with temperature readings of the oven and specimen. Once the first data point had been collected, the vacuum pump was started, and the next data point was collected after a steady-state value of vacuum pressure had been obtained. Data continued to be collected at this value of vacuum pressure without heat applied until specimen expansion/contraction was no longer observed. At this point heat was applied to the specimen by radiation from the heating plate within the vacuum oven. The heating control for the vacuum oven had a scale of zero to 10. Once heating had begun the control was increased one full increment every second reading on all specimens to ensure a uniform rate of heat application. This rate was selected after preliminary testing revealed that it allowed for tests to be completed in a timely fashion (approximately five hours) without introducing significant temperature gradients within the specimens. After the heating process began, data were collected at a preferred rate of one point every five to 10 minutes. This corresponded to a temperature change of approximately four to six degrees Celsius, which was found to provide good readability on the measurement surface for all specimens. For specimens that experienced dramatic expansion, however, data could not be collected during the whole range of the test. The limiting factor was the size of the glass opening on the vacuum oven door which was not sufficiently large for all specimens, so that at some point the laser light would become blocked from reaching the measurement surface. As described in the results sections to follow, however, valid results could still be obtained from such tests.

A test was concluded when a specimen experienced pronounced collapse, or the specimen temperature reached a quasi-steady state, which typically occurred near 135°C. Once a test had been concluded, the vacuum pump and heating element were turned off and the specimen was exposed to atmospheric pressure. After the specimen had cooled, it was weighed and measured for comparison with the values recorded before testing. Note, however, that due to the gross deformation of some specimens, no meaningful dimensional measurements could be taken for precise comparison.

After a test was completed, the paper from the measurement surface was removed and secured along a smooth horizontal surface. A ruler was then used to make measurements between readings to the nearest 1 mm, which were matched with the temperature data recorded based upon time.

Strain and coefficient of thermal expansion (CTE) values were calculated using the following data reduction procedure. First, the actual specimen expansion was determined by subtracting the reference laser light movement along the measurement surface from that of the specimen, and multiplying the result by the inverse of the displacement amplification. This expansion value was converted to a strain by dividing by the original specimen thickness. The CTE was calculated by taking the slope of a linear fit of strain versus specimen temperature over a range of every three data points.

9.6 PE Foam Results and Discussion

Presented in Figure 124 and Figure 125 are plots of specimen strain and CTE as functions of temperature for the three plain PE foam specimens tested. Three distinct segments of behavior can be observed for the PE foam specimens. The first segment covers the range from room temperature (20°C) to approximately 80°C. During this period, the CTE of the foam increases at a relatively constant rate, leading to a smooth increase in foam expansion. It can also be observed that the three specimens show excellent agreement over this temperature range.

Beyond 80°C, the foam CTE increases dramatically with the corresponding significant increase in specimen strain as shown in Figure 124. This period of rapid expansion lasts only until approximately 95°C to 110°C, after which the foam begins to contract. The period of rapid expansion is hypothesized to correspond to yielding of the material due to internal cell pressure while the third period of contraction is associated with foam failure (cell wall rupture and degassing). A model to predict these transitional periods based upon foam cellular structure, internal gas expansion and degradation of material properties with temperature is discussed in further detail in Chapter 10. There is noticeable variation as to when the transition from expansion to cell rupture occurs for each specimen, which can be ascribed to the inherent variability associated with the foaming process. In spite of this fact, the overall behavior of the three specimens corresponds well.

As described previously, the limited glass size on the oven door resulted in a loss of data for specimen 2. It is still possible, however, to estimate that foam cell rupture occurred near 110°C, and the data available from the specimen correlates well with the other two specimens.

From Figure 124 it can be observed that by approximately 130°C all three specimens had begun showing rapid contraction with little increase in temperature. This indicates clear failure of the foam, with little to no ability to maintain pressurized cells.

Upon the reintroduction of atmospheric pressure following completion of the test, the specimen exhibited catastrophic collapse as shown in Figure 126. This behavior can be explained in terms of two factors: loss of internal cell pressure from degassing and reduction in foam material properties due to elevated temperature. These combined effects resulted in a specimen that was not capable of adequately resisting external loading from atmospheric pressure, resulting in pronounced collapse. The specific specimen shown in Figure 126 experienced a decrease in thickness of approximately 43%, although it should be noted that the warping of the specimen made accurate measurements impossible.

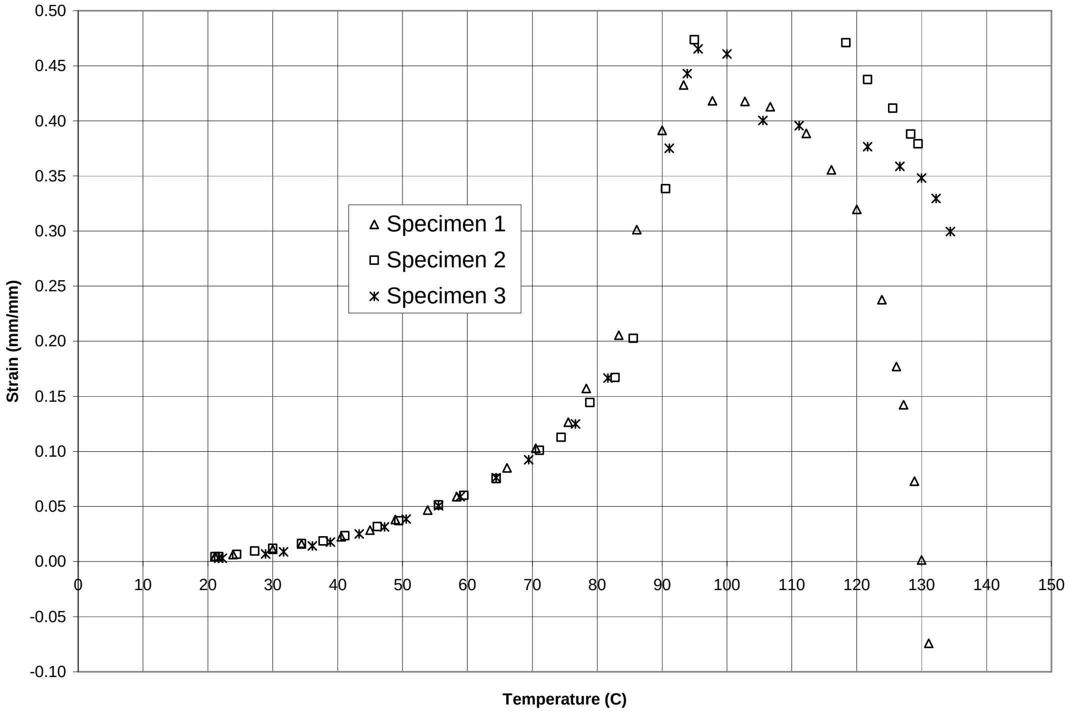

Figure 124. Strain versus temperature plot for the PE configuration.

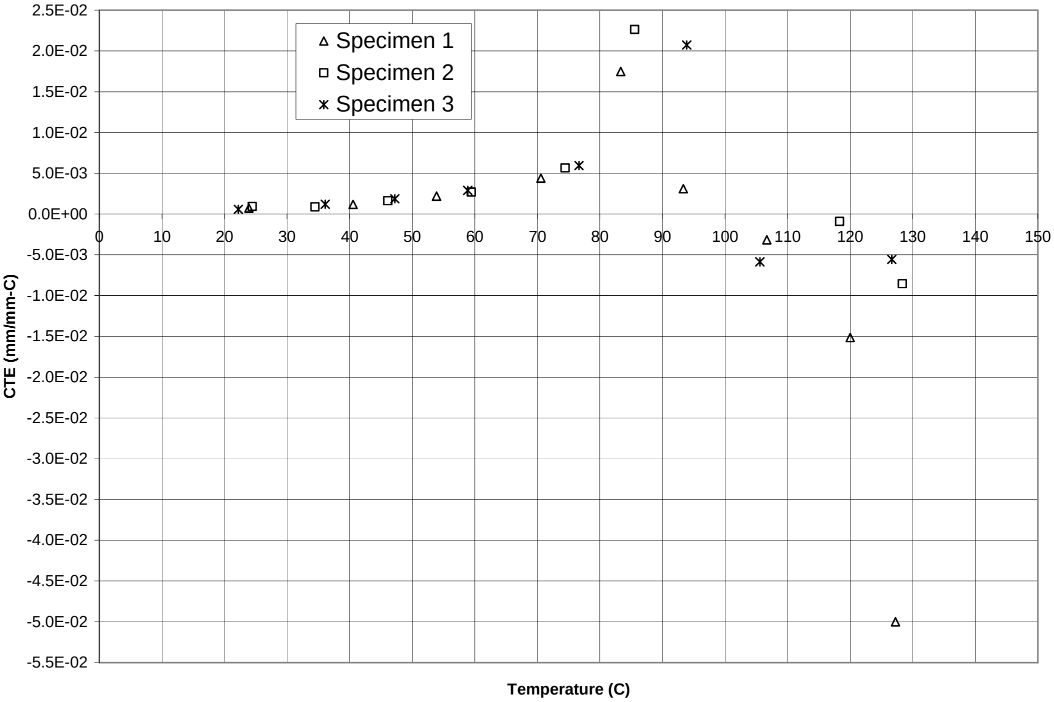

Figure 125. CTE versus temperature plot for the PE configuration

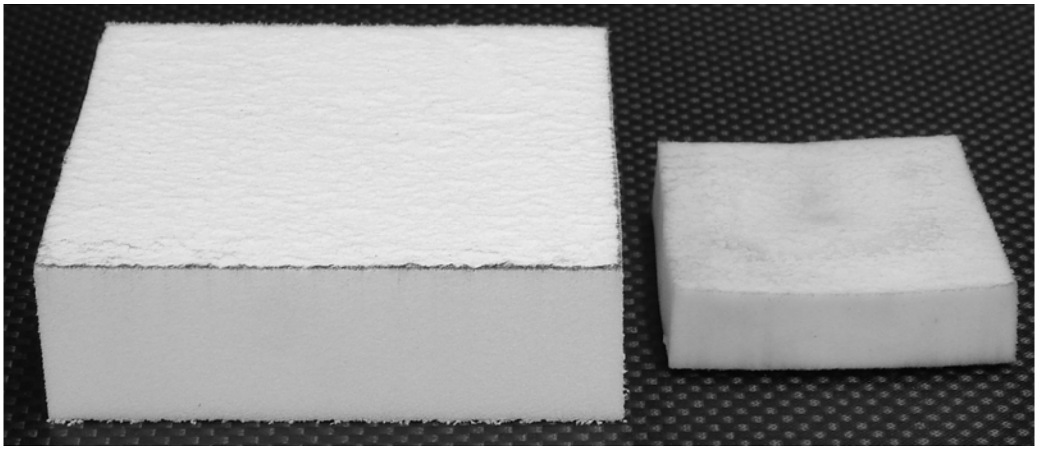

Figure 126. Representative PE foam specimen before and after environmental testing.

9.7 PE/Spectra Results and Discussion

Consideration of a 0.16 stitch/cm^2 PE/Spectra configuration provides a means of assessing the affect of introducing facesheets and transverse reinforcement on the expansion/contraction of plain PE foam discussed in the preceding section. Presented in Figure 127 and Figure 128 are plots of specimen strain and CTE as functions of temperature for the three 0.16 stitch/cm^2 PE/Spectra specimens tested.

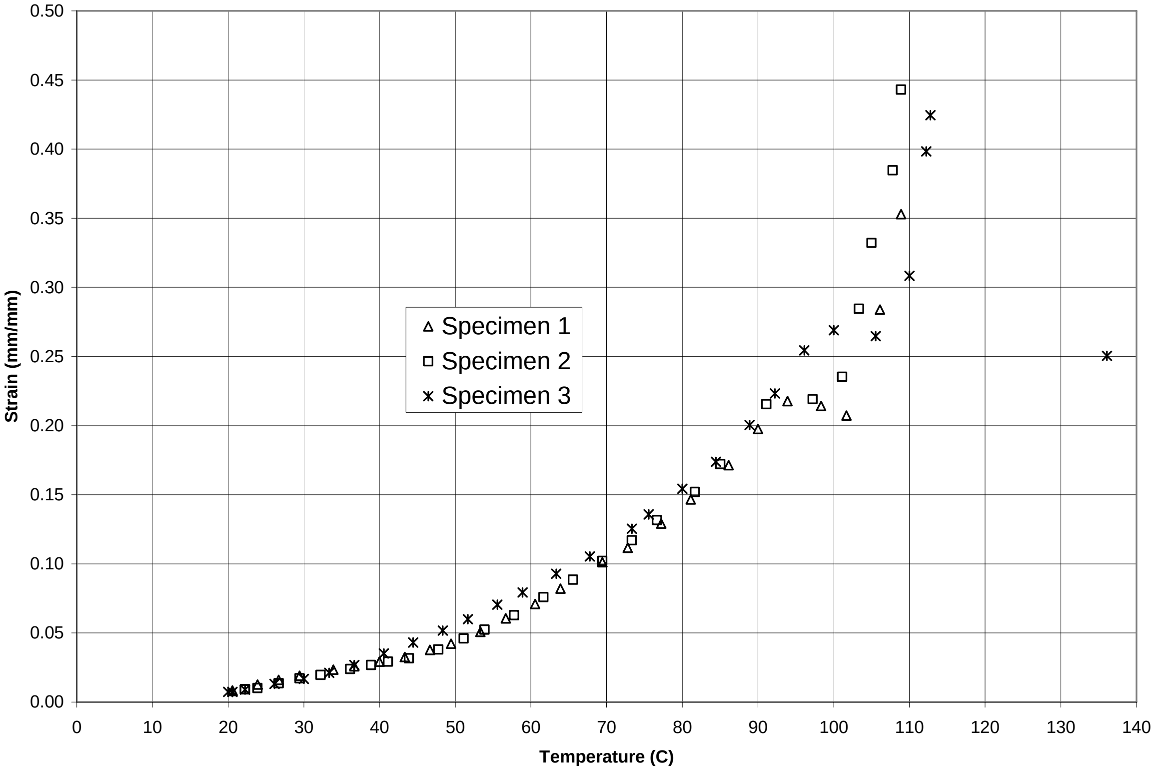

Figure 127. Strain versus temperature for the PE/Spectra configuration.

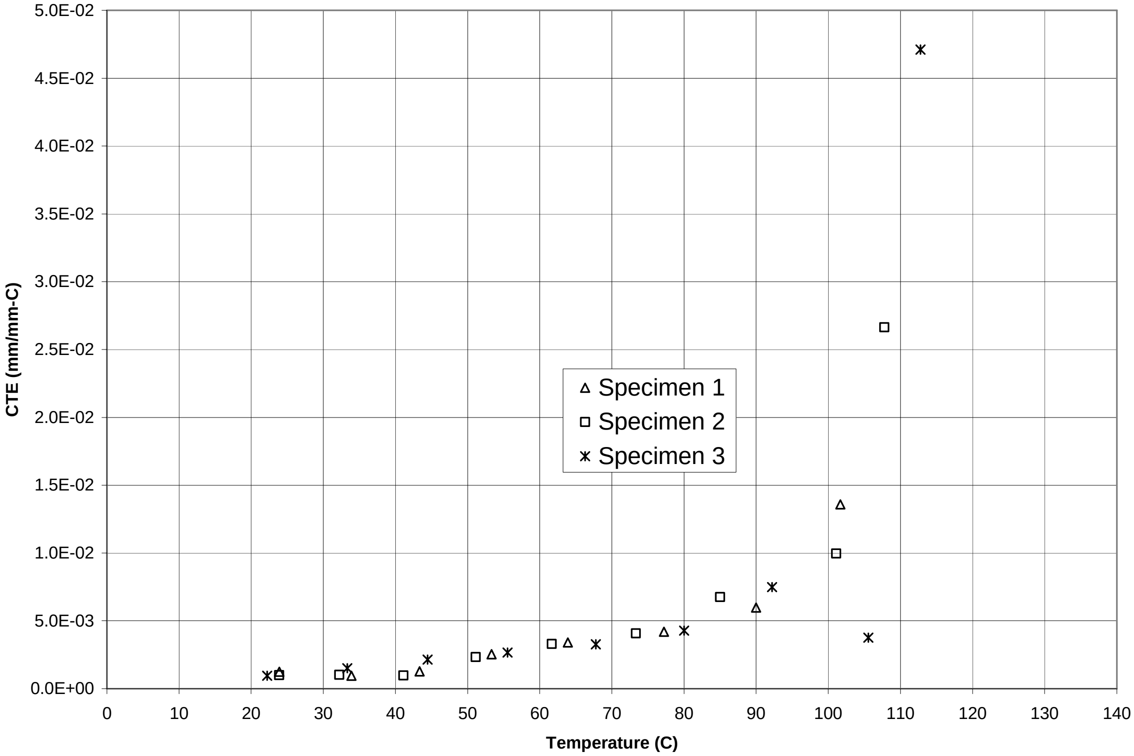

Figure128. CTE versus temperature for the PE/Spectra configuration.

Comparison of Figure 124 and Figure 127 reveals that the PE/Spectra and plain foam PE specimens displayed similar expansion behavior until approximately 80°C, with similar total strains of 0.15 mm/mm. This temperature corresponds to the approximate transition period from initial expansion to rapid expansion of the plain PE foam described in the previous section. During the start of the period of rapid expansion, it is clear from Figure 127 and Figure 128 that the facesheets and transverse reinforcement serve to significantly restrain foam expansion. In particular, a noticeable plateau of specimen strain can be observed in the temperature range of 90 to 105°C for all specimens.

Beyond approximately 100°C, Figure 127 and Figure 128 reveal a rapid increase in CTE and specimen expansion for the PE/Spectra specimens. This expansion ultimately led to a loss of data for all three specimens, with only specimen 3 eventually collapsing to the extent that it was visible once again at approximately 135°C. The more pronounced expansion of the PE/Spectra specimens can be explained in terms of the thermal breakdown of the Spectra facesheets and stitching. Note that the rapid expansion of the PE/Spectra specimens occurs in the same approximate temperature range in which the PE specimens began to transition from rapid expansion to foam failure. For the PE specimens, this indicated failure of the polymer to withstand the cell internal pressure due to reduction in material properties with temperature. Because Spectra is also a polyethylene product, it would also be expected to experience failure in this temperature range. As a result, the facesheets and stitching were no longer capable of restraining the expansion of the foam. Furthermore, as the facesheets continued to heat, they tended to bow in the middle which led to extensive rotation of the specimen mirror and thus the high expansion readings.

After the conclusion of the test, atmospheric pressure was reintroduced to the oven chamber, causing catastrophic collapse of the specimen, similar to that observed with the plain foam specimen. This is shown in Figure 129. Note that the warping of the specimen described above is particularly evident, and as a result no meaningful thickness measurement could be taken for comparison with the initial thickness of the specimen.

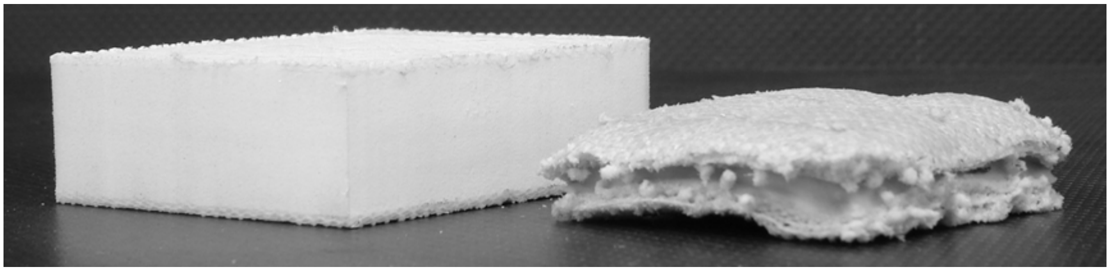

Figure 129. Representative PE/Spectra specimen before and after environmental testing.

9.8 PE/T300 Results and Discussion

Presented in Figure 130 and Figure 131 are plots of specimen strain and CTE as functions of temperature for the three 0.16 stitch/cm^2 PE/T300 specimens tested. The preceding section provided evidence that the introduction of facesheets and transverse reinforcement does serve to better constrain the pronounced expansion of the PE foam under consideration. The Spectra facesheets and reinforcement were limited in their effectiveness, however, because the material began to show significant signs of thermal degradation near 100°C. In order to examine the effects of transverse reinforcement at higher temperatures, a PE specimen with T300 carbon facesheets and 0.16 stitch/cm^2 Kevlar stitching was tested.

Comparison of Figure 124, Figure 127, and Figure 130 demonstrates that the introduction of T300 facesheets and Kevlar stitching causes a pronounced decrease in the amount of expansion versus the PE and PE/Spectra configurations. The PE and PE/Spectra configurations both had exceeded a strain of 0.10 mm/mm by a temperature of 70°C. However the PE/T300 specimens never exceeded a total strain of 0.09 mm/mm over the course of the entire test. Similarly, Figure 131 shows that the CTE of the PE/T300 configuration remains relatively constant up to the point of foam collapse, in contrast to the dramatic increases in CTE witnessed for the PE and PE/Spectra configurations near 100°C.

Further evidence of the influence of vertical stitching can be seen in Figure 132, which shows the specimen during testing at approximately 100°C. Of particular interest in the figure is the expansion of the foam core from the sides of the composite, which results from the constraint against expansion in the specimen thickness. The better performance of the PE/T300 configuration is attributed to the better thermal stability of the carbon facesheets and Kevlar reinforcement.

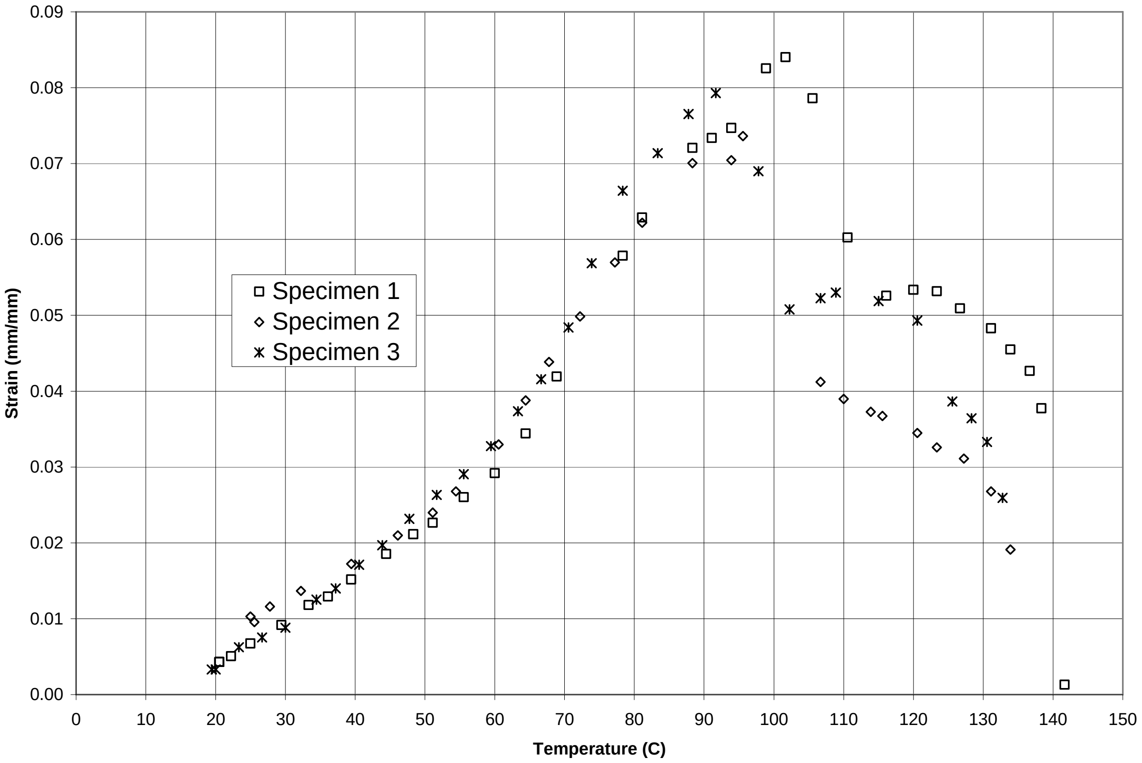

Figure 130. Strain versus temperature for the PE/T300 configuration.

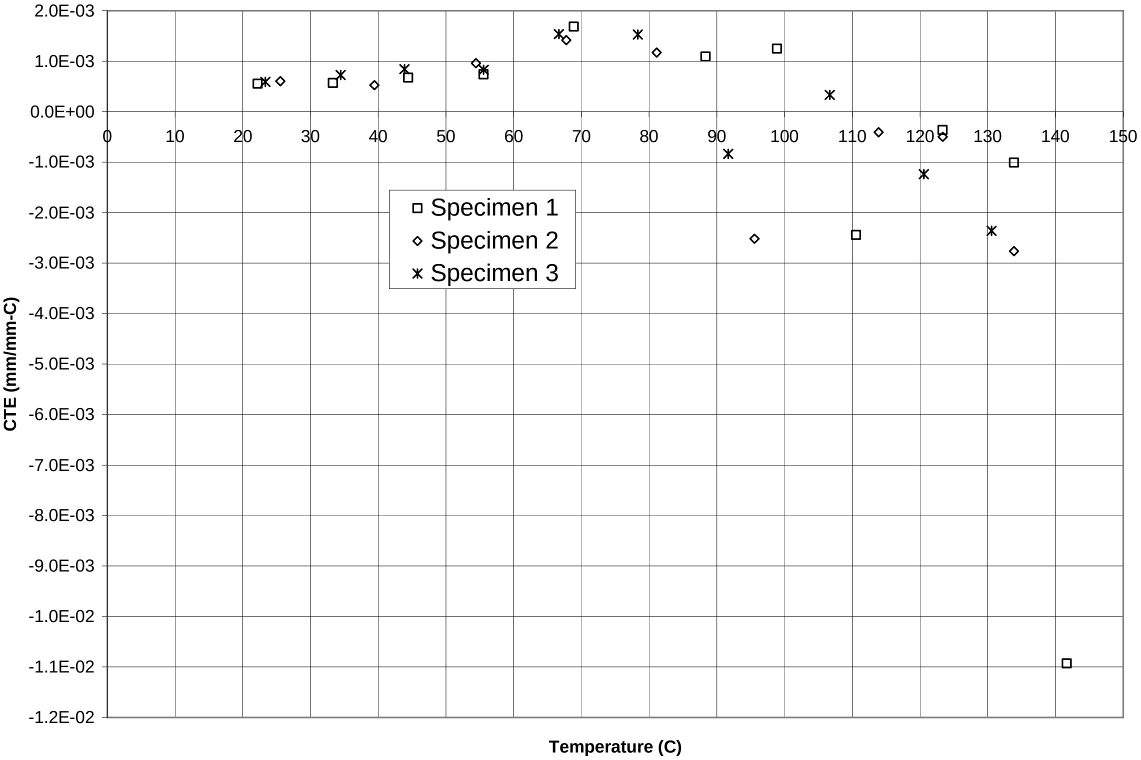

Figure 131. CTE versus temperature for the PE/T300 configuration.

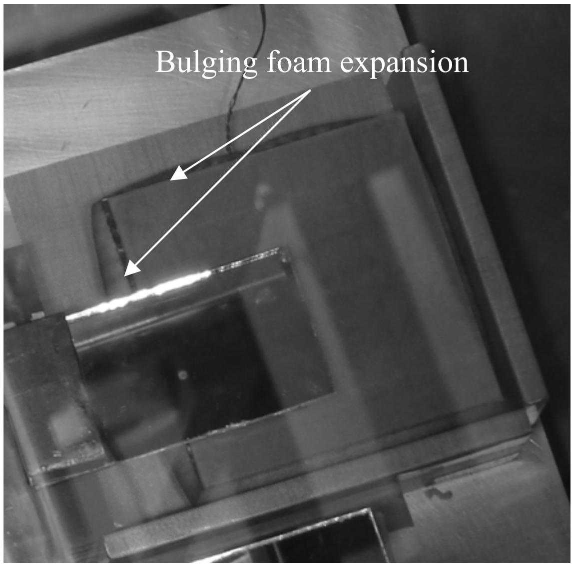

Figure 132. Representative PE-T300 specimen showing core expansion.

Near 100°C, all three specimens began to shrink, as witnessed with both previous PE configurations. As shown in Figure 130, the process of foam collapse above 100°C can be broken into three sections. The initial section shows pronounced rapid collapse associated with failure of the foam from internal pressure loading of the cells and the external pressure exerted by the facesheets and transverse reinforcement. Beyond that initial collapse, the specimens had a tendency to plateau. This can be explained in terms of the stiffness of the infiltrated Kevlar stitching and the bond between the PE and carbon facesheets. Because of the bond between the foam core and facesheets, as the PE begins to shrink the Kevlar stitching experiences compressive loading, which is initially low in magnitude. As the foam continues to collapse, however, the compressive load exceeds that which can be tolerated by the infiltrated Kevlar stitches, resulting in buckling or debonding from the facesheets. Once either scenario has occurred, the specimen can continue to shrink with little resistance.

The unrestrained collapse of the specimen is particularly evident after atmospheric pressure is reapplied following the conclusion of the test as demonstrated in Figure 133, which shows a PE/T300 specimen before and after testing. Notice that neither the vertical stitching nor the facesheet appeared to suffer thermal damage; however, the configuration still showed dramatic collapse due to the inability of the stitches to handle the compressive loading resultant from core shrinkage. As described previously, no meaningful thickness measurement could be taken after the test was concluded for comparison with the initial thickness due to warping of the specimen.

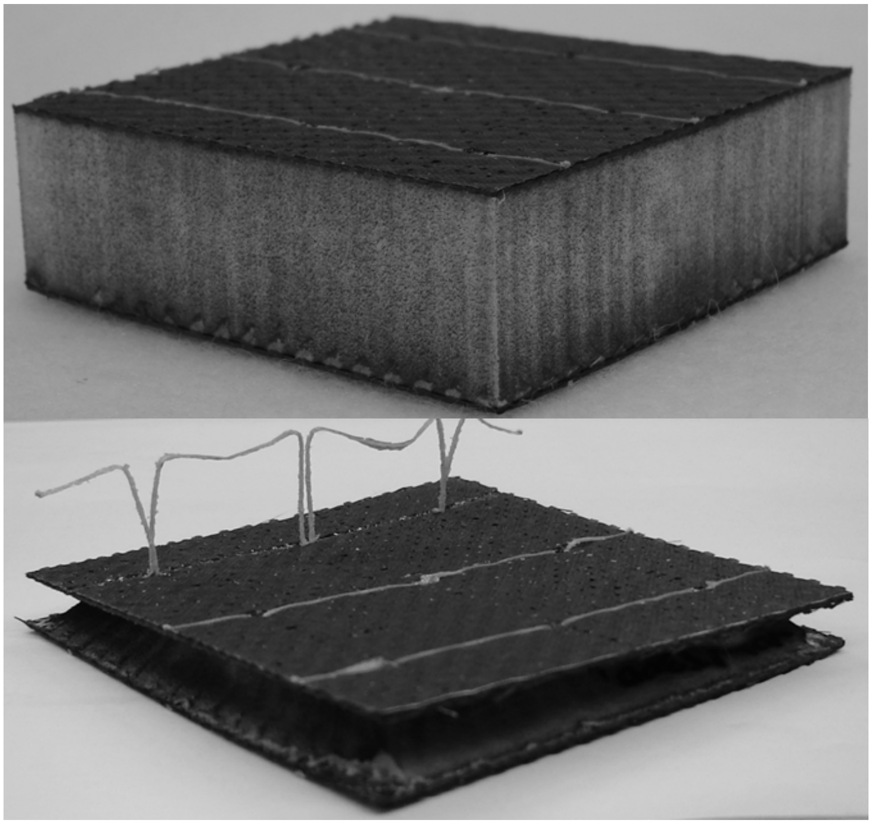

Figure 133. Representative PE/T300 specimen before and after environmental testing.

9.9 PET Foam Results and Discussion

Figure 134 and Figure 135 show the specimen strain and CTE as functions of temperature for the three plain PET foam specimens tested. These results show that the PET specimen configuration follows some of the general trends of the PE configuration shown in Figure 124. In particular, the foam expansion is characterized by low initial values of CTE followed by a large increase. The CTE then drops and the expansion begins to level-off near the maximum testing temperature of 135°C. The overall strain of the PET specimen configuration is significantly less than that of the PE configuration, however, with the maximum value observed for PET configuration being nearly seven times below the maximum of the best PE configuration specimen. As further evidence of the improved performance of the PET specimen, consider that the ultimate strain observed is appreciably lower than that of even the PE/T300 reinforced configuration.

Returning to the comparison in general behavior with the PE configuration, it is believed that the PET specimen would eventually experience foam cell rupture and collapse in a manner analogous to the PE configuration, though limitations of the test equipment prevented this from being demonstrated. The pronounced reduction in CTE near the final testing temperature of 135°C, however, does provide indication that the PET foam would be expected to begin showing signs of cell rupture and collapse shortly thereafter.

The final data point for specimen 3 in Figure 134 (134°C, 0.043mm/mm) was recorded following the reintroduction of atmospheric pressure while the specimen was still heated. As would be expected due to the added external pressure, the specimen reduced in size. It is noteworthy, however, that the specimen did not display catastrophic collapse or warping, but rather retained dimensions similar to those measured initially. This same general behavior was observed for all PET specimens, and is demonstrated in Figure 136. The average final specimen thickness after returning to ambient conditions was approximately 1.5% larger than its initial value.

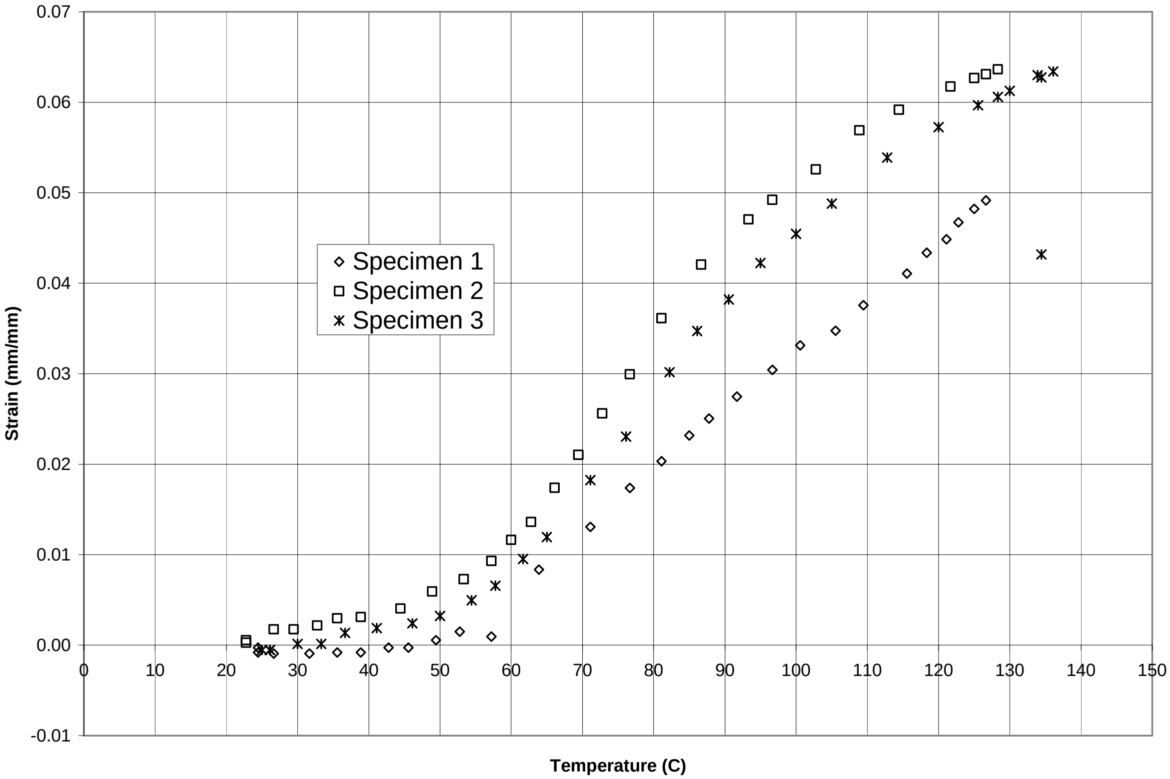

Figure 134. Strain versus temperature for the PET configuration.

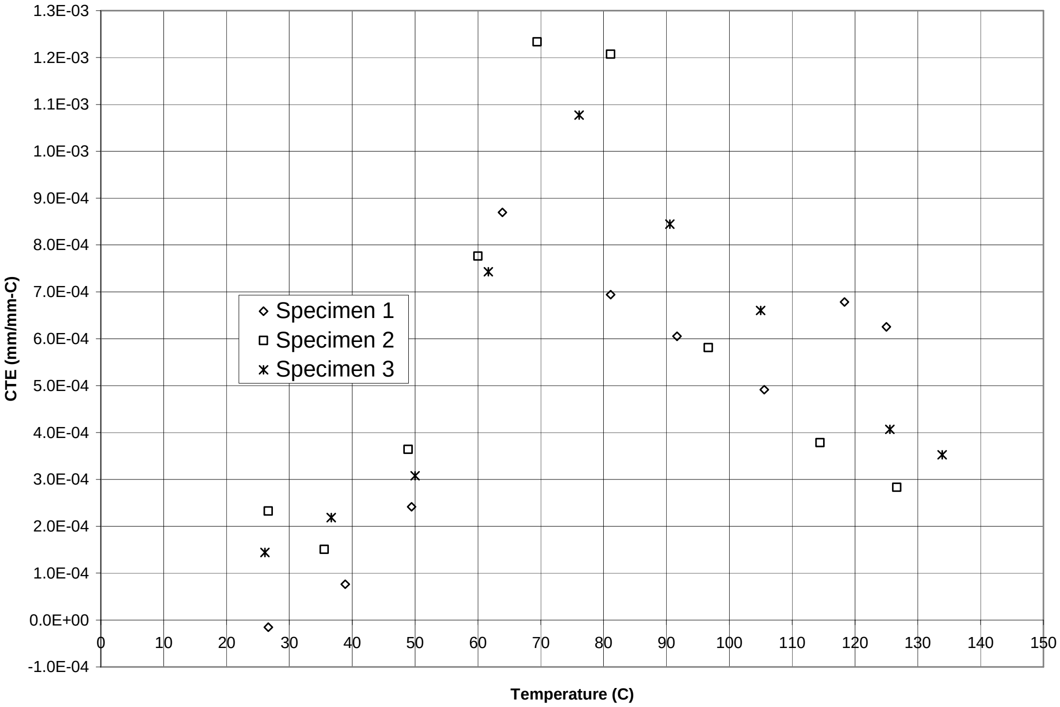

Figure 135. CTE versus temperature for the PET configuration.

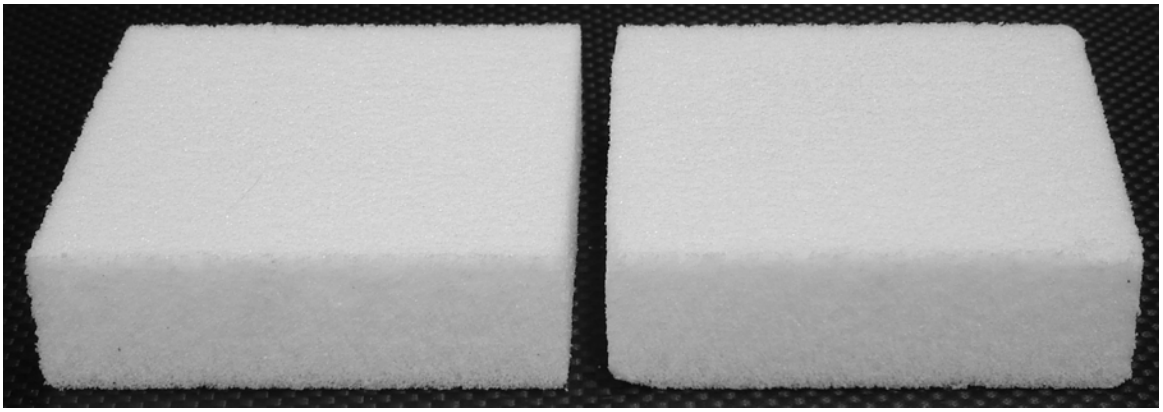

Figure 136. Representative PET specimen before and after environmental testing.

9.10 PET/Spectra Results and Discussion

Figure 137 and Figure 138 show the specimen strain and CTE as functions of temperature for the three 0.16 stitch/cm^2 PET/Spectra specimens tested. As with the PE configurations, comparison between the PET/Spectra and the plain PET foam specimen provides a means to assess the influence of facesheets and vertical stitching on foam expansion. As shown in Figure 137, the PET/Spectra configuration actually increased in thickness with temperature at a rate greater than that of the plain foam, which is particularly evident beyond 100°C. Note that this was the same temperature noted in Section 9.7 with regard to pronounced increase in expansion and CTE of the PE/Spectra configuration. The last recorded data for all specimens is near 120°C because the expansion of the PET/Spectra specimens ultimately exceeded the measurement range at that point.

In general, these results were expected based upon the behavior observed for the PE/Spectra configuration: the expansion and warping of the Spectra facesheets led to increased measurements of specimen expansion. The change in a typical PET/Spectra specimen over the course of the test is shown in Figure 139. As can be seen in the figure, the facesheet displayed noticeable warping and ultimately peeled away from the PET core near the edges. The deformation of the facesheets also induced a bending moment on the PET core, which is evident in the figure. As a final note, a comparison of Figure 134 and Figure 137 suggests that the introduction of stitching through the foam core has little effect on the nature of the expansion below 70°C.

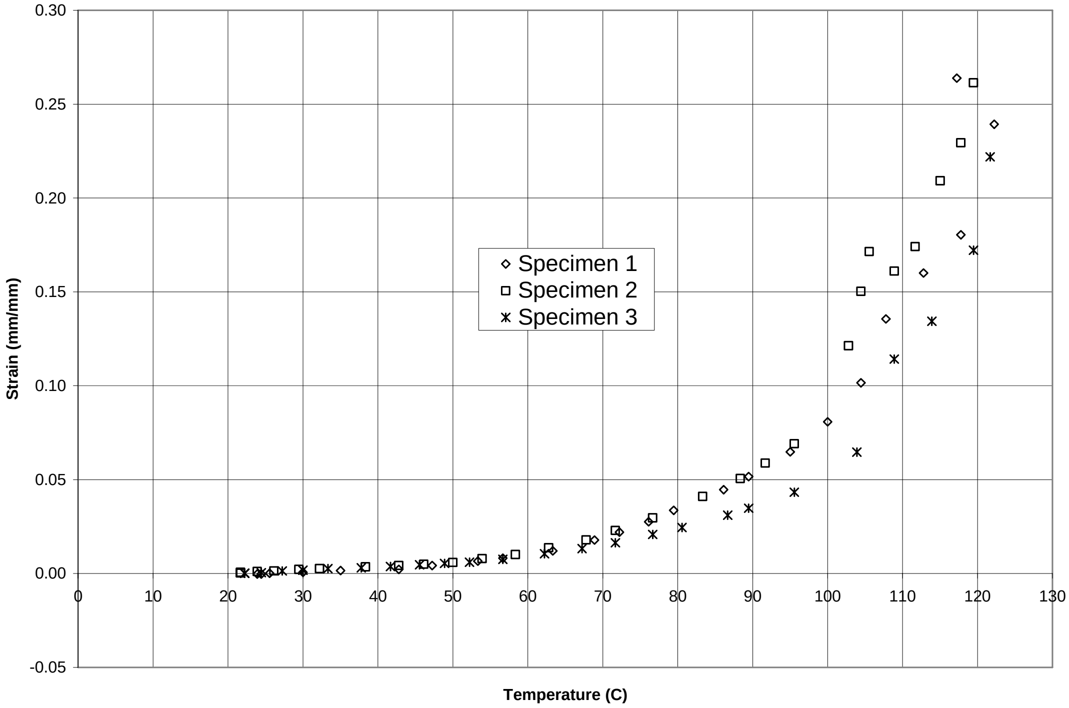

Figure 137. Strain versus temperature for the PET/Spectra configuration.

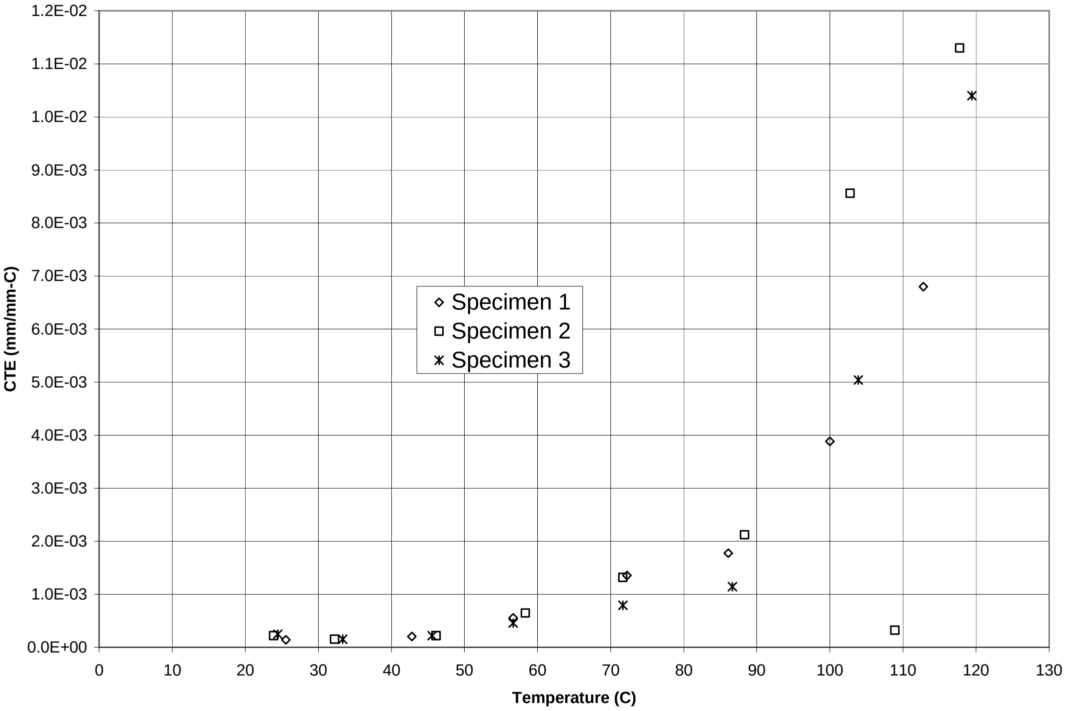

Figure 138. CTE versus temperature for the PET/Spectra configuration.

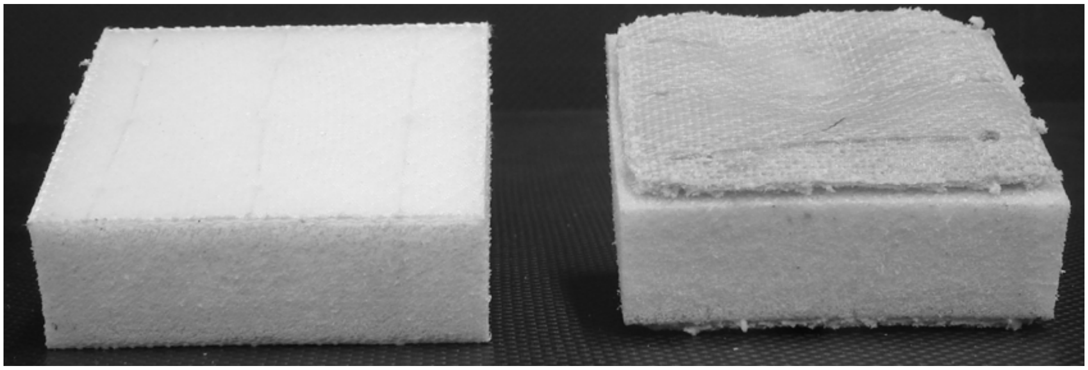

Figure 139. Representative PET/Spectra specimen before and after environmental testing.

9.11 PET/T300 Results and Discussion

Figure 140 and Figure 141 show the specimen strain and CTE as functions of temperature for the three 0.16 stitch/cm^2 PET/T300 specimens tested. As discussed in Section 9.10, the introduction of transverse reinforcement with the PET/Spectra configuration did little to constrain foam expansion. In order to examine the effects of transverse reinforcement at higher temperatures and greater strain, PET specimens with T300 carbon facesheets and Kevlar stitching were tested.

Comparison of Figure 140 and Figure 141 with Figure 134 and Figure 135 reveals the same general trends in terms of variation in expansion and CTE with temperature for the PET/T300 and plain PET configurations. In each case, however, the introduction of Kevlar stitching and carbon facesheets serves to reduce the amount of expansion, though not dramatically. This result can be explained by the relatively low expansion of the PET configuration as discussed in Section 9.10. The PET/T300 configuration does show pronounced improvement over the PET/Spectra configuration, and is attributed to the better thermal stability of the carbon facesheets and Kevlar reinforcement.

Upon reintroduction of external atmospheric pressure, the foam core and facesheets displayed no warping discernible to the naked eye, in sharp contrast with the PE and PET/Spectra configurations. Measurements taken on the specimens following their return to ambient conditions revealed an average overall increase in thickness of less than 0.5%. The excellent stability of the configuration can be further observed from Figure 142, which shows a representative specimen before and after testing.

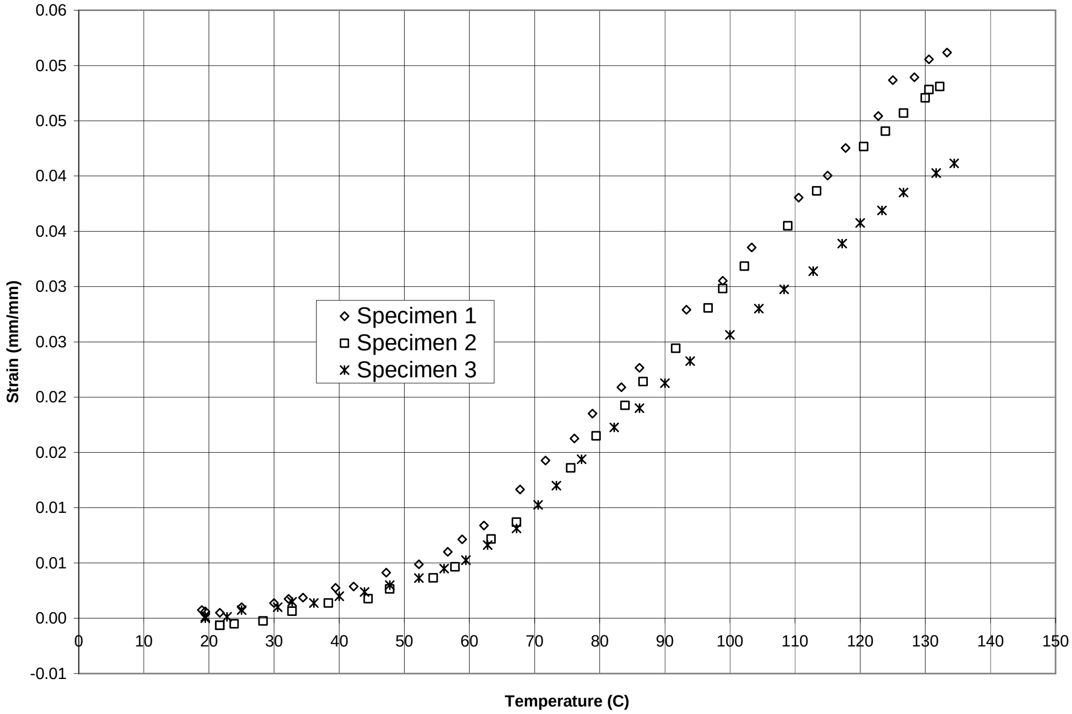

Figure 140. Strain versus temperature for the PET/T300 configuration.

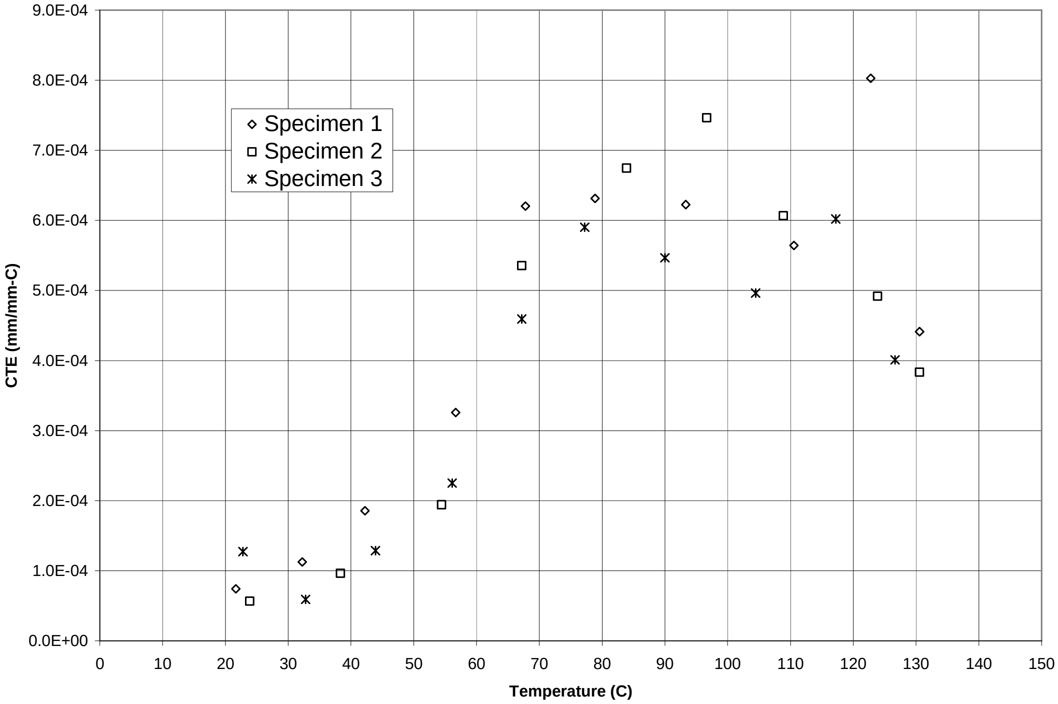

Figure 141. CTE versus temperature for the PET/T300 configuration.

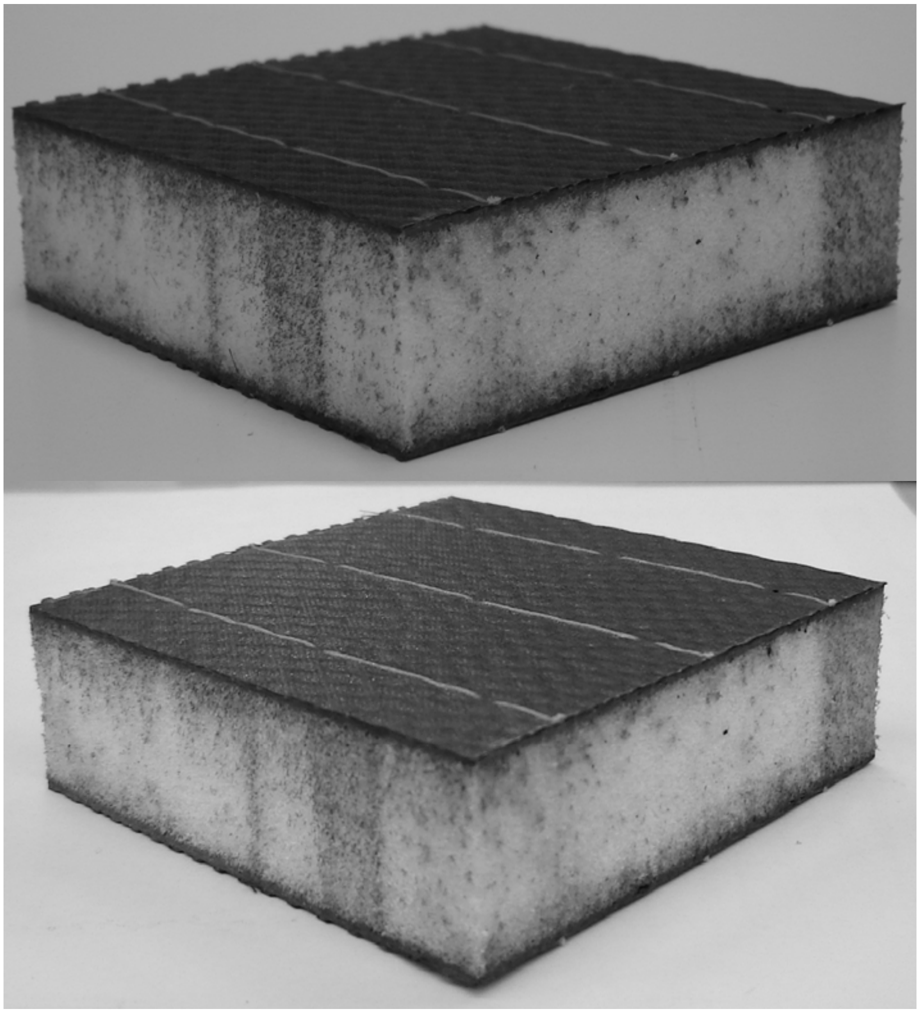

Figure 142. Representative PET/T300 specimen before and after environmental testing.

9.12. Overall Results and Discussion

Figure 143 and Figure 144 present a comparison of representative strain versus temperature and CTE versus temperature plots for all six tested configurations. The two plots highlight the overall greater expansion and CTE of the PE configurations, as well as the excellent behavior of the PET/T300 configuration, which successfully provides the desired constraint against out-of-plane expansion.

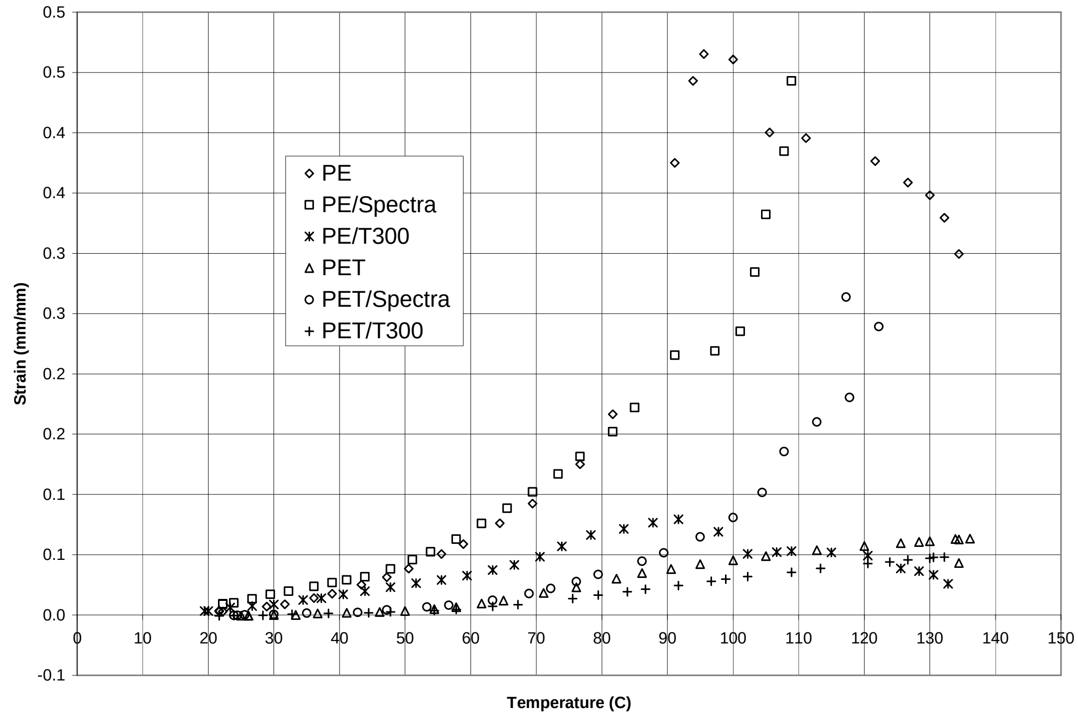

Figure 143. Representative strain versus temperature plots for all six configurations.

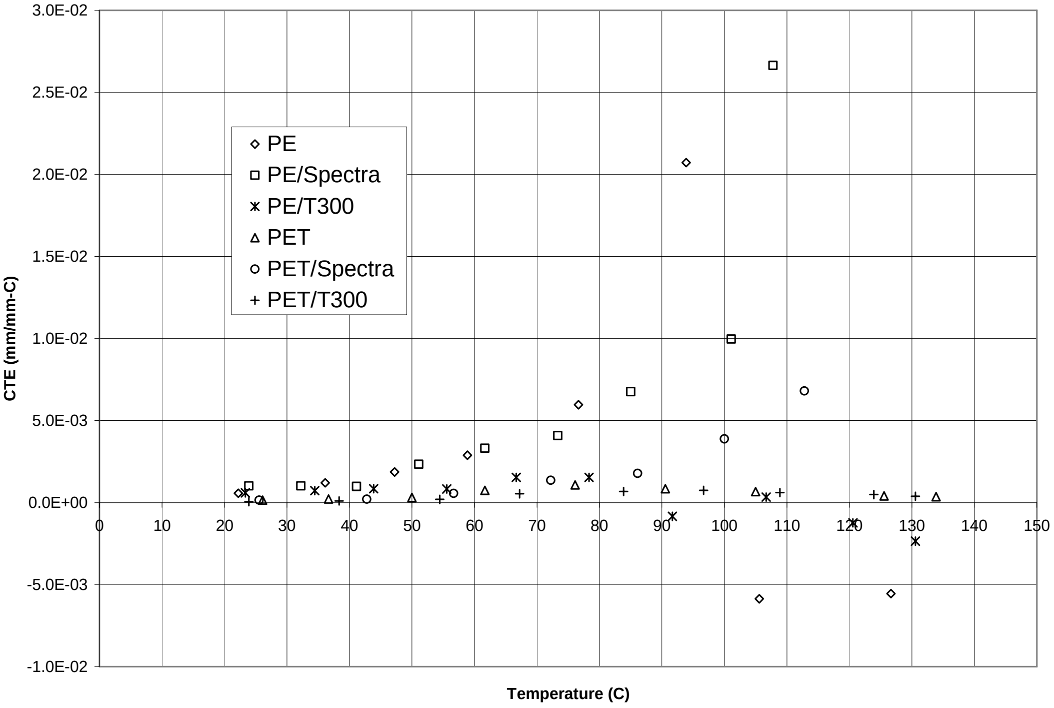

Figure 144. Representative CTE versus temperature plots for all six configurations.

10. FOAM ENVIRONMENTAL RESPONSE MODELING

10.1 - Model Background and Development

Based upon the results described in Chapter 9, a model was desired to predict the thermal expansion of a closed-cell foam in a vacuum environment as a function of temperature. Over relatively low temperatures, the coefficient of thermal expansion (CTE) of the foam was shown to be relatively small, but increasing with temperature. At some elevated temperature, the CTE of the foam experiences a dramatic increase over a limited temperature range. After the period of rapid expansion, foam failure occurs, characterized by cell rupture and collapse. Within this general response, however, there can be a pronounced difference in the magnitude of CTE observed, the temperature ranges over which the periods of initial expansion, rapid expansion and collapse occur, and the extent to which each period occurs. Such differences were evident when comparing the response of the PE and PET configurations, as discussed in Chapter 9.

As outlined in Chapter 2, significant research has focused on understanding the performance of foams during heating for manufacturing and processing purposes. Some general rules developed for the thermal expansion of PE foam, which has been the focus of extensive research [24], include that the CTE: (1) varies over the range of 0 to 40°C only slightly: (2) is approximately equal to that of the base polymer for densities greater than 80 kg/m^3; (3) is inversely related to the tensile modulus; and (4) can be dependent upon cell structure, including anisotropy.

Several different models have been proposed in the literature to predict the thermal expansion of polymeric foams. The models vary in complexity from simple strutless membrane and membraneless strut models [25] to more advanced considerations such as a regular Kelvin foam model [26]. The research completed to date, however, has only considered thermal expansion at normal atmospheric pressure. No extension has been made to consider the behavior of foam within a vacuum, which would increase the role of gas expansion that has already been shown to be significant under atmospheric conditions [22].

Comparing the general conclusions described above for thermal expansion of PE foam with the results outlined in Chapter 9 reveals that conclusions (1), (3) and (4) appear to be unchanged. The two foam configurations examined did show little change in CTE over the tested range of 20°C to 40°C, and the added influence of a vacuum would not be expected to remove the dependence of foam response upon material properties and cellular structure. The second conclusion, however, is clearly invalid for thermal expansion in a vacuum environment. The PE foam configuration tested had an average CTE of 750 μm/m-°C at 20°C whereas a typical value for CTE of film grade LDPE (the type of resin used in the foaming process) is listed as less than 230 μm/m-°C at 20°C [63]. Furthermore, the foam CTE was shown to increase dramatically over the tested temperature range, furthering the disparity between the foam and resin value.

Due to the notable departure from typical foam expansion under atmospheric conditions, it was of interest to develop a relatively simple model to predict the thermal expansion of foam in a vacuum. The proposed model would be capable of predicting actual expansion values and identifying the transition between periods of initial expansion, rapid expansion and cell collapse.

Because the foam expansion observed during environmental testing greatly exceeded that of the base polymer, it was assumed that the thermal expansion of the struts within the cellular structure was negligible compared to the expansion of the cell walls (membranes) that resulted from internal pressure loading and polymer softening with temperature. The model found in the literature that best matched these conditions was a strutless membrane model [25]. This model, however, used an equation for the deflection of a circular plate based upon the Kirchhoff hypothesis [64] to predict the deflection of cell membranes, and hence the overall expansion of the foam. Due to the use of the Kirchhoff hypotheseis, it was believed that the model would not appropriately describe the large-scale expansion of the cell membranes under vacuum heating. For this reason, a new model was proposed that idealized the foam as a collection of spherical cells, with empty interstitial spaces. This model retains the membrane dominated expansion, while removing the limitation of small deflections.

Considering a sphere under internal pressure loading, the in-plane principal stresses σ_1 and σ_2 in the wall (membrane) are given by [65]

$$\sigma_1 = \sigma_2 = \frac{pr}{2\delta} \quad , \tag{12}$$

where p is the applied pressure, r is the radius of the sphere, and δ is the thickness of the cell membrane. The radial expansion u_r of a sphere under uniform displacement from internal pressure loading can be calculated from the in-plane membrane stress as [66]

$$u_r = \frac{\sigma_1 r(1-\nu)}{E} \quad , \tag{13}$$

in which ν is Poisson's ratio and E is the tensile modulus of elasticity.

In order to account for total foam expansion, the result for radial displacement of one cell must be doubled to account of the expansion of the cell diameter, and then multiplied by the number of cells in the thickness of the foam. The appropriate factor is given by

$$N = \frac{L}{r} \quad , \tag{14}$$

where L is the thickness of the foam in the direction of interest and r is the radius of each cell as defined previously.

The total strain of the foam specimen ε_{foam} can be found from Hooke's law for the case where $\sigma_1 = \sigma_2$ as

$$\varepsilon_{foam} = \frac{\sigma_1(1-\nu)}{E} \quad . \tag{15}$$

The variation of the pressure within each cell can be related to the change in temperature of the gas and volume of the cell through the ideal gas law [67] as

$$p_2 = p_1\left(\frac{V_1}{V_2}\right)\left(\frac{T_2}{T_1}\right) \quad , \tag{16}$$

where p is the cell gas pressure in Pascals, V is the volume of the cell in cubic meters and T is the temperature of the gas in degrees Kelvin. The subscript "1" refers to the initial state and the subscript "2" to the final state.

To use the model to predict thermal expansion, an iterative approach using a MATLAB script was implemented. Using this method, an initial pressure was applied based upon the vacuum pressure obtained using the vacuum oven as discussed in Section 9.2. This pressure was used to calculate an initial stress in the cell membranes, and a corresponding amount of deflection and specimen strain, using Equations 12-15. The temperature applied to the specimen was then raised slightly, and the pressure in the cell was recalculated based upon the amount of expansion and temperature change using Equation (16). The process was then repeated with the new pressure. Rapid expansion of the foam was detected by comparing the principal stress in the cell membrane to the yield stress of the foam resin (base polymer) at the relevant temperature. When the principal stress was equal to the yield stress, the value of tensile modulus was reduced to allow relatively uninhibited expansion of the cell membrane.

In order to examine the accuracy of the selected model under vacuum conditions, additional environmental testing was performed using PE foams with a range of densities. The results of this testing are presented in Section 10.2. Section 10.3 and Section 10.4 provide a detailed discussion of the methodology used to obtain the foam cellular structure and resin properties needed to complete the analyses described above. In particular, measurements of cell size and wall thickness were obtained as well as the temperature-dependent tensile yield strength and tensile modulus of the PE foam resin.

10.2 - Environmental Testing

Testing was performed on four different densities of Voltek L series PE foam, as listed in Table 21. Three specimens were tested at each density; however, since three specimens of the mid-high density foam had already been tested for the results presented in Chapter 9, no further experimentation of this foam density was performed. The foam materials were machined to a thickness of 21 mm to correspond with the thickness used in all previous testing. Testing was performed using the procedure outlined in Section 9.5.

Table 21. Specimen Configurations Used for Environmental Response Modeling

Configuration	**Average Core Density (kg/m^3)**	**Density Standard Deviation (kg/m^3)**	**Density Coefficient of Variation (%)**
Low Density	20.5	3.07	15.0
Mid-Low Density	51.5	0.06	0.12
Mid-High Density	127	0.87	0.68
High Density	208	0.75	0.36

10.2.1 Low-Density Foam Results and Discussion

Figure 145 and Figure 146 show the specimen strain and CTE as functions of temperature for the three low-density (20.5 kg/m^3) PE foam specimens tested. The most noticeable aspect of the low density PE foam is the pronounced early foam failure and minimal positive strain with relatively constant CTE prior to that point. Both specimens 1 and 2 demonstrated foam failure by a temperature of 60°C, followed by rapid contraction. Specimen 3 did not experience failure until nearly 70°C, and this can be explained in part by the higher density of the foam. As shown in Table 21, the density of the low-density foam samples was highly variable, due primarily to specimen 3 which had a density of 23.9 kg/m^3, though it was taken from the same location on the foam panel as specimens 1 and 2.

Note that the tests were concluded prior to 90°C because the specimen thickness had decreased below the point of measurability. Despite this relatively low temperature, significant collapse of the specimens was observed when they were subjected to atmospheric pressure following the conclusion of the test. This behavior is illustrated in Figure 147. Note that no meaningful dimensional data could be obtained following the test due to extreme collapse and warping of the specimen.

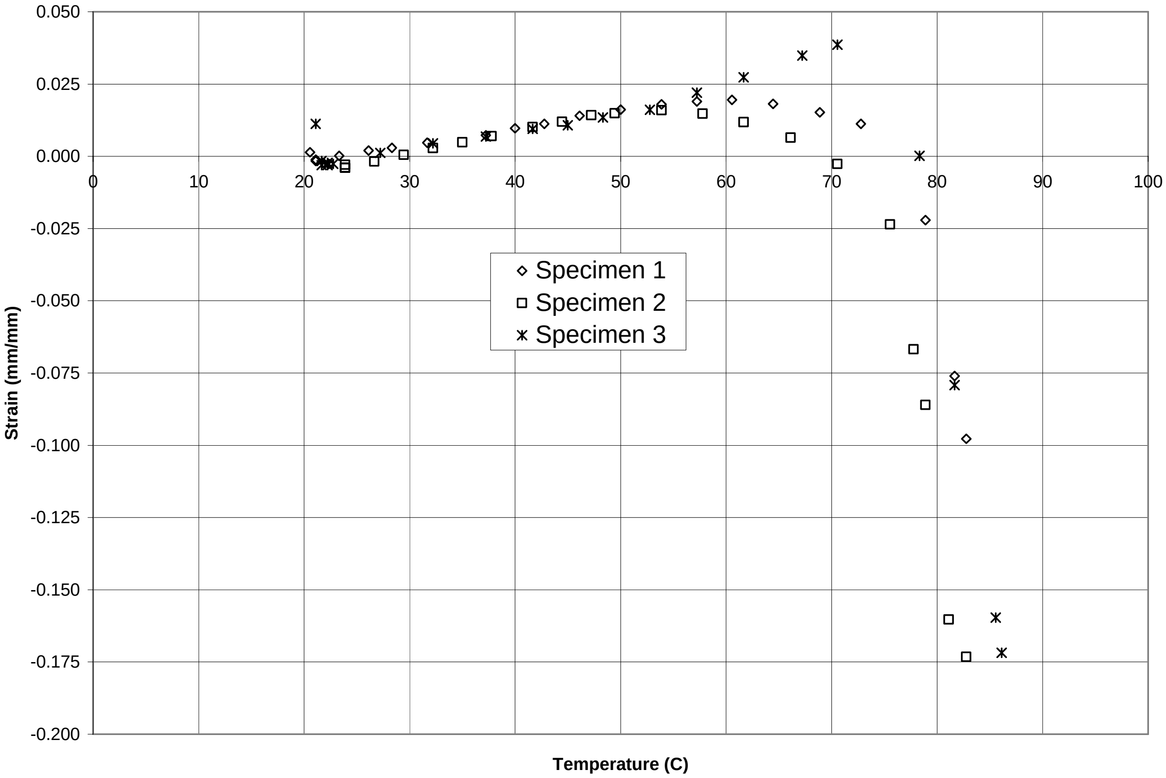

Figure 145. Strain versus temperature for low density PE foam.

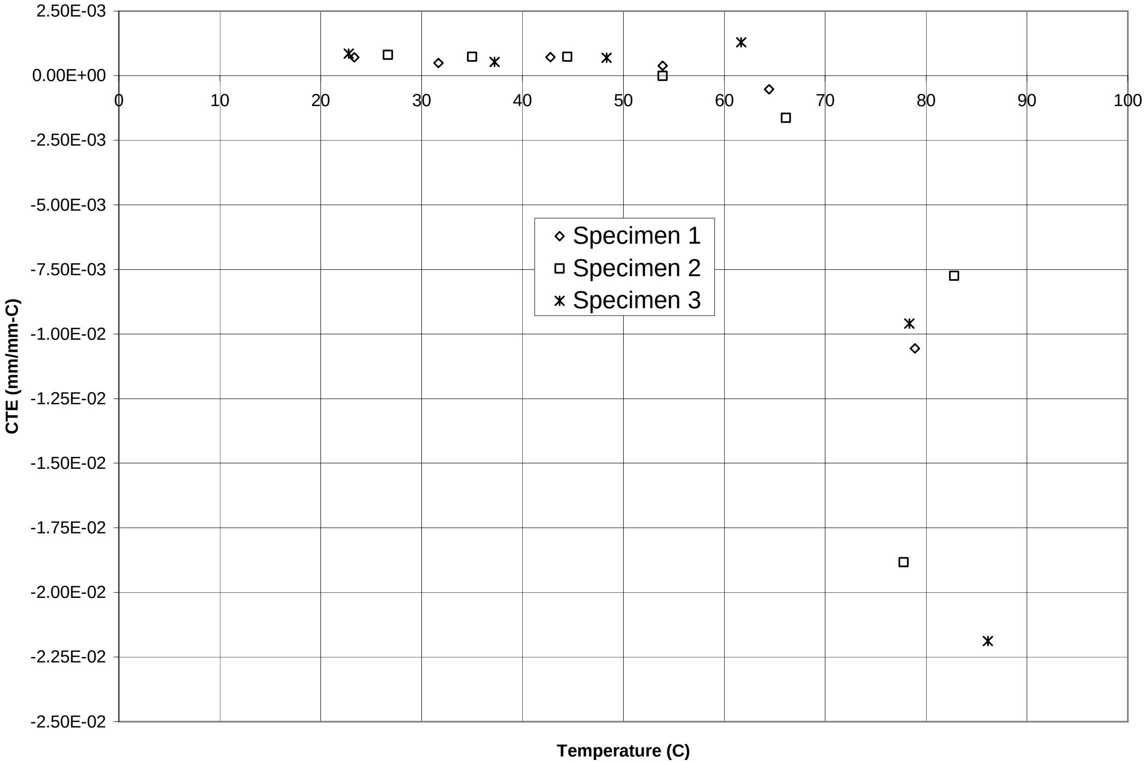

Figure 146. CTE versus temperature plot for low density PE foam.

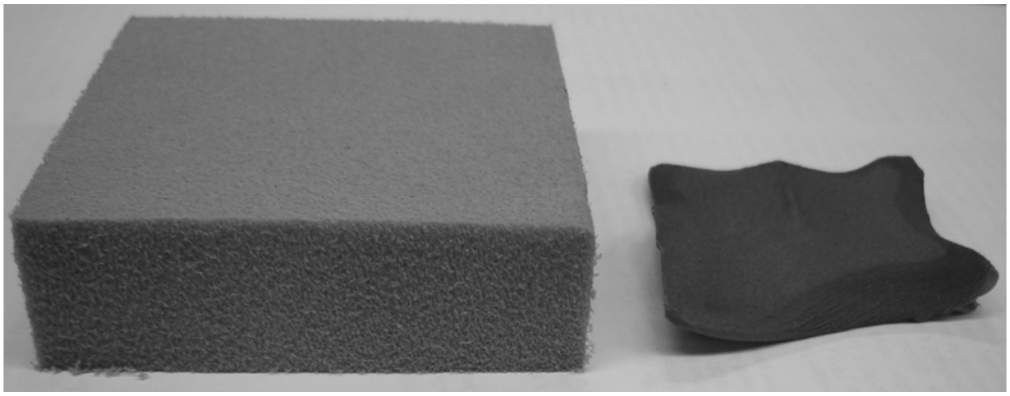

Figure 147. Representative low-density PE foam specimen before and after environmental testing.

10.2.2 Mid-Low Density Foam Results and Discussion

Figure 148 and Figure 149 show specimen strain and CTE as functions of temperature for the three mid-low density (51.5 kg/m^3) PE foam specimens tested. Apparent from these figures is the early and pronounced expansion and increase in CTE for the mid-low density PE. In sharp contrast to the low density configuration, the specimen could no longer be measured after a temperature of only 70°C due the level of expansion. The expansion eventually reached a point that the specimen mirror tipped backward such that no further data could be collected beyond approximately 90°C. Visual inspection of the specimen was used instead to determine an approximate range of temperature at which foam failure could be observed. This was estimated at approximately 110°C. A time sequence showing continued foam expansion and ultimate collapse from the time that the mirror fell off the specimen is provided in Figure 150.

A pronounced collapse was observed once the foam was subjected to atmospheric pressure following the conclusion of the test. As shown in Figure 151 the collapse was significantly less than that of the low density PE foam, but the warping present still prevented any accurate measurements of size from being taken.

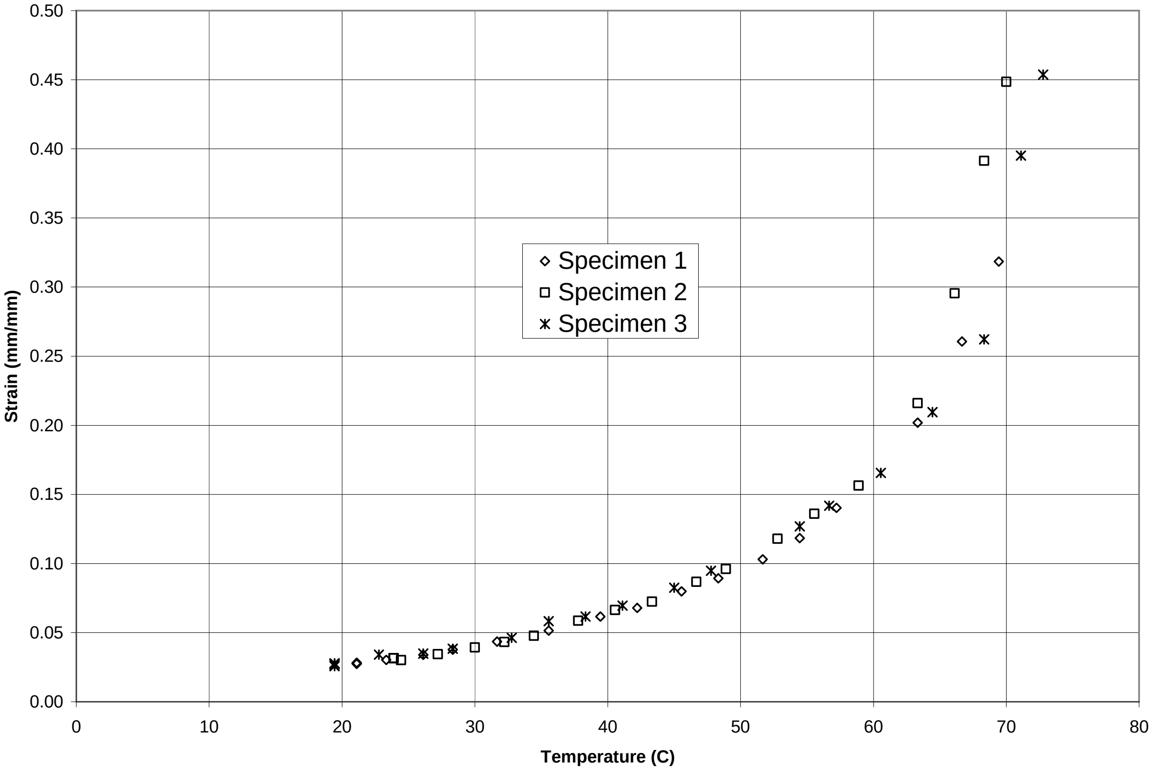

Figure 148. Strain versus temperature for mid-low density PE foam.

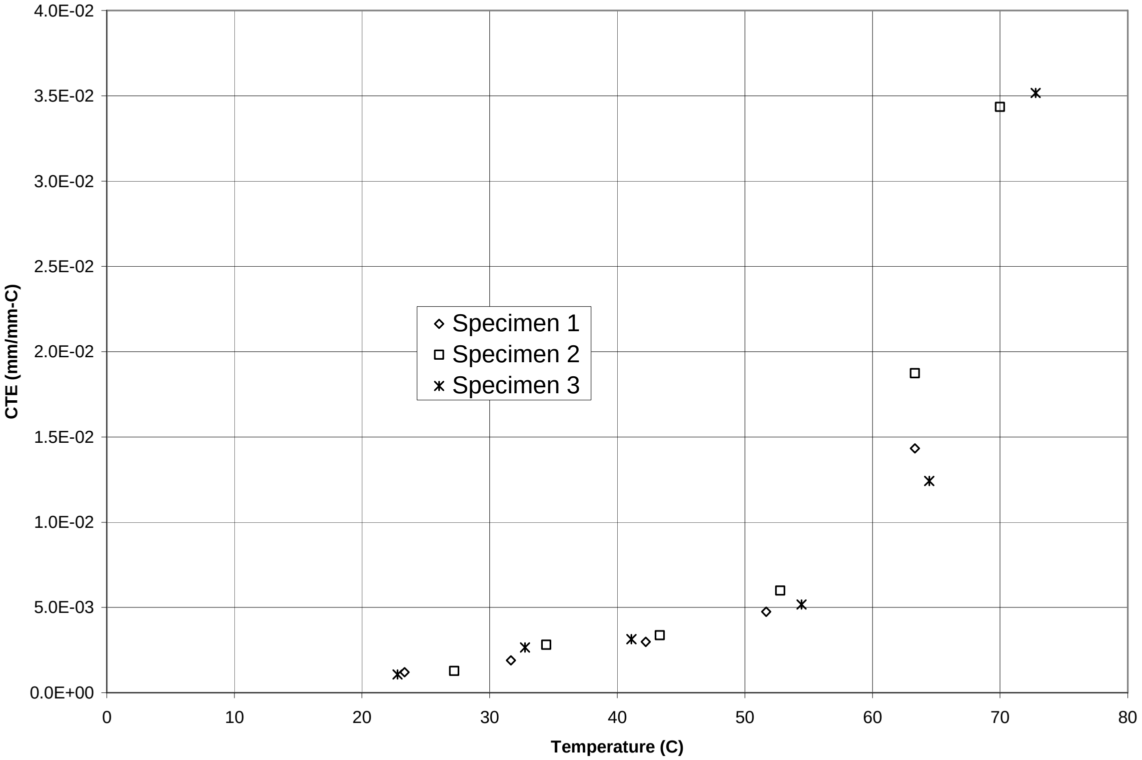

Figure 149. CTE versus temperature for mid-low density PE foam.

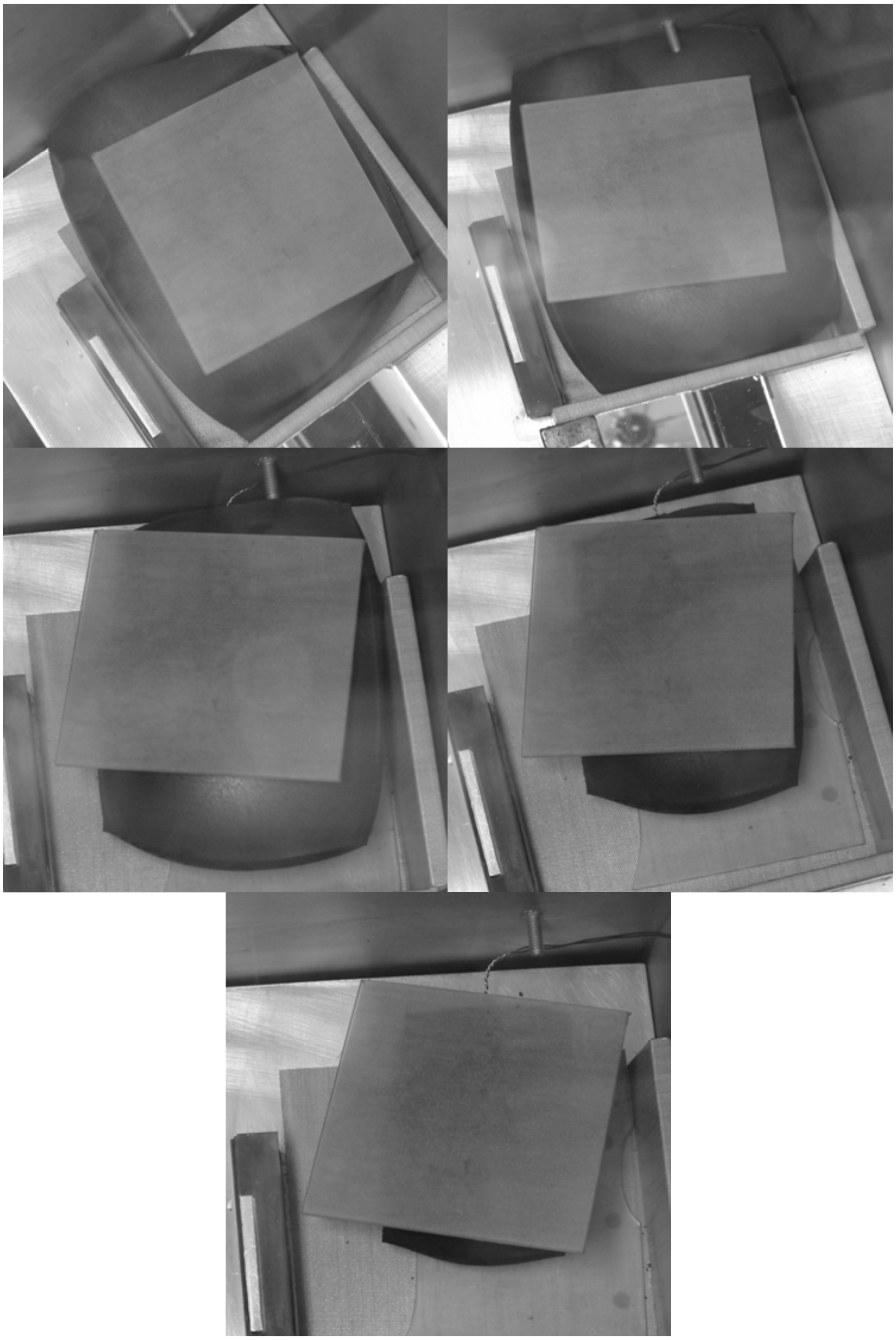

Figure 150. Time series of photographs depicting mid-low density PE behavior at: (A) 93°C, (B) 107°C, (C) 121°C, (D) 127°C, and (E) 131°C

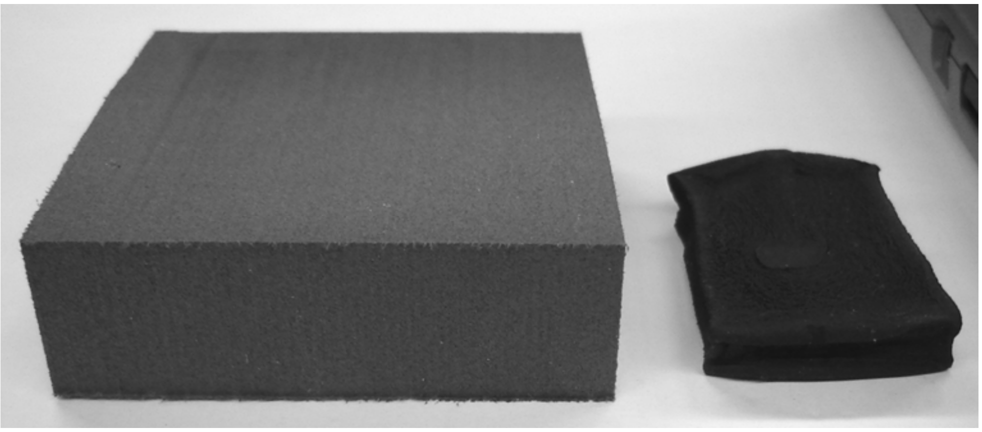

Figure 151. Representative configuration 2 (mid-low) specimen before and after environmental testing.

10.2.3. Mid-High Density Foam Results and Discussion

Figure 152 and Figure 153 show the specimen strain and CTE as functions of temperature for the three mid-high density (127 kg/m^3) PE foam specimens tested. These plots are repeated from Section 9.6 for convenience. Though originally discussed in Section 9.6, some new information can be presented for the mid-high density PE configuration. In particular, it is evident from comparing Figure 152 and Figure 153 with Figure 148 and Figure 149 that the mid-high and mid-low density PE configurations display the same general behavior, but with the mid-high density PE experiencing lower expansion at a given temperature. This result is particularly evident from the first data point where the vacuum alone causes an initial expansion of the mid-low density PE that is not equaled by the expansion of the mid-high density PE until a temperature of approximately 40°C. Also apparent is that both configurations begin to display foam collapse in the same 100°C to 110°C temperature range.

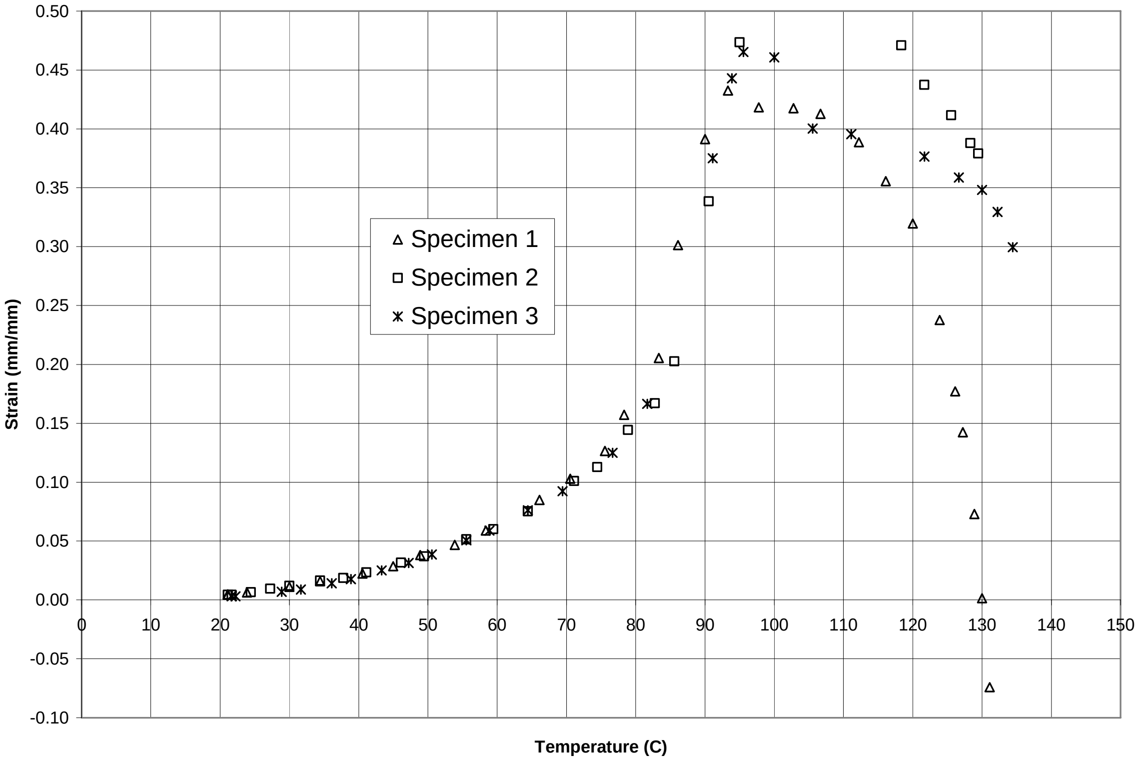

Figure 152. Strain versus temperature plot for mid-high density PE foam.

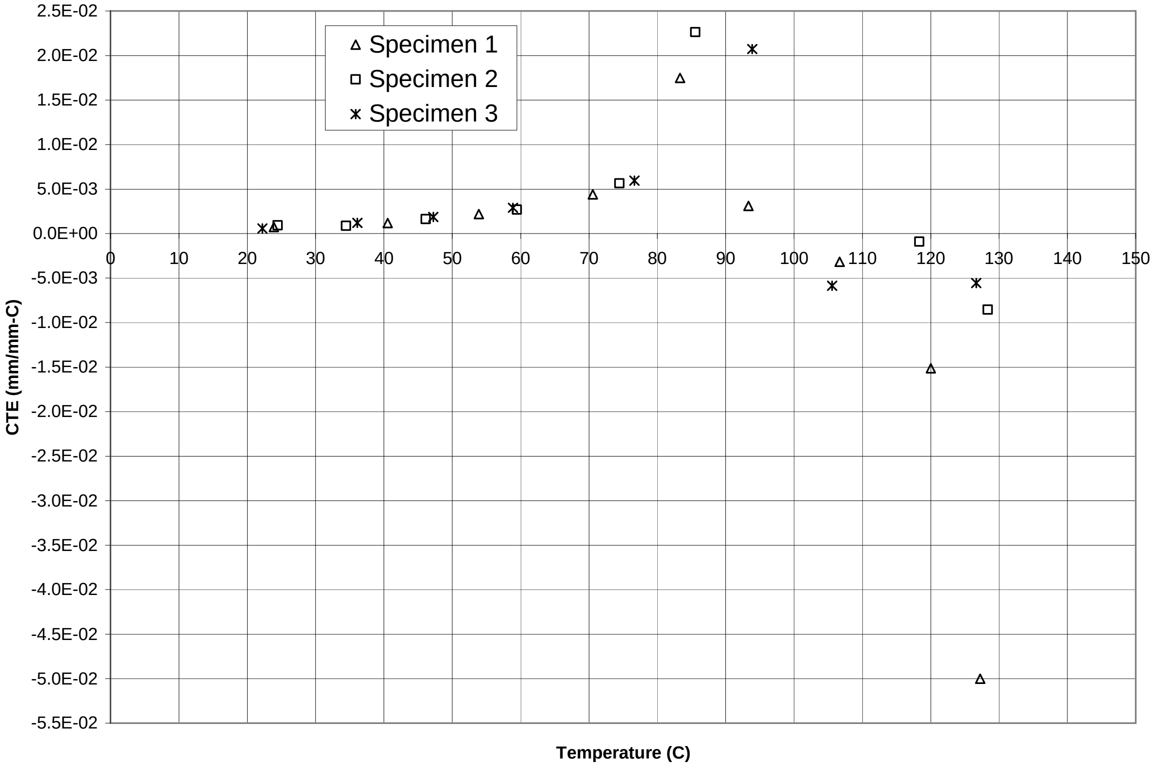

Figure 153. CTE versus temperature plot for mid-high density PE foam.

10.2.4. High-Density Foam Results and Discussion

Figure 154 and Figure 155 show the specimen strain and CTE as functions of temperature for the three high density (208 kg/m^3) PE foam specimens tested. Comparison of Figure 154 and Figure 155 with Figure 152 and Figure 153 reveals that the mid-high and high density configurations display similar characteristics up to approximately 90°C, when the amount of expansion exceeds that detectable with the experimental apparatus. Both have similar values of CTE and strain, particularly during the lower temperature periods. The most apparent difference in the behavior of the two configurations was associated with the point of foam failure. As described in Section 9.6 and shown visually in Figure 152 and Figure 153, the mid-high density configuration experienced foam failure at approximately 110°C. In contrast, the high density configuration continued to display rapid expansion well beyond that temperature, to the point that the specimen mirror tipped backward off the specimen. No discernible decrease in specimen size could then be detected until approximately 125°C, and that which was detected was relatively minor.

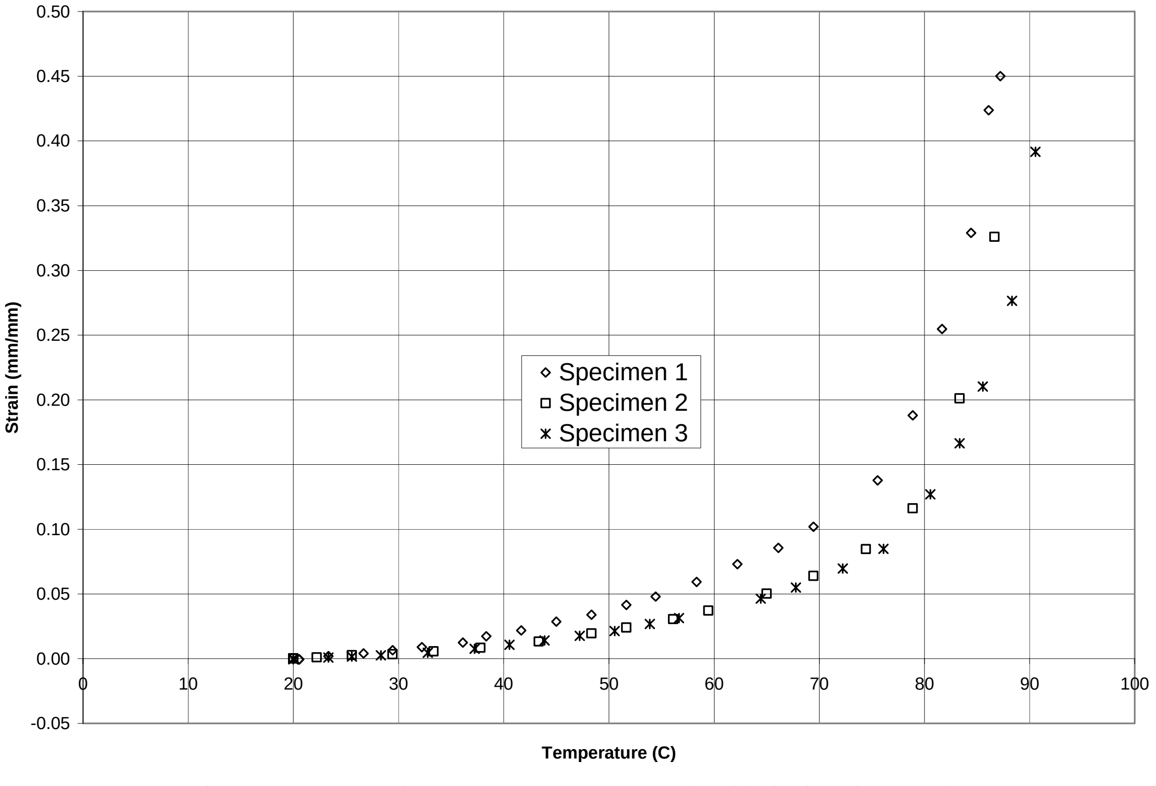

Figure 154. Strain versus temperature for high density PE foam.

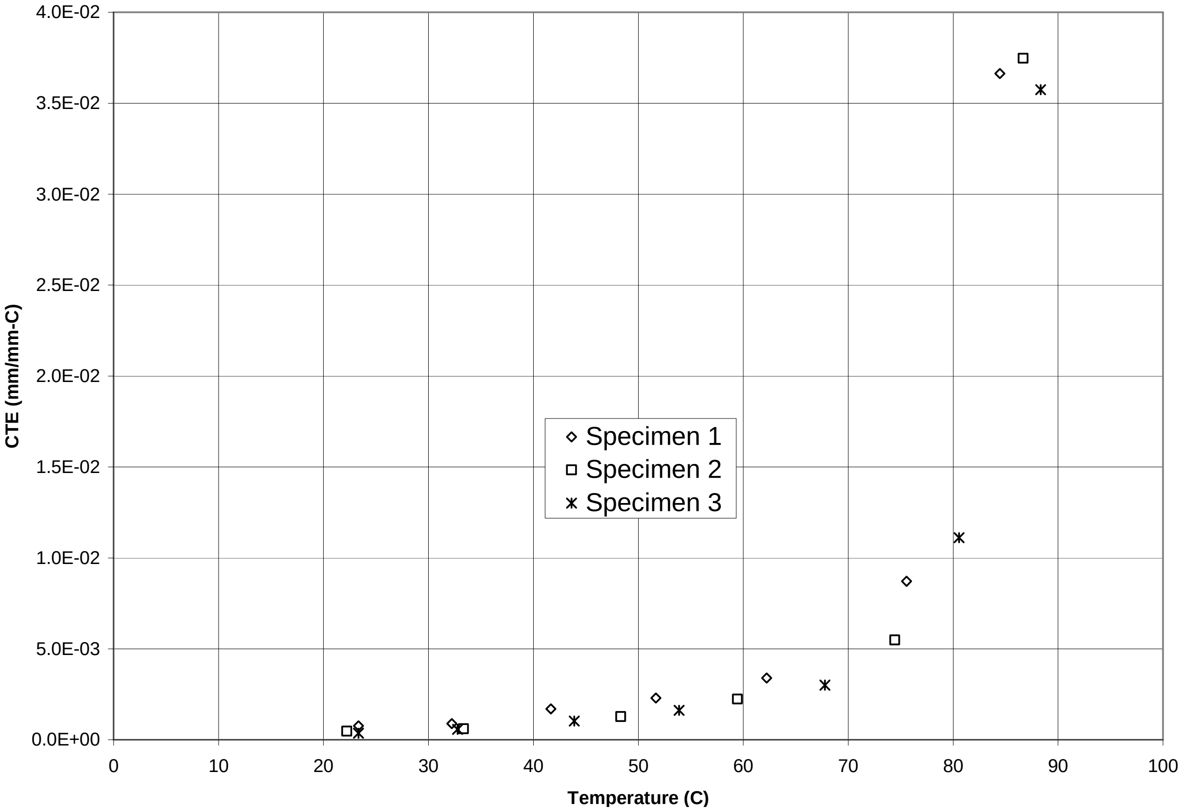

Figure 155. CTE versus temperature for high density PE foam.

A representative photograph of the level of expansion observed for the high density configuration is provided in Figure 156. In particular, comparison with Figure 150 shows the expansion of the high density configuration to be significantly greater than that of the mid-low density configuration, to the point that the high density configuration foam enveloped the reference clear fused quartz stand for the specimen mirror. From Figure 157 it can be seen that the high density configuration did not display the same extent of collapse witnessed for the previous configurations after application of atmospheric pressure following the conclusion of the test. This result can be explained in terms of the greater quantity of polymer due to the higher density of the foam and the inability to cause complete failure of the foam due to the temperature limitation of the experimental apparatus.

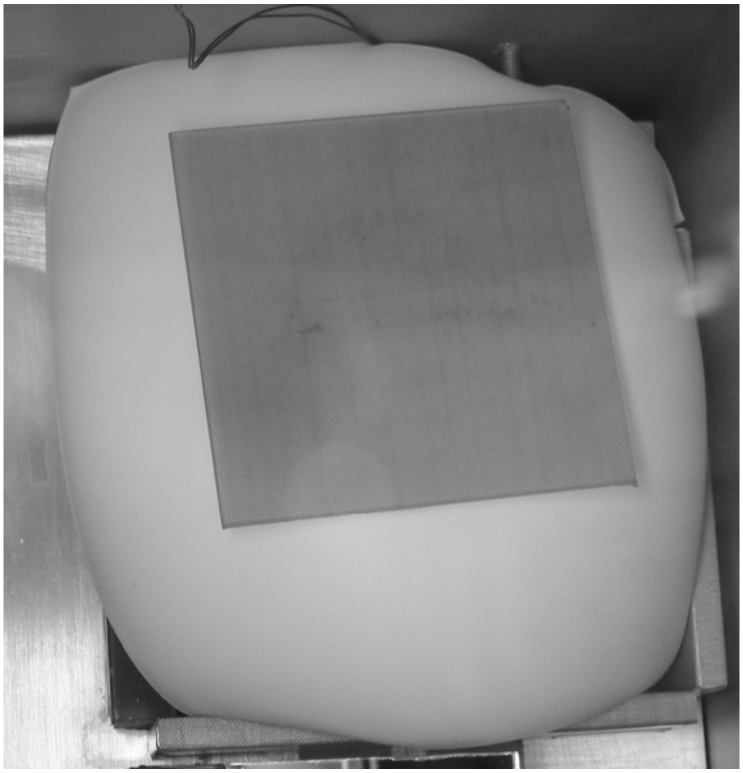

Figure 156. Expansion of a representative high density PE foam specimen during testing.

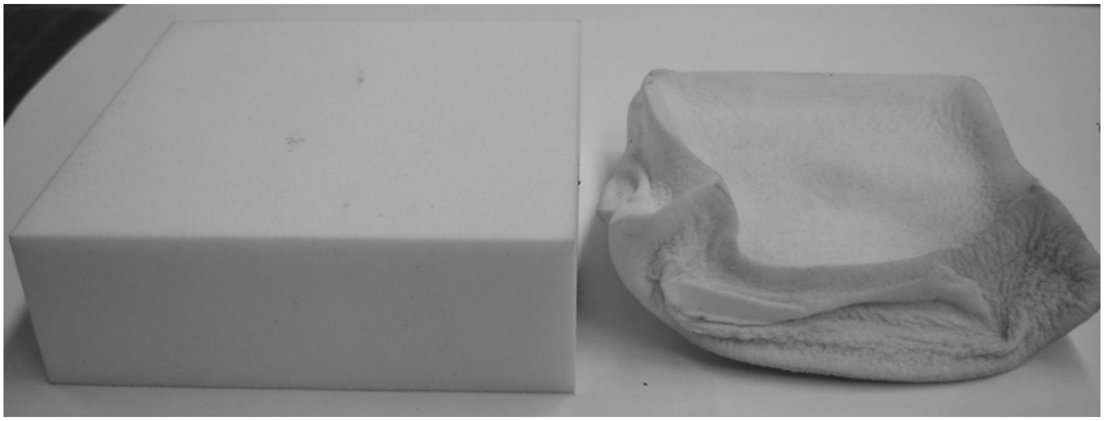

Figure 157. Representative high density PE specimen before and after environmental testing.

10.2.5 Overall Results and Discussion

Figure 158 and Figure 159 present a comparison of representative strain versus temperature and CTE versus temperature plots for all four tested configurations. The two plots highlight the characteristics described in the previous sections, including the pronounced early failure of the low density PE configuration and the general lowering expansion and CTE for a given temperature with increasing foam density.

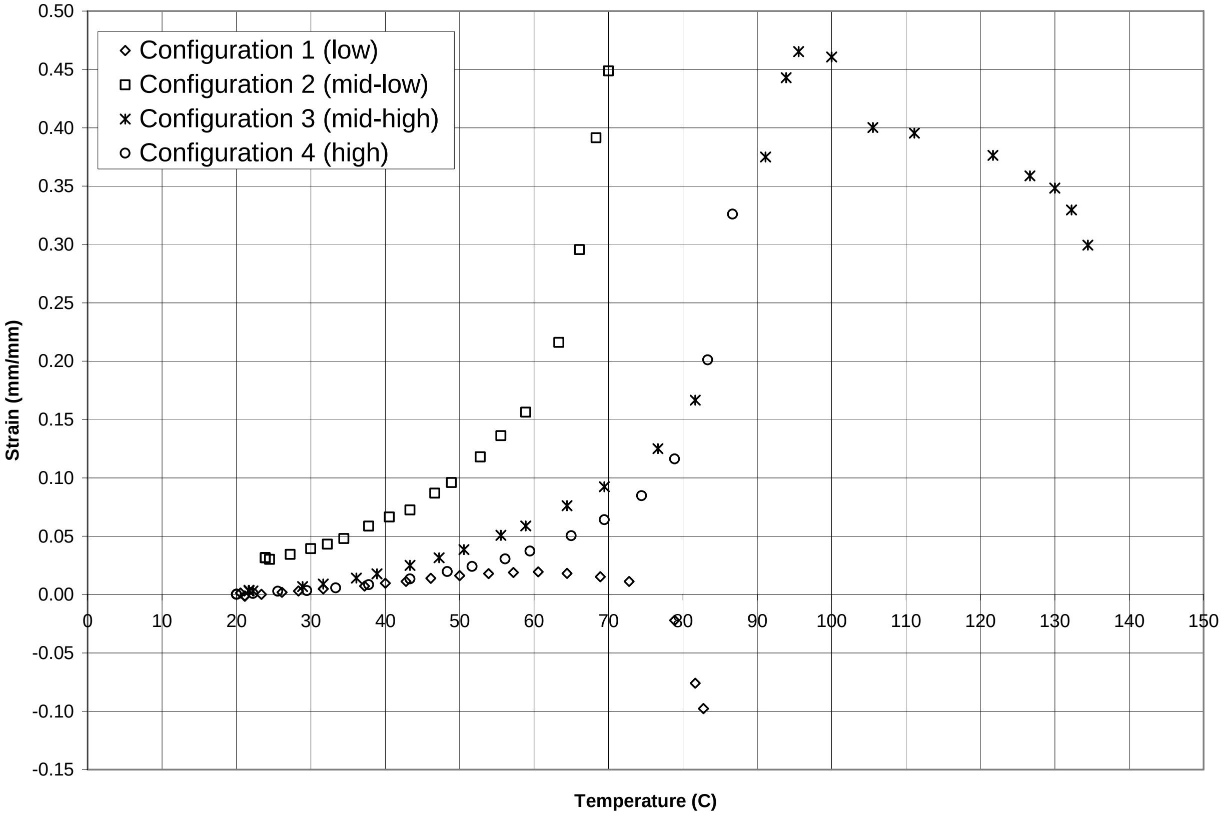

Figure 158. Representative strain versus temperature plots for all four PE foam densities.

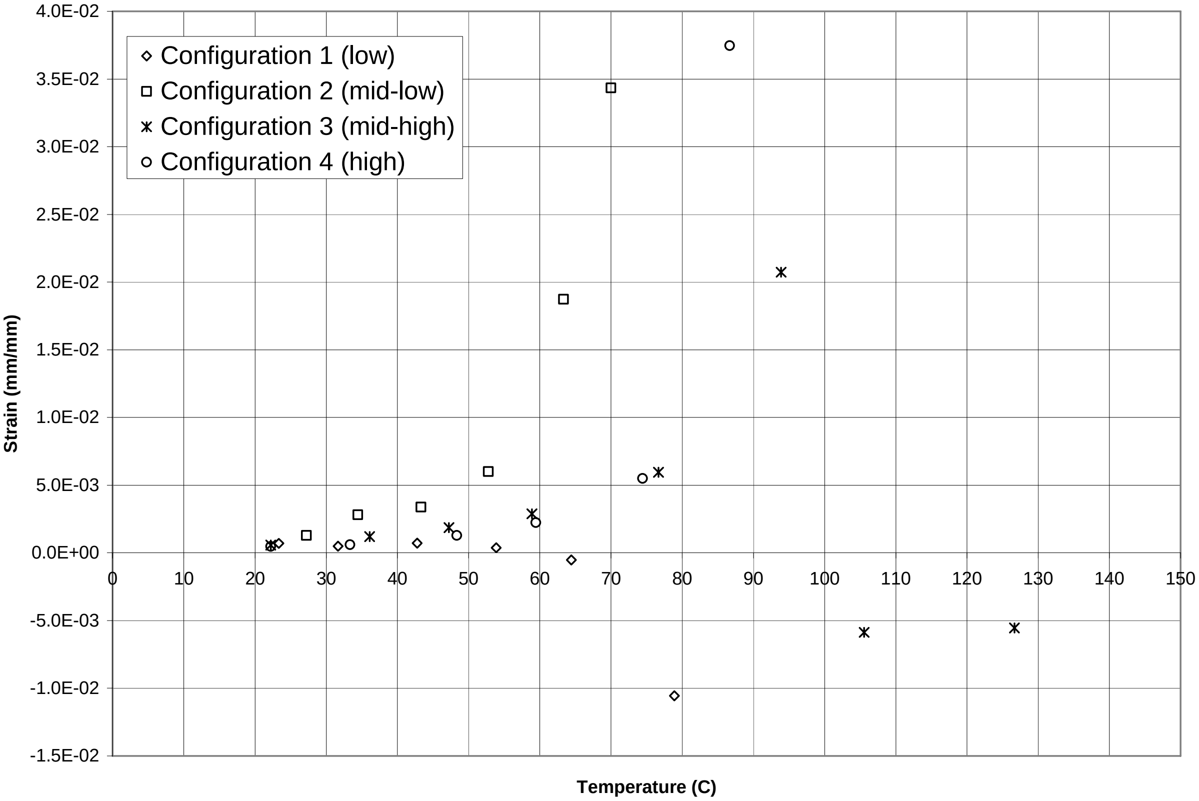

Figure 159. Representative CTE versus temperature plots for all four PE foam densities.

10.3. Foam Characterization

In order to perform the model calculations outlined in Section 10.1 it is necessary to determine dimensions of the cellular structure. In particular, the wall thickness and a measurement of cell diameter were needed. To characterize the cellular structure of each of the four foam densities, standard practices were followed using scanning electron microscopy (SEM). Specimens were prepared for SEM by using a freezing microtome to section thin specimens of foam with a smooth surface. For each foam density, two different sections were taken such that the cell size in all three foam directions (X,Y,T) could be measured, as shown in Figure 160. Once the sections had been microtomed, they were vacuum coated with gold and examined using a LEO 440i SEM.

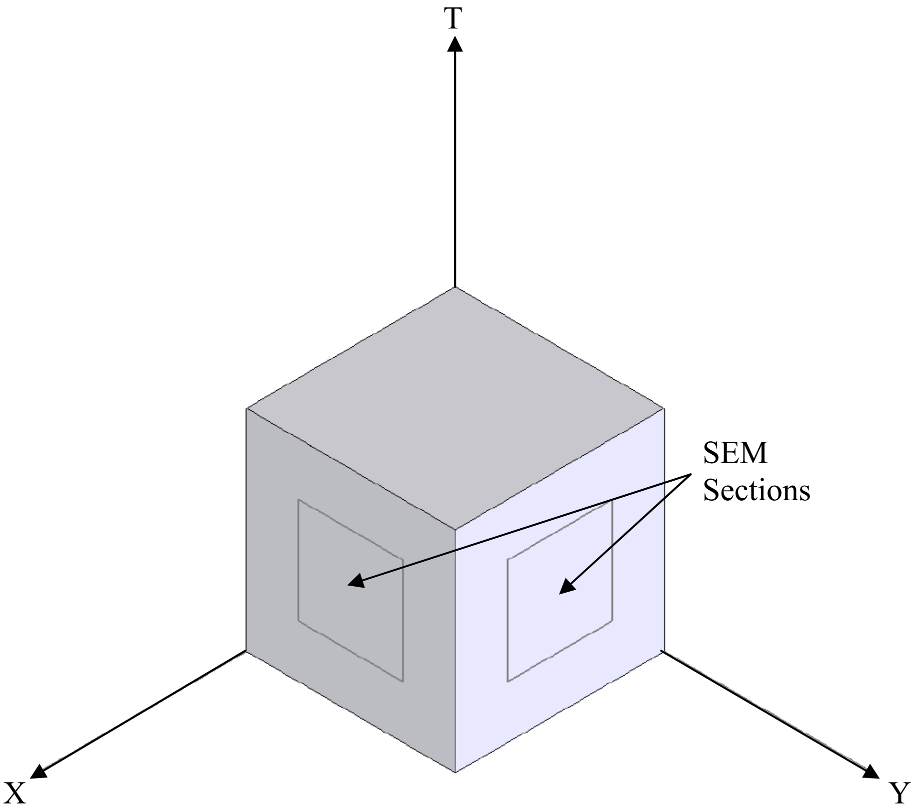

Figure 160. Diagram of foam orientation for SEM observation.

For each of the eight microtomed sections described above (two for each foam density), three photomicrographs at separate locations were taken at low magnification. Examples of the photomicrographs for each type of foam configuration are provided in Figure 161. For each micrograph the foaming direction (T) was aligned in the vertical direction. Parallel and equidistant lines were then placed on each micrograph, 10 each in the vertical (foaming) and horizontal directions. This provided a total of 60 lines in the foaming direction and 30 lines in each perpendicular direction for each foam density. The cell size could then be calculated in each principal direction by dividing the length of each line (in actual distance) by the number of cells that the line intersected [68]. This result was then multiplied by a factor of 1.623 in order to account for the random truncation of cells with respect to their depth during the microtoming process [69]. The coefficient of anisotropy, *CA*, for each of the four foam configurations was calculated using the expression

$$CA = \frac{(X+Y)/2}{T} \quad , \tag{17}$$

where *X*, *Y* and *T* are the cell size dimensions in the longitudinal and thickness (foaming) directions, respectively, in μm.

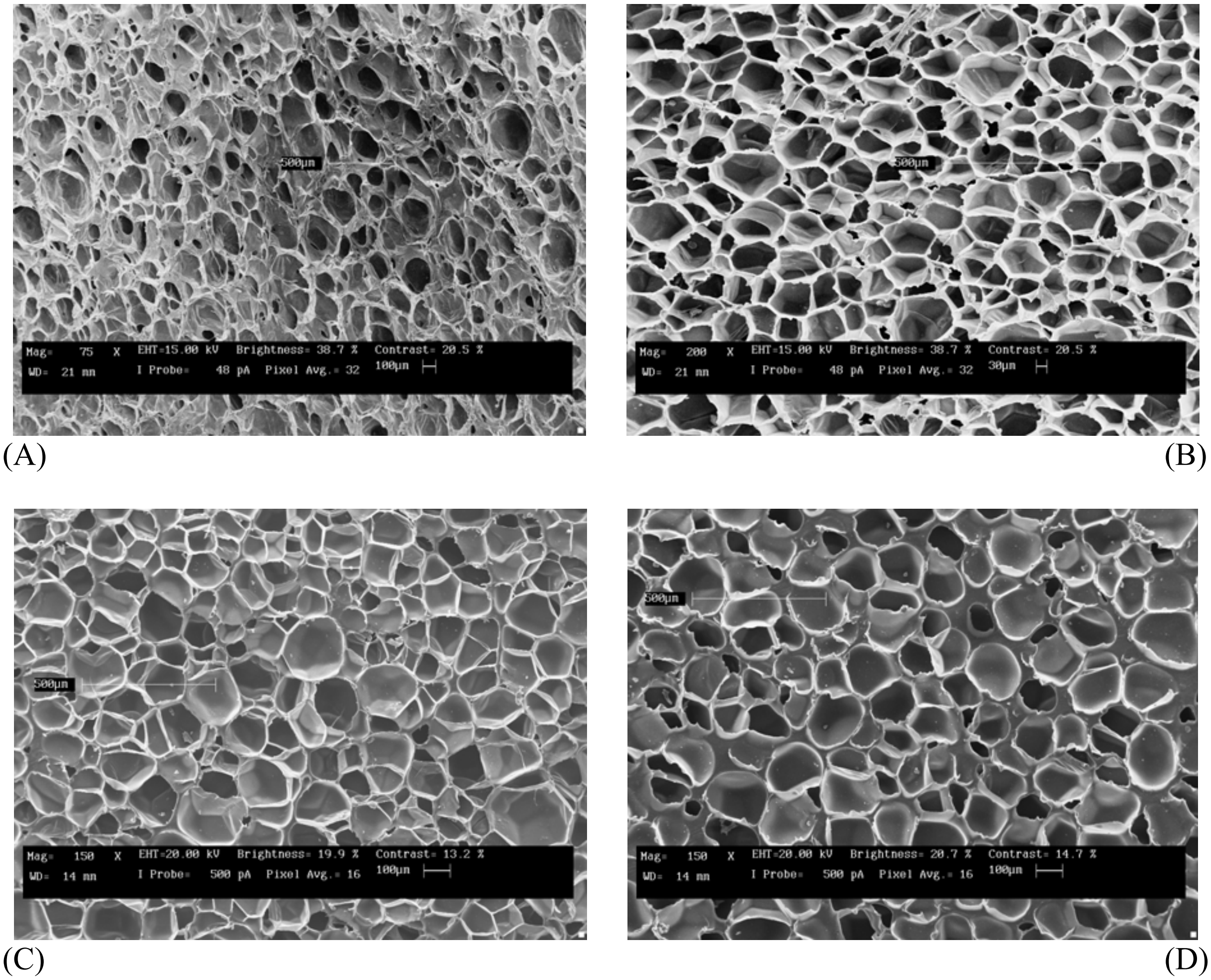

Figure 161. SEM images at low magnification (A) Low density, (B) Mid-low density, (C) Mid-high density, (D) High density

Measurements of wall thickness (δ) were taken directly on the screen of the SEM using the point-to-point distance tool. A representative image depicting this process is provided in Figure 162. For the low density PE foam, only four measurements of wall thickness were taken when it was observed that the recorded values matched well what had previously been published in the literature [70]. The wall thickness for the three other foam densities was determined from an average of at least 20 cell wall measurements. The results for average cell size in the X, Y, and T orientations, the Coefficient of Anisotropy (CA) and average cell wall thickness (δ) for all four foam densities are presented in Table 22.

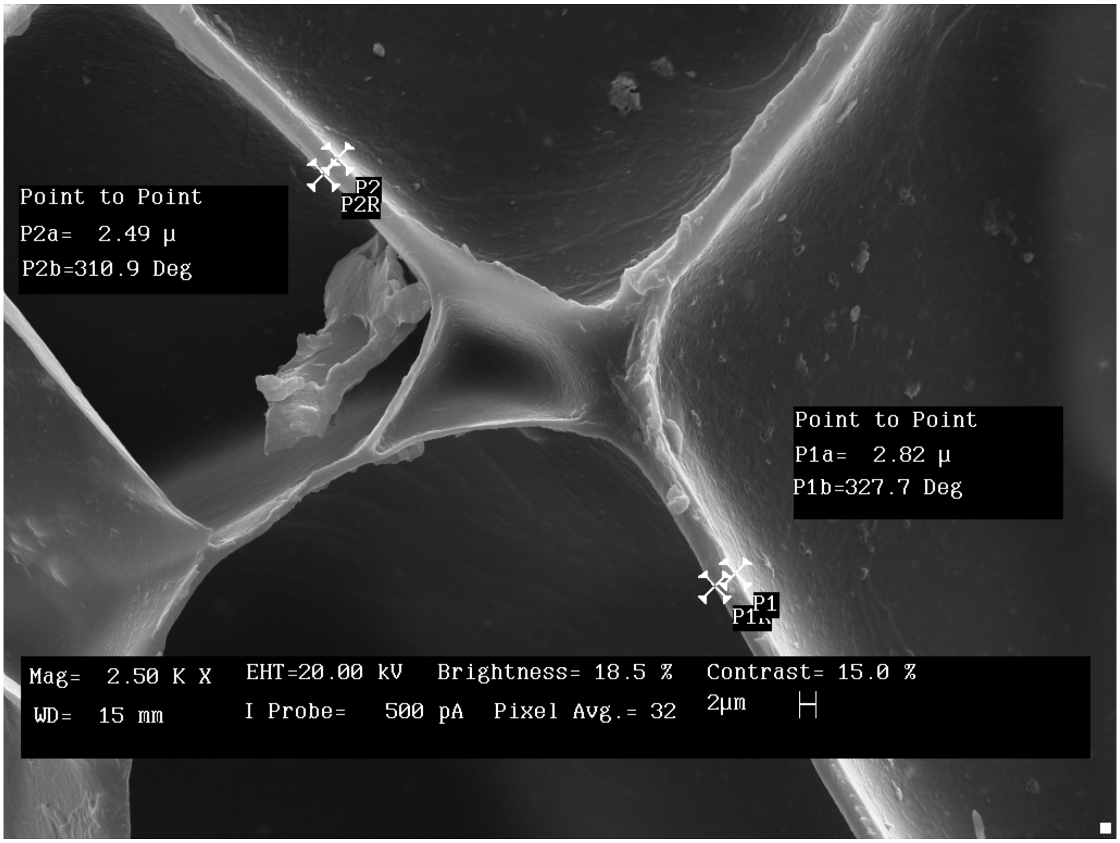

Figure 162. Representative cell wall thickness data.

Table 22. Foam Cellular Structure Characterization Data

Foam Density	***X* (μm)**	***Y* (μm)**	***T* (μm)**	**CA**	***δ* (um)**
Low density	371	375	416	0.90	2.2
Mid-low density	121	136	179	0.72	2.6
Mid-high density	212	214	202	1.05	3.4
High density	263	266	241	1.10	5.1

Several observations can be made based upon the data presented in Table 22. As expected, the average cell wall thickness increases with foam density. However, this trend was not witnessed with the size of the cells. The low density foam had the largest overall cell size by a significant margin, although cell size did increase with density for increasing foam densities. It is also apparent that the lower density foams tend to show a far greater degree of anisotropy (CA), which can be explained in terms of the thinner cells walls being more susceptible to deformation during the manufacturing process.

10.4. Base Polymer Characterization with Temperature

To perform the calculations for the model outlined in Section 10.1, it is necessary to determine the variation with temperature of the tensile modulus and tensile yield strength of the low-density polyethylene (LDPE) resin (base polymer) used in the foaming process of the Voltek L series PE foam. In order to obtain these data, tensile tests were performed on the resin material following ASTM D 638 [4] at 20°C intervals over the range of 20°C to 100°C. A total of 40 Type I bars were produced in accord with ASTM D 4703 [71] by the manufacturer of the resin and shipped to the University of Utah for testing. A typical test specimen is shown in Figure 163.

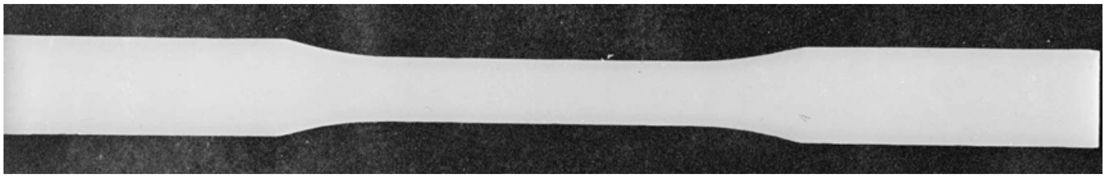

Figure 163. Representative LDPE tensile specimen.

Testing was performed using an electromechanical testing machine with National Instruments data acquisition software. Values of specimen extension were measured using an Epsilon [72] 25 mm gage length extensometer shown in Figure 164. Figure 165 shows the extensometer attached to a tensile specimen.

Figure 164. Extensometer used for displacement measurements.

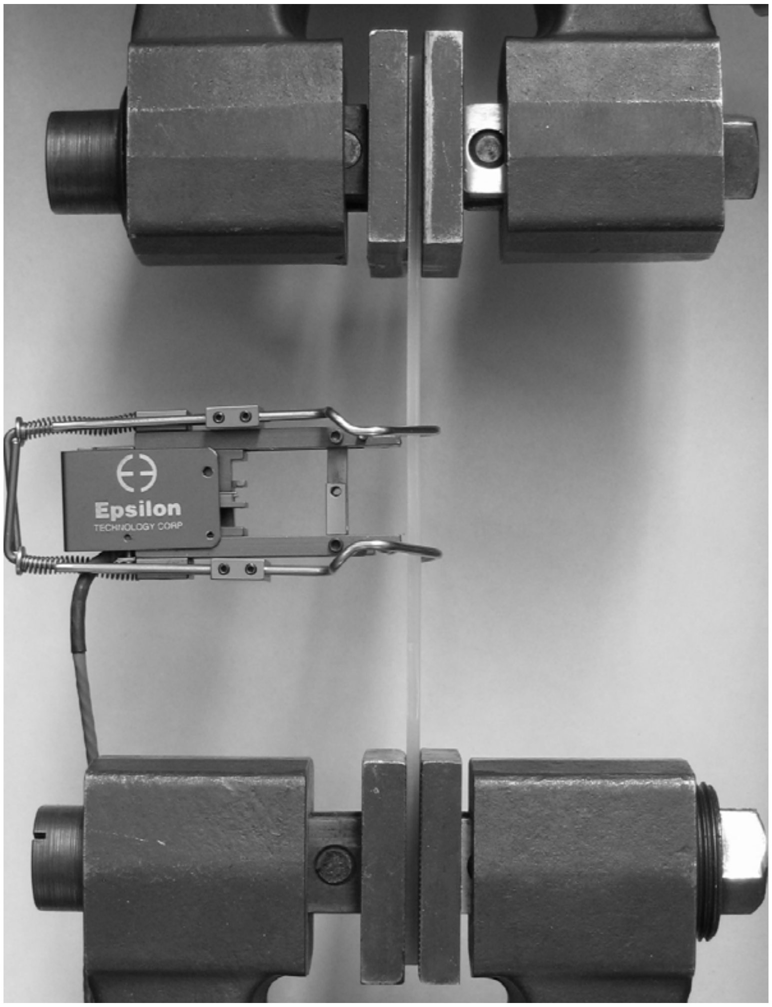

Figure 165. LDPE tensile specimen with extensometer attached.

Test specimens were allowed to reach equilibrium by heating in a convection oven at the desired temperature for at least 30 minutes prior to testing. During the test, a circulating hot air oven was used to maintain the appropriate temperature of the specimen and load train. Figure 166 shows a specimen being tested within the circulating convection oven.

Figure 166. Tensile specimen within a circulating convection oven.

.

During the course of testing, it was discovered that the extensometer could not be used to obtain reliable data above a temperature of 60°C. This was due to the lengthwise compressive force exerted on the specimen from the springs in the extensometer, as well as the bending moment introduced in the specimen due to the weight of the extensometer. The warping present in an 80°C specimen with extensometer attached is shown in Figure 167. As a result of this behavior, the only data available for specimens tested above 60°C were crosshead movement and applied load.

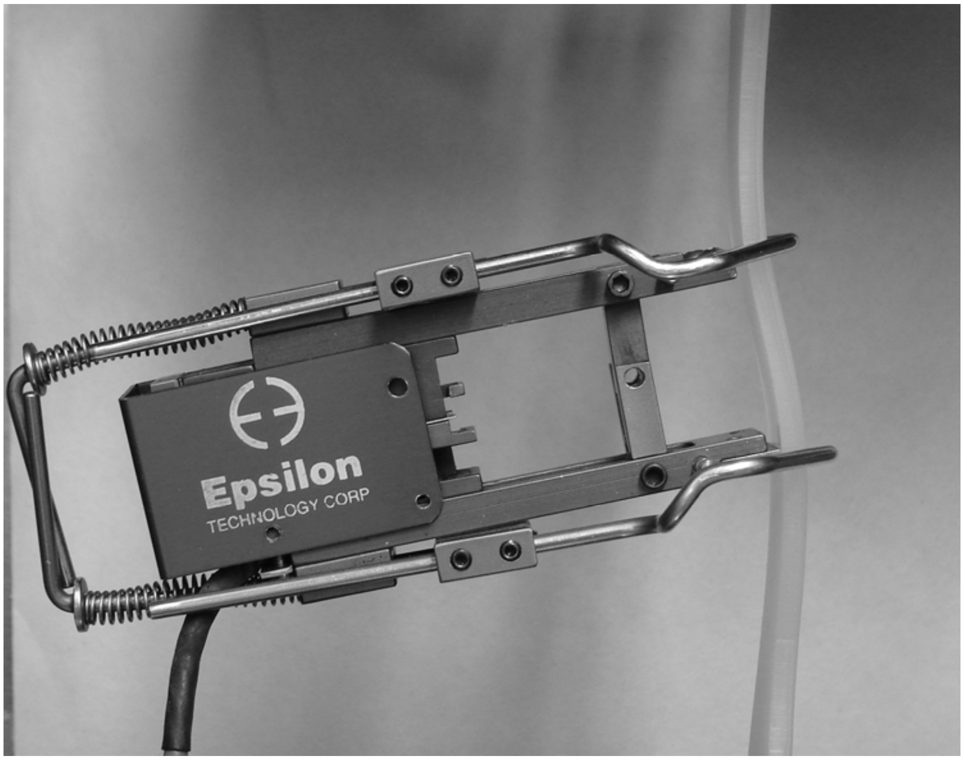

Figure 167. LDPE specimen deflection introduced by the attached extensometer.

The crosshead movement includes compliance in the load train, and thus by itself does not provide an accurate means to determine specimen strain. It was determined, however, that an appropriate conversion could be applied to relate crosshead displacement to specimen strain using data obtained from specimens with an attached extensometer. The conversion factor was determined by plotting specimen strain calculated from the data obtained by the extensometer versus crosshead deflection and performing a linear regression on the data. An example of this type of analysis is shown in Figure 168. This process was repeated for each specimen with an extensometer applied, yielding an average conversion factor of 9.14×10^{-3} with a standard deviation of 3.89×10^{-4}. This factor was then used to obtain specimen strain data from crosshead displacement for tests performed at temperatures above 60°C.

Using this technique, it was possible to prepare a plot of specimen stress versus strain and stress versus crosshead displacement for each specimen. Representative plots of this type are provided in Figure 169 and Figure 170, respectively.

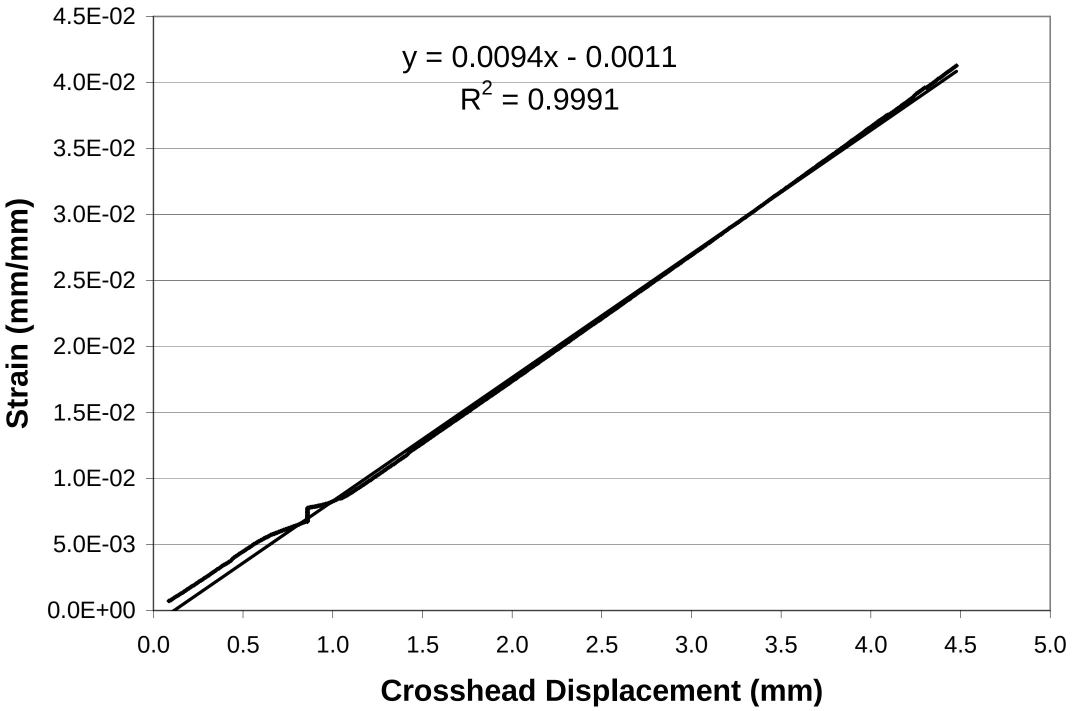

Figure 168. Representative strain versus crosshead displacement relationship.

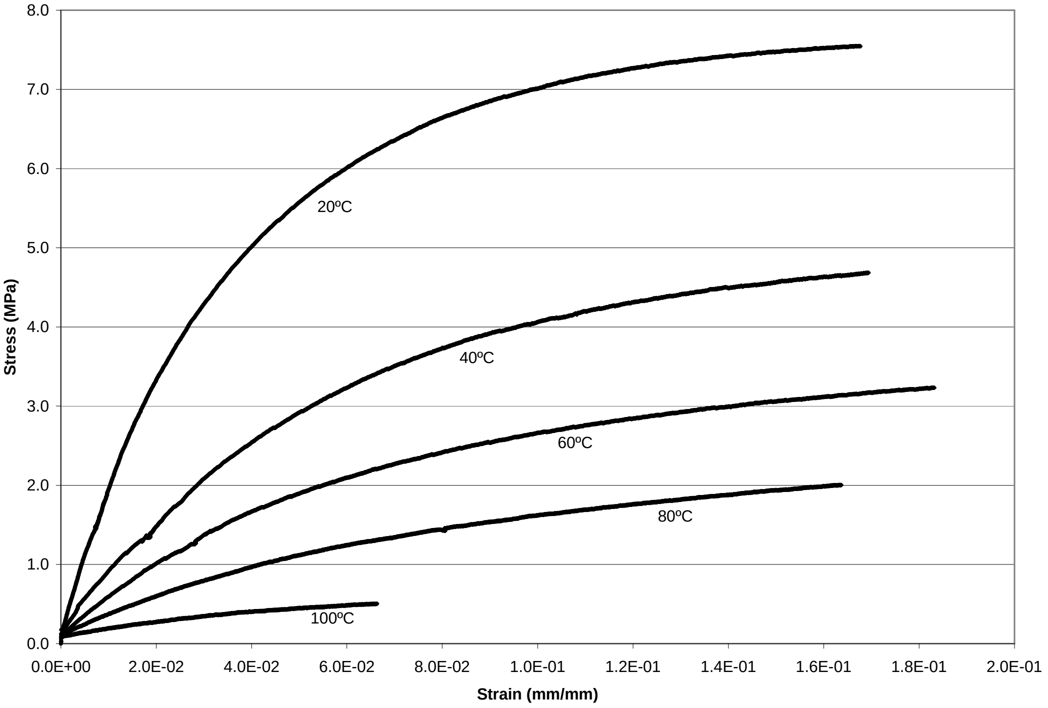

Figure 169. Representative stress versus strain response for varying specimen temperatures.

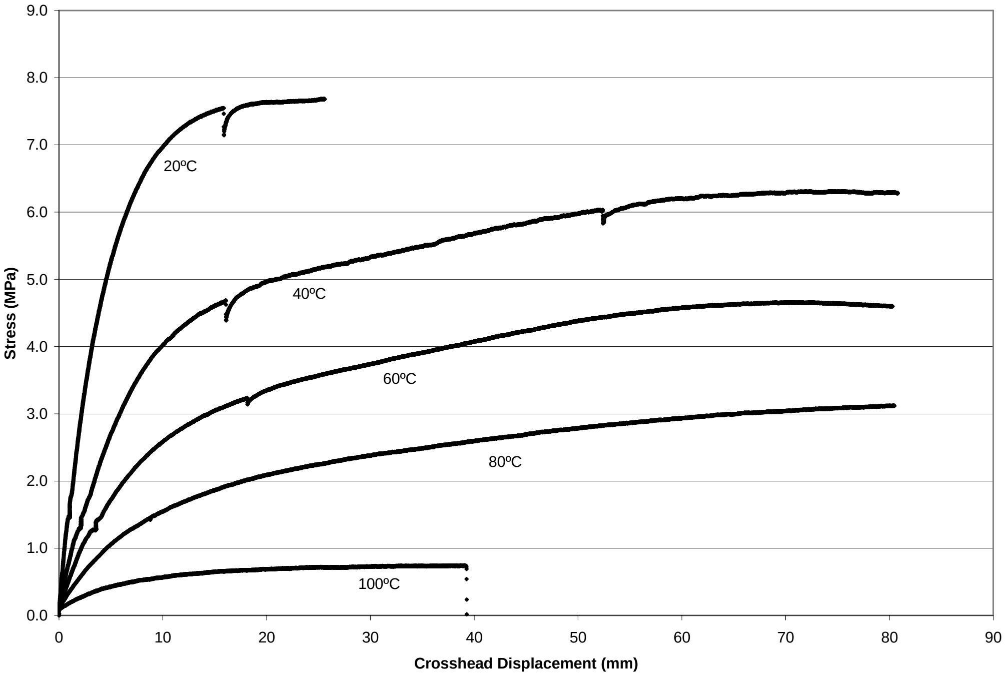

Figure 170. Representative stress versus crosshead displacement for varying specimen temperature.

Several observations can be made from the data presented in Figure 169 and Figure 170. First it should be noted that the drops in load near a displacement of 15 mm for the 20°C, 40°C and 60°C specimens correspond to the times at which the attached extensometers were removed. The smaller initial disturbances at a stress of approximately 1.3 MPa correspond to the transition from the lower grip resting on the crosshead to being supported by the specimen. Also shown in the figures is that the test was concluded at approximately 80 mm for the mid-range temperature specimens. This amount of displacement was a constraint imposed by the physical dimensions of the circulating air oven. It is evident from the figures, however, that an approximate stress plateau could be reached for all specimens by this amount of extension. This stress value was recorded as a yield stress for the material, for the purpose of modeling foam expansion. It can also be observed that the 20°C specimens reached a state of relatively constant stress significantly earlier than the higher temperature specimens, with the exception of the 100°C specimens. The 100°C specimens exhibited a tensile failure near the upper fillet, as shown in Figure 171. As a result, the final stress value obtained is not appropriate for use in design or material characterization, but was deemed sufficient for the purposes of modeling as performed is this report. No tests could be run above 100°C because the specimens were no longer capable of sustaining appreciable load.

Figure 171. Representative failed 100°C tensile specimen.

As expected, the results presented in Figure 169 and Figure 170 show a general trend of decreasing tensile yield strength and modulus values with increasing temperature. The average value, standard deviation and coefficient of variation of the tensile strength and modulus for the resin at each of the specified temperatures are presented in Table 23. To obtain the data presented in Table 23, at least four specimens were tested at each temperature.

Table 23. Variation of LDPE Tensile Stress and Modulus with Temperature

Temperature (°C)	σ_Y			**E**		
	Average (MPa)	St Dev (MPa)	Coeff of Variation (%)	Average (MPa)	St Dev (MPa)	Coeff of Variation (%)
20	7.61	0.08	1.05	118	2.73	2.32
40	6.55	0.19	2.89	46.7	4.24	9.08
60	4.67	0.06	1.37	33.3	3.35	10.0
80	3.09	0.10	3.12	11.2	1.24	11.1
100	0.74	0.02	3.27	5.61	0.73	13.1

As discussed previously, the tensile strength was recorded as a yield value noted when specimen deflection was observed with no appreciable increase in load. The modulus was calculated by a linear fit of the stress-strain data over a wider range than is typical. This was done to better capture the behavior of the polymer for modeling of foam expansion. Specifically, the ranges used extended from the start of the initial linear response of the specimen to 5 MPa at 20°C, 3.5 MPa at 40°C, 2.0 MPa at 60°C and 80°C and 0.5 MPa at 100°C. Also observed from the table is that the conversion of crosshead data to strain for the 80°C and 100°C specimens did not seem to strongly effect modulus variability, which is comparable to that of the 40° and 60° specimens.

Plots of the data presented in Table 23 are provided in Figure 172 and Figure 173. The decrease in tensile strength with temperature displayed a strong linear trend, while the decrease in tensile modulus was more complex. A power fit was found to adequately describe the variation observed. The resulting linear and power-law equations were used in the proposed model, as described in Section 10.1.

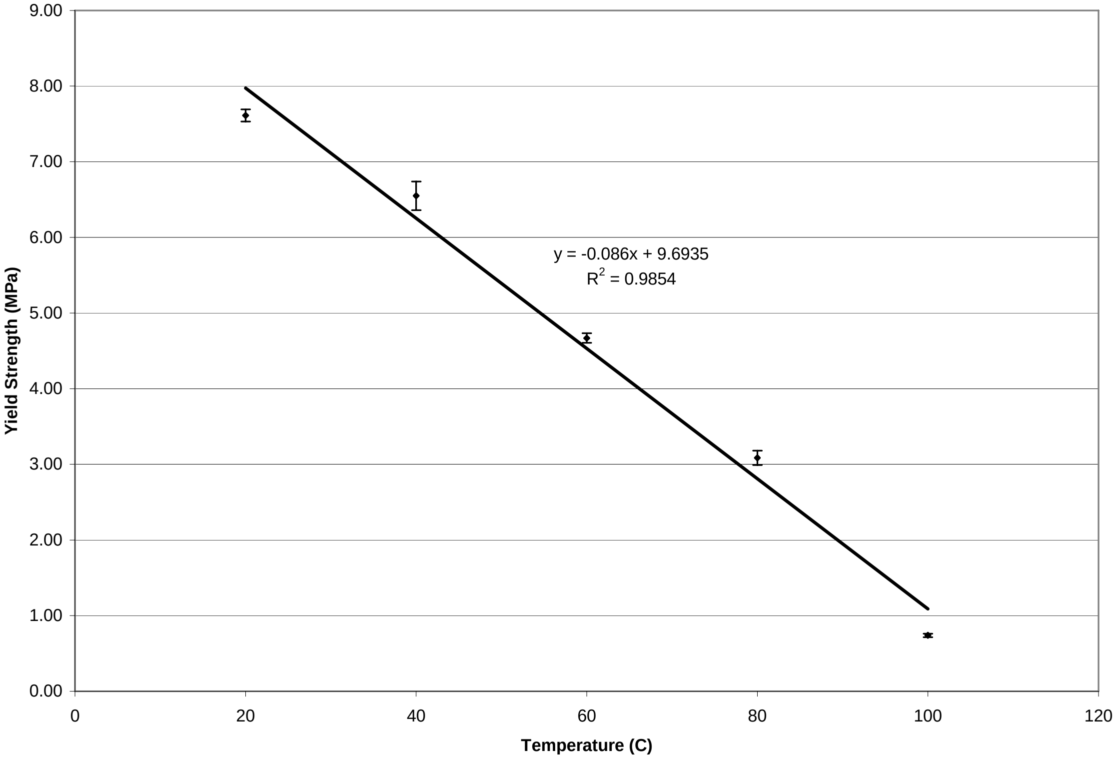

Figure 172. Variation of LDPE tensile yield strength with temperature.

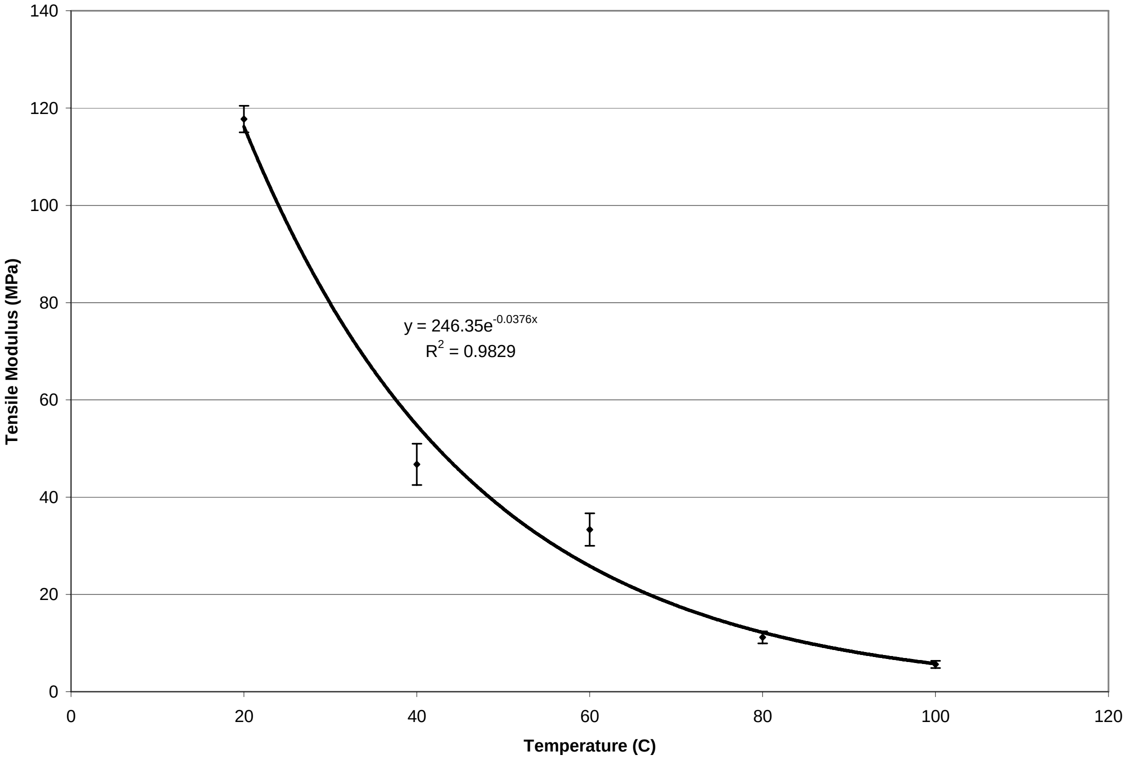

Figure 173. Variation of LDPE tensile modulus with temperature.

10.5. Model Results

With the data presented in Sections 10.3-10.4, it was possible to perform the calculations for the analytical model using a MATLAB script as outlined in Section 10.1. The model prediction of foam strain for each of the four foam densities from Table 21 are plotted in Figure 174 and 177. Three lines for analytical prediction are presented in each figure, corresponding to a range of cell geometry from the results presented in Section 10.3. The line that first demonstrates yield behavior, characterized by increased expansion, results from considering a diameter equal to the average plus one standard deviation and a wall thickness of 1μm under the mean value. Note that a value of 1μm was selected as representative of the range of wall thicknesses observed, though this does not correlate with an exact value of standard deviation due to a shortage of available thickness data. The line that demonstrates yielding last was created using a diameter equal to the average minus one standard deviation and a wall thickness equal to the average plus 1μm. Finally, the middle analytical line was created using the average cell diameter and wall thickness. Representative experimental data for each of the four configurations from Section 10.2 are plotted with asterisks for comparison.

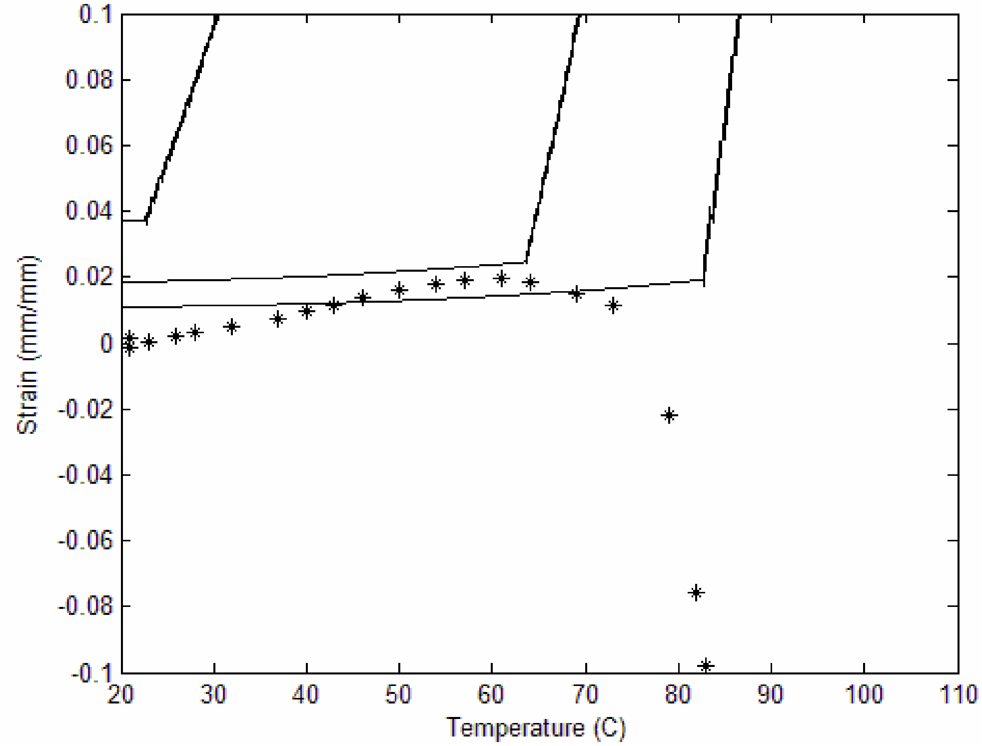

Figure 174. Predicted foam environmental response for low density foam.

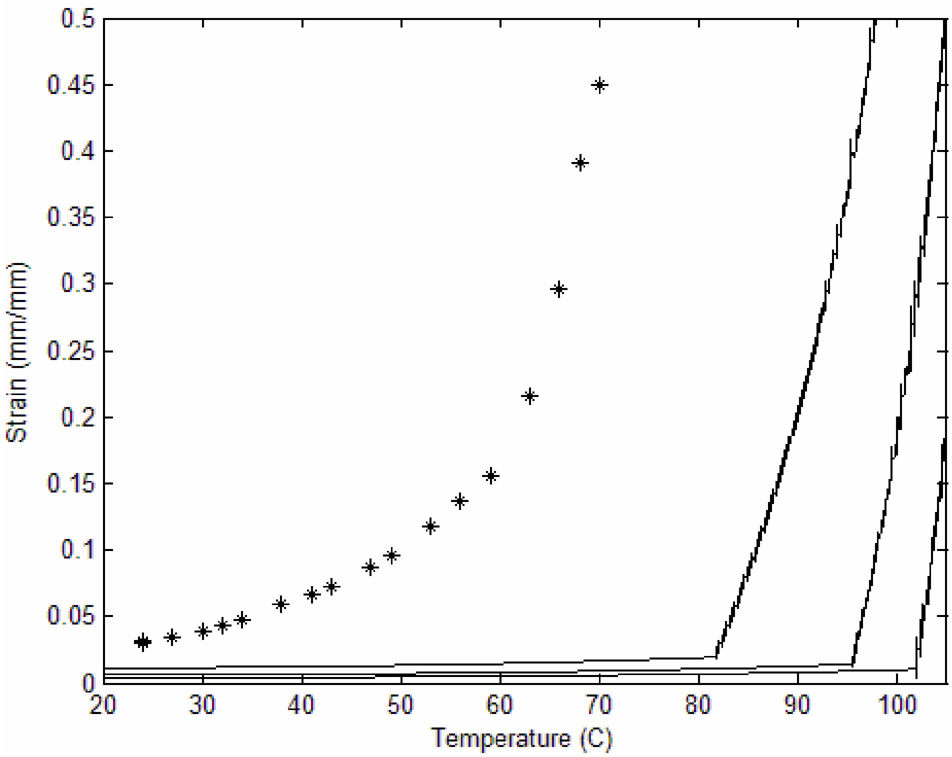

Figure 175. Predicated foam environmental response for mid-low density foam.

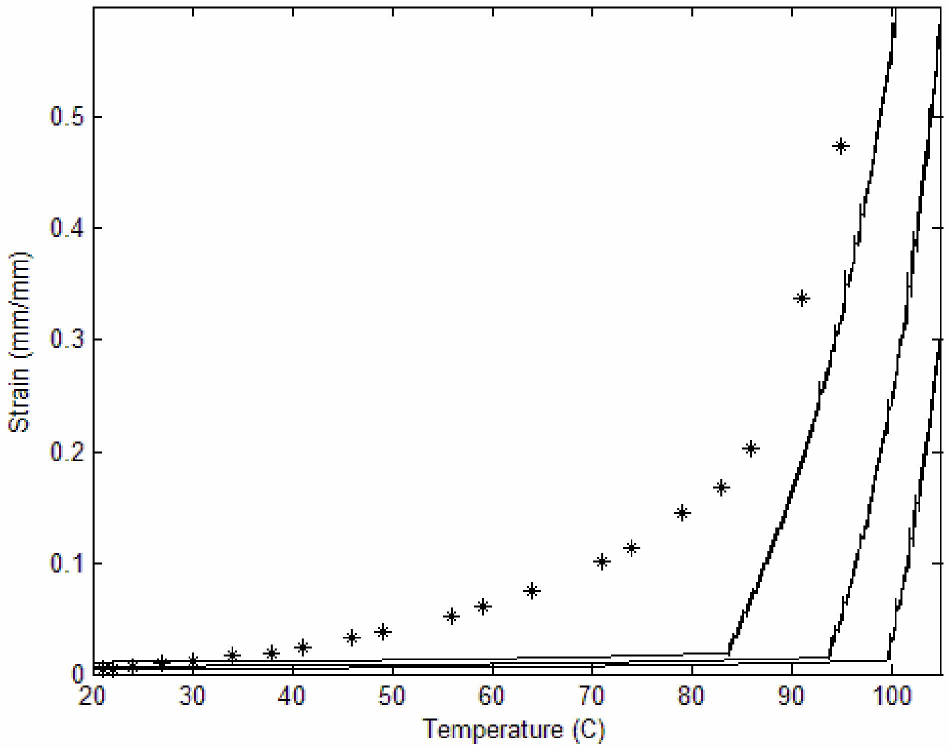

Figure 176. Predicated foam environmental response for mid-high foam density.

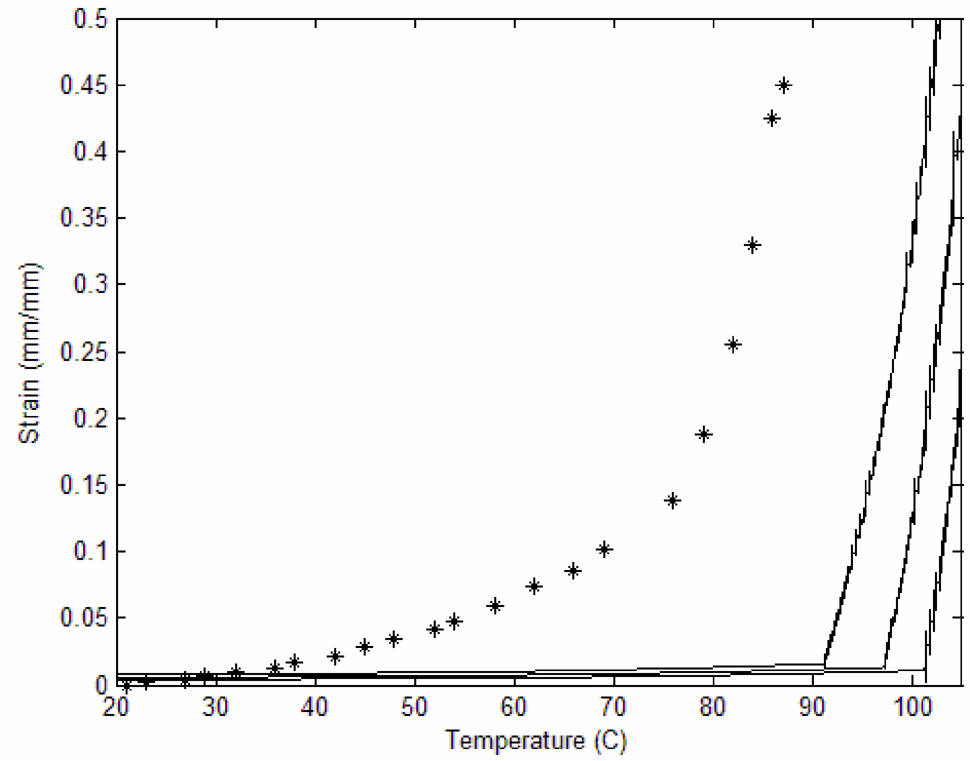

Figure 177. Predicated foam environmental response for high foam density.

10.6. Discussion

Comparison of the model results and experimental results, as shown in Figure 174 to Figure 177, reveals areas of agreement and discrepancy. In particular, the response of the low-density foam is opposite of that predicted, with pronounced contraction of the foam experienced when rapid expansion was predicted. The agreement obtained for the higher density foams was greatly improved, with the overall trend of an initially low expansion, transitioning to rapid expansion. The CTE (slope of the curve) in the rapid expansion region appears to be predicted well by the model, but the transition temperature is overestimated consistently. Furthermore, the model predicts the transition to rapid expansion to occur more abruptly than observed experimentally. Detailed discussions of these observations are presented in the following sections.

One possible explanation for the failure of the model to accurately capture the behavior of the low-density foam involves the manner in which cell rupture was predicted. Foam failure (rupture) was predicted to occur for all configurations between 100°C and 120°C. This was based on three considerations: (1) the elongation to failure at room temperature of the foam resin was listed by the manufacturer at 650%, (2) tensile failure was produced in specimens tested at 100°C but all those tested at lower temperatures experienced over 150% elongation without failure; and (3) no appreciable load could be applied to specimens at 120°C. This method of failure prediction produced acceptable results for the prediction of mid-low and mid-high density foam specimens. However, this temperature range for failure did not address the rate effects that appear to be of critical importance in modeling the low-density foam. Specifically, the model did not take into account the strain rate of the cell membranes associated with the heating rate of the foam during testing. This is particularly important for the thin membranes of the low density foam, which are predicted to be close to yielding under the application of the vacuum alone (Figure 174). Thus, it appears that the amount of expansion of the low density foam is limited by early rupture and degassing of the foam cells, leading to early failure of the foam. This finding is further supported by the significant collapse of the foam following the reintroduction of atmospheric pressure.

Another potential explanation for the early collapse of the low density foam is the increased variability of the foam product with lower densities. As highlighted previously, significant deviations in density throughout the thickness of a foam panel were observed when preparing specimens. Such deviations would be expected to increase the variability in cell geometry, with a higher proportion of cells with excessively thin membranes. Such cells would experience premature collapse, contributing to the behavior observed.

For the higher density foams, the model consistently underpredicted the amount of expansion in the transition region from initial expansion to rapid expansion, with a shift in CTE that is significantly more abrupt than that observed experimentally (Figure 175 through Figure 177). One possible explanation for this behavior is the use of an oversimplified stress-strain response of the foam resin. For modeling purposes, a linear fit was applied over a wide range of stress values to obtain a single value of modulus to the point of yield. At yield, this value was then reduced dramatically to allow pronounced deformation of the specimen. The model thus represented the actual stress-strain response as a straight line with a slope equal to the modulus until yield, at which point the slope became essentially zero. In reality, the modulus gradually reduces to a point of yielding as illustrated for representative specimens in Figure 169. Had the complexity of the model been increased by more accurately modeling the stress-strain response of the foam resin, such as with a higher-order polynomial fit, it would be expected that the model prediction for expansion in the transition region would be improved.

Another observation for the higher density foam configurations (Figure 175 through Figure 177) is that the temperature at which the foam transitions from initial expansion to rapid expansion is consistently overestimated. This result was counterintuitive, since the model neglects the strut-like members within the foam cellular structure that would tend to stiffen the membranes of the actual foam. To better understand why this discrepancy was observed, additional testing was performed. In these tests, high density foam specimens were heated at atmospheric pressure after which vacuum conditions were applied. A total of three specimens were tested in this manner. The first specimen was heated to a temperature of 80°C, after which the vacuum was applied. The second and third specimens were heated to temperatures of approximately 95°C and 100°C, respectively. The measured strain results for specimens 1 and 2 are presented in Figure 178 along with the corresponding model predictions shown previously. Results for specimen 3 are not shown because the foam experienced catastrophic expansion upon application of the vacuum.

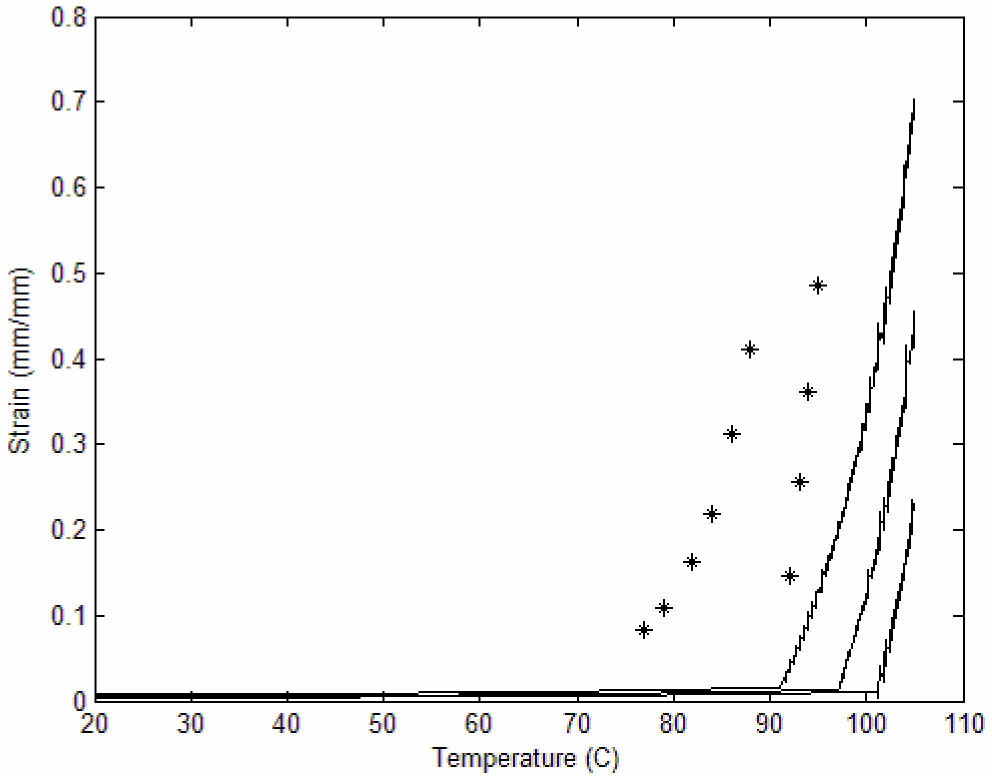

Figure 178. Strain results for high density foam specimens heated prior to vacuum.

The results shown in Figure 178 reveal that the history of the foam is critical in determining the amount of strain experienced. This is highlighted by the observation that the same amount of specimen strain may be observed at the same applied vacuum pressure, but at two different temperatures. The most likely explanation for this observed behavior is that significant creep of the foam cell membranes occurs under the test conditions. This would explain the observed increased expansion prior to the period of rapid expansion and the onset of rapid expansion prior to the model prediction. The initial offset of strain observed for the mid-low density specimens (Figure 175) could also be described as creep dominated, particularly in view of the significant time required to reach the steady value of strain after the application of the vacuum. These results suggest that the viscoelastic properties of the foam resin must be incorporated into the model to more accurately model the foam thermal expansion under vacuum conditions.

A final note on the model results can be made regarding the assumption of perfectly spherical cells. As mentioned in the preceding paragraph, an initially high value of strain was observed for the mid-low density foam specimens that were not predicted by the model. In addition to the possibility of creep deformation, it is also possible that this behavior results from the anisotropy of the foam. As shown in Table 22, the Coefficient of Anisotropy (CA) for the mid-low density foam was 0.72, indicating a high level of deviation from the model of a perfectly spherical cell. Such a deviation would be expected to cause preferential expansion along the longer dimension of the cell, which corresponds with the direction of expansion measured in the experiments conducted. In contrast, the two higher density foams both demonstrated initial expansion values as predicted by the model, and both have coefficient of anisotropy values significantly closer to unity.

Although the proposed model was able to predict a period of initial expansion followed by a second period of rapid expansion, it did not accurately predict the strain response observed when testing with increasing temperature under vacuum conditions. It is believed that greater modeling accuracy would require a more accurate representation of the temperature-dependence on elastic modulus of the foam resin, the incorporation of the viscoelastic response properties of the resin, and an improved criterion for predicting the failure of cell membranes.

11. SUMMARY

The objective of this research investigation was to provide an initial assessment regarding the use of multi-functional sandwich composites for space applications. The proposed sandwich concept utilized non-traditional materials within a conventional sandwich composite design that included a lightweight core material bonded to a series of fiber reinforced facesheets, with transverse reinforcement.

The initial focus of this investigation involved identifying sandwich constituents that could provide structural integrity, damage tolerance, radiation protection, debris/micrometeoroid shielding and thermal insulation within the proposed sandwich design concept. Of these requirements, radiation shielding received the highest priority, which narrowed the focus to three candidate sandwich configurations. Each configuration featured facesheets composed of Spectra® 900 fabric (ultra-high molecular weight polyethylene) infiltrated with epoxy resin. The configurations were distinguished by the use of different closed-cell foams as core materials: polyethylene terephthalate (PET), polyethylene (PE), and polypropylene (PP).

With the desired constituents selected, the focus of the investigation shifted to developing a manufacturing technique to successfully create prototype sandwich composite panels. It was determined that a Vacuum Assisted Resin-Transfer Molding (VARTM) process could be used to create sandwich panels using the selected facesheet and core materials. Following the successful manufacturing of the first round of sandwich panels, additional research was performed to investigate the feasibility of incorporating transverse reinforcements, internal facesheet layers, and self-healing membrane layers. Sandwich panels were manufactured that featured two densities of vertical stitching reinforcement as well as an angled-stitching reinforcement that formed a truss-like network within the foam core. Additionally, it was demonstrated that internal layers of Spectra/epoxy and an internal Surlyn self-healing membrane could be incorporated into the core of the sandwich with minimal alterations to the manufacturing process.

Radiation shielding tests and simulations were performed for five candidate sandwich composite components as well as two complete sandwich composite specimens. Beam exposure measurements were performed at the Brookhaven National Laboratory Alternating Gradient Synchroton (BNL-AGS). Incident ^{35}Cl ion particles with an approximate beam kinetic energy of 1 GeV/n was used. Computational simulations to assess the radiation shielding capabilities of candidate sandwich materials were performed using the heavy ion code GRNTRN. Simulations were performed for the tested materials to determine their ability to fragment highly energetic chlorine ion (^{35}Cl) particles. Results of tests and simulations indicated that the polymeric materials proposed for sandwich construction proposed are attractive materials for space radiation shielding.

Following the evaluation of radiation shielding, the structural properties of the proposed multi-functional sandwich configurations were evaluated. Both flatwise tensile testing and core shear testing were performed. These tests served to identify any material compatibility problems associated with the facesheet and core materials as well as manufacturing-related problems such as core crushing and improper facesheet consolidation. Finally, these tests were used to evaluate the performance of the facesheet-to-core bond. The three sandwich configurations outlined above, with Spectra facesheets and differing core materials (PE, PET, PP), were used in mechanical testing. In addition to the plain sandwich design, mechanical testing was performed on each configuration with three different types of transverse stitching reinforcement: 0.16 stitch/cm^2 and 0.62 stich/cm^2 vertical reinforcement and angle-stitched reinforcement. The PET sandwich specimens consistently exhibited core failure for all types of transverse reinforcement, indicating excellent bonding between the core and facesheet with the selected manufacturing process. In contrast, the PE and PP sandwich specimens typically demonstrated failures at the facesheet/core interface, signifying poor bonding. The effect of incorporating transverse reinforcement was determined to be highly dependent on the nature of the foam core used as well as the orientation of the stitching with respect to the orientation of the applied loads.

Quasi-static indentation testing was performed on sandwich configurations containing interior layers of Spectra/epoxy. Results showed that significant advantages in damage tolerance can be gained with the implementation of transverse stitching reinforcements. Progressive improvements in damage tolerance were observed following indentation and penetration for two different stitch densities. These improvements included significantly reduced delamination of the interior laminate from the core around the loading site, the ability to keep the sandwich structure intact following failure, and a reduction in the permanent deformation of the interior laminate and facesheets. Subdividing the interior laminate throughout the core had unfavorable effects, reducing the maximum load the sandwich was capable of supporting. Computational modeling of the indentation tests revealed the state of stress produced in the sandwich constituents. Results showed that transverse stitching reinforcement allows stress to be distributed to the upper section of core, which corresponds well with damage observed in this area following mechanical testing.

Upon completion of mechanical testing, research focused on evaluating the proposed sandwich constituents for application in a space environment. An experimental apparatus was developed that could be used to measure the out-of-plane expansion of foam blocks and sandwich specimens in response to the application of increasing temperature under a vacuum. Based upon the results of mechanical testing, only PE and PET foams were tested. In addition to foam specimens, sandwich specimens were tested that featured Spectra/epoxy and carbon/epoxy facesheets as well as vertical stitching reinforcement. Testing revealed an overall superior performance of the PET foam core, with the PE core exhibiting catastrophic collapse in each configuration over the tested temperature range of 120°C to 125°C. Additionally, results showed that the incorporation of transverse stitching reinforcement could successfully constrain out-of-plane expansion of a sandwich specimen, though Spectra fiber stitching was ineffective due to its low melting point. Overall, the PET core with carbon fiber facesheets and Kevlar stitching proved to be the most dimensionally stable, with final dimensional changes of less than 0.5% percent.

After noting the significant deviation in the performance of the PET and PE foam core materials, interest was placed in developing a model that could be used to predict general foam behavior within a vacuum and subjected to elevated temperature. After a review of the literature, a simple model was developed that idealized the foam as spherical cells with empty interstitial spaces. In order to assess the validity of the proposed model, additional environmental testing was performed on four densities of Voltek L series PE foam. The experimental results were compared with the model predictions based upon foam cellular characterization performed by scanning electron microscopy and foam resin tensile testing at elevated temperatures.

In summary, the results of this research investigation illustrate the potential for multifunctional sandwich composites to meet these diverse design requirements of future spacecraft. Although specific designs were not investigated, the findings from this investigation provide an initial assessment regarding the use of multi-functional sandwich composites from which further application-specific research may proceed.

ACKNOWLEDGEMENTS

The authors express their appreciation to John Wilson and Mia Siochi of NASA Langley Research Center, to Francis Badavi of Christopher Newport University, and to Cary Zeitlin and Jack Miller of Lawrence Berkeley National Laboratory for their technical assistance. Additionally, the authors wish to thank Erik Saether of NASA Langley Research Center, Technical Monitor of this research grant, for his technical direction and encouragement.

REFERENCES

1. ASTM C 297 (2004), "Standard Test Method for Flatwise Tensile Strength of Sandwich Constructions" ASTM International, West Conshohocken, PA.

2. ASTM C 273 (2000), "Standard Test Method for Shear Properties of Sandwich Core Materials" ASTM International, West Conshohocken, PA.

3 ANSYS 8.0 (2002), Ansys Inc., Canonsburg, PA.

4. ASTM D 638 (2002), "Standard Test Method for Shear Properties of Sandwich Core Materials" ASTM International, West Conshohocken, PA.

5. Gibson, L. J. and Ashby, M. F., Cellular Solids: Structure and Properties, 2nd ed., Cambridge University Press, Cambridge, (1997).

6. Stanley, L. E., Gharpure, S. S. and Adams, D. O., "Mechanical Property Evaluation of Stitched Composite Sandwich Panels," *International SAMPE Symposium and Exhibition (Proceedings)*, v 45 (II), 2000, pp. 1650-1661.

7. Potluri, P., Kusak E. and Cumellas A.J., "Structural Performance of Orthogonal and Bias Stitched Sandwich Structures with Rigid Close-Cellular Foams," *Collection of Technical Papers - AIAA/ASME/ASCE/AHS/ASC Structures, Structural Dynamics and Materials Conference*, v 7, 2003, pp. 4991-4997.

8. Skelton, T. J. and Adams, D. O., "Localized Stitching to Increase Insert Pullout Load in Sandwich Composites," Proceedings of the 49th International SAMPE Symposium and Exhibition, Long Beach, CA, May 2004.

9. Wen, H.M., "Indentation, penetration and perforation of composite laminates and sandwich panels under quasi-static and projectile loading," *Key Engineering Materials*, vol. 141, issue 2, 1998.

10. Parker, Eugene N. "Shielding Space Travelers," *Scientific American*, Vol. 294 Issue 3, March 2006, pp. 40-47.

11. Thibeault, S.A., Kim, M.-H., Wilson, J.W., Long, Jr, E.R., Kiefer, R.L., Glasgow, M.B., Orwoll, R.A.,"Chapter 19: Shielding Materials Development and Testing Issues," in Shielding Strategies for Human Space Exploration, Wilson, J.W., Miller, J., Konradi, A. and Cucinotta, F.A., eds., NASA CP 3360, 1997.

12. Kim, M.Y., Wilson, J.W., Thibeault,, S.A., Nealy, J.E., Badavi, F.F. and Kiefer, R.L., "Performance Study of Galactic Cosmic Ray Shield Materials," NASA TP-3473, 1994.

13. Wilson, J.W., Townsend, L.W., Schimmerling, W., Khandelwal, G.S., Kahn, F., Nealy, J.E., Cucinotta, F.A., Simonsen, L.C., Shinn, J.L. and Norbury, J.W., "Transport Methods and Interactions for Space Radiation," NASA RP-1257, Washington, DC., 1994.

14. "Honeywell Advanced Fibers and Composites – Spectra Fiber," Honeywell International Inc., http://www.honeywell.com/sites/sm/afc/spectra_fiber.htm.

15. DuPont Surlyn® product details. www2.dupont.com/Surlyn/en_US/.

16. Fall, R. "Puncture Reversal in Ethylene Ionomers- Mechanistic Studies," M.S. Thesis. Virginia Tech. August 2001.

17. Kalista, Jr., S. J. "Self-Healing of Thermoplastic Poly(Ethylene-co-Methacrylic Acid) Copolymers Following Projectile Puncture," Master's Thesis, Virginia Tech. September 2003.

18. Huber, A. and Hinkley, J., "Impression Testing of Self-Healing Polymers," NASA/TM-2005-213532, March 2005.

19. Williams, M.K., et al. "Effects of Cell Structure and Density on the Properties of High Performance Polyimide Foams," *Polymers for Advanced Technologies*, v 16, 2005, pp. 167-174.

20. Veazie, D. R., Wright, M. O. and Weiser, E. "Polyimide Foam Development and Characterization for Lightweight Integrated Structures," 45th AIAA/ASME/ASCE/AHS/ASC Structures, Structural Dynamics and Materials Conference, Palm Springs, California, April 2004.

21. Rodríguez-Pérez, M.A., González-Peña, J.I., Witten, N., and de Saja, J.A., "The Effect of Cell Size on the Physical Properties of Crosslinked Closed Cell Polyethelyne Foams Produced by a High Pressure Nitrogen Solution Process," *Cellular Polymer*, vol. 21, no. 3, 2002, pp. 165-194.

22. Rodríguez-Pérez, M.A., Alonso, O., Duijsens, A. and de Saja, J.A., "Thermal Expansion of Crosslinked Closed-Cell Polyethylene Foams," *Journal of Polymer Science Part B: Polymer Physics* vol. 36, 1998, pp. 2587-2596.

23. Rodriguez-Perez, M.A., Duijsens, A., De Saja, J.A. "Effect of Addition of EVA on the Technical Properties of Extruded Foam Profiles of Low-Density Polyethylene/EVA Blends," *Journal of Applied Polymer Science*, v. 68, n. 8, pp. 1237-1244.

24. Rodríguez-Pérez, M.A., "Crosslinked Polyolefin Foams: Production, Structure, Properties, and Applications," *Advanced Polymer Science,* (2005), vol. 184, pp 97–126.

25. Throne, James L., "Polystyrene Foam Sheet Expansion During Heating," *Journal of Polymer Engineering*, Vol. 6, n.1-4, 1986, pp. 313-344.

26. Almanza, O., Masso-Moreu, Y., Mills, N.J. and Rodríguez-Pérez, M.A. "Thermal Expansion Coefficient and Bulk Modulus of Polyethylene Closed-Cell Foams," *Journal of Polymer Science Part B: Polymer Physics* vol. 42, 2004, pp. 3741–3749.

27. Cellect LLC, St. Johnsville, NY. www.cellectfoam.com/.

28. Dow Performance Foams, Midland, MI. www.dow.com/perffoam/market/products/index.htm.

29. Fortifoam Inc., Ft. Worth, TX. www.fortifoam.com/.

30. Merryweather Foam Inc., Anthony, NM. www.merryweather.com/.

31. Sealed Air Corporation, Elmwood Park, NJ. www.sealedair.com/na_home.htm.

32. Voltek LLC, Lawrence, MA. www.voltek.com/main.html.

33. Alcan Baltek Corporation, Northvale, NJ. www.alcanbaltek.com/alcan/acsites.nsf/pages_accm3_en/index.htm!Open&v=3.

34. Fagerdala World Foams AB, Sweden. www.fagerdala.com/.

35. Keyston BROS, Salt Lake City, UT. E-mail: info@keystonbros.com.

36. General Plastics, Tacoma WA, www.generalplastics.com.

37. Illbruck Inc., Minneapolis MN, www.customfoamfab.com.

38. Crest Foam Industries, Inc., Moonachie NJ, www.crestfoam.com.

39. Marko Foam Products Inc., Salt Lake City UT, www.markofoam.com.

40. JSP International, Milledgeville, IL. www.jsp.com/index_en.php.

41. Resolution Performance Products EPON Resin 862 and EPIKURE Curing Agent 9553 product details. www.resins.com/resins/am/pdf/SC1546.pdf.

42. Stanley, L.E. and Adams, D.O. "Damage Tolerance of Stitched Composite Sandwich Structures" International SAMPE Symposium and Exhibition (Proceedings), v. 46 II, 2001, pp. 1947-1957.

43. Butterfield, J.M and Adams, D.O. "Effects of Stitching on the Compression After Impact Strength of Sandwich Composites," International SAMPE Symposium and Exhibition (Proceedings), v. 49, 2004, pp. 3544-3557.

44. J. W. Wilson, J. Miller, A. Konradi, F. A. Cucinotta; "Shielding Strategies for Human Space Exploration," NASA Conference Publication 3360, December 1997.

45. J. W. Wilson, M. Kim, W. Schimmerling, F. F. Badavi, S. A. Thibeault, F. A. Cucinotta, J. L. Shinn, R. Kiefer, "Issues in Space Radiation Protection," *Health Physics* 68, 50-58, 1995.

46. F. F. Badavi, J. E. Nealy, G. de Angelis, "Radiation Environment and Shield Modeling Validation for CEV design," AIAA-2005-6651, 2005 Space Conference, Long Beach, August 2005.

47. G. D. Badhwar, F. A. Cucinotta, "A Comparison of Depth Dependence of Dose and Linear Energy Transfer Spectra in Aluminum and Polyethylene," *Radiation Research* 153, pp. 1-8, 2000.

48. J. Miller, C. Zeitlin, F. A. Cucinotta, L. Heilbronn, D. Stephens, J. W. Wilson, "Benchmark Studies of the Effectiveness of Structural and Internal Materials as Radiation Shielding for the International Space Station", Radiation Research 159, pp. 381-390, 2003.

49. S. A. Walker, "The Straggling Green's Function Method for Ion Transport," Doctoral Dissertation, Old Dominion University, May, 2006.

50. S. A. Walker, J. Tweed, J. W. Wilson, F. A. Cucinotta, R.K. Tripathi, S. Blattnig, C. Zeitlin, L. Heilbronn, J. Miller; "Validation of the GRNTRN Code for Laboratory Exposures with 1A GeV Iron Ions in Several Targets.", 35th COSPAR Paris, France, 18-25 July 2004.

51. Loctite® Hysol® 907 product details. www.loctite.com/int_henkel/loctite_ar/binarydata/pdf/HYSAE-907.pdf.

52. Dynaloy LLC, Indianapolis, IN. Dynasolve 185 product details. www.dynaloy.com/Products/tech_data_sheets/Dynasolve%20185%20PDF.pdf.

53. Interface Advanced Force Measurement, Scottsdale, AZ. www.interfaceforce.com/index.htm.

54. Belk C.A., Robinson J.H., Alexander M.B., Cooke W.J. and Pavelitz S. D., "Meteoroid and Orbital Debris: Effects on Spacecraft", NASA Reference Publication 1408.

55. Ellerbeck, N., "Characterization of Sandwich Composites for Automotive Applications", Master's Thesis, Department of Mechanical Engineering, University of Utah. (September 2005).

56. General Plastics Manufacturing Company, Nominal Physical Property Data for LAST-A-FOAM® FR-6700 Rigid Foam at 8 pounds per cubic foot density, http://www.generalplastics.com/products/idatasheets.php?pfoamname=FR-6700%20Aircraft%20Foam&.

57. Colvin E. G. Jr., Adams D. S., 'A Finite Element Overlay Technique for Modeling Pinned Composite Joints', AIAA/ASME/SAE/ASEE 22nd Joint Propulsion Conference, Huntsville, Alabama, 1986.

58. Precision Scientific Inc., Chicago, IL.

59. Gardner Denver Welch Vacuum Technology, Inc. Skokie, IL. www.welchvacuum.com/.

60. GE Quartz, Inc. Willoughby, OH. www.gequartz.com/en/contact.htm.

61. GM Associates, Inc. Oakland, CA. www.gmassoc.com/index.htm.

62. Kevlar PVA size 400. Synthetic Thread Company. Bethlehem, PA. www.syntheticthread.com/kevlar.htm.

63. Matweb, "Overview - Low Density Polyethylene (LDPE), Film Grade" www.matweb.com/search/SpecificMaterial.asp?bassnum=O3805.

64. Ugural, A.C. Stresses in Plates and Shells. McGraw-Hill, 1981.

65. Gere, James M. Mechanics of Materials. Fifth Edition. Brooks-Cole, 2001, p. 557-560.

66. Barber, J.R. Intermediate Mechanics of Materials. McGraw-Hill, 2001, pp 386-387.

67. Masterton, W.L. and Hurley, C.N. Chemistry: Principles and Reactions. Fourth Edition. Harcourt, 2001, p. 120.

68. Sims, G.L.A. and Khunniteekool, C. "Cell Size Measurement of Polymeric Foams," *Cellular Polymers*, vol. 13, 1994, pp. 137-146.

69. ASTM D 3576, (1998), "Standard Test Method for Cell Size of Rigid Cellular Plastics" ASTM International, West Conshohocken, PA.

70. Campo-Arnáiz, R. A., Rodríguez-Pérez , M. A., Calvo, B. and de Saja, J. A. "Extinction Coefficient of Polyolefin Foams," *Journal of Polymer Science Part B: Polymer Physics*, v. 43, n. 13, 2005, pp. 1608 – 1617.

71. ASTM D 4703 (2003), "Standard Practice for Compression Molding Thermoplastic Materials into Test Specimens, Plaques, or Sheets," ASTM International, West Conshohocken, PA.

72. Epsilon Technology Corporation. Jackson, WY. www.epsilontech.com/.

REPORT DOCUMENTATION PAGE

Form Approved
OMB No. 0704-0188

1. REPORT DATE *(DD-MM-YYYY)*
01- 06 - 2007

2. REPORT TYPE
Contractor Report

3. DATES COVERED *(From - To)*

4. TITLE AND SUBTITLE
Multi-Functional Sandwich Composites for Spacecraft Applications: An Initial Assessment

5a. CONTRACT NUMBER

5b. GRANT NUMBER
NAG1-03085

5c. PROGRAM ELEMENT NUMBER

6. AUTHOR(S)
Adams, Daniel O.; Webb, Nicholas Jason; Yarger, Cody B.; Hunter, Abigail; and Oborn, Kelli D.

5d. PROJECT NUMBER

5e. TASK NUMBER

5f. WORK UNIT NUMBER
732759.07.09

7. PERFORMING ORGANIZATION NAME(S) AND ADDRESS(ES)

NASA Langley Research Center
Hampton, VA 23681-2199

University of Utah
Department of Mechanical Engineering
Salt Lake City, UT 84112

8. PERFORMING ORGANIZATION REPORT NUMBER

9. SPONSORING/MONITORING AGENCY NAME(S) AND ADDRESS(ES)
National Aeronautics and Space Administration
Washington, DC 20546-0001

10. SPONSOR/MONITOR'S ACRONYM(S)
NASA

11. SPONSOR/MONITOR'S REPORT NUMBER(S)
NASA/CR-2007-214880

12. DISTRIBUTION/AVAILABILITY STATEMENT
Unclassified - Unlimited
Subject Category 24
Availability: NASA CASI (301) 621-0390

13. SUPPLEMENTARY NOTES
Langley Technical Monitor: Eric Saether
An electronic version can be found at http://ntrs.nasa.gov

14. ABSTRACT

Current spacecraft implement relatively uncoupled material and structural systems to address a variety of design requirements, including structural integrity, damage tolerance, radiation protection, debris shielding and thermal insulation. This investigation provided an initial assessment of multi-functional sandwich composites to integrate these diverse requirements. The need for radiation shielding was addressed through the selection of polymeric constituents with high hydrogen content. To provide increased damage tolerance and debris shielding, manufacturing techniques were developed to incorporate transverse stitching reinforcement, internal layers, and a self-healing ionomer membrane. To assess the effects of a space environment, thermal expansion behavior of the candidate foam materials was investigated under a vacuum and increasing temperature. Finally, a thermal expansion model was developed for foam under vacuum conditions and its predictive capability assessed.

15. SUBJECT TERMS
Sandwich Composites; Structural Mechanics; Nonmetallic Materials; Space Radiation; Damage Tolerance; Stitching Reinforcement

16. SECURITY CLASSIFICATION OF:			17. LIMITATION OF ABSTRACT	18. NUMBER OF PAGES	19a. NAME OF RESPONSIBLE PERSON
a. REPORT	b. ABSTRACT	c. THIS PAGE			STI Help Desk (email: help@sti.nasa.gov)
					19b. TELEPHONE NUMBER *(Include area code)*
U	U	U	UU	184	(301) 621-0390